Wind Flow Structures and Wind Forces in Forests

Bryan Jonathan Marshall

Jesus College
University of Oxford

Trinity Term 1998

Wind Flow Structures and Wind Forces in Forests

Bryan Jonathan Marshall **Jesus College, University of Oxford**

Abstract of thesis submitted for the degree of Doctor of Philosophy, Trinity Term 1998

This thesis describes a series of 1:75 scale wind tunnel experiments investigating the wind flow over, and through, three different forest models and the resultant wind loading on individual model trees. The experiments were designed to lead to a quantitative assessment of the wind stability of the particular forest arrangements and also to permit a study of the coherent gust structures in the flow.

Forest canopy flow is dominated by a plane mixing layer flow regime with a shear layer close to the canopy top. It has been confirmed that data can be correlated usefully in terms of a shear length, L_s, related to the form of this shear layer. Frequency analysis has confirmed that the flow structures have the same frequency as the swaying of the tallest trees in each forest. A mechanism is proposed whereby upstream turbulence induces swaying of trees at and near the upwind edge region of the forest, which in turn perturbs the air in the unstable shear layer. This leads to a roll-up of the shear layer and the creation of coherent flow structures. Conditional sampling of the gust structures, using wavelet analysis, has also supported the theory of a plane mixing layer type flow. An eddy-pair structure was revealed, the arrangement of which accounts for the intermittent strong downward sweeps of air into the canopy that have been reported by many observers.

The large downward sweep of air was also shown to be responsible for the highest bending moments experienced by individual trees. Assessments of the different forest formations showed that in a forest consisting of a 50/50 mix of 200 mm and 100 mm model trees, gusts did not penetrate the lower forest. This arrangement should improve the protection of younger trees and may be worth investigating in field trials.

Acknowledgements

The journey taken in the creation of this thesis has been a long, sometimes difficult, but always enjoyable experience and I would like to personally thank numerous people for the help in making this work possible.

Many thanks to Dr. Colin Wood, my supervisor, who has picked me up many a time from the depths of thesis despair and brought me back to earth with solid fundamental engineering thinking. I am especially grateful for having a supervisor who has looked after my well being as well as my research.

Thanks to Dr. Barry Gardiner, my CASE supervisor at the Forestry Commission, for all the helpful advice and assistance in the course of this project, not forgetting the construction of 10,000 plastic trees!

I am indebted to Rex Belcher for all the writing of logging programs, his continual computer and tunnel assistance and many bad jokes! Also in the Wind Engineering Research Group, thanks to my old colleague Dr. Richard Marwood for taking me under his wing and explaining the mysteries of wind tunnel experiments. Thanks are also in order to his successor Sarah Nelmes for sound advice on many subjects and for making me feel grateful for not having to do field experiments.

Many thanks to Emma Hill for all the encouragement and help in getting this thesis to the final finishing line!

A mention also, for all my friends at my own college of Jesus and elsewhere, who made the whole Oxford experience so enjoyable.

Special thanks to my Mother, for all those years of caring support, and to my late Father, who I'm sure would have been equally proud of what I've achieved.

The thesis would not be possible without funding from the EPSRC and the UK Forestry Commission and assistance from Jesus College.

CONTENTS

Chapter 1: Introduction and Literature Survey

1.1 Introduction

Each year there is an estimated nine million pounds worth of wind damage sustained by forest plantations in the UK. The scale of this destruction in the UK, and elsewhere in the world, has led to investigation of the mechanisms and causes of mass tree instability during high winds. The study has brought together silviculturists, biologists, meteorologists and engineers in an attempt to understand some of the complex biological and physical systems that occur. Coutts and Grace (1995), provide a good review of this collaboration and its benefits.

It is recognised that the strength of the wind is not necessarily the most important factor of tree stability. A wind risk model, 'GALES', being developed by the UK Forestry Commission identifies some of the parameters that define tree stand stability. Factors such as soil types, water basins (before and after rains), geological and topographical features are extremely important. In addition, there is the complex issue of how different species of trees and plants interact and grow with the wind environment (the so-called 'Adaptive Growth Hypothesis' - Mattheck 1991), and how this can be modelled. For example, knowledge of local environment parameters can lead to predictions, and possible enhancement, of wood yield, quality and strength.

The majority of wind damage in the UK is represented by windthrow, that is, the overturning of the tree at the roots. The remaining damage is covered by branch failure and by stem breakage. Foresters are obviously interested to know how to reduce windthrow risk and are experimenting with plantation patterns and forests of irregular height. They therefore need to

know how the turbulence of the wind is structured over such forests and what the associated wind forces are.

The wind structure of forests is of interest not only to those concerned with trees. It also provides an opportunity to study fundamental turbulence structures over rough, porous and compliant surfaces. As explained in this thesis, it is believed that turbulent features in forest canopy flows are very similar to other shear flows in general.

The main subject of *this thesis* is concerned with the physical and fluid mechanical processes of wind above and within forest canopies and the forces exerted by wind on trees. The conclusions will be utilised to further improve the GALES model which it is hoped will decrease the risk of future catastrophic destruction.

1.2 Atmospheric Wind Flows

Whatever the nature of the ground surface, wind speeds are always reduced by friction near the ground. This creates an Atmospheric Boundary Layer (ABL). In neutral conditions (where buoyancy effects are negligible) the thickness of the boundary layer can be of the order of 2000 m. The ABL can be subdivided into two regions: the high Outer Layer and the Inner (or Surface) Layer which occupies approximately the first 200 m up from the ground. The Surface Layer is then divided up into the Roughness Layer and the Inertial Layer, as shown in Figure 1.1. It is these lower parts of the atmospheric boundary layer that are usually simulated in wind tunnels.

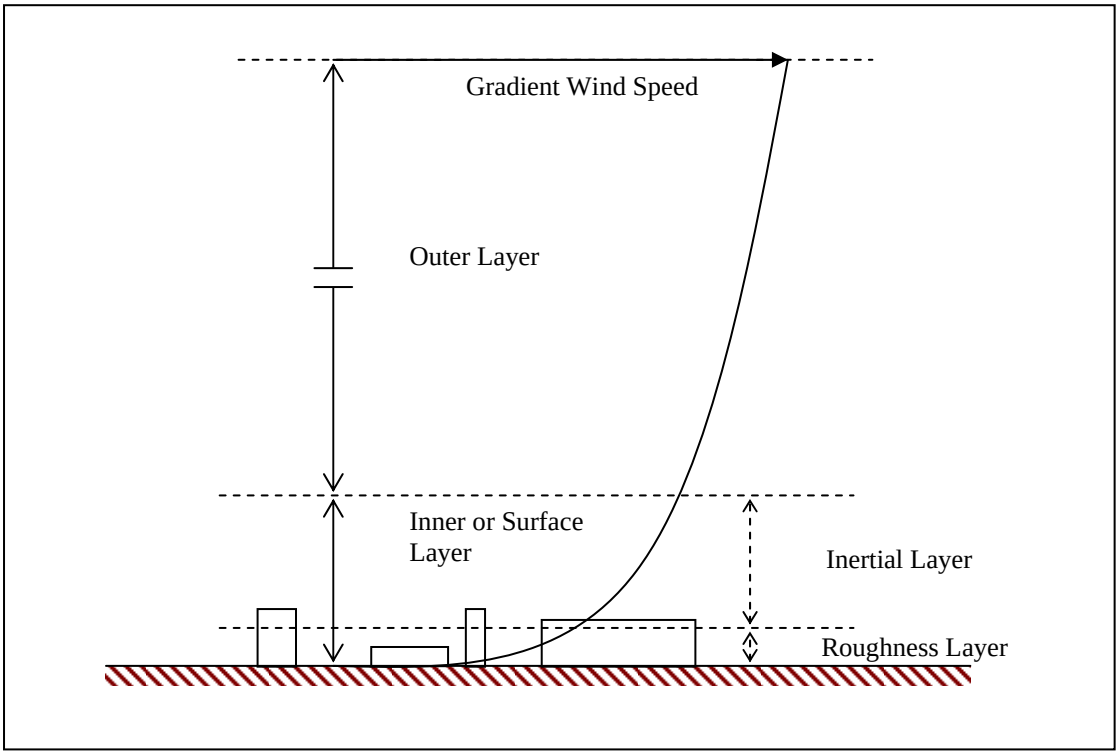

Figure 1.1 Atmospheric boundary layer subdivisions.

The properties of the Outer Layer have little dependence upon the nature of the surface whereas the Surface Layer has an approximately constant shear stress, when in equilibrium with the roughness of the surface. Reynolds stress ($-\overline{u'w'}$ - overbar denotes time average) can

be related to the frictional drag of a forest by considering the 2-D control volume flow in Figure 1.2.

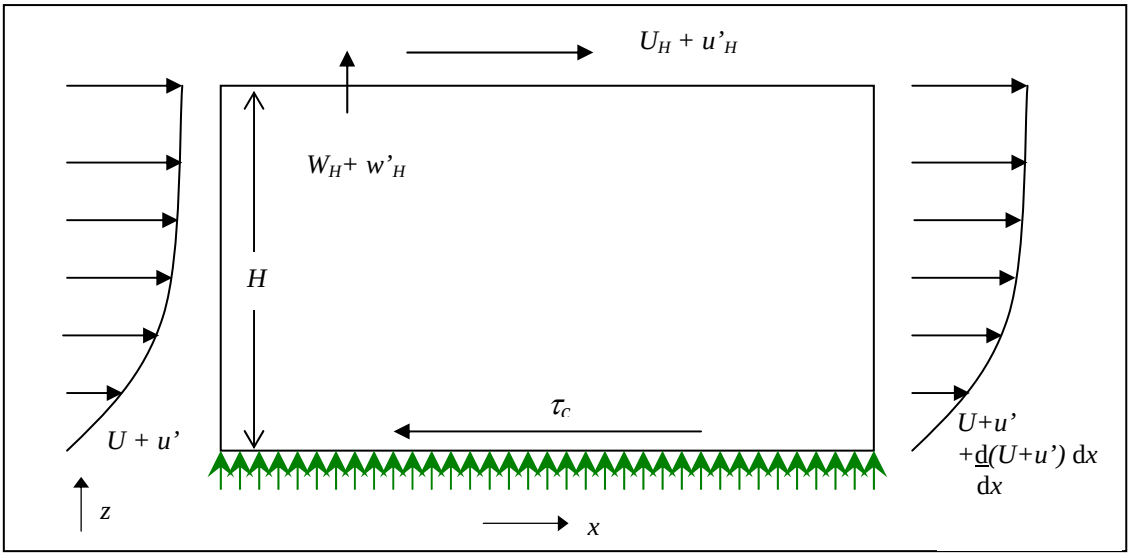

Figure 1.2 Control volume analysis of flow over forest.

The time averaged momentum balance equation for the control volume is:

$$U_H W_H + \overline{u'_H w'_H} + \frac{\tau_c}{\rho} + \frac{d}{dx}\int_{z=0}^{H} \overline{(U+u')^2}\, dz = 0 \qquad [1.1]$$

Where U and W are the mean streamwise and vertical velocities (respectively), u' and w' are the fluctuating streamwise and vertical velocity components (respectively), ρ is the air density and τ_c is the shear stress at the canopy top. The corresponding time averaged (thus- $\overline{u'} = 0$) continuity equation is:

$$W_H + \frac{d}{dx}\int_{z=0}^{H} U\, dz = 0 \qquad [1.2]$$

Equation 1.2 implies that if the mean velocity profile does not vary in the streamwise direction then $W_H = 0$. If in addition the turbulence profile does not vary in the streamwise direction Equation 1.1 reduces to:

$$\tau_c = -\rho\, \overline{u'_H w'_H} \qquad [1.3]$$

Equation 1.3 is termed the Reynolds stress. It represents the special case that when a boundary layer is spatially uniform the mean wind force on the trees below can be related to the time averaged velocity fluctuations at any height H above. A friction velocity u_* is defined in $\tau = \rho u_*^2$, thus:

$$u_*^2 = - \overline{u'w'} \qquad [1.4]$$

Velocity profiles in the surface layer follow a Logarithmic Law (Schlichting 1979) such that:

$$V = (u_* / \kappa) \ln[(z - d)/ z_0] \qquad [1.5]$$

where κ is the von Karman constant, usually taken as 0.4 in atmospheric boundary layers, and z_0 is the *roughness length* of the boundary layer. z_0 is commonly mistaken as the height of surface obstacles, but looking at Equation 1.5 more closely reveals that it is in fact is the y-intercept of a V against $\ln(z\text{-}d)$ plot.

1.3 Roughness Layer Interactions in the Forest Canopy

The lower atmospheric boundary layer is highly turbulent and the velocity fluctuations, more familiarly known as gusts, are responsible for the extreme wind speeds which can cause structural damage. Gusts may be described in purely statistical terms, but it is potentially more instructive, and certainly more challenging, to seek a physical explanation in terms of eddy structures in the turbulent flow.

Within the forest canopy or between buildings of a city, the flow cannot be generalised as a boundary layer, but is influenced by the local shapes of particular obstacles. It is in this region that forest canopy flows become distinctive because the roughness elements are compliant and not rigid.

One obvious benefit of a compliant system is that the effect of gusts can be observed visually. These visual observations appear as intermittent wave-fronts of displaced plants that translate quickly across the canopy top. In tall crops this gust phenomenon is called the *Honami gust* (Honami is Japanese for waving wheat, Inoue (1955a,b)). Finnigan (1979a,b) observed that when the gust arrivals are in phase with moving crops an impression of waves moving through the crop can be seen. Stacey *et al*. (1994) (and also the present author) witnessed this phenomenon in a wind tunnel, reporting that the model trees could be seen to shake violently as a gust passed through the canopy. Finnigan reported waves in groups of three or four and extending in the streamwise direction up to 5-8*h* downstream and 1-2*h* wide, where *h* is the canopy height. Gardiner (1994) reported a similar observation and judged a typical wave to extend 10*h* in the streamwise direction and be less than 2*h* across.

The apparent scaling of these Honami gusts with canopy height has led researchers to believe that gust structure depends upon properties of the tree or crop canopy. In other words, the canopy motion is not just a visual representation of oncoming turbulent wind but the motion itself influences the wind gusts. The impression is reinforced by the fact that the motions appear *coherent.*

The term coherent is applied to apparently well organised fluid motion events in an otherwise random turbulent flow. Examples of coherent structures are found in flows behind cylinders (Williamson 1996, Mumford 1983) and backwards facing steps (Simpson 1991). They have also been observed in jets (Mumford 1982), boundary layers (Head and Bandyopadhyay 1981) and plane mixing layers (Brown and Roshko 1974). Cantwell (1981) provides a useful review of a number of different coherent structures and associated flows. In a forest canopy,

the interaction between coherent gusts and trees are believed to be one the major sources of damage and uprooting (Gardiner *et al.* 1997, Baker 1995, Marshall *et al*. 1998).

1.4 Mean Flow Statistics in Forest Canopies

Figure 1.3 is reproduced from Raupach *et al.* 1996 (from here onwards termed 'Raupach *et al.*'). It shows the mean flow statistics for a range of real forest canopies and wind tunnel models. The statistics shown are:

U - the mean streamwise velocity

$\sigma_{u,\,w}$ - standard deviation (or rms) of the fluctuations *u'* or *w'* about the mean. A measure of the spread of fluctuations about the mean.

$Sk_{u,\,w}$ -Skewness (*i.e.* u^3/σ_u^3) of the turbulent fluctuations. A measure of deviation from the standard gaussian distribution and thus an indication of extreme positive or negative velocity fluctuation.

Kaimal and Finnigan (1994) originally found that with suitable scaling ratios canopy wind statistics have consistent similarities. Figure 1.3 shows that for quite dissimilar types of crop and forest canopies, velocity profiles become similar when scaled by the canopy height. This, together with related similarities in standard deviation and skewness profiles suggested universal turbulence mechanism for canopy flows.

The $\overline{u'w'}$ term and standard deviations give similar profiles when scaled by the square of the friction velocity, u_*^2, and friction velocity, u_*, respectively, at canopy height (Figures 1.3b, c and d). This suggests that any characteristic flow structures are related to the shear caused by

the canopy. This was first noted by Baines (1972). When studying corn crops he suggested that 'the turbulence within corn crops derive from eddies generated through shearing'.

There are some important points to note regarding Figure 1.3:

1.3a - The most obvious feature in the velocity profile is the inflexion point which is caused by the mean wind being slowed by drag from tree and plant parts. This represents an area of high shear between the slow lower flow and the faster upper flow.

1.3b - The constant Reynolds stress above the canopy top is a measure of the mean wind force on the trees below when in equilibrium, as stated in Section 1.2.

1.3c and d - The values of σ_u and σ_w are not constant in the canopy, indicating that the turbulence gust structure changes.

1.3e and f – The streamwise velocity skewness is positive at the canopy top whilst the vertical skew is negative. These two facts indicate a predominance of downward gusts with large streamwise speed.

Ratios of σ_u/u_* and σ_w/u_* near the canopy top are presented ranging from 1.5-2 and *ca.* 1.1 respectively. Raupach emphasises the fact that in the region of constant shearing stress well above a canopy (where $z > 2h$) the ratios σ_u/u_* and σ_w/u_* are expected to be approximately 2.5 and 1.25 respectively (Garrat 1992). However, it is uncertain whether these values were achieved in the wind tunnel, as the turbulence profiles presented do not extend to sufficient height.

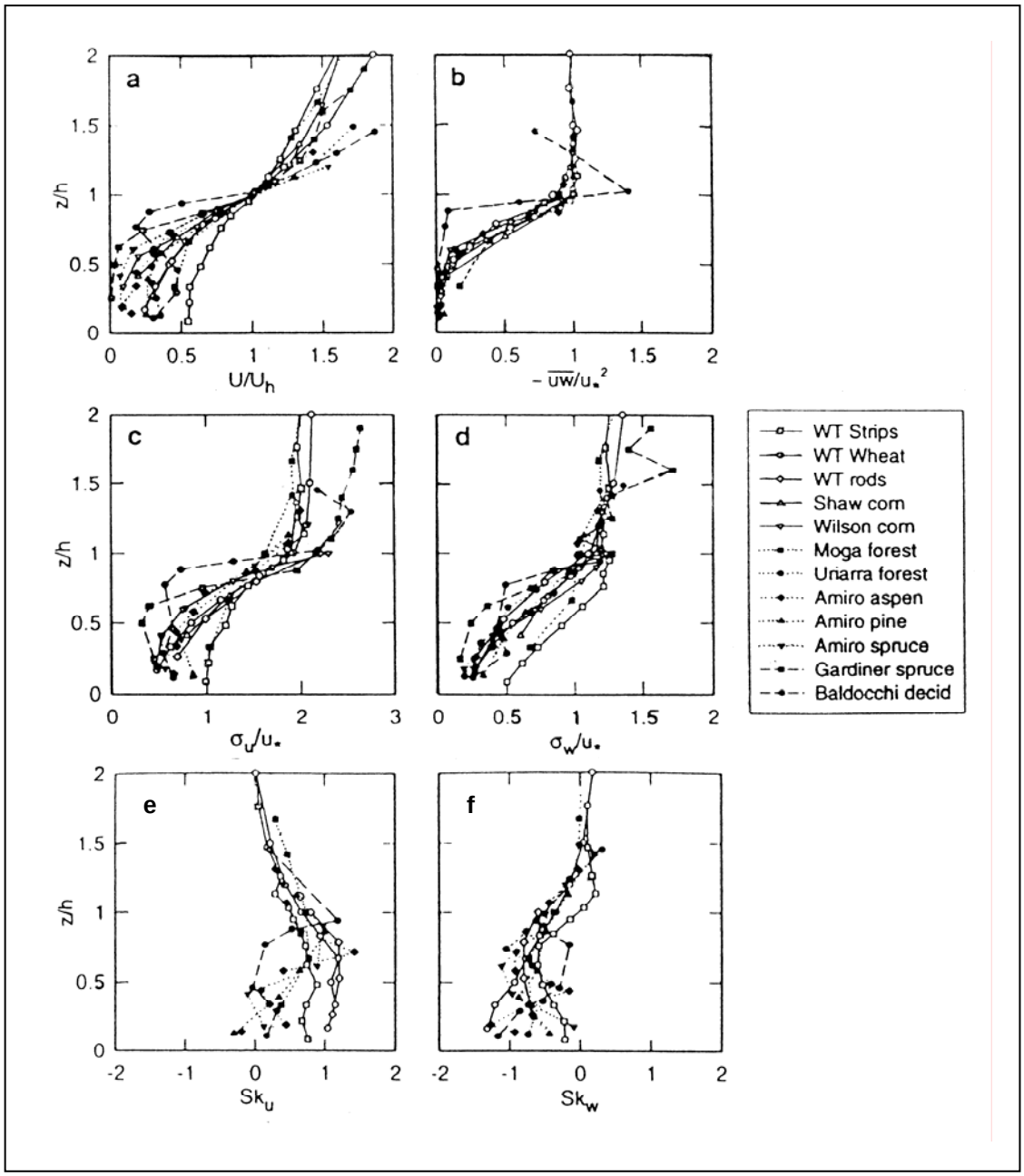

Figure 1.3 Reproduced from Raupach et al. 1996,
The collapsed mean velocity statistics of different types of crops (WT indicates wind tunnel tests). a) streamwise velocity profile, b) Reynolds stress, c) streamwise standard deviation, d) vertical standard deviation, e) streamwise skewness, f) vertical skewness.

1.5 Frequency and Length Scale Data

There have been numerous measurements of gust frequency spectra in canopies. For example, Finnigan and Mulhearn (1978), Baldocchi and Meyers (1988a,b), Gardiner (1994) and Irvine (1994) all used power spectra measurements of single point velocity components to identify the dominant eddy frequencies. Kaimal and Finnigan (1994) found that in the inflexion region of the canopy the frequency spectral peaks remain invariant with height. To compare results for different canopies the non-dimensional Strouhal Number was used:

$$Stouhal\ Number,\ S_T = \frac{nh_c}{U(h_c)} \qquad [1.6]$$

where n is the frequency (Hz), $U(h_c)$ is the streamwise velocity (ms^{-1}) at the canopy top, and h_c is the height of the canopy (m). Kaimal and Finnigan (1994) found the non-dimensional frequency peak to be S_T= 0.15 for the streamwise component and S_T= 0.45 for the vertical component. The physical meaning of such results had to be carefully interpreted since they were only single point measurements. Nevertheless, Finnigan (1979a, and b) correlated the streamwise spectral peaks with the streamwise separation between eddies in a moving corn field. Two point spatial correlations carried out by Shaw *et al.* (1995) suggested that gust size was of the order of canopy height. This added weight to the argument that the wind structure is strongly influenced by the canopy itself.

In the canopy region a secondary spectral process was termed a ‘spectral shortcut’ (Baldocchi and Meyers 1988b), whereby plant canopy movement tends to ‘chop’ the lower frequency eddies up into high frequency wake eddies. This caused attenuation at low frequency and amplification at high frequency. However, evidence of this mechanism remains inconclusive. Generally, in the canopy region, the streamwise frequency peaks increase with decreasing

height, whilst the vertical frequency peak remains the same (Seigner *et al.* 1976, Irvine 1994). This point is important and is explained in Chapter 4.

1.6 Modelling of Forest Wind Flow

The use of Computation Fluid Dynamics (CFD) is growing rapidly, but reproducing any type of turbulent flow is still extremely difficult. The inherent difficulty of solving the Navier-Stokes equations is the root of the problem and has led to a number of simpler models being produced. In canopy flows, both the mixing length and the κ- ε models have been used (Lee *et al.* 1994, Li *et al.* 1985, 1990). They tend to predict mean velocity trends reasonably well but are not very accurate overall. These models oversimplify the role of time-dependent coherent structures in flows and more experimental information is needed to improve them.

1.7 The Mixing Layer Analogy

As already mentioned, Raupach *et al.* suggested that the most important feature of the mean velocity profile above plant canopies is the inflexion point, see Figure 1.3a. In this region they observed that the mean streamwise velocity profile is very similar to that of a plane mixing layer. They then inferred that it was reasonable to assume other flow characteristics should be analogous to a mixing layer also.

A plane mixing layer is the term used to describe the flow when two parallel streams, with different velocities, are allowed to mix after being separated initially by a solid barrier (Figure 1.4).

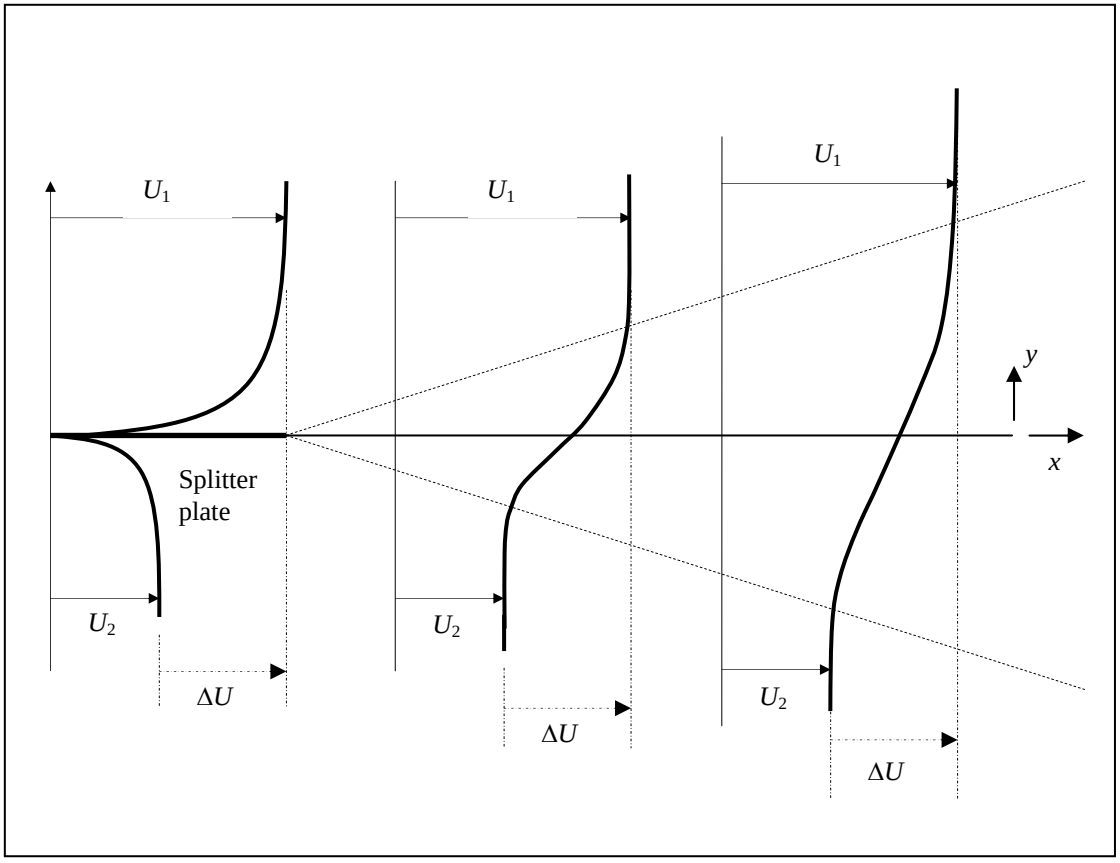

Figure 1.4 The development of a plane mixing layer.

U_1 and U_2 are the freestream velocities of the upper and lower boundary layers respectively, and ΔU is the difference U_1-U_2. A key parameter in the evolution of the mixing layer is the vorticity or shear depth, δ_w, (Brown and Roshko 1974) which is defined by:

$$\delta_w = \Delta U / (\delta U/\delta y)_{max} \qquad [1.7]$$

δ_w is assumed to increase linearly with distance downstream of the origin:

$$\delta'_w = \delta_w / (x\text{-}x_o) \qquad [1.8]$$

where x_o is a *virtual origin* of the mixing layer and δ'_w is the rate of growth of δ_w. In practice there is a small distance beyond the trailing edge of the splitter plate where the characteristic mixing layer profile forms from the two original boundary layers. The convection velocity, U_c, represents the speed at which the eddies move downstream and is equal to the mean of the two freestream velocities:

$$U_c = 0.5\ (U_1 + U_2) \qquad [1.9]$$

The classic visualisation experiments of Brown and Roshko (1974), an example of which is presented in Figure 1.5, showed clearly the coherent structures in the flow. It is these flow structures that are believed to be Honami gusts in plant canopies.

Figures 1.6a,b, and c present the mean velocity statistics associated with a typical mixing layer (from Raupach *et al*.). The vertical traverse height is normalised by the shear depth, δ_w. The standard deviation (or variance in this case) and skewness profiles are similar to plant canopy flows in the lower region of the layer. This similarity degenerates in the upper, high speed, layer where normal atmospheric boundary layer characteristics dominate.

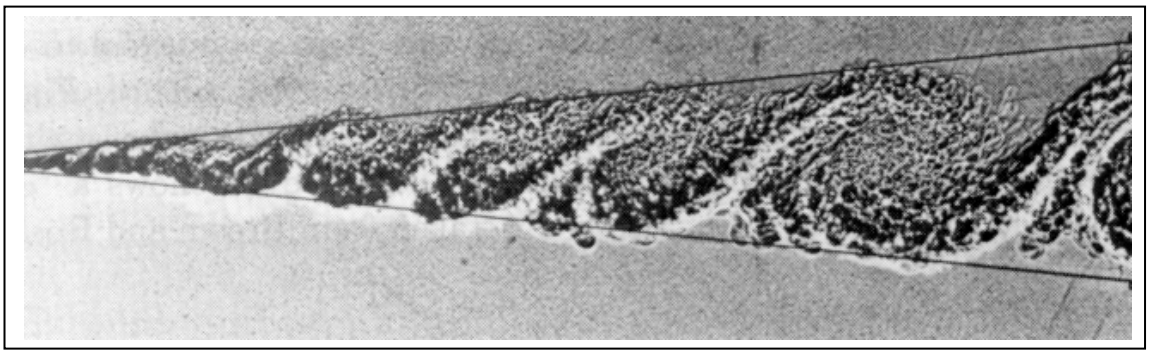

Figure 1.5 Spatial mixing layer reproduced from Brown and Roshko (1974) (with streamwise direction from left to right).

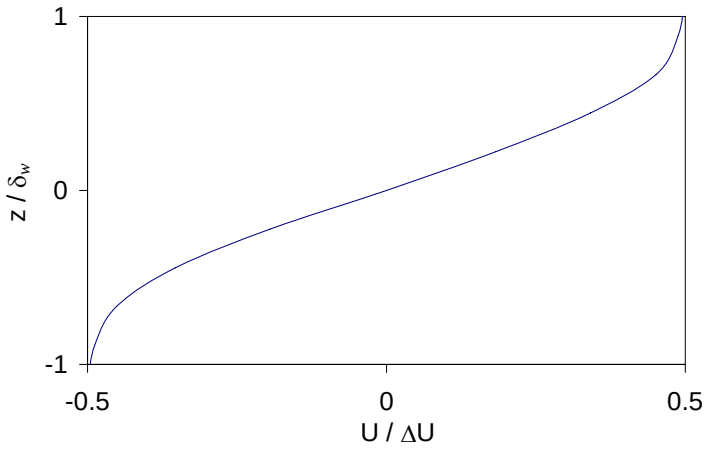

a) Velocity profile

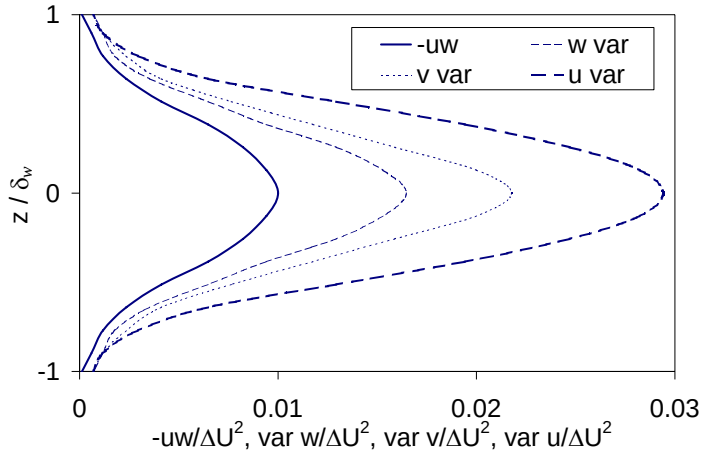

b) Variance profiles

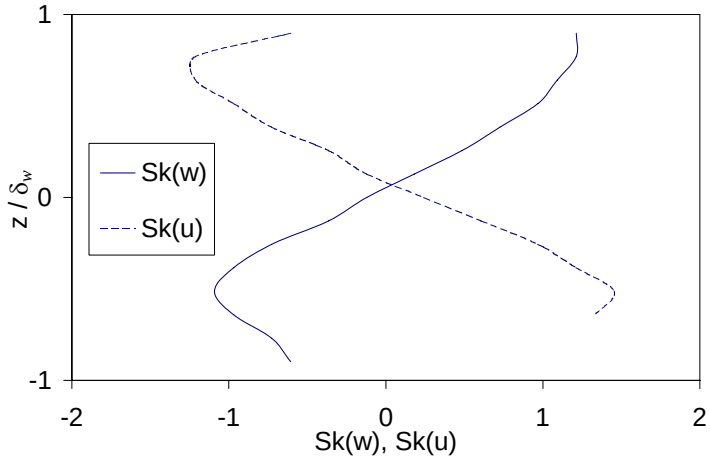

c) Skewness profiles

Figure 1.6 Typical statistical measures of a mixing layer (reproduced from Raupach et al. 1996).

1.7.1 Evolution and Structure of Mixing Layer Gusts

To study the formation of mixing layers in turbulent flows it is useful to consider the initial instability mechanisms of more fundamental flows. It is well documented that laminar shear layers are unstable (*e.g.* Schlichting 1979) past a critical Reynolds number, and leads to turbulence. Small disturbances are amplified and lead to a degeneration of parallel streamlines into a sequence of discrete vortices. This mechanism can be simplified and illustrated using discrete line vortices to represent a shear layer as shown in Figure 1.7. Each vortex induces a velocity on the surrounding vortices proportional to $1/r$, where r is the distance between vortices. If the shear layer is infinite and the vortices directly in line with each other, there will be no change in the layer since the downward and upper induced velocities will be equal. If however one of the vortices is perturbed, there will no longer be a balance and the disturbance will be amplified. In very low turbulence experiments, initial disturbances are due to waves known as Kelvin-Helmholtz (KH) waves. The presence of these waves cause the shear layer to roll up and form well structured ‘spanwise rollers’ (Acton 1976) as shown in Figure 1.8. These rollers are separated with wavelength equal to the initial disturbance.

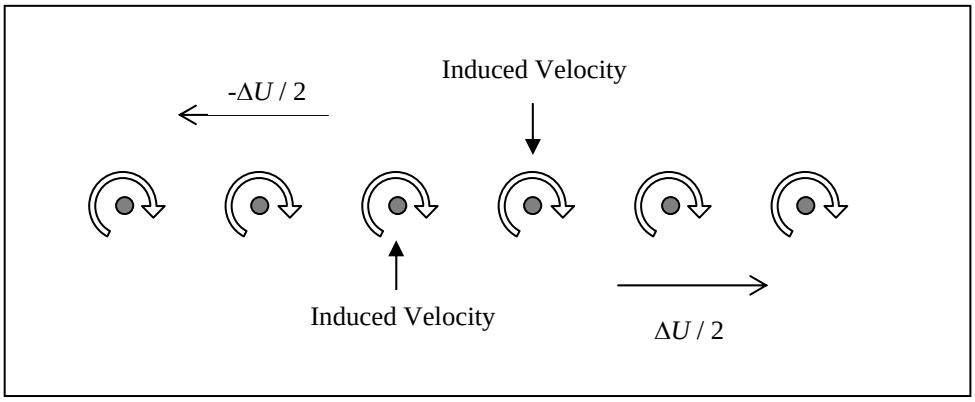

Figure 1.7 Shear layer represented by discrete vortices. Induced velocities of middle two vortices shown.

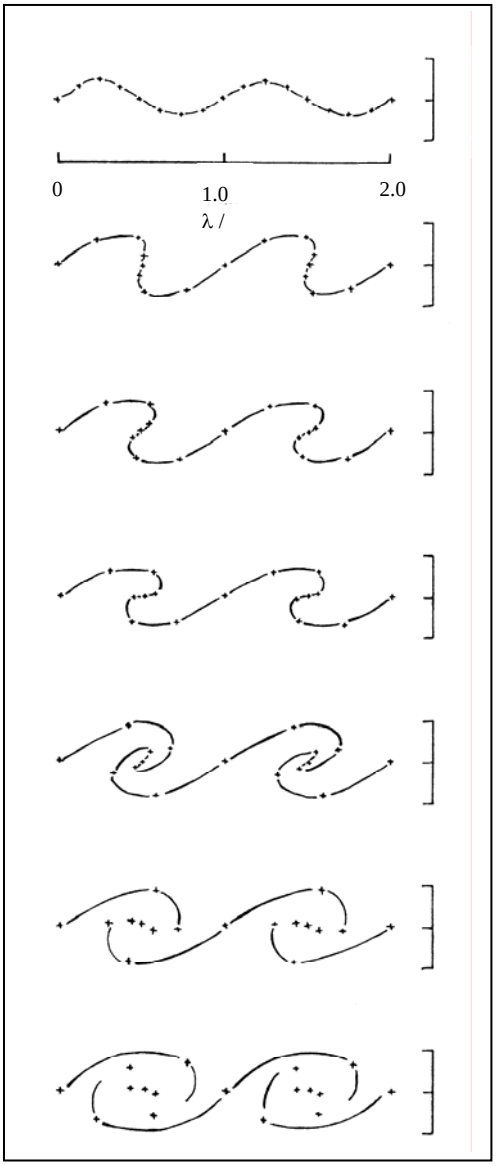

Figure 1.8 Roll up of discrete vortex line sheet (reproduced from Acton 1976).

This representation of shear layer instability by an agglomeration of small vortices into fewer, larger vortices is not the end of the story. The vortex lines themselves are unstable and do not remain straight in the spanwise direction. This three dimensional instability has been studied by Rogers and Moser (1992) at high Reynolds numbers (Re ≈ 10^6). The mechanism causes kinks in spanwise rollers in the vertical direction and streamwise vorticity emerges in the form of braids connecting adjacent roller pairs, see Figure 1.9. The kinked rollers tilt forward with spanwise vorticity concentrated in cups on the outer corners of the kinks.

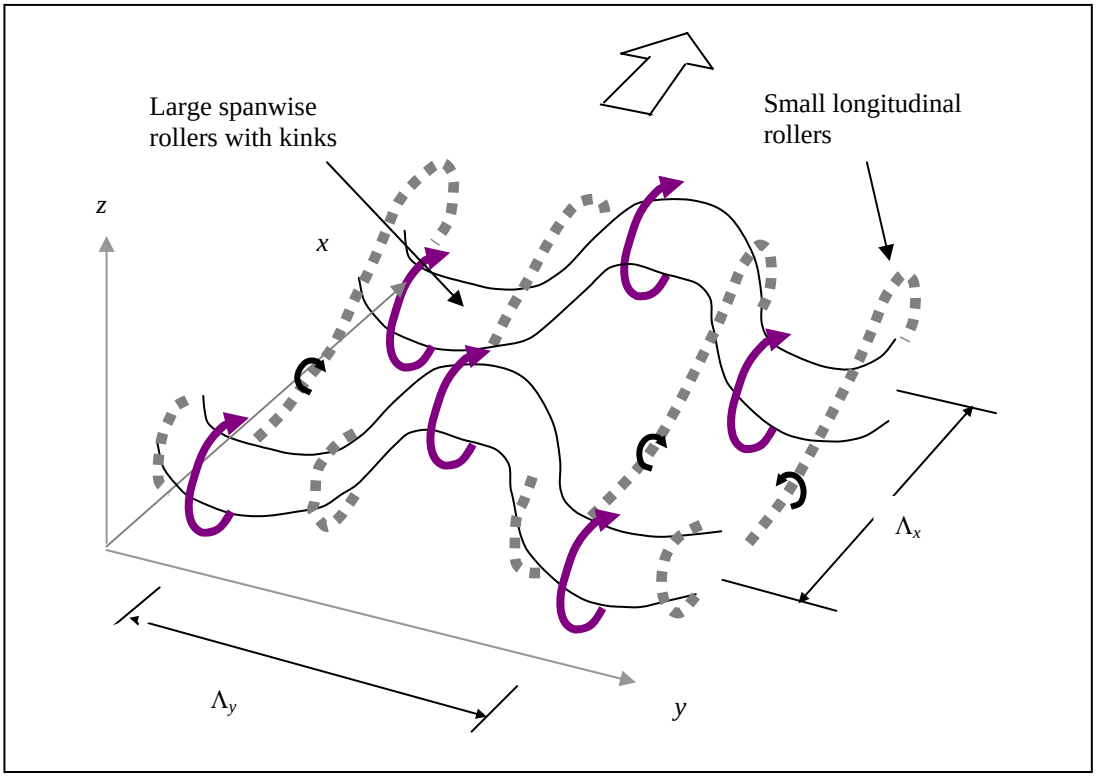

Figure 1.9 Diagram to illustrate the three-dimensional non-linear roll up.

Adjacent spanwise rollers start attracting each other and a stochastic 'pairing' process occurs where the eddies amalgamate and double in size (Brown and Roshko 1974, Ho and Huang 1982). Finally a fully developed state is established, which is of self-similar nature (a repeating pattern of flow that can be scaled) similar to those seen in most experimental visualisations (Figure 1.6 is two-dimensional view in the vertical-streamwise plane).

As can be seen in Figure 1.9, the initial wavelength of the disturbance dominates the features of the flow. The origins of the KH waves have been investigated by Michalke (1964, 1965) using linear stability analysis in the shear layer of the form $U(z)/U$ = tanh (z/h). Linear stability analysis assumes that a disturbance in the form of a wave-function is superimposed onto a flow stream function, in this case a hyperbolic-tangent profile. The eigenfunctions for the composite stream function are then evaluated and the fastest growing, most amplified mode determined. The fastest growing mode wavelength is, in terms of shear length (defined in Section 1.7.2), $\Lambda_x = 15.7L_s$ (Raupach *et al.*).

The attempt by Raupach *et al*. to apply linear stability analysis to canopy flow must be assessed with care. Linear stability assumes infinitesimal disturbances, whilst in canopy flows turbulence intensity can be up to 40%. Raupach *et al*. assumed that in these cases the turbulence is superimposed upon the mean velocity profile and it is that which is assumed to be unstable. In addition, Townsend (1976) asserted that in the presence of turbulence the initial disturbances are caused by the turbulence itself. The fastest growing infinitesimal disturbances, such as those reported by Michalke, may be damped by viscosity and the overall mechanism may favour stronger initial disturbances.

Experimentally, Wygnaski *et al.* (1979) demonstrated that even in the presence of strong random perturbations, primary large-scale vortices emerge downstream in turbulent mixing layers, whilst Brown and Roshko (1971) produced coherent structures in a wind tunnel mixing layer with Reynolds numbers of up to 3×10^6.

1.7.2 Properties of the Mixing Layer and Application to Canopy Flows

On the evidence presented, the chance of the formation of a mixing layer type flow in forest canopy conditions is highly plausible.

When applying the parameters of the mixing layer in terms of canopy flows, the lower boundary speed U_1 is assumed to be zero because of the presence of the wall. In practice, many stands have a high density of foliage located at the top with less below thus an increase in velocity is found underneath. Nevertheless, it was decided to ignore this localised increase of velocity because U_1 is defined as the freestream velocity far from the mixing layer. Therefore U_1=0 is a reasonable assumption.

On the high speed side of the shear layer it is more difficult to define U_2 because the shear continues to a great height. Consequently, it would not be practical to measure a freestream velocity at full scale or in a wind tunnel. To overcome this difficulty, Raupach *et al*. defined the *shear length* L_s using only the measurement of the low speed side:

$$L_s = U_c / (dU/dz)_{max} \qquad [1.10]$$

where U_c is the speed at inflexion height h_i and $L_s \approx \delta_w /2$.

Rogers and Moser (1992) found that for a separation wavelength, Λ_x, and shear depth, δ_w, the ratio Λ_x / δ_w was equal to 3.5-5 for fully developed flows. From compiled canopy results Raupach derived the value 4.05. This agreement gives further evidence for the mixing layer mechanism.

Irvine (1994) and Shaw *et al*. (1995) both used two point velocity correlations to calculate convection velocities of dominant flow structures. Both showed that the streamwise convection velocity is considerably faster than the predicted value of U_c (by as much as 80% according to Irvine) and therefore the use of Taylor's 'Frozen Turbulence' Hypothesis to calculate length scales from local mean velocities is invalid. To explain this, Finnigan and Brunet (1995) suggested that the magnitude of shear will be altered when a gust in the surface layer moves over the canopy top, increasing dU/dz and thus increasing the shear possibly to the point where the canopy gust evolves. Therefore, the canopy gust would only occur at high speeds, explaining the high convective velocities. This hypothesis is plausible but it does not take into account other effects on convection velocity, such as the induced velocity caused by vortex images with the ground plane. There are no studies of this aspect of canopy flow to date and there have been few noteworthy studies on the effect of ground presence on mixing layers. One exception is Wood and Bradshaw (1982,1984) who looked at the wall effects on the high-speed side of a mixing layer, far downstream from the initial splitter plate. They found that the effect of the wall was to stretch the stream and spanwise scales of the vortex structures.

Another aspect of ground presence on the mixing layer so far not studied, is the amount of entrainment into the layer that is possible with a bounded flow. Simpson (1991) showed that a mixing layer formed behind a rearward facing step drops and inevitably reattaches with the wall. This is believed to be due to the momentum exchange between coherent structures and the bound flow beneath. There is also evidence of a larger ratio of strong *sweeps* (or downsweeps) to *bursts* caused by coherent structures near a wall. Respectively, these terms refer to the large positive and downward excursions of fluid, and the upward and backwards

movement of fluid. The pattern of small bursts followed by large downsweeps are commonly observed in a forest canopy.

1.8 Trees and Tree Forces

The first section of this thesis was dedicated to the flow over and in plant canopies. I will now consider the actual forces experienced by individual trees and the possibilities of reducing risk from wind damage. Several authors have approached this problem with field, wind tunnel and theoretical studies.

The greatest risk to trees in a forest is windthrow, so a natural measurement is that of the bending moment at the base of the tree. It is difficult to model the complexity of a tree's movement, with bending in branches, stem and root. Therefore, Gardiner (1989, 1992) and others have tended to regard trees as simple cantilevers firmly rooted into the ground.

To allow vibration analysis with a single degree-of-freedom, some authors have also tried replaced the mass distribution with a point mass near the centre of the canopy. Enhanced models include details such as distributed stem mass (*e.g.* Wood 1995) and a root-hinge stiffness (Wood and Neild 1998, Baker 1995). Whatever the analytical models, measurements show that a tree appears to act as a simple damped harmonic oscillator in the form:

$$\frac{\mathrm{d}^2 x}{\mathrm{d}t^2} + 2\zeta\omega_n \frac{\mathrm{d}x}{\mathrm{d}t} + \omega_n{}^2 x = 0 \qquad [1.11]$$

where x is the displacement at small angles, ω_n is the natural sway frequency, and ζ is the damping ratio. Damping arises from hysteresis in the soil and timber and from the aerodynamic drag of the tree elements (see Section 3.4).

Stacey *et al.* (1994) modelled Sitka Spruce forests in the wind tunnel using aeroelastic tree models with scaled drag and swaying characteristics. He found evidence to suggest that wind induced resonant swaying motion significantly increased extreme base bending moments. Gardiner (1994) and Finnigan (1978) also found evidence to support this.

Although many measurements of velocities in forests have been made, deriving values of bending moment from velocity measurements is fraught with difficulties. Baker (1995) pointed that previous attempts by Meyer (1987) using a transfer function of $\overline{u'w'}$ spectra depended on a purely stochastic flow, whilst evidence now shows there are recurring coherent structures present in the flow. Instead Baker put forward a more appropriate model for a canopy flow based on a step input from an extreme gust. To add to these difficulties, there is the problem of considering the drag mechanism in a such a highly sheltered environment.

1.8.1 Spacing and Plantation Patterns

The largest problem associated with analysing plantation patterns is that any change to the patterns and spacing *etc.* may induce a change in the physical characteristics of a tree. Baker (1996) found that 'natural frequency is a function of tree spacing, with closely planted trees with near vertical main branches and constrained rooting systems having considerably lower values than those trees which are more widely spaced'. This is because trees grown in thinner plantation densities tend to have higher taper ratio (diameter at breast height / diameter at top), stiffness *EI*, and damping coefficient. Despite the physical difference caused by these adaptations, Gardiner *et al.* (1997) found that wind tunnel results, of the same tree model in different plantations, agreed closely with the field data.

These wind tunnel studies also demonstrated, as expected, that as the tree spacing increased the zero plane displacement height (the apparent vertical displacement of the atmospheric boundary layer velocity profile) decreased. It was also found that in mid-forest simulation the maximum normalised bending moment increases linearly with spacing to height ratio.

When a small area was thinned in the model forest it was found that mean moments did not increase, but the extreme moments did. This would suggest that gusts penetrate from above, whereas the mean flow does not have time to change significantly. This constitutes yet another piece of evidence to support the coherent gust mechanism.

1.8.2 Forces at the Forest Edge

Stacey *et al.*'s (1994) wind tunnel measurements at the forest edge showed, for the most closely spaced tree patterns, both mean and extreme bending moments were extremely large on the outer edge of the forest. These bending moments decrease rapidly over 1-2 tree heights downstream of the edge. Fraser (1962) similarly concluded a stabilised region was obtained approximately 2 tree heights downstream. However, he also observed that there was a slight rise in forces just before this region.

Stacey devised edge treatments to reduce the initial large bending moments. One of these was the tapering of the leading edge of the forest with smaller trees. This increased shelter and created a longer and less abrupt transition region for the flow to adapt to the new roughness.

Somerville's (1980) post-mortem of windthrow sites revealed that damage to forests is usually concentrated in the first 100-200 m downstream of the forest edge. Interestingly, observations of damaged stands typically show that for older trees (> 25 years for *Pinus*

Radiata) the very edge group of trees are left intact. This is possibly explained by the fact that the edge trees, being permanently exposed to winds, grow to be stronger than the inner trees.

Chapter 2: Aims and Experimental Plan

Chapter 1 examined the present knowledge and ideas about forest flows. Chapter 2 now presents how this thesis will test and expand those ideas.

2.1 Irregular Height Forests

Seeking to apply the knowledge of the flow over plant canopies and the associated forces, foresters have been keen to devise new methods of minimising windthrow risks. Foresters are now aware that the vulnerability of a tree varies with its age, Quine (1995). Thus different ages of trees will have different threshold windspeeds. Applying this understanding, it has been suggested that if a forest consists of stands planted at different time intervals, then the total risk due to a gale will be reduced. The reasons for reduced risk, in terms of the turbulent structure of the flow, tree resonance or structural adaptation, has not been explained. This thesis aims to address the first two of these issues, using wind tunnel tests of forests of irregular height. The Forestry Commission was specifically interested in two types of forest layout termed the *group selection* forest and the *random* forest. These are explained in fuller detail in Section 2.2.

The evidence for Raupach *et al*.'s mixing layer flow analogy presented in Chapter 1 is compelling, and the idea provides a platform on which to study the similarities between three different forest configurations. It becomes evident that there are three main points that need addressing in this project.

- To investigate the applicability of the mixing layer analogy as a universal flow mechanism in different forests.

- To acquire useful information for the Forestry Commission on the forces experienced in different forests.
- Finally, to tie up the two issues raised above, to investigate a possible interaction mechanism between flow structures and tree forces.

The way in which these issues have been explored in this thesis has been highly dependent upon the facilities and equipment that were available. To help understand the strategy and final direction the experimental study took, the next section briefly describes these facilities. Full details of the equipment used are described in Chapter 3.

2.2 Measurement and Experimental Facilities

There are obvious difficulties associated with field testing, such as finding a suitable forest and wind location, making instruments work in the field, limited height (and expense) of instrument towers, and of course waiting for the wind to blow! Wind tunnel testing is seen to be a more convenient, controllable and flexible method to gather new detailed data.

The wind tunnel at Oxford was already set up for studying forests following the work of Stacey *et al.* (1994). They used a 1/75th scale Sitka Spruce forest which consisted of 200 mm model trees with correctly scaled drag, damping ratio, and natural frequency. Bending moments on the trees were measured with a miniature strain gauge balance.

To have forests of irregular height, new trees had to be designed to complement the existing 200 mm ones. The group selection forest, mentioned above, contains trees of two different heights in an alternate ‘diamond pattern’ (see Table 2.1). This is representative of a forest with one tree group far older than the other. The belief is that the shelter provided by the

larger trees will decrease wind risk to vulnerable young trees. The younger trees may also provide a form of shelter for the older trees.

The random forest is a more complex forest, with 6 different tree heights (in the form of 5 trees and a space). It is far more representative of a natural wild forest, diverse in age. The positions of model trees in the random forest were generated with a random number algorithm in an Excel spreadsheet. An equal number of model trees of each height were assigned along each row and then randomised in plantation order as dictated by the spreadsheet. The result was a 'pseudo random' pattern which ensured a reasonably homogenous pattern, but with a random element. For simplicity it will be termed from here onwards as the 'random forest'.

In addition to the work with the two irregular forests, tests were also carried out on a uniform forest. This was for control purposes and also to repeat the experiments of Stacey in greater detail. Table 2.1 summarises the plantation patterns used in the experiments. Photographs of each model forest are presented in Figures 2.1-2.3.

Forest Pattern	**Description**
Uniform	200 mm high trees, for repeatability testing of original results.
Group Selection	100 mm and 200 mm high trees. Arranged in continuous 'diamond pattern' e.g.: ○ ● ○ 100 mm ● ○ ● 200 mm ○ ● ○
Random	100, 150, 200, 250, 300 mm trees and spaces in a random arrangement.

Table 2.1 Description of the various forest plantation patterns.

Stacey made most of his velocity measurements with standard hot-wires but some, particularly near and within the canopy, were made with a Laser Doppler Anemometer (LDA). The LDA is capable of taking measurements in high turbulence intensity and reversed flows, unlike hot-wire anemometers. In addition the LDA is robust and it is not damaged when hit by swaying tree models. A photograph of the LDA probe is shown in Figure 2.4.

Both hot wires and LDA's are limited to single point measurements and reveal little of the structural nature of turbulence. Alternative techniques have been developed that allow measurements of the 2-D flow field, such as Particle Image Velocimetry (PIV). This is a relatively new flow measuring system that derives velocities by analysing successive two-dimensional flow field video images (Adrian 1986). PIV is extremely useful for detecting coherent structures in the wind tunnel but unfortunately was not available for this study. Thus alternative methods of discovering the structure of the flow using the available equipment had to be devised.

2.3 Approach

With the available wind tunnel, forest set up and instrumentation an overall approach to meeting the three objectives stated in Section 2.1 was defined as follows:

To investigate the applicability of the mixing layer analogy as a universal flow mechanism in different forests:

Mean velocity statistics were needed to compare data with real forests and check the applicability of Raupach's scaling suggestions. Measurements were taken with the LDA in a

mid-forest and forest edge situation, thus allowing the study of fully developed and initially forming canopy flows. To obtain some idea of the structure of the flows, gust frequency analysis was applied to these measurements. These results are presented in Chapters 4 and 5.

To acquire useful information for the Forestry Commission on the forces experienced in different forests:

The miniature bending moment balance allowed the forces on the model trees to be assessed. Thus measurements were taken in the three forest configurations on the different types of trees. Once again measurements were made in mid-forest and forest edge scenarios and results were analysed to assess the usefulness of the forest configurations. The method of extreme value analysis was used to differentiate between mean and gust wind forces. These results are presented in Chapter 6.

Finally, to tie up the two issues raised above, to investigate a possible interaction mechanism between flow structures and tree forces:

This proved a very difficult problem to solve with the available equipment. A method was devised of piecing together single point LDA velocity measurements to form a 2-D velocity field. This was achieved after a long experimentation period with conditional sampling and wavelets. The method allowed a correlation to be made between gust structure and extreme bending moments on trees and is presented in Chapter 7.

Figure 2.1 Uniform forest.

Figure 2.2 Group selection forest.

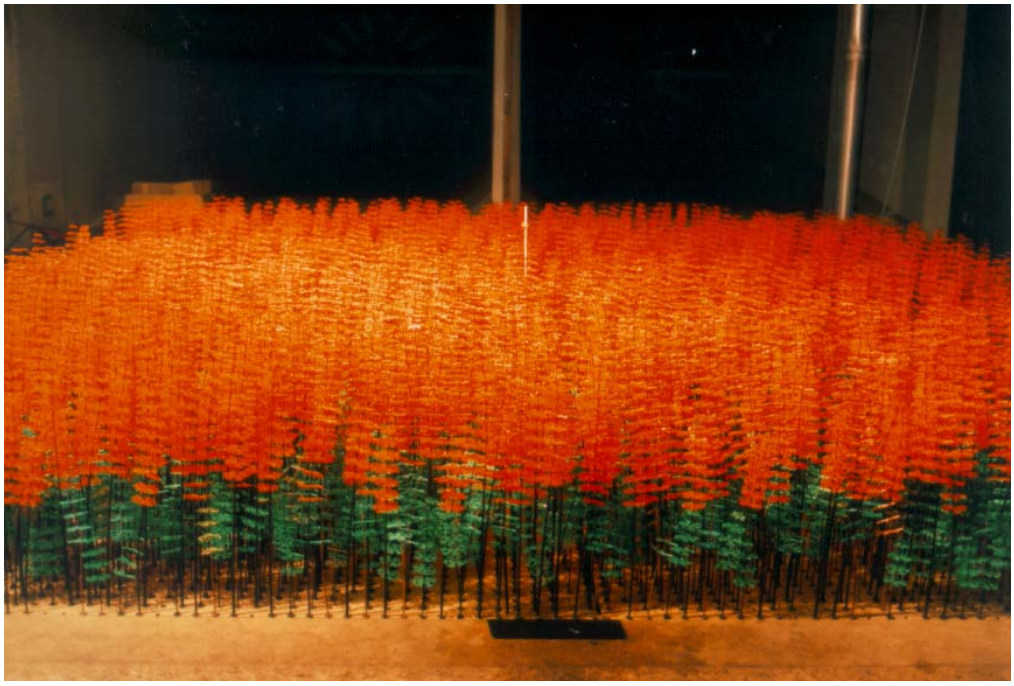

Figure 2.3 Random forest.

Figure 2.4 LDA probe and support.

Chapter 3: Experimental Methods

3.1 Wind Tunnel

All the work presented in this thesis was carried out in the Oxford University 4 m x 2 m environmental wind tunnel, where an artificial atmospheric boundary layer can be simulated at 1/75th scale. Larger scale models are not well reproduced because they require some eddies larger than the cross section of the wind tunnel. The layout of the tunnel is presented as shown in Figure 3.1 and is described in detail by Wood (1977).

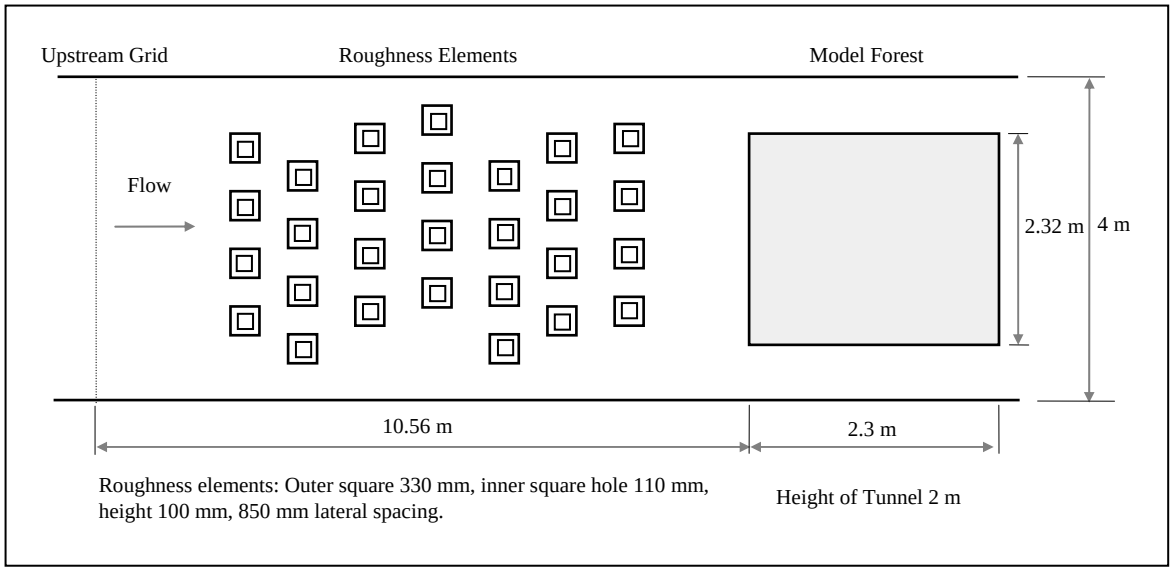

Figure 3.1 Plan view of the Oxford University Environmental Wind Tunnel.

The boundary layer simulation is developed using an upstream grid (see Figure 3.2) and roughness elements placed on the tunnel floor. The effect of the roughness elements can be represented by a surface roughness parameter z_0 (Equation 1.5).

The flow in the centre of the model area was measured using a Dantec 55 series anemometer with P01 Hot-wire probe. The measured horizontal mean velocity profile, turbulence intensity profile and frequency spectra for all tunnel boundary layers were compared with simulation targets derived from full scale data correlations published by the Engineering

Sciences Data Unit (ESDU International Ltd.) in their Wind Engineering Series (items 82026, 83045, 84011 and 85020).

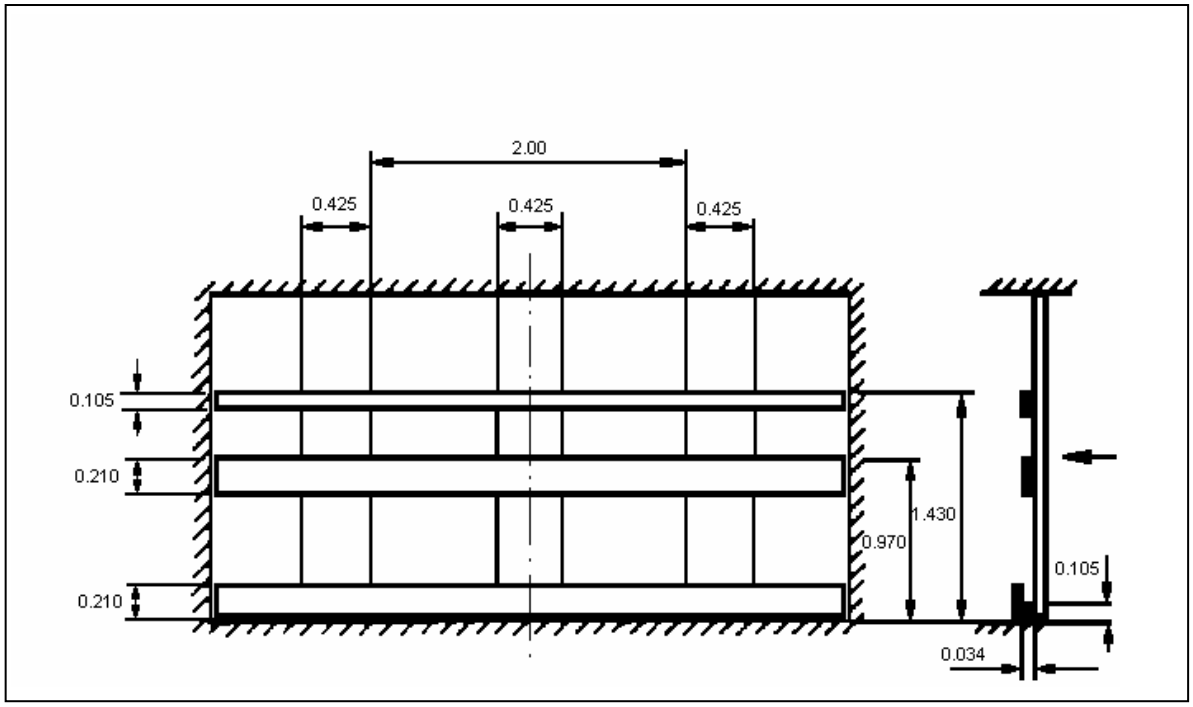

Figure 3.2a) Grid for forest edge z_o=0.05 m simulation. All dimensions in metres.

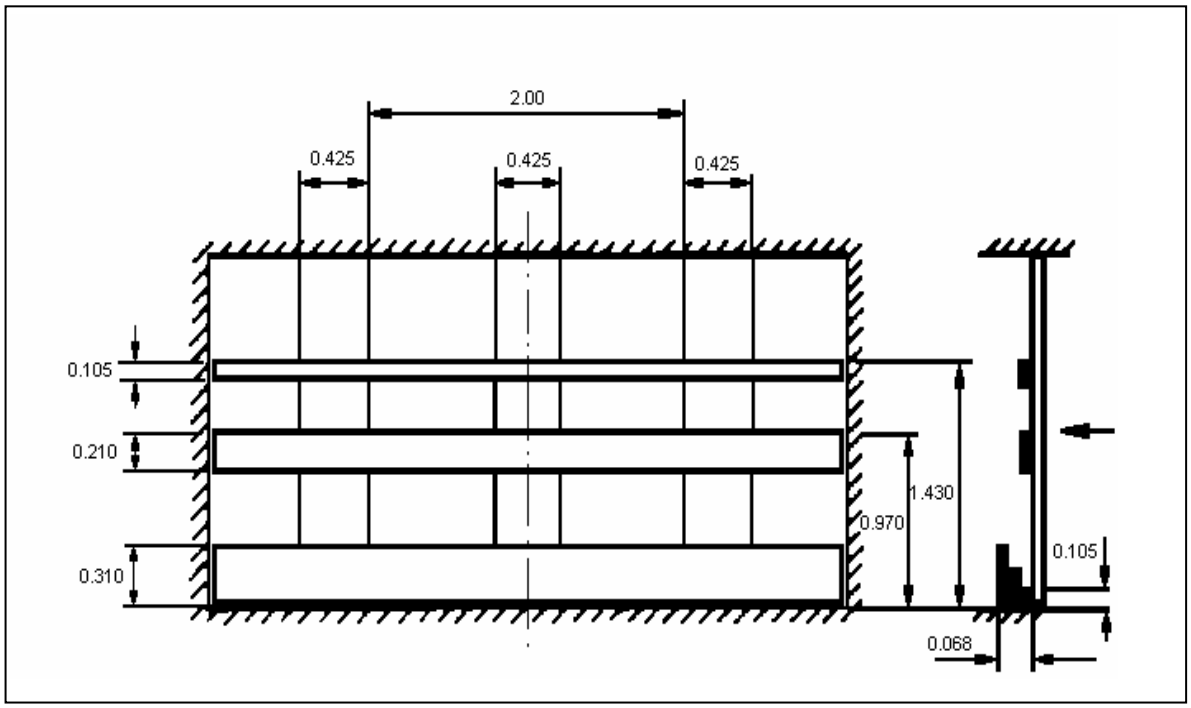

Figure 3.2b) Grid for mid-forest z_o =0.5 m simulation. All dimensions in metres.

There is a general routine which is followed whilst setting up the boundary layer in the wind tunnel.

- First the model usually occupies the turntable area of the wind tunnel (indicated by the forest section in Figure 3.1). With the model in place it is not possible to measure directly the velocity profile so an alternative method of establishing the profile is desired.
- The alternative method is to assume that the desired roughness ends at the start of the turntable and there is a distance of known roughness to the centre of the turntable. Thus the velocity profile measured at the centre of the turntable represents the transitional boundary layer from rough to smooth.
- ESDU algorithms allow this change to be calculated and a full-scale velocity profile is compared to the wind tunnel velocity profile. From this the original roughness before the turntable can be determined.
- The model can then be placed back onto the turntable with the desired upstream roughness.

3.2 Boundary Layers for Forest Experiments

In 1994 Stacey originally developed two 1/75th scale flow environments for the forest model. The first is termed a *forest edge* simulation of roughness z_0 = 0.05 m (full scale) which is appropriate for wind flow over open farmland. The velocity and turbulence intensity profiles measured at the turntable centre are shown in Figures 3.3a and b. The power spectra for two heights are presented in Figure 3.4, and show that frequency scales are quite well matched at the forest height (200 mm) but are not so good above the forest (>380 mm).

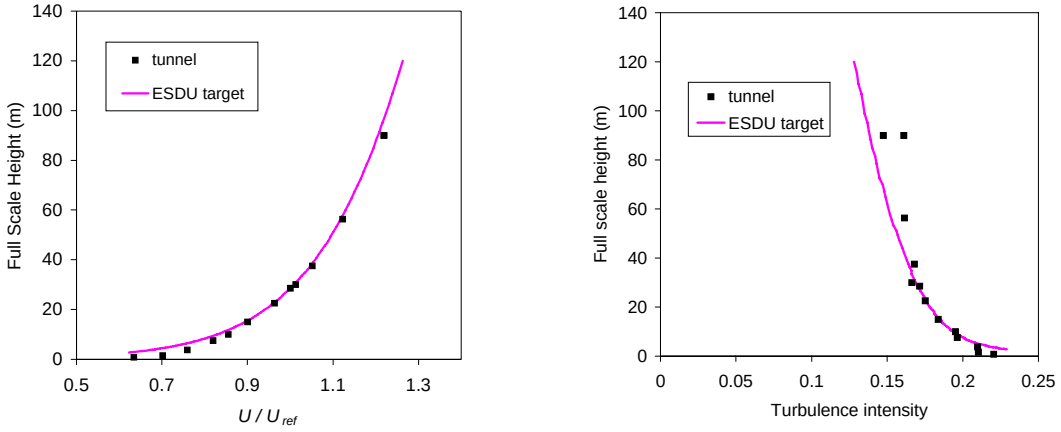

Figure 3.3 Forest edge wind simulation a) Velocity profile b) Turbulence intensity profile.

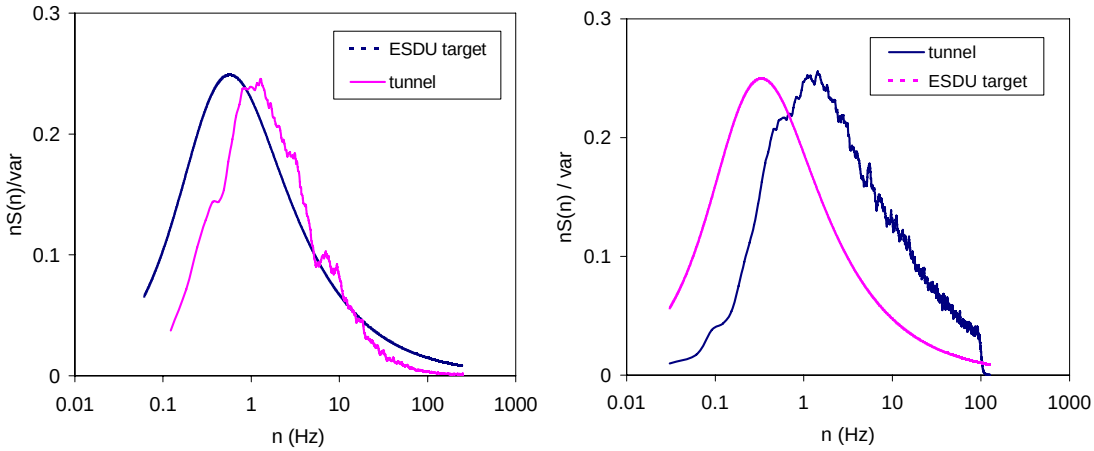

Figure 3.4 Forest edge wind simulation power spectra a) at 200 mm b) 380 mm.

The second flow developed by Stacey had z_0=0.5 m and is termed the 'mid-forest' simulation. This simulation is used to provide the scaled turbulence and mean velocity profile that would occur in the fully developed flow above a 15 m high, full scale forest. Using the method described above to determine the upstream roughness, the small section of the forest wind tunnel was placed on the empty turntable to create a theoretically seamless roughness surface. Of course, in reality the representation remains imperfect in that the compliant nature of the trees is not replicated over the entire floor. Nevertheless the results from the flow appear to agree well with the field data of Gardiner *et al.* (1997).

Figure 3.5 shows the velocity and turbulence intensity plots measured over the centre of the empty turntable. The fit of the data points with the target lines is good and note these profiles have a clear kink where the local smooth-wall boundary layer grows under the generalised rough-wall boundary layer after transition. The power spectra plots in Figure 3.6 once again show a good fit of measured and target data at z =200 mm but deviate from the ideal target at z = 380 mm.

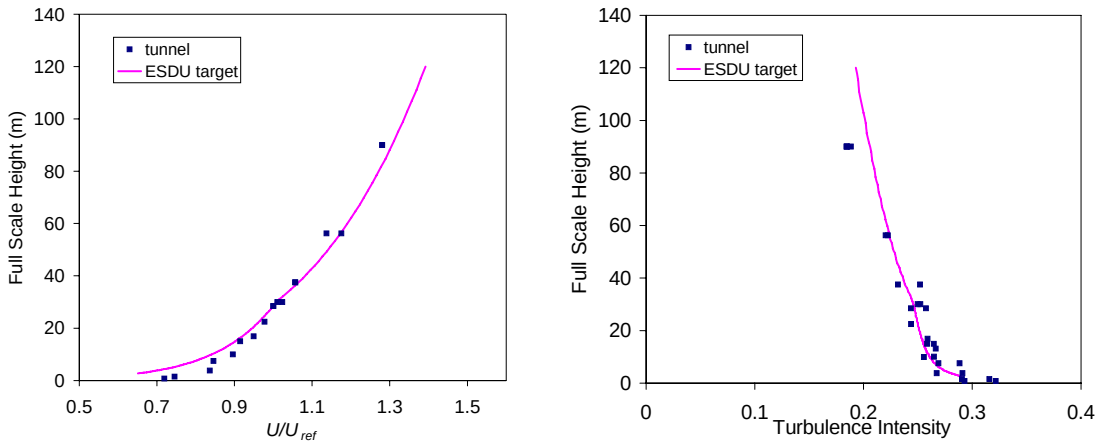

Figure 3.5 Mid-forest wind simulation a) Velocity profiles b) Turbulence intensity profiles.

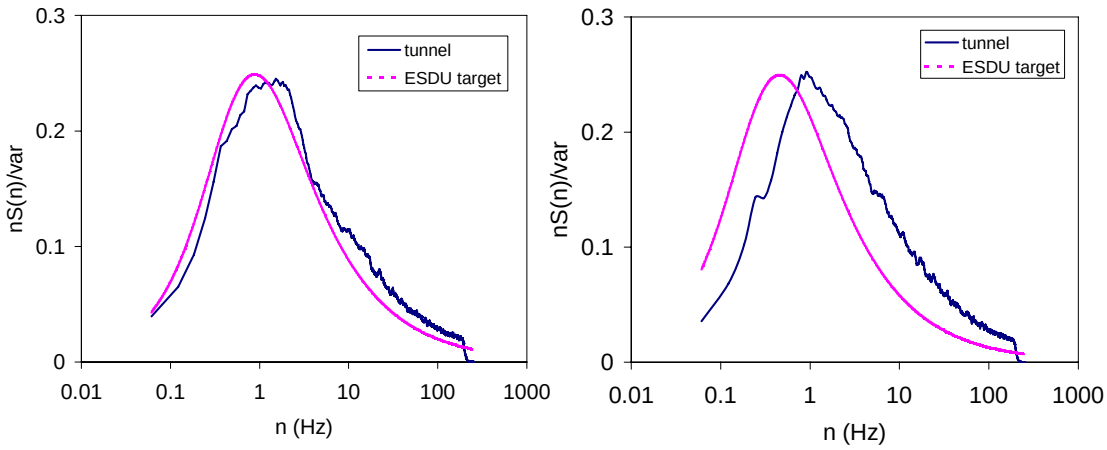

Figure 3.6 Mid-Forest wind simulation power spectra a) at 200 mm b) 380 mm.

Stacey *et al.*'s (1994) original experiment was designed to relate to the full-scale data of Gardiner (1994) which had a reference velocity at height 28.5 m in the centre of a large fetch forest. The equivalent scaled height in the wind tunnel was 380 mm. The reference velocity at that height was used to normalise all measurements for each run and thus eliminate drift in wind tunnel speed. It was not practical to measure at that height for every measurement with the model present and so the wind tunnel has a reference pitot-static tube positioned 1.6 m upstream from the turntable centre, and 0.6 m from the wind tunnel wall. A factor V_{tun} / U_{ref} was used between the pitot measurement and reference height measurement in the z_0=0.5 m mid-forest simulation. U_{ref} could then be calculated from the pitot reading.

Having established these relationships it was possible to compare data from the model forest with data from a full scale Sitka spruce forest (Gardiner 1994) as well with the ESDU target line, as is shown in Figure 3.7. The displacement height (the height to which the logarithmic profile is theoretically displaced over rough surfaces) of the ESDU target was taken to be 13 m. The results were in good agreement and instill confidence in the use of the wind tunnel for this type of study.

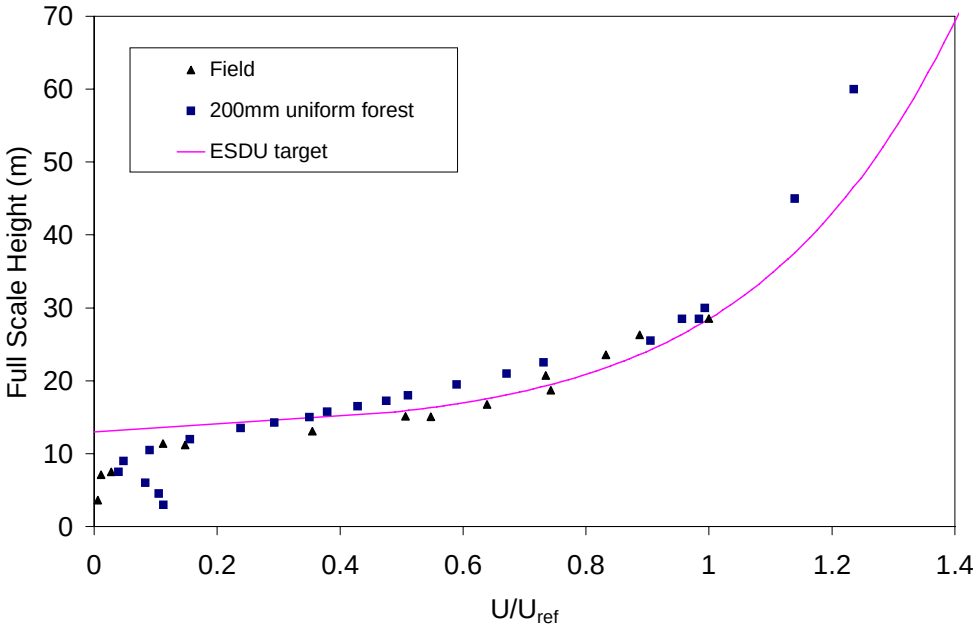

Figure 3.7 Comparison of model and field data.

However, profiles of $\overline{u'w'}$ values (Figure 3.8) over the forest were not as they should be. For a spatially uniform flow $\overline{u'w'}$ should be invariant with height and equal to the canopy shear stress (see Figure 1.2). However, this was not thought detrimental to the study for the following reasons:

- Mid-forest velocities and bending moments presented in Chapters 5 and 6 suggest that both types of measurements reach a maximum plateau near the centre of the forest.
- Ratios of σ_u/u_* and σ_w/u_* at tree top height are very close to generic values of full-scale canopies near equilibrium. Thus this would suggest that flow in the canopy and in the equilibrium layer (see Chapter 1) is correct despite the fact that the flow far above is not.
- If the simulation is the same as Stacey *et al.*'s, then results from this study may be compared to results from their experiments (*e.g.* comparison with thinned density forests in Chapter 6).

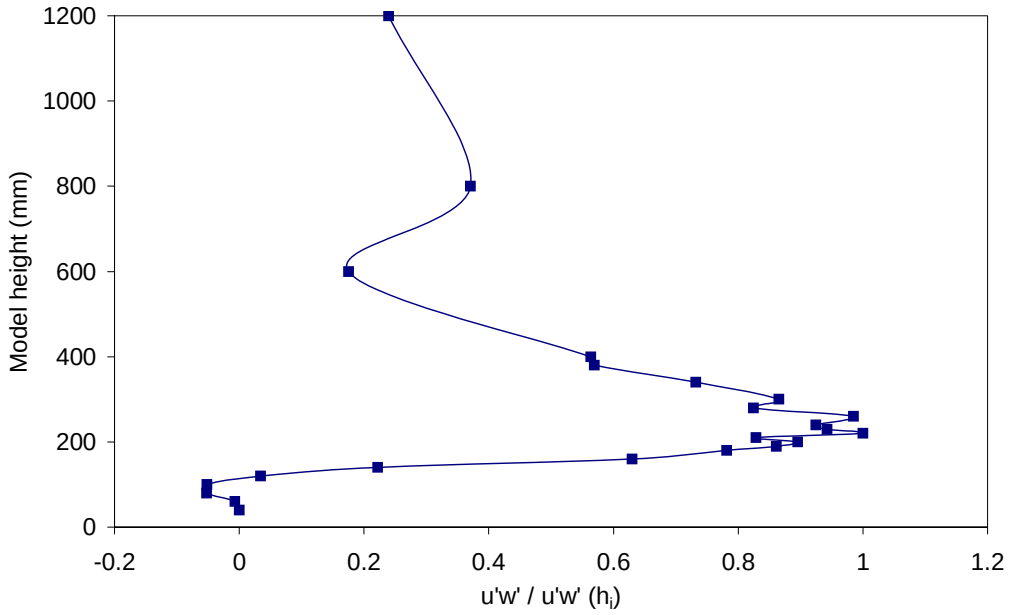

Figure 3.8 Reynolds stress profiles over and in the uniform mid-forest.

3.3 Model Forest

In the UK, Sitka Spruce planting is usually dense, approximately 3500 trees per hectare. This corresponds to a spacing of approximately 1.7 m. In the present 1/75th scale model forest, 10,816 (104 x 104) model trees were placed in pre-drilled wood boards with 23.1 mm spacing. The boards were interlocking and could be reconfigured to leave spaces for model bending moment balances. The boards were levelled on the windward side with a low inclined ramp.

3.4 Design of Model Trees

The original design of the aeroelastic trees posed difficult problems. The non-dimensional parameters that were identified by Stacey *et al.* (1994) are shown in Table 3.2. Stacey *et al.* designed trees of heights 190 mm, 200 mm and 210 mm to reproduce a full scale forest with average height of 15 m, but with some natural variation in growth. Variations in properties

between the different types of tree are described later in this chapter but for the moment only average properties are shown in Tables 3.1 and 3.2.

Absolute variables	Symbol	Full Scale	Model
Height (m)	H	15	0.2
Total Mass (kg)	M	211.8	1.04×10^{-3}
Natural Sway frequency (Hz)	F	0.33	5.2
Reference mean wind speed (ms^{-1})	U_{ref}	30	6
Nominal air density ($kg\ m^{-3}$)	ρ	1.225	1.225
Nominal air viscosity (Pa s)	μ	1.8×10^{-5}	1.8×10^{-5}

Table 3.1 Absolute values of variables.

Name of Parameter	Non-dimensional Parameter	Full Scale Value	Model Value
Tree Characteristics			
Mass	$M / \rho H^3$	0.051	0.102
Natural sway frequency	fH / U_{ref}	0.165	0.173
Still-air damping ratio	ζ	0.048	0.05
Drag Coefficient in uniform flow U	$D / (½\ \rho U_{ref}^2\ H^2)$	Equation 2.4 (0.018 at 30 ms^{-1})	0.018
Wind Flow			
Reynolds Number	$\rho UH / \mu$	3.1×10^7	8.2×10^4
Result of Experiment			
Bending Moment Coefficient at base of tree	$Q / (½\ \rho U_{ref}^2\ H^3)$	**	**

Table 3.2 Identification of non-dimensional parameters.

Flow characteristics and aerodynamic forces are dependent upon the Reynolds number $\rho Ud / \mu$, where ρ is the density of fluid, U is the mean velocity, d is the characteristic dimension and μ is the viscosity of fluid. When the Reynolds number is not matched between full-scale and model flows, details such as drag coefficients are usually incorrect. In wind engineering experiments, the scale is inevitably very small (in this case 1:75), but unfortunately it is impossible to increase the wind speed by a corresponding factor. As Table 3.2 shows, the wind tunnel Reynolds numbers are usually too low by two or more orders of magnitude. To overcome this problem a manageable wind speed was chosen (6 ms^{-1}) and the tree models were designed with a distribution of branch area that gave the correct drag coefficient.

When the wind tunnel speed was chosen, the natural sway frequencies of model trees were calculated to match the full-scale non-dimensional frequency (Strouhal Number). The natural sway frequency of 15 m high Sitka Spruce trees was reported by Gardiner (1989). These values were obtained by simply swaying a tree gently by hand. Recalling Equation 1.11, the trees were assumed to be simple damped harmonic oscillators in terms of natural frequency, ω_n, and damping ratio, ζ. Adding a forcing function due to drag of $D(t)$ gives:

$$\frac{d^2x}{dt^2} + 2\zeta\omega_n \frac{dx}{dt} + \omega_n{}^2 x = \frac{D(t)}{m} \qquad [3.1]$$

The damping ratio, ζ, was calculated from amplitude ratios of successively damped peaks in the response to an impulse. From vibration theory:

$$\zeta = \ln(A_0/A_n) / 2\pi n \qquad [3.2]$$

where A_o is the initial amplitude and A_n is the amplitude n cycles later. In a real forest, damping is increased by the crown clashing of a test tree with surrounding trees ($\zeta = 0.068$). In the model forest however, it was found that crown clashing caused more disruption than damping. The trees were thus designed to have the same damping ratio as full-scale trees ($\zeta = 0.048$ when the surrounding trees are pulled back slightly and in calm conditions).

From Equation 3.1, the amplitude ratio of the response X to a steady state sinusoidal forcing is:

$$\frac{X}{D/m} = \frac{1}{\sqrt{(\omega_n{}^2-\omega^2)^2 + (2\zeta\omega_n\omega)^2}} \qquad [3.3]$$

where at resonance: $$\omega = \omega_n \sqrt{1-2\zeta^2} \qquad [3.4]$$

From Equation 3.3, it can be seen that the sway amplitude X is proportional to D/m. This highlights a discrepancy between full scale and model scale tree dynamics. The drag

coefficient of the full scale tree and model are the same, but Table 3.2 shows that the mass of the model tree is too large by a factor of two. This implies sway amplitudes for the model are too small by a factor of 2. The consequences of reduced sway amplitude are not certain. The two main concerns are the reduced feedback to the local turbulence and the reduction in crown clashing between trees.

The ratio of bending moment, Q, to drag force, D, is not affected by the large mass ratio, since it represents the *transmissibility factor*, T, which is a function of ω_n and ζ only. Any concerns with the underestimation of contribution from overhanging weight, when the trees are displaced are also unwarranted. This is because any amount of reduced sway is accompanied by a proportional increase in mass.

The point of greatest uncertainty in the design of the model trees was the target value of the drag coefficient. The full-scale drag was not measured by Gardiner so instead an empirical formula by Mayhead *et al.* (1975) was used. This formula gives the drag, D (N), of an isolated Sitka Spruce tree, in terms of live branch mass m (kg) and the onset uniform wind speed U (ms^{-1}).

$$D = 0.4352U^2m^{0.667}\exp\{-0.0009779U^2\} \qquad [3.5]$$

When transformed into a drag coefficient (Table 3.2) and substituting values of m, H, and ρ for a 15 m tree gives:

$$C_D = 0.04257\exp\{-0.0009779U^2\} \qquad [3.6]$$

In this equation, C_D decreases with increasing wind speed, due to bending and streamlining of branches and leaves in the wind. This effect was impossible to simulate in the model and Stacey *et al.* used a constant drag coefficient, based on a full-scale reference velocity of 30 ms^{-1}. This velocity represented a storm wind at which most forests are damaged. It might

be argued that the models should have been designed with the higher drag coefficient appropriate to the lower mean speeds within the canopy. On the other hand Gardiner *et al.* (1997), showed that damaging wind forces arise when the canopy is penetrated from above by an extreme gust. Stacey *et al.* showed that at 80% tree height the gust speed was frequently greater than $0.85U_{ref}$ (25 ms^{-1}) and occasionally greater than $1.05U_{ref}$ (31 ms^{-1}). The models were designed to have an arbitrary centre of pressure at 80% tree height, in uniform flow.

The final models were manufactured by experimental trial and error. As stated earlier the stems were fabricated by injection moulding using Nylon 66 and the canopy drag elements using low density polyethylene (LDPE). The parts were assembled by hand.

3.4.1 Variations from the Ideal Models

The original uniform forest trees were made up of an equal ratio of 190 mm, 200 mm and 210 mm trees. As well as variation in the model properties, there was variation between these sets of trees. From tests of 10 trees from each set, the range of sway frequencies in the uniform forest was found to be 5.2 ± 0.8 Hz (one standard deviation). The 210 mm trees tend to vibrate at the higher frequencies whilst the 190 mm trees vibrate at the lower frequencies. The still air damping ratios were 0.05 ± 0.01. However the issue of whether the damping ratio varies with mean wind speed (Wood 1995) must be addressed. For instance if the sway velocity of the tree is u_t and there is a mean wind velocity U then the relative velocity is $(U\text{-}u_t)$. Drag can be represented by:

$$D = K\,(U - u_t)^n \qquad [3.7]$$

where n varies for trees, but is 2 for solid objects, and K can be considered constant. For small values of u_t/U, a binomial expansion yields:

$$D = KU^n - nKU^{(n-1)}u_t - \ldots \quad [3.8]$$

The second term is the primary contribution to aerodynamic damping force and is proportional to U. Although Equation 3.8 is not rigorous it demonstrates that damping can be expected to increase with mean velocity.

To test this hypothesis the variation of the damping ratio of a 200 mm model tree against mean velocity was tested in the wind tunnel. Figure 3.9 shows that damping ratio, ζ, does indeed increase with mean velocity. In fact, as the velocity increased the damping increased almost to the point where it became critical and measurements could no longer be made. However, the velocity ratio in the uniform forest (taken at the height of centre of pressure) was 0.26 which gives an effective damping coefficient of 0.081. This value is used in the bending moment analysis in Chapter 7.

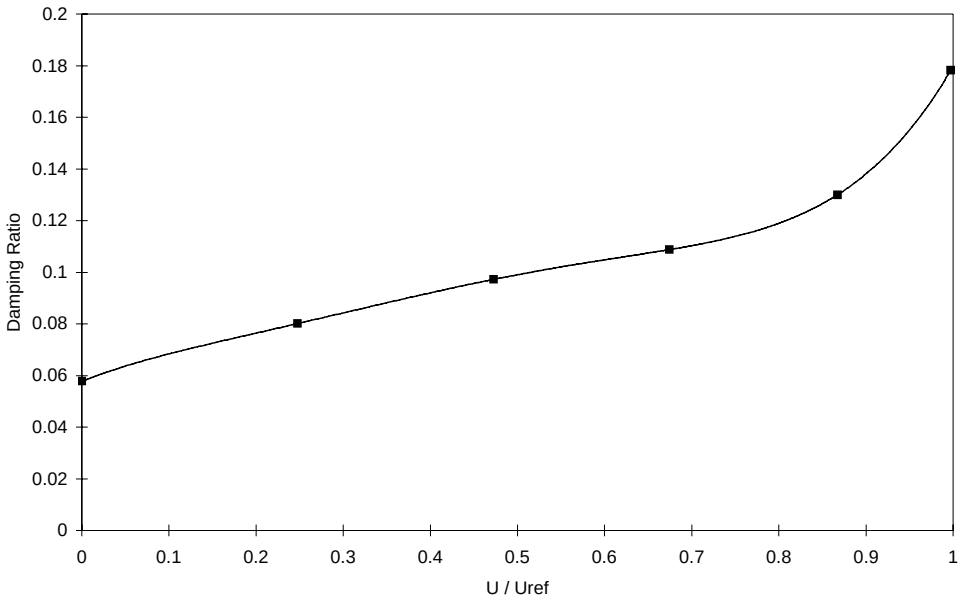

Figure 3.9 Variation of damping coefficient with mean wind speed.

3.5 New Tree Designs

New trees of heights 100 mm, 150 mm, 250 mm and 300 mm were required by the Forestry Commission to carry out tests on forests of irregular height (see Chapter 1). It is important at this stage to stress that the physical characteristics of these trees were modelled on trees grown in an irregular forest environment. That means that these trees are *not simply scaled versions of the 200 mm tree* but have individual properties based on that height. Therefore drag coefficients, bending moment coefficients *etc.* are not necessarily applicable and must be used with care.

Estimates of physical data for the new trees were obtained from the Forestry Commission (Gardiner personal communication). Unlike the original 15 m trees, only full-scale diameters and estimated natural sway frequencies were available. This, coupled with a lead-time of a year for manufacturing led to the new trees being far more simplistic in design. The original trees were designed using a time consuming 'trial and error' method. This was avoided in this study by using analytical modelling, with only one stage of design feedback before final production.

The new model trees were designed using the Stodola method, a numerical solution to bending modes of a non-uniform cantilever with arbitrary mass distribution (see Appendix A). This was implemented using a spreadsheet, with the main controlling parameters being the natural sway frequency, breast height diameter (diameter at 1.3 m full-scale), and a tip diameter of 1 mm (with linear taper). Existing drag elements (as used on the 200 mm trees so simplifying the manufacturing process) were added along the stem until the correct natural frequency was arrived at.

The difference in material properties of Nylon and wood made the final model a compromise between frequency and stem diameter, especially for the taller trees where the low frequencies were very difficult to reproduce. Table 3.3 gives the properties of the newly designed trees.

Tree Height (Full Scale)	Tree Height (Model)	Diameter at breast height (Full Scale)	Diameter at breast height (Model)	Sway Freq. (Full Scale)	Target Sway Freq. (Model)	Actual Model Sway Freq.
m	**m**	**mm**	**mm**	**Hz**	**Hz**	**Hz**
7.5	0.1	112.5	1.5	0.85	12.7	12.4
11.25	0.15	150	2.0	0.51	7.5	8.69
15*	0.2	165	2.2	0.33	4.9	5.2
18.75	0.25	225	3.0	0.27	4.1	4.3
22.5	0.3	300	4.0	0.25	3.8	4.8

Table 3.3 Full scale and model characteristics, where * denotes the original model.

As can be seen by the difference between target and final sway frequency, the results are reasonably good, with the exception of the 300 mm tree. This was thought to be due to errors in manufacture. Drag and masses for the new trees are presented in Table 3.4.

Tree (mm)	Drag (N)	Drag Coefficient (based on H)	Centre of Pressure (m)	Mass (kg)	Mass Coefficient
100	0.0157	0.048	0.073	0.86×10^{-3}	0.702
150	0.0120	0.028	0.096	1.14×10^{-3}	0.276
200	0.0156	0.018	0.160	1.04×10^{-3}	0.051
250	0.0241	0.017	0.177	2.83×10^{-3}	0.148
300	0.0251	0.015	0.181	3.94×10^{-3}	0.119

Table 3.4 Properties of new model trees.

Although the absolute values of drag are greater for the larger trees, the reducing drag coefficient reflects the smaller branch mass length to stem length ratio.

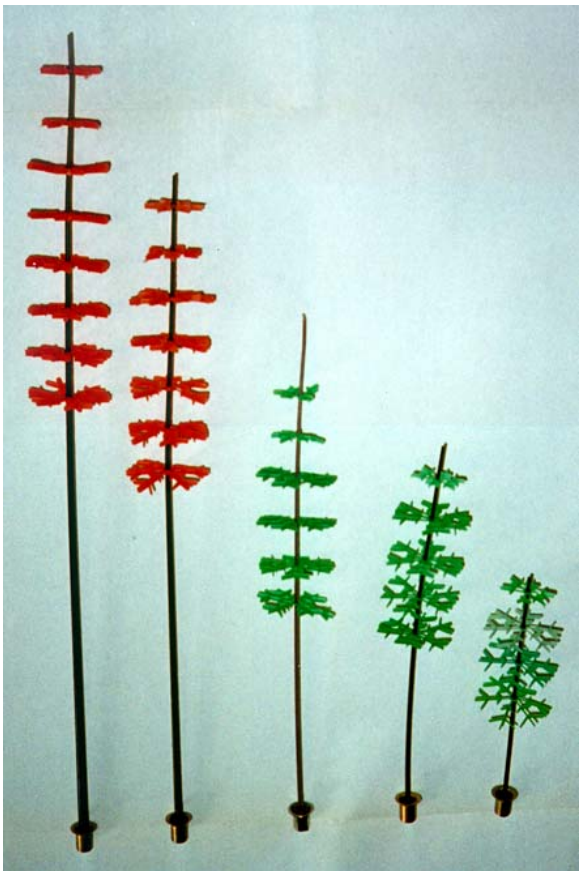

Figure 3.10 1/75th scale model trees. From left to right, 300 mm, 250 mm, 200 mm, 150 mm, 100 mm.

3.6 Bending Moment Balance

The wind forces that act upon the trees were measured with a strain gauge bending-moment balance. The balance was designed to measure the two components of bending moment about orthogonal axes in the ground plane. Two balances were made for Stacey's experiments and one is shown in Figure 3.11.

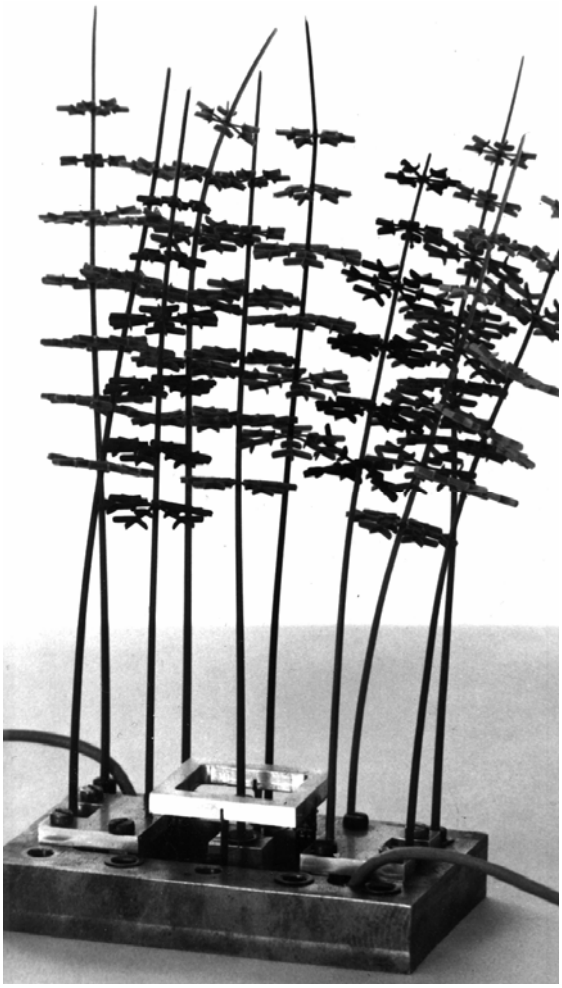

Figure 3.11 Miniature force balance with model trees. The model tree under test is in the centre square of the base.

Each moment balance consisted of four strain gauges that linked the outer steel base with an inner rectangular balance. The test tree was then mounted on the inner balance. Changes in the resistance of the gauges were detected with a Welwyn strain gauge bridge. The signal was then amplified before being sent to a CED A/D converter and PC computer. Stacey *et al.* showed that the natural frequency of the balance was approximately 200 Hz, greatly in excess of frequencies of interest in the forest (<25 Hz), and thus its effect on measurements was negligible.

Before each experiment the bending moment balances were calibrated by applying loads along a stiff arm in the balance. The balance had a sensitivity of approximately

0.0026 Nm V^{-1} over a range of ± 0.03 Nm. Care was taken before each experiment to avoid contact between the test tree and adjacent trees.

3.6.1 Effects of Crown-clashing on Stiffness and Sway Frequency

In Chapter 4, the relationship between the sway frequency of a forest and the generation of canopy gusts is discussed. However, it was discovered late in the study that the effective sway frequency for the uniform forest was higher than that of the individual trees (from Section 3.4.1, the expected range was 4.4-6 Hz). The reason for this discrepancy was thought to be due to the large amount of crown clashing and entanglement when the model trees were closely spaced. Figure 3.12 shows the bending moment spectrum of a test tree with sway frequency of 5.47 Hz. The first peak in the figure is for the test tree in an isolated environment, being released from a 10 mm tip offset position. The second peak is due to an analogous experiment, this time with the test tree surrounded by a group of trees. All the trees were released from the same offset position (the trees being held back with a flat board, which was suddenly raised). As can be seen the group of trees caused a higher sway frequency (approximately 6.2 Hz). Because care was originally taken to avoid surrounding tree contact in the tests, it is possible that any resonant effects were underestimated. The group selection and random forest tests did not suffer from this since the contrasting branch heights minimised entanglement.

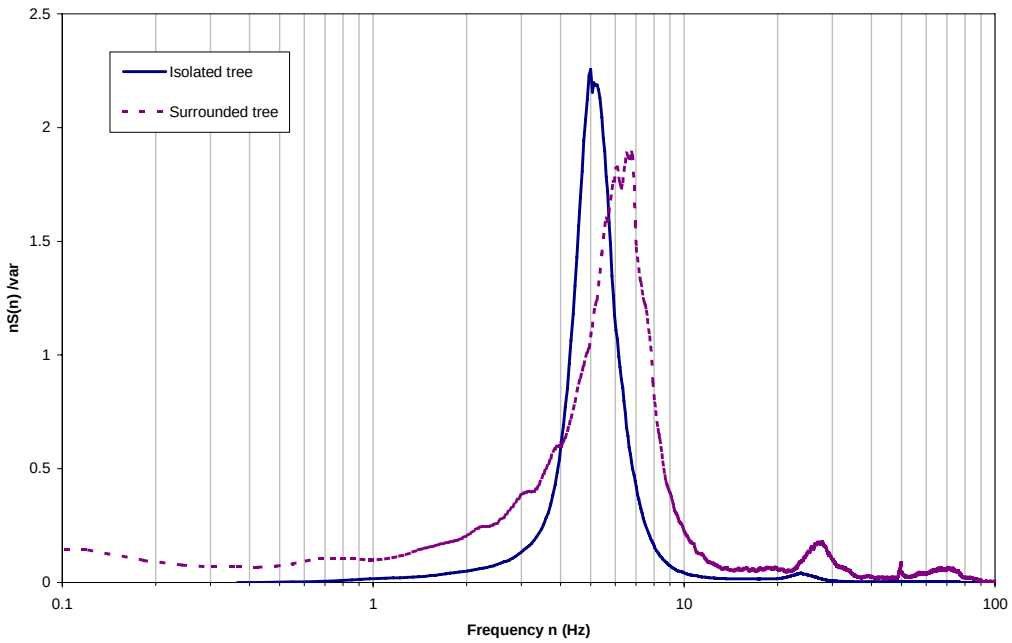

Figure 3.12 Normalised bending moment spectra of an isolated tree and a surrounded tree.

3.7 Laser Doppler Anemometer

Velocity measurements were taken with a Dantec two-component Laser Doppler Anemometer. The laser source was connected to a 14 mm diameter probe (46 mm focal length) via fibre optics with back-scatter detector. Data was collected and verified by two Dantec Burst Spectrum Analysers with post processing carried out with Dantec software. Seeding of the flow was provided by two TSI Model 9306 atomisers which used a 5:1 water/glycerine mixture to create particles in the order of 1 μm. Particles of this size have been proved to follow flows with frequencies over 700 Hz with an accuracy of 99%, (Durst *et al*. 1976), whereas the present flows show no significant frequencies above 100 Hz (for example see Figure 3.6).

The LDA works on the principle that two coherent laser beams cross over at the measuring volume creating an interference pattern, see Figure 3.13. Seed particles, travelling through the control volume, scatter back the light in the bright fringes. The velocity of the particle

determines the frequency of fringe-crossing back-scatter, hence the velocity of the wind can be inferred. Frequency shifting of one of the crossing lasers allows the detection of the direction of a motion.

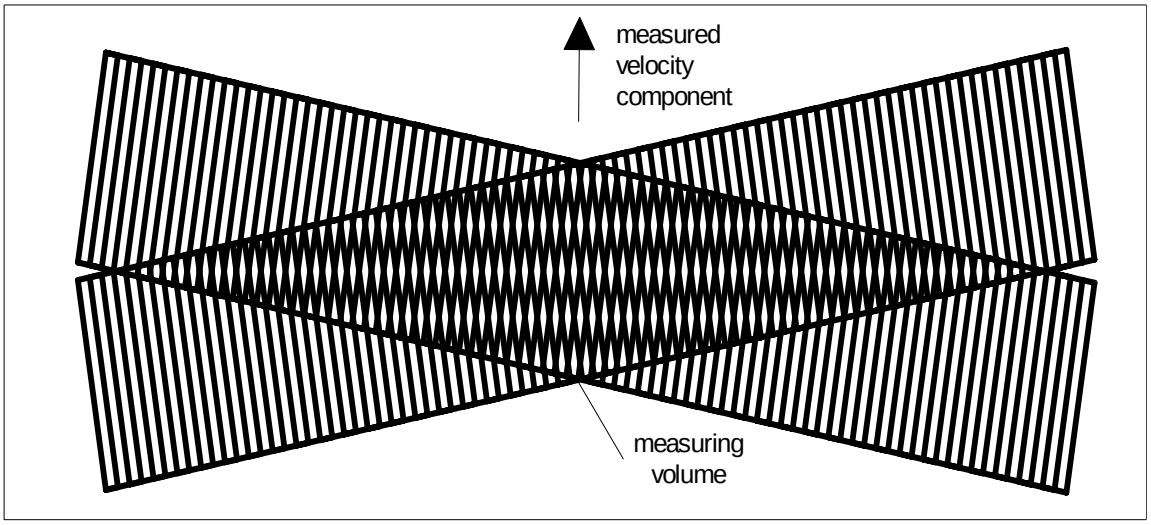

Figure 3.13 The interference pattern set up by two laser beams crossing.

The output from the Burst Spectrum Analyser, BSA, is a list of particle velocities with their occurrence times. Since a velocity is only measured when a particle passes through the measuring volume the time series is non-uniform.

If the mean velocity is calculated by averaging all the particle velocities, the non-uniformity in the time series can result in a bias away from the true mean. If the flow is uniformly seeded then more particles will pass through the measuring volume when high velocities occur and so the mean velocity will be overestimated. This biasing is corrected by a technique known as ‘time interval weighting’ or ‘sample and hold’.

A true mean velocity can be determined from the integral of a smooth curve fitted through the non-uniformly spaced data points. Figure 3.14 shows an example of measured data points, a full time series and a sample and hold reconstructed time series. If the data points

are separated by a non-uniform time interval, Δt, then the mean velocity from the sample and hold technique is given by Equation 3.9:

$$\text{Sample and hold mean} = \frac{\sum \text{Particle velocity} \times \Delta t}{\sum \Delta t} \qquad [3.9]$$

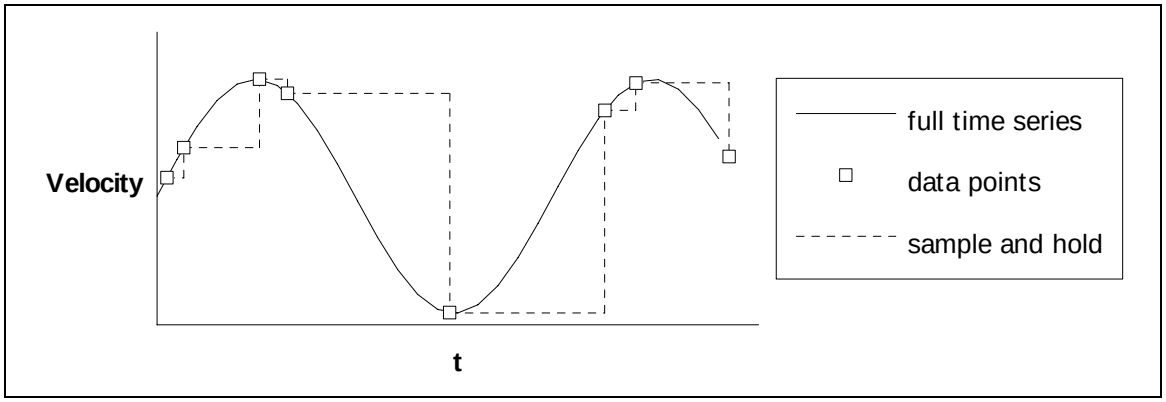

Figure 3.14 Sample and hold time series.

LASER/OPTICS		
Type	Argon-ion	
Power	300 mW	
Bragg Cell Frequency	40 MHz	
Beams Transmitted	488.0 nm	
	488.0 nm Bragg Cell shifted	
	514.5 nm	
	514.5 nm Bragg Cell shifted	
PROBE		
Type	Back-Scatter	
Length	105 mm	
Diameter	14 mm	
Focal Length	50 mm	
Beam Separation	8 mm	
Receiving Aperture	11 mm	
Working Distance	46.3 mm	
MEASURING VOLUME		
Beam wavelength	488.0 nm	514.5 nm
Length	1.44 mm	1.52 mm
Width	0.115 mm	0.122 mm
Number of fringes	37	37
SEEDING		
Generator type	TSI Model 9306 Atomiser	
Material	Water/Glycerine Ratio 5:1	
Mean Aerodynamic Diameter	Approximately 1 μm	
PROCESSORS		
Type	Burst Spectrum Analyser	
Manufacturer/Model	DANTEC 57N14	
Peak Data Rate	1.5 MHz	
Capacity	16384 bursts	

Table 3.5 Properties of LDA.

3.7.1 Accuracy of LDA Measurements

The LDA gives absolute measurements without calibration, as the accuracy depends on the optical geometry and the wavelength of laser light. However, to ensure an adequate data sampling rate *etc*., care must be taken in the use of seeding. If the seeding generator outlets are too close to the laser, any large-scale turbulence will redirect the seeding away from the laser probe leading to intermittent large gaps in the velocity time series. However, placing the

outlets far from the laser probe allows a greater distance for diffusion but dramatically decreases concentration and hence data sampling frequency (Minson 1993).

In a related problem, the presence of coherent turbulent structures in the model forest shear flow meant that the seed did not diffuse evenly. Care had to be taken to position two seeding generator outlets above and below the estimated mixing layer in the forest (see Chapter 4) to ensure an ample sampling rate of more than 50 Hz.

The sampling rate and sampling period affects the statistical accuracy of the estimate of velocity. This was highlighted by Edwards and Jensen (1983). Assuming no systematic measuring error, they derived the standard deviation error, Σ, of an estimated mean velocity to be:

$$\Sigma = (\sigma_u^2 / N) * ((2\tau_c N / T) + 1) \qquad [3.10]$$

where N is the total number of samples in a period T, σ_u^2 is the variance of velocity and τ_c is the flow correlation time. For example if σ_u is 0.1 then the estimate of velocity was $\pm$ 0.1 ms^{-1} with a confidence limit of 66%.

Equation 3.10 was applied to the mean velocity, U, at uniform forest top height where turbulence is highest. From spectral analysis τ_c was estimated to be 0.5 s. Realistic sampling rates of 50 Hz and 100 Hz were chosen at different periods of 60 s and 120 s. These estimates are shown in Table 3.6.

T (s)	Approx. Norm. σ_u^2	Σ	Approx. Normalised U	% error
60	0.2	0.0574	0.4425	12.97
60	0.2	0.0577	0.4425	13.03
120	0.2	0.0406	0.4425	9.18
120	0.2	0.0408	0.4425	9.22

Table 3.6 Estimated errors for repeatability of LDA measurements.

As the last column shows, a halving of the sampling rate does not affect the accuracy significantly, whilst increasing the sampling time increases accuracy up to 4%. Thus 120 s was chosen as the standard observation time in all LDA experiments (unless otherwise specified). In reality it was very difficult to control the sampling rate, especially in the canopy area. It was also desirable to increase the rate of sampling to a maximum when linear interpolating of non-uniform data was to be used (*e.g.* for calculating spectra). To check the estimates in Table 3.6, twenty measurements were taken in the same position in the uniform forest, ten of 60 s periods and ten of 120 s periods. The standard errors are presented in Table 3.7 and suggest that the estimated accuracy is grossly conservative.

T (s)	Norm. Mean U	Σ	% error
60	0.4423	0.01464	3.03
120	0.4425	0.01109	2.50

Table 3.7 Errors derived from experiments.

Chapter 4: Velocity Measurements in Mid-Forest

4.1 Introduction

Evidence was presented in Section 1.3 that in extensive areas of forest or other uniform plant growth, the wind-canopy interaction is dominated by shear at the canopy top. In particular, Raupach *et al.* (1996) proposed scaling ratios in this region that reduce different canopy profiles onto a single curve. This chapter aims to check the scaling techniques of Raupach *et al.* by studying the mean flow above the three different types of forest formations (uniform, group selection and random). Spectral analysis is used to study the differences in eddy structures between these three forests. Finally, analogies with mixing layer type flows are made to account for the intermittent ejection-sweep nature of canopy flows.

4.2 Experimental Description

In the wind tunnel a boundary layer flow was established using the mid-forest simulation as described in Chapter 2. The three types of forest layout and tree formations, see Section 2.2, were tested in this wind simulation. Vertical traverses of velocity measurements (streamwise and vertical components) were made in the centre of each forest with the Dantec LDA. Observation lengths of 120 s were used and results normalised by the reference velocity, U_{ref}, the velocity at z = 380 mm in the centre of the forest. From this point onwards, heights are expressed in terms of z/H, where H is based on the uniform forest height of 200 mm.

4.3 Velocity Profiles

Streamwise velocities are plotted against height in Figure 4.1. The characteristic inflexion point can be seen immediately. The random forest has the largest displacement height (see

Section 2.2), as would be expected with the presence of the tallest trees. The streamwise velocity in the lower part of the random forest is considerably higher than the other two forests. This is because the spread of tree types creates a lower density of foliage at each height. The smaller trees in both the random and group selection forests are subjected to mean winds far less than the highest trees. Note that at heights of z/H = 6 the streamwise velocities are very similar.

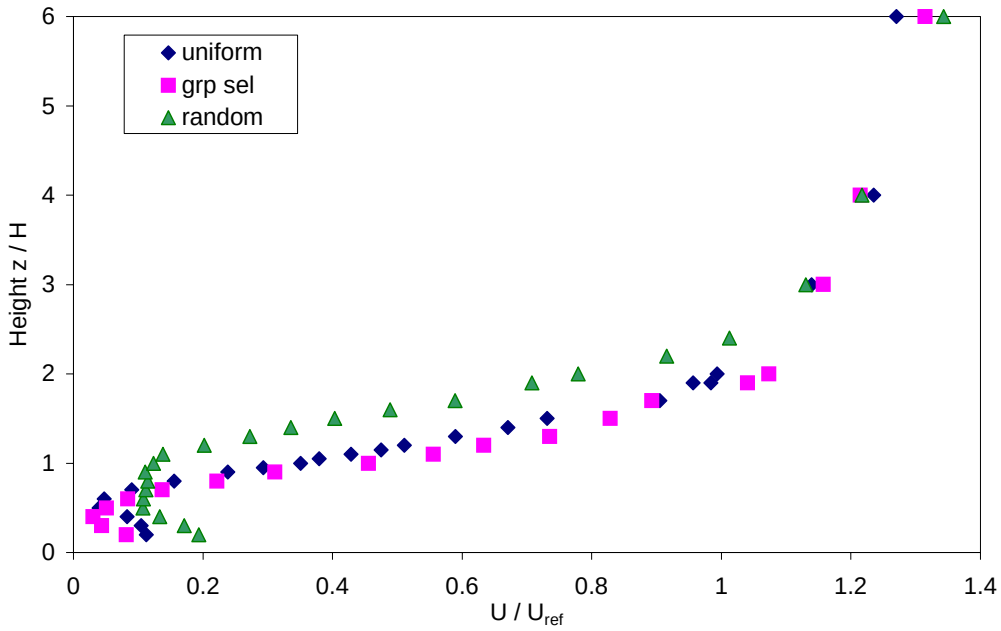

Figure 4.1 Streamwise velocity profiles.

The regions of high shear are clearly seen in Figure 4.2. The absence of a region of constant shear stress above the forests, discussed in Section 1.2, is clearly evident for all three cases. Towards the ground the shear is almost zero.

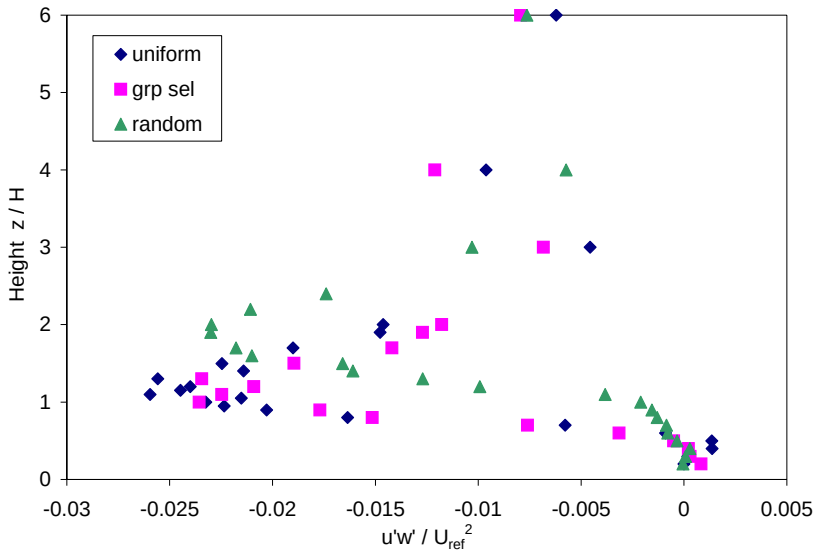

Figure 4.2 Reynolds stress profiles.

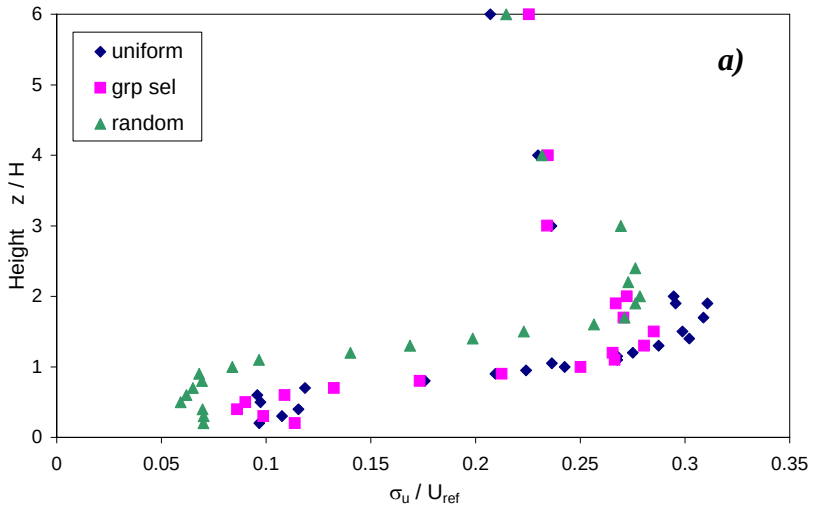

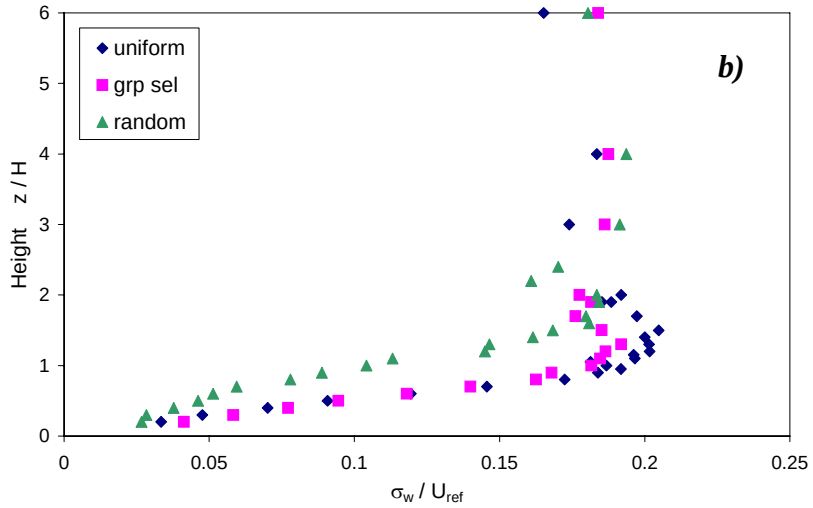

Figures 4.3 Standard deviation profiles for forest models, a) σ_u/U_{ref} and b) σ_w/U_{ref}.

Values of *u* standard deviation, σ_u, and *w* standard deviation, σ_w, shown in Figure 4.3, follow a pattern of a large increase from the bottom of the canopy (where only tree stems are present to obstruct the flow) to the highly turbulent area at the top of the canopy. Above the canopy the rms. values slowly decrease to magnitudes of turbulence generated in the tunnel simulation.

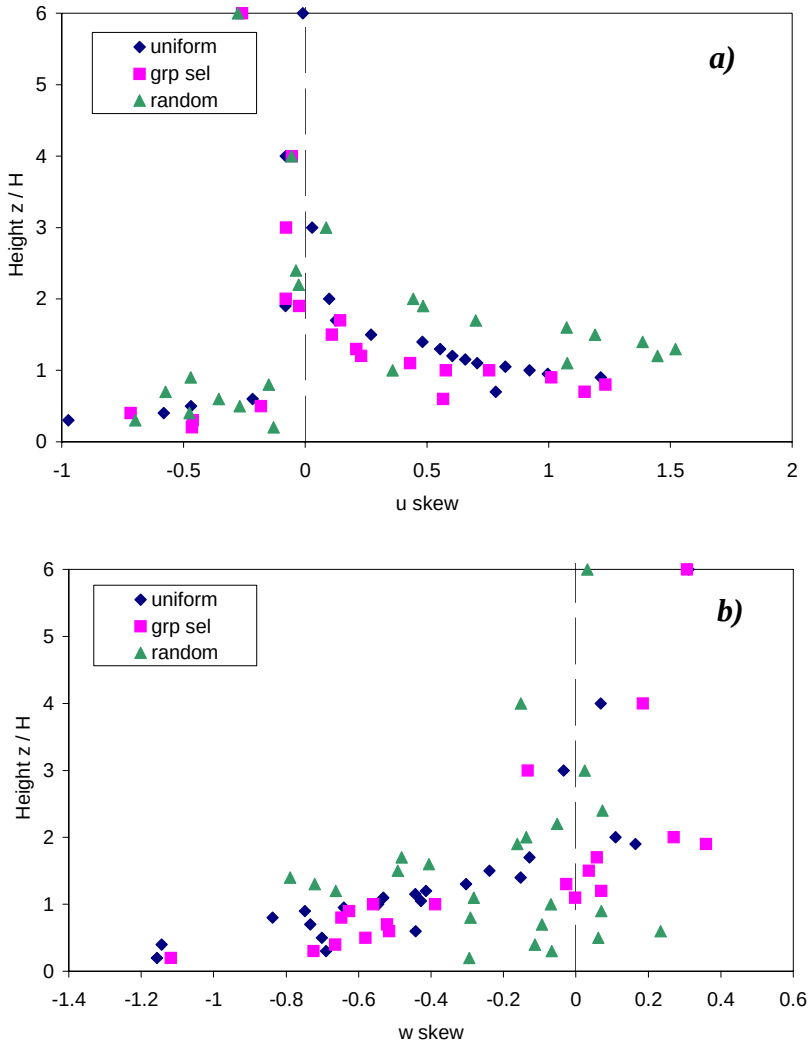

Figure 4.4 Skewness profiles in forest models, a) u skewness and b) w skewness.

The characteristics of the *u* and *w* skewness profiles in Figure 4.4 are similar to those of Raupach *et al.* discussed in Section 1.4. The largest positive *u* skewness values are just below the canopy top where also negative *w* skewness values are at or near a minimum. This would

indicate sweeps of air forward and downward into the canopy. Further down in the canopy the

evidence of coherent patterns is less obvious. The profiles appear to indicate that the smallest trees are sheltered from the intermittent downward sweeping gusts.

4.3.1 Normalisation of Velocity Profiles by Shear Length Scaling

From Section 1.8, Raupach *et al*. suggest that vertical height scaling can be based on the shear length scale defined by:

$$L_s = U(h_i) / dU/dz \qquad [4.1]$$

where $U(h_i)$ is the streamwise velocity at inflexion point height, and dU/dz is the velocity gradient at that height (Section 1.8).

To test the scaling hypothesis it was necessary to determine a value of inflexion point height and gradient from the velocity profiles in the last section. This process was made very difficult by the scatter of the mean readings. By definition, inflexion points are defined by a maximum in dU/dz but the scatter meant that there was not a clear maximum. Smoothing and central differentials also did not help. Curve fitting of hyperbolic tangent functions was not possible because the upper part of the boundary layer does not become asymptotic. The most reliable method of determining the gradient was found to be linear regression of the points which made up the 'linear section' of the graph. The number of points in the 'linear section' was found by eliminating edge points, by an iterative trial and error process, until the regressed gradient reached a maximum. The inflexion height was then taken as the middle measurement point in that section. Inflexion heights are shown in Table 4.1 and shear length scales, L_s, shown in Table 4.2.

Forest	Inflexion height h_i (mm)	h_i / H
Random	340	1.7
Uniform	220	1.1
Group Selection	200	1.0

Table 4.1 Inflexion point heights h_i.

Forest	$U(h_i) / U_{ref}$	$d(U/U_{ref})/dz$ (m^{-1})	L_s (m)	L_s/H
Random	0.5639	3.670	0.154	0.77
Uniform	0.4937	4.162	0.101	0.51
Group Selection	0.4442	5.045	0.088	0.44

Table 4.2 Shear length scales L_s.

Normalised profiles in the following section are shown against z_i/L_s, where $z_i = (z-h_i)$ and $z_i/L_s = 0$ is the inflexion height. This scaling places importance on the shear length rather than canopy height and is better suited to a mixing layer analogy (as opposed to Raupach *et al*.'s use of z/h_i presentation of data).

Another important parameter in scaling is the friction velocity u_* defined as $u_* = \sqrt{\overline{u'w'}\,(h_i)}$ where $\overline{u'w'}\,(h_i)$ is the Reynolds stress at the inflexion height. As mentioned earlier there is no obvious region of constant shear stress in the wind tunnel experiments and thus the value at inflexion height was used. It is noted that Raupach *et al*. and also Finnigan and Brunet (1995), use the same procedure.

The values of u_* obtained from the present study, indicated in Table 4.3, suggest that the uniform forest was the most aerodynamically rough surface, followed by the group selection and then random forest. Although the random forest would be assumed to be the roughest, since it is the tallest, in fact it is the smoothest. This is because it is the least dense of the three forest types.

Forest	Friction Velocity u_*
Random	0.148
Uniform	0.161
Group Selection	0.154

Table 4.3 Values of friction velocity u_* at inflexion height.

4.3.2 Scaled Profiles

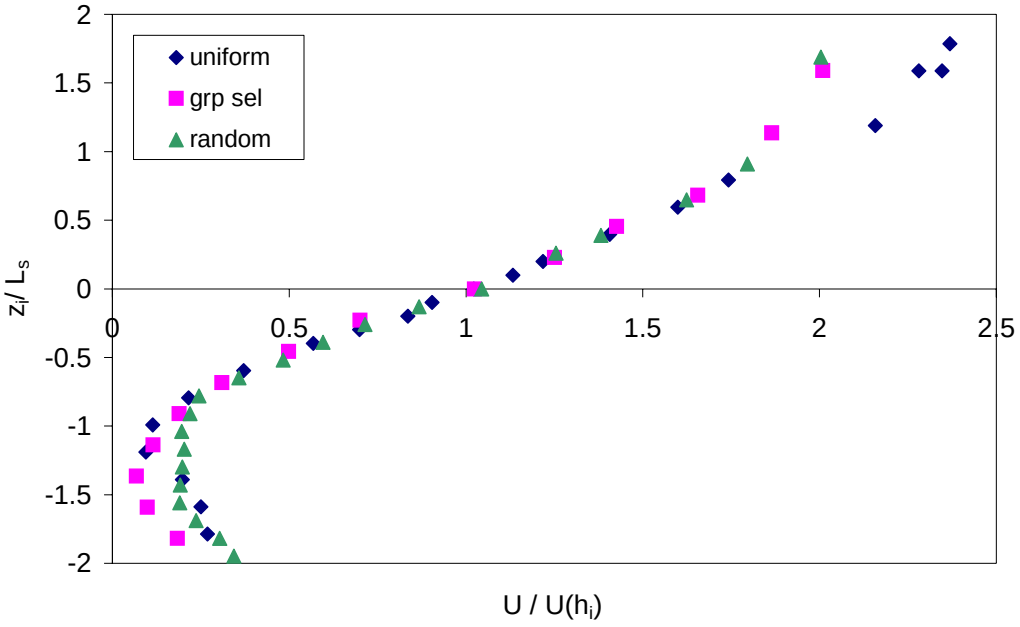

Figure 4.5 Normalised streamwise velocity profile.

Figure 4.5 shows that the three curves coincide extremely well in the region $-1 < z_i/L_s < +1$. This distance is equivalent to the shear depth δ_w in a mixing layer (Equation 1.7). Above and below this region scaling breaks down. Theoretically, the points above the region should then obey the standard Inertial Layer log law profile.

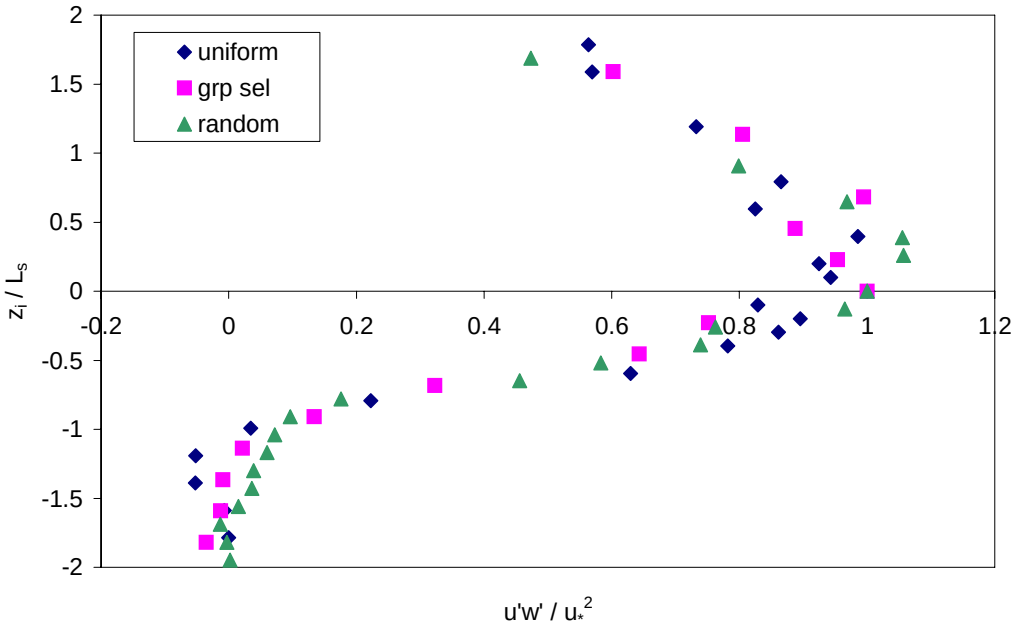

Figure 4.6 $\overline{u'w'}$ / u_*^2 profiles.

For the values of z_i/L_s between –1 and 0, the $\overline{u'w'}$ / u_*^2 profiles coincide well with each other. For $z_i/L_s > 0$ the data is more scattered, but a common profile is still visible. It is curious to note that the shear is dramatically reduced below the z_i/L_s = -1 region but is still high near the z_i/L_s = +1 region, and continues well into the region z_i/L_s = +2 as well.

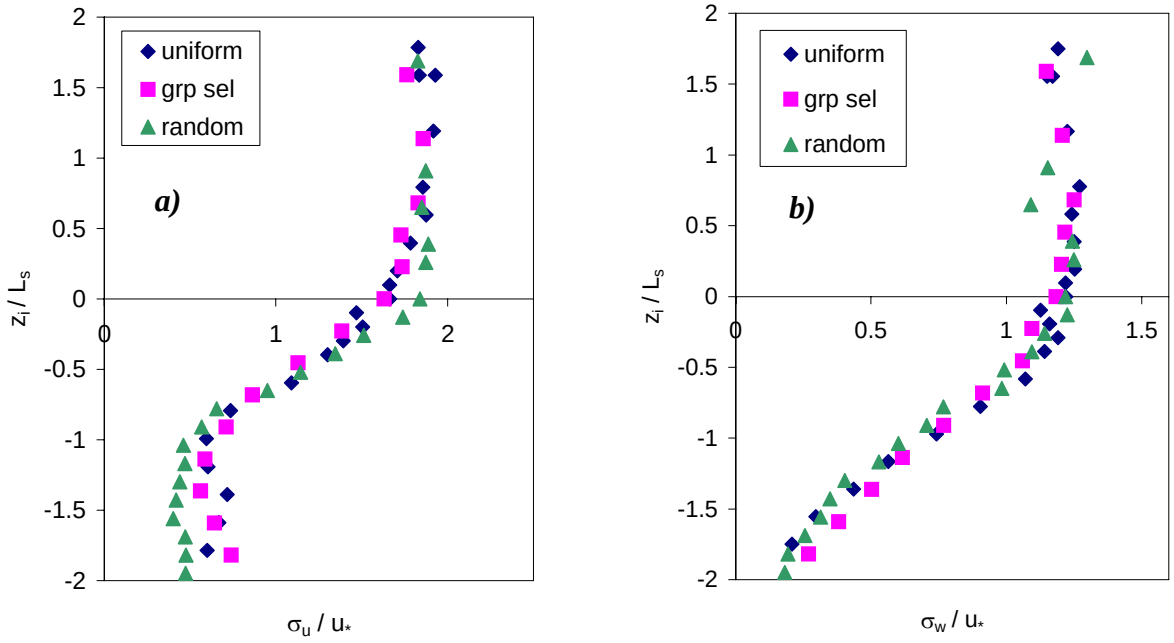

Figure 4.7 Normalised standard deviation profiles for a) σ_u/u_* and b) σ_w/u_*.

The well-collapsed normalised standard deviation profiles in Figure 4.7 support the idea that the friction velocity can scale turbulent fluctuations. At the inflexion height, the compiled records of Kaimal and Finnigan (1994) gave values of σ_u / u_* of 1.5-2 and σ_w / u_* to *ca.* 1.1. The values of σ_u / u_* for this reported study, fall into the same range, whilst the ratio σ_w / u_* is slightly higher at 1.2. Typically, in a constant stress layer high above a surface, the values of these ratios are expected to be 2.5 and 1.25 for σ_u / u_* and σ_w / u_* respectively (Garrat 1992). The present values would suggest that the streamwise turbulence is not quite in equilibrium whilst the vertical turbulence is.

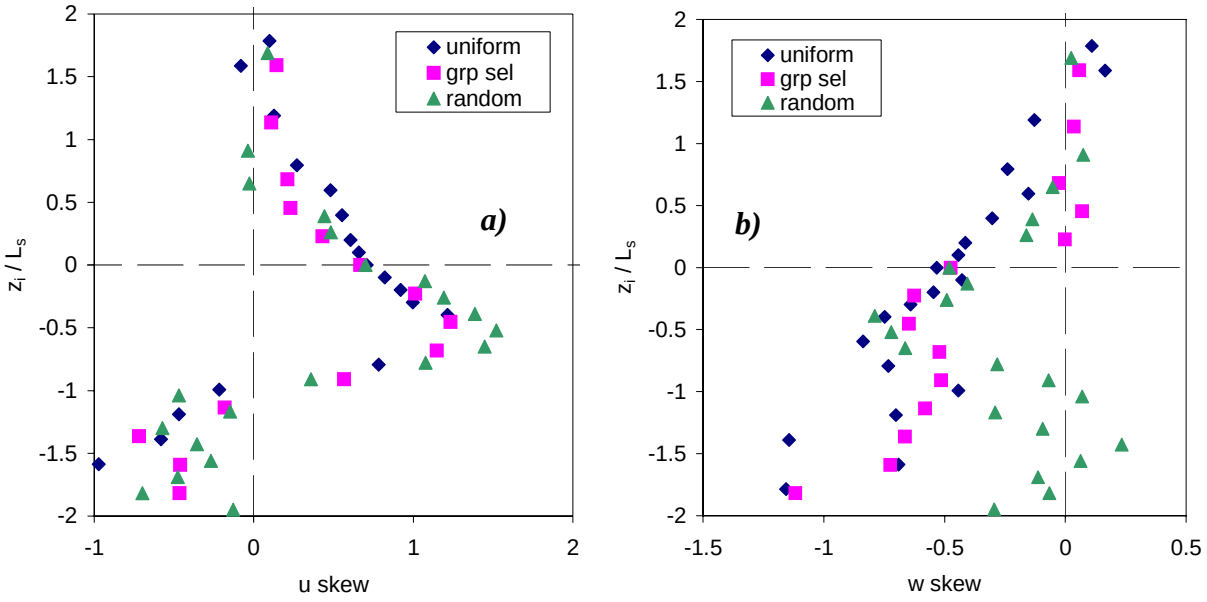

Figure 4.8a) u skewness and b) w skewness against normalised height.

The skewness profiles of Figure 4.8 also compare well with the mixing layer characteristics in Figure 1.6c. Once again the scaling gives good agreement within the shear region but deviates outside of it.

Comparing all the present profiles with example profiles of a mixing layer, presented in Figure 1.6, it becomes apparent that there are many similarities, but also some exceptions, as follows. The negative z_i/L_s region resembles the mixing layer very well, with profiles all

coinciding and reducing to approximately zero at z_i/L_s = -1. Maxima appear to be at, or just above, z_i/L_s =0. However in the upper region, although the profiles are still coincident, the shear and high turbulent regions appears to 'stretch' to z_i/L_s > 2. Obviously, in a fully developed flow, the shear region would be constant with height above z_i/L_s = 0 and so this would be expected anyway.

4.4 Gust Frequency Spectra

Frequency power spectra can give an indication of the presence of dominant frequencies in wind fluctuations. The power spectra coefficients $S(n)$ are usually plotted in the form $nS(n)/variance$ against the logarithm of frequency, n. The frequency biased term, $nS(n)$, creates a characteristic peak in the power spectra which would otherwise be dominated by low frequency components. The division by variance allows inter-comparison of plots.

Alternatively some authors present the results in the form log ($nS(n)/var$) against log n. This allows a comparison with the Kolmogorov hypothesis which predicts spectral densities in the inertial sub-range for isotropic turbulence in the form:

$$nS(n) = \alpha_u \varepsilon^{2/3} (2\pi n/U)^{-2/3} \qquad [4.2]$$

$$nS(n) = \alpha_w \varepsilon^{2/3} (2\pi n/U)^{-2/3} \qquad [4.3]$$

where α is a constant, ε is the dissipation rate (Lesieur 1997) and U is the local stream velocity. When logs are taken of both sides and divided by the variance the plot of log ($nS(n)/var$) against log n gives a –2/3 gradient on the dissipative slope. Although purely theoretical, and applicable only to isotropic turbulence, it is remarkably well verified in experiments (Lesieur 1997) and canopy situations (Gardiner 1992, Raupach *et al*. 1986, Baldocchi and Meyers 1988a and b).

Studies (Raupach *et al.*, Gardiner (1994) and Irvine (1994)) suggest that the frequency spectra of canopies can be put into three bands of height. The first is above the canopy where normal atmospheric conditions reign. The second is inside the canopy and main canopy shear region where the power spectra vary little with height. This would suggest a dominant structure throughout the height independent of local velocity (which by definition varies a great deal in the shear region). The third section is below the main branch mass where the 'spectral short cut' process is thought to occur, see Section 1.5. The result of this process is a sharp drop in energy in the frequency band between the canopy gust frequency, and a higher frequency, representative of eddies being shed from small plant parts.

Power spectra measured in the present wind tunnel experiments tended to reproduce these trends. The following Figures 4.9-4.16 attempt to demonstrate how the power spectra vary throughout the uniform forest. It was found the trend was similar for all three forests.

Spectral analysis of LDA data was carried out using a FORTRAN program (written by R.E.Belcher, Oxford University Wind Engineering Research Group) which linearly interpolates the non-uniform raw LDA data before carrying out F.F.T.'s. Data samples of 120 s were used.

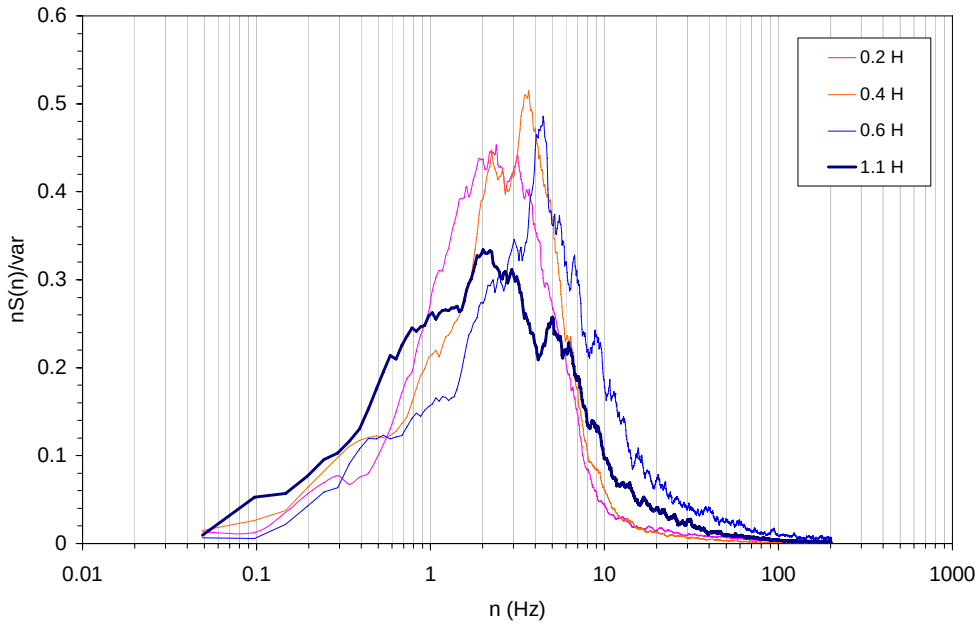

Figure 4.9 U spectra below shear region of uniform forest.

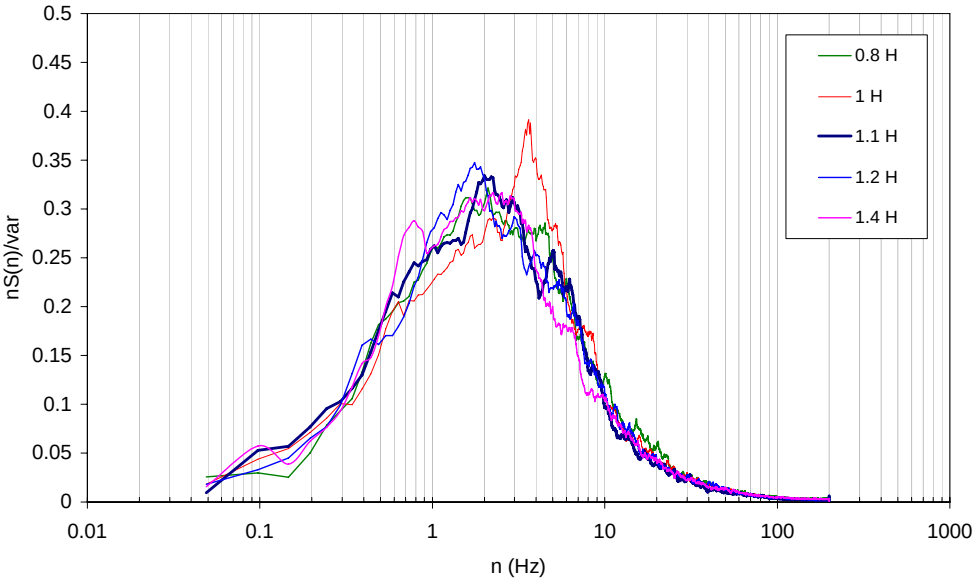

Figure 4.10 U spectra in shear layer of uniform forest.

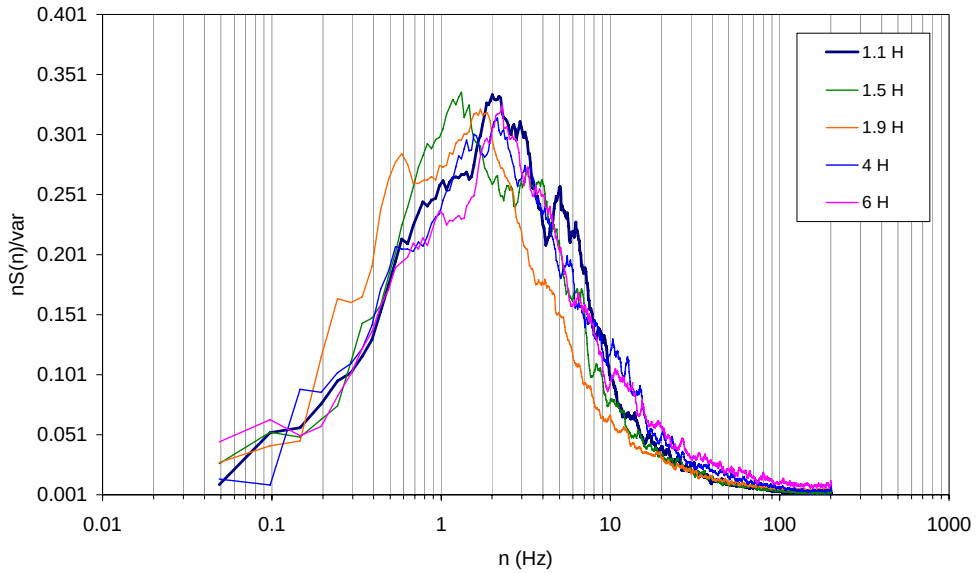

Figure 4.11 U spectra above shear region of uniform forest.

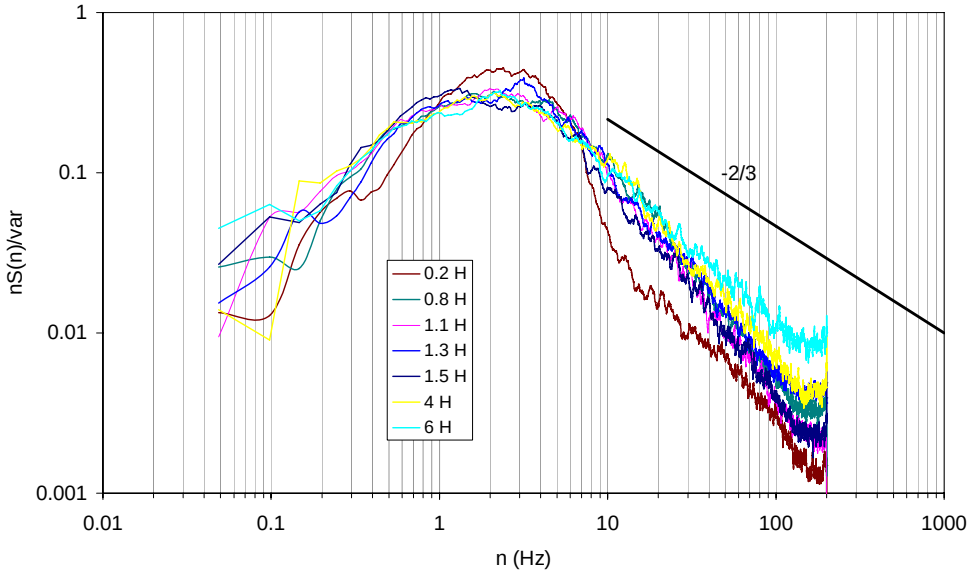

Figure 4.12 log-log form of U spectra for various heights throughout uniform forest.

The collective grouping in the shear layer, shown in Figure 4.10, indicates the presence of a separate flow regime as expected. The general peak is quite wide and invariant, however the major peaks tend to be at higher frequencies lower down in the forest and at lower frequencies higher up. At the edge of the shear region (0.6*H* in Figure 4.9) there is a clear peak at a higher frequency (4-5 Hz). Below that point the peak frequency drops once more

but there is very sharp drop in slope as expected. This is best illustrated in Figure 4.12 at 0.2*H*. Above the shear region the spectra slowly return to inertial layer atmospheric conditions.

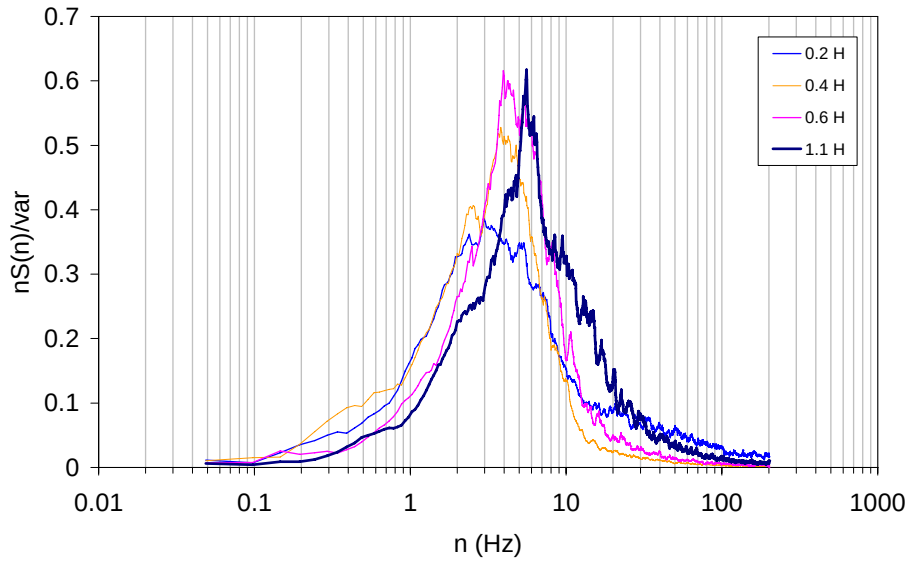

Figure 4.13 W spectra below shear region of uniform forest.

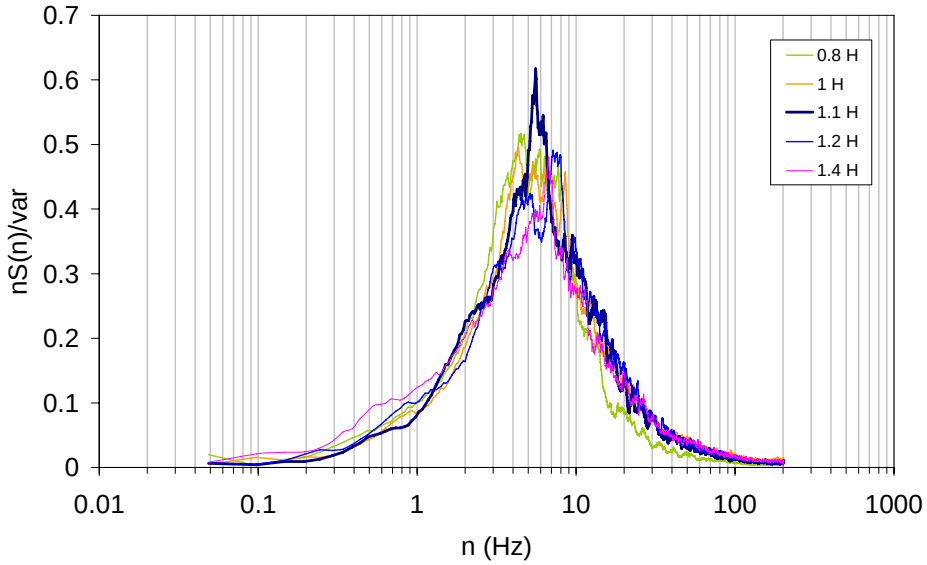

Figure 4.14 W spectra in shear region of uniform forest.

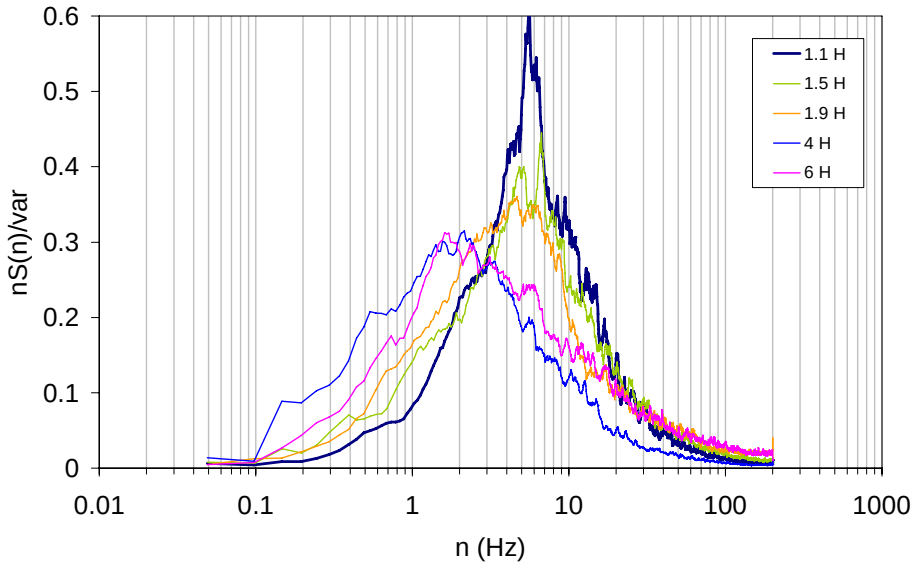

Figure 4.15 W spectra above shear region of uniform forest.

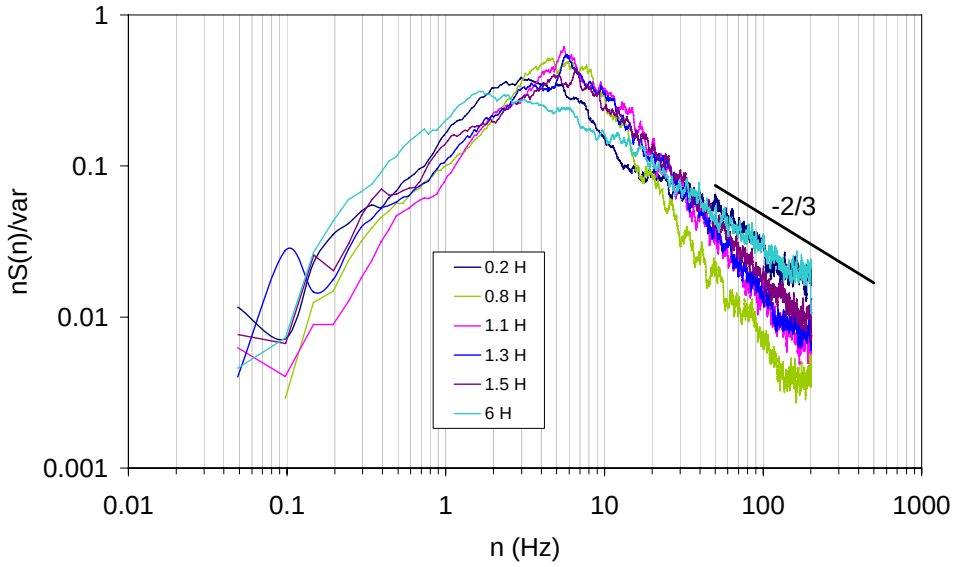

Figure 4.16 log-log form of W spectra for various heights throughout uniform forest.

The vertical power spectra in the shear layer (Figure 4.14) appear to have a smaller and more distinct spread of frequencies than the streamwise spectra, with peaks at 5-6 Hz. Below the shear layer (Figure 4.13) the steep-drop off is more marked. For both velocity components at

6*H*, it is observed that the –2/3 rule is generally obeyed. At lower heights the gradients become steeper suggesting that Kolmogorov dissipation does not occur.

Peak frequencies for most of the presented spectra are difficult to determine exactly, but at inflexion height they are approximately $f_p(u) \sim 2$ Hz and $f_p(w) \sim 6$ Hz. To compare these results with Raupach *et al.*'s data the frequency is normalised by inflexion height and local mean velocity, *U*. This gives a non-dimensional frequency values of 0.15 and 0.42 for *u* and *w* respectively. This compares well with the values of Raupach *et al.*, who obtained 0.15 and 0.45 respectively.

4.4.1 Application of Mixing Layer Scaling

If the scaling of the *z* axis by L_s is used in the shear layer region it is possible to compare the spectra of the three different forests. Power spectra for four heights ($-L_s$, -0.4 L_s, 0 L_s, and +0.4L_s) are shown in Figures 4.17-4.20 (for streamwise velocities) and Figures 4.21-4.24 (for vertical velocities). The results are presented in the $nS(n)/var$ against $\log(n)$ form so that the spectra from the three different forests can be compared.

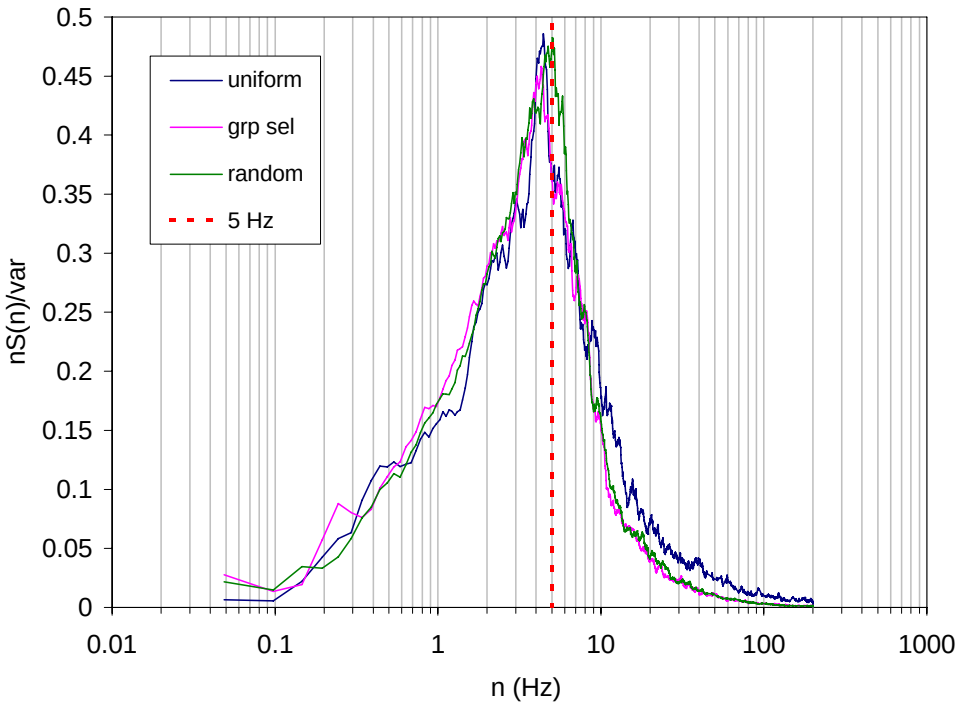

Figure 4.17 U spectra at $z_i L_s$ = -1. (5 Hz line shown as an approximate guide to tree sway frequencies.)

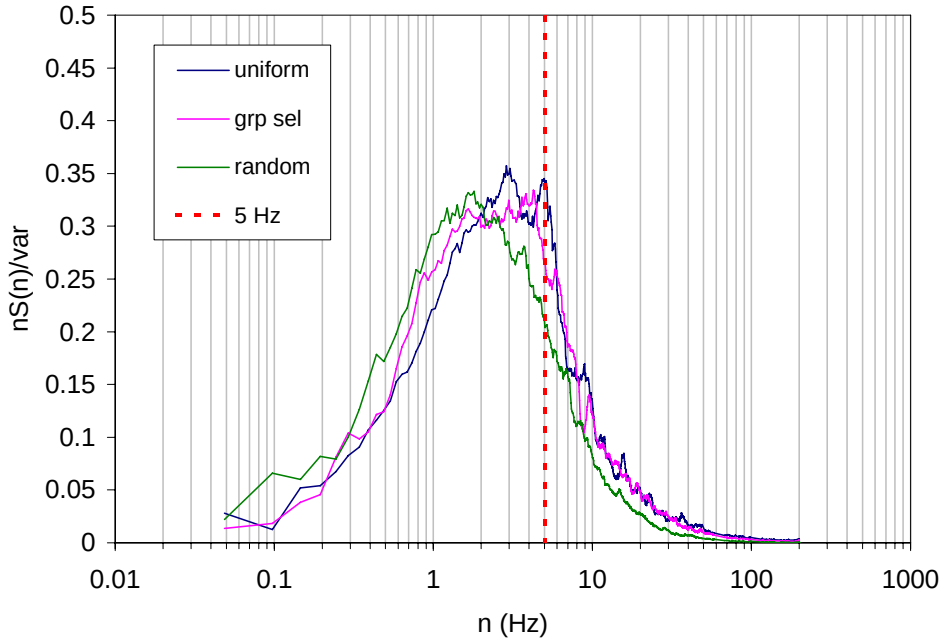

Figure 4.18 U spectra at z_i/L_s = -0.4.

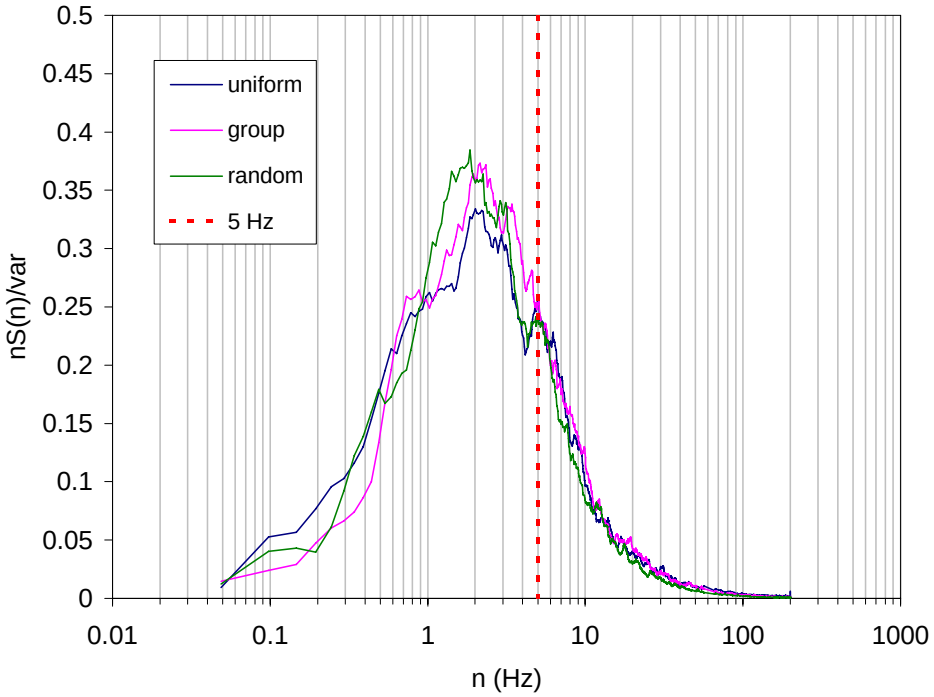

Figure 4.19 U spectra at z_i/L_s = 0.

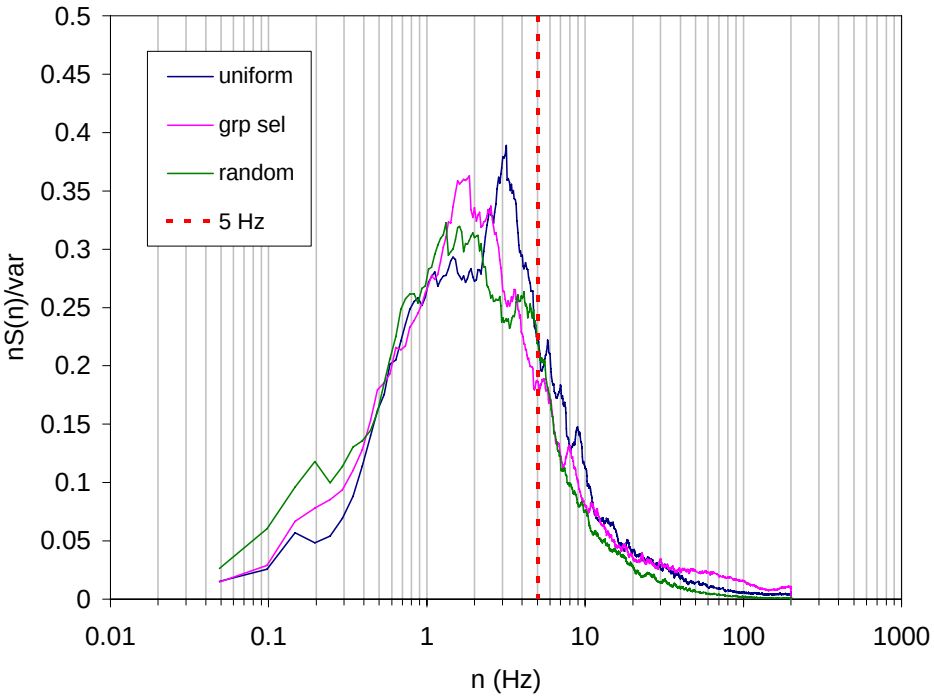

Figure 4.20 U spectra at z_i/L_s = 0.4.

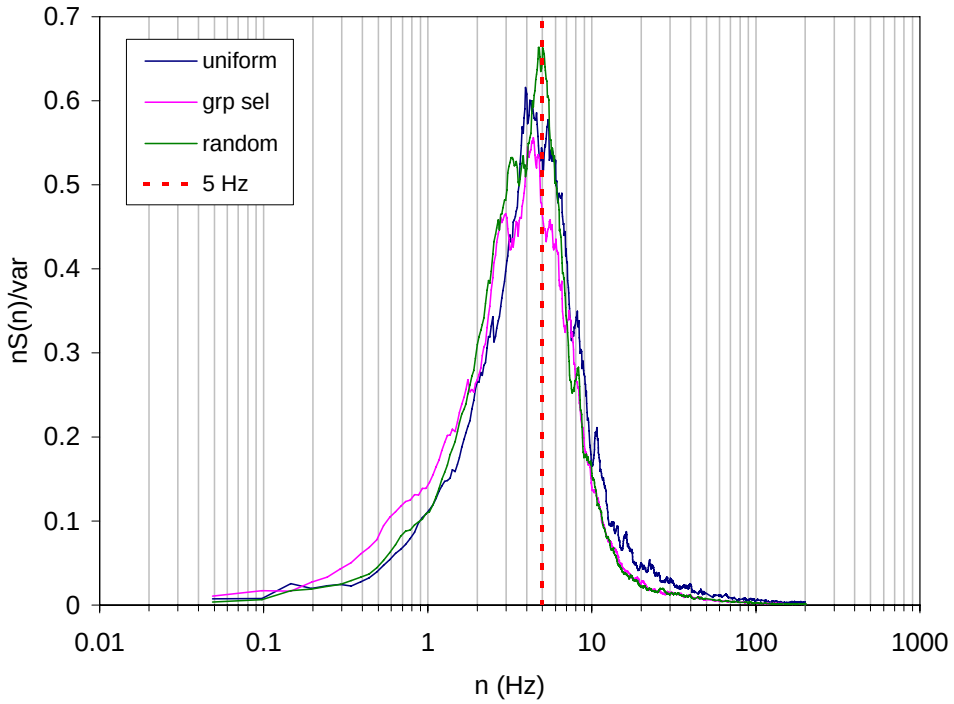

Figure 4.21 W spectra at z_i/L_s = -1.

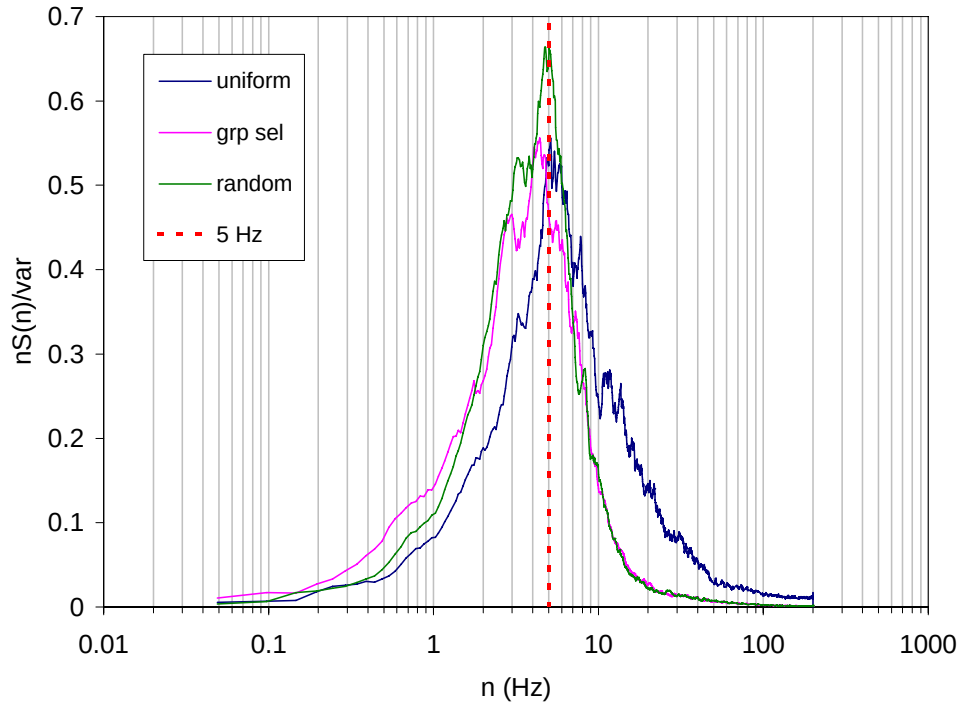

Figure 4.22 W spectra at z_i/L_s = -0.4.

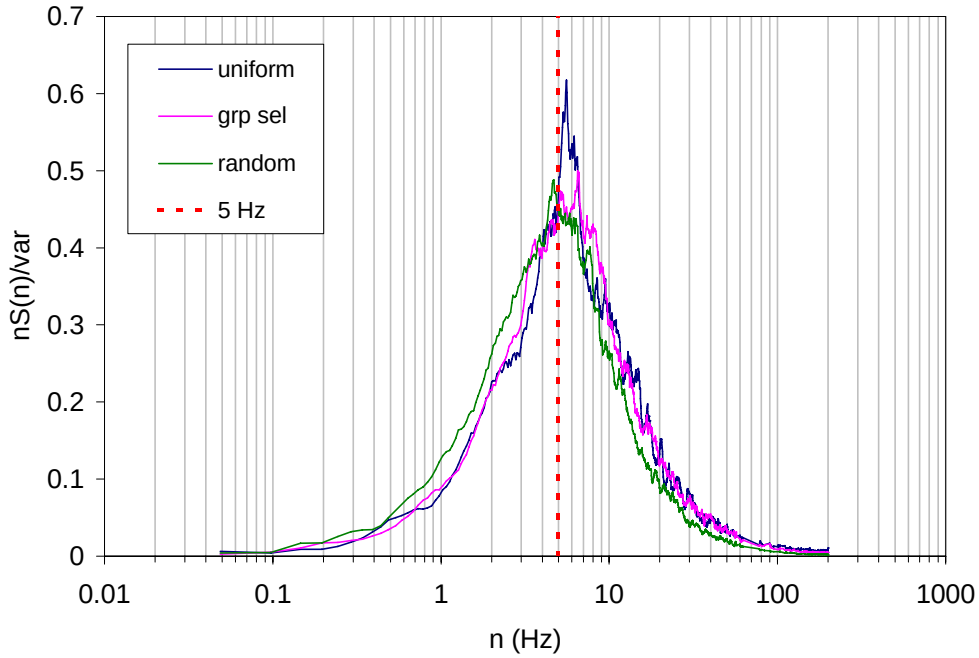

Figure 4.23 W spectra z_i/L_s = 0.

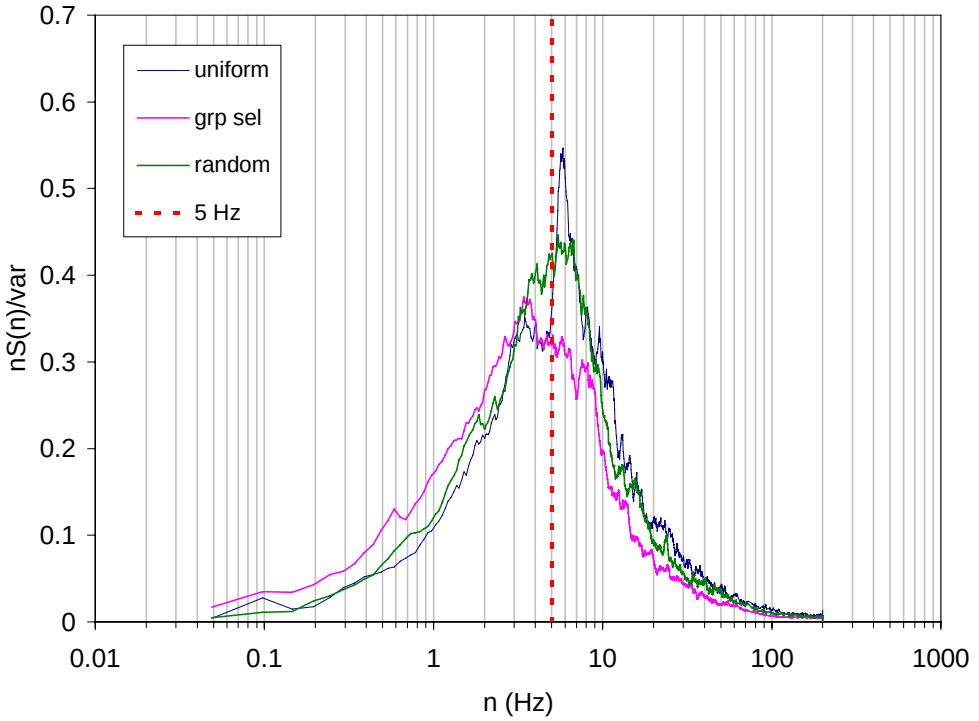

Figure 4.24 W spectra z_i/L_s = 0.4.

Note first that the *x* axis units are in Hz and not Strouhal number. Considering the vertical velocity spectra first, for all three forests the graphs show a tight peak at approximately 4-6 Hz in the range $-1 < z_i/L_s < 0$. At $z_i/L_s = 0.4$ the general trend is still followed but the peak is far more spread out. The frequency of the 200 mm trees in the uniform forest is approximately 6 Hz (see Section 3.6.1) and the frequency for the 300 mm trees in the random forest is 4.8 Hz. The question has to be asked whether this is pure coincidence (or at least extremely good modelling of a) the wind and b) a tree adapted to that exact wind!) or an inextricable coupling of the wind and tree movement. In agreement with the latter are the field results of Finnigan (1979a,b) and Segnier *et al.* (1976). It is noted however, that the results of Gardiner (1994) disagree with this. He found the trees in the field to vibrate at frequencies higher than the peak of the vertical power spectra.

The streamwise velocity spectra are quite different. At inflexion height ($z_i/L_s=0$) there is a dominant peak at approximately 2 Hz. However, on closer inspection there are small secondary peaks at 5-6 Hz, indicating the possible presence of two structures. This was reported by Segnier *et al.* (1976) as small 'humps' in the *u* velocity spectra. It is possible that this small detail is missed by some authors because of the use of log-log presentations, which have a tendency to smooth out details. At $z_i/L_s = -1$ existence of the 2 Hz peak is not evident, leaving *extremely well defined spectra* with a peak band of 4-6 Hz. A band in the high frequency region of the spectra also disappears leaving the sharp drop reported by Gardiner amongst others.

4.5 Discussion

The results presented in Section 4.3 and 4.4 appear to obey the scaling ratios suggested by Raupach *et al*. If the assumption is then made that the main flow is based on a mixing layer flow then some of the extra features in the results can be explained.

Neglecting tree resonance for a moment, the characteristic eddy frequency in the lower canopy is approximately 5 Hz. This describes the *u* and *w* fluctuations and would appear to suggest a series of eddies, separated by a wavelength, Λ_x. Close to the inflexion height, a second peak at a lower frequency dominates the streamwise velocity. This idea contradicts the structure of a mixing layer with similar sized and spaced eddies (see Figure 4.26) because the peak would surely be in the vertical fluctuations as well. Raupach *et al*. have rationalised the unexpected low frequency *u* turbulence as 'inactive turbulence' where the larger eddies of the boundary layer have an affect on the streamwise motion, but not on the vertical motion, due to the presence of a near wall (Perry *et al*. 1986).

To investigate this theory, Figure 4.25 shows the *U* turbulence spectra, at inflexion height, for the uniform forest and the oncoming turbulence (*i.e.* with the forest removed). Note the scale on the *y*-axis is not normalised by variance and thus is a direct comparison of spectral energy. The graph shows that the oncoming turbulence could be responsible for the majority of the spectral energy in the forest present case, especially in the lower frequency range. However, it does not explain the main 2 Hz peak. The consistent calculation of a non-dimensional value for the peak of 0.15 by different authors would also not suggest oncoming turbulence as the dominating regime. It is possible that the instability wavelength described by Michalke (1964, 1965) may have an effect on the flow. In terms of shear length, (see Section 1.7.1) the instability wavelength is given by $\Lambda_x = 15.7L_s$, which for a uniform forest,

and using the mean streamwise velocity at inflexion height, gives a frequency of 1.88 Hz. Neither of these theories are conclusive, but lower frequency structures are examined in more detail in Chapter 7.

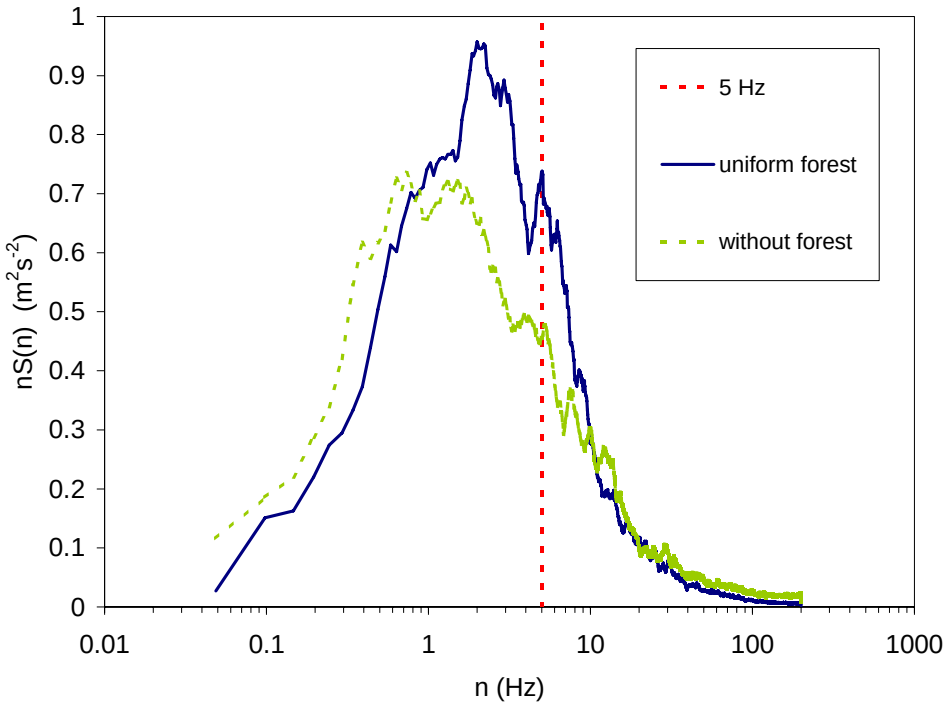

Figure 4.25 Comparison between u turbulence spectra at z= 220 mm, with and without the presence of the uniform forest.

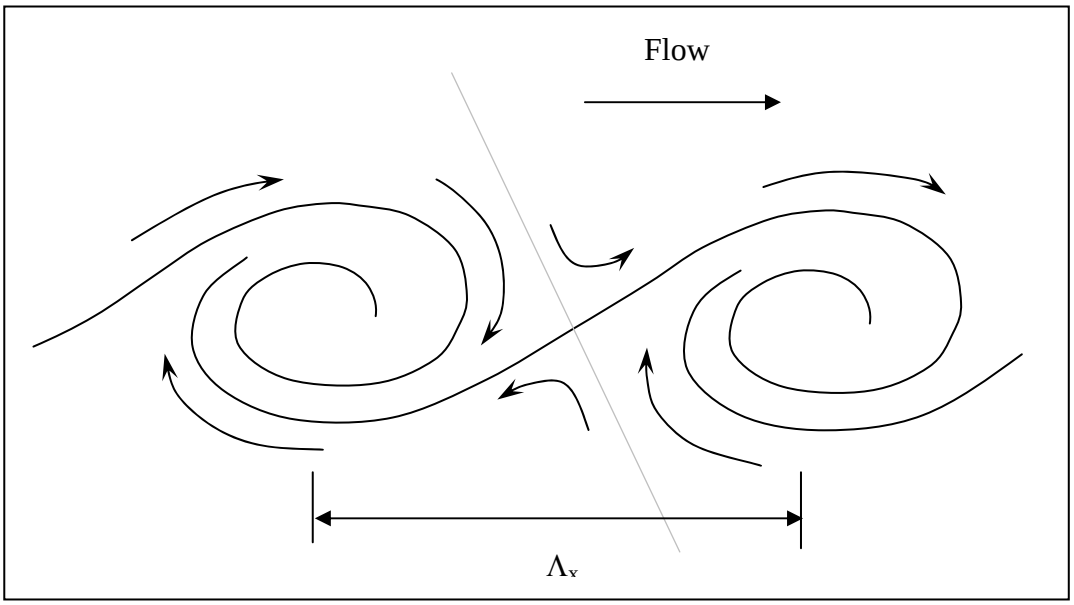

Figure 4.26 Simplified structure of a 2-D mixing layer.

With inertial layer turbulence dominating the upper mixing layer, the underside of the mixing layer is far more organised. The spectra obtained at the edge of the shear layer, shown in Figures 4.17 and 4.21, are well organised with well-defined peaks at approximately 5 Hz. This would correspond to the outer edges of the vortices in Figure 4.26. Observations made of experimental mixing layers and numerical simulations show fine scale turbulence arising at the interface between the two flows (Dimotakis and Brown 1976). This is where actual mixing occurs between the two fluids and leads to the development of fine scale turbulence. The density of this mixing increases towards the centre of the mixing layer. This may explain why the gradient on the high frequency side of the main peak at $0L_s$, is greater than the gradient at $-L_s$.

A model of eddies separated by distance $\Lambda_{x,}$ and approximate height, $2L_s$, may be formulated, as presented in Figure 4.26. To understand how this is derived we must consider mixing layer theory. In an experiment, a mixing layer is formed by allowing two co-flowing streams, of velocity U_1 and U_2, to merge at the end of a splitter plate. For the shear layer to roll up there must be perturbations in the vertical direction. Originally, mixing layer experiments were carried out at very low turbulence levels and the dominating wavelength was set by the instability wavelength. However, Wygnaski *et al*. (1979) used acoustic forcing, utilising an organ pipe near the splitter plate, to produce similar frequencies in the mixing layer. The initial frequency forcing near the splitter plate is the most important parameter in the forming process of mixing layers (Ho and Huang 1982). It is therefore possible that a tree's movement, at its sway frequency, causes fluctuations in the flow, and thus providing a frequency to enable the shear layer to roll up.

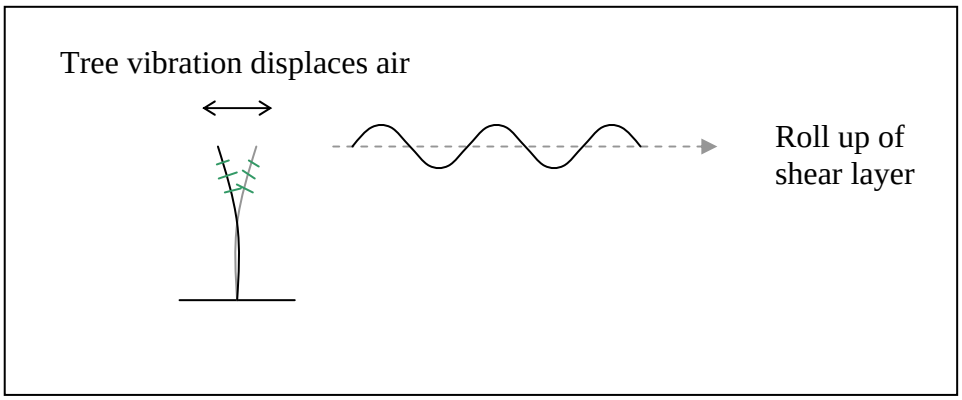

Figure 4.27 Formation of a mixing layer due to wavelength perturbation.

Once a mixing layer is formed it is expected to grow downstream. Obviously it is impossible to observe this phenomenon with single point measurements. These questions will be addressed in the next section on forest edges.

4.6 Conclusions

There are several very important points that derive from the results of this chapter:

- The scaling parameter, L_s, suggested by Raupach *et al*., successfully scales vertical heights in three different forest canopies, providing more substantial evidence that there is a universal flow mechanism at work. The nature of the scaling also suggests that a mixing layer type flow is a strong contender for the lead role of such a mechanism.
- Gust power spectra also support the mixing layer flow postulation, with nuances in the vertical velocity spectral peaks adding further weight to the argument. The streamwise velocity spectra are well defined lower in the canopy and also help support the mixing layer theory. Higher up in the shear layer the streamwise spectral peaks are no longer invariant with height, and possibly become diluted by a secondary mechanism or the oncoming turbulence.

- Importantly there appears to be a clear connection between tree sway frequency and peak gust frequency. Inferences from mixing layer theory suggest tree swaying directly injects air motion into the shear layer and produces coherent structures of similar frequency. The tallest trees in the forests appear to be the main culprits for the input of sway energy.

The interconnection of tree sway frequency and canopy gusts frequency has been noted many times in canopy studies but has never been fully investigated. Field studies are unreliable because of limited data on the variation of tree sway frequencies throughout the forest. The controlled environment of the wind tunnel is the only reliable method to investigate the theory. The following chapter investigates the flow over forest edges and in doing so also proposes that gust production is inherently linked to the swaying of edge trees.

Chapter 5: Forest Edge Velocities

5.1 Introduction

At the up-wind end of a forest, the wind flow changes from open country flow to forest canopy flow. The transition is not immediate but develops, as illustrated in Figure 5.1. Each terrain has a characteristic roughness length, z_0, and velocity profile. Immediately prior to the leading edge of the rough region the flow speeds up over the new objects. Past the leading edge a new, rough surface boundary layer begins to grow under the old smooth-surface boundary layer. In addition, the velocity profile becomes displaced to a new height, *d*, usually just below tree top height in forests. The transitional process is well documented by ESDU items 82026, 83045, 84030, 86035.

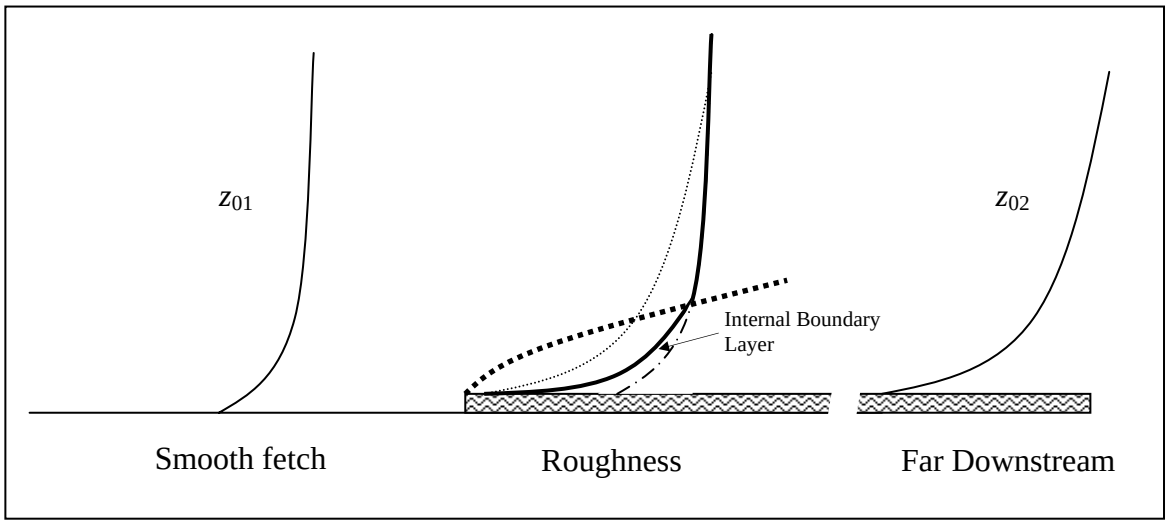

Figure 5.1 Transition from smooth to rough terrain.

The flow is not in complete equilibrium until the new roughness velocity profile entirely eliminates the older one. However, within the internal boundary layer (IBL) the flow is believed to approach equilibrium rather more quickly. There are also suggestions that there is a thin equilibrium layer in the IBL that is in complete equilibrium with the surface. Very few measurements exist to confirm this but estimates suggest that in low vegetation the

thickness of the equilibrium layer is 1%-2% of the distance downstream from the leading edge (Bradley 1968), and 5% for a forest (Gash 1986).

Few measurements have been made of wind-flow near forest edges. Irvine (1994) carried out tests in the field, but was limited to just three streamwise measurement positions in the forest. He found that there was a large increase in the Reynolds stress at tree height, between x =3.6H and x= 14.6H. Kruijt *et al.* (1995) and Stacey *et al.* (1994) carried out wind tunnel experiments on a forest transition. Stacey simulated an 'open farmland' wind approaching a model forest edge. Velocity contours were produced over the model but he was not able to use his fragile hot-wire anemometers between the trees. However, the speed up over the top of the leading edge was confirmed and Stacey also found an increase in standard deviation of the streamwise velocity further back into the forest. Irvine's field measurements confirmed this these observations and he also observed a delay between the increase in streamwise standard deviation and a similar increase in vertical standard deviation.

Li *et al.* (1990) carried out CFD studies on the leading edge of a plant canopy and found a large pressure gradient over the leading edge of the modelled forest. A pressure minimum existed about 4 tree heights in from the edge and near the canopy top. Prompted by concern over the effect of clear felling on the nesting of the Abbot's Booby on Christmas Island, Raupach *et al.* (1987) investigated an edge in the wind tunnel. They found that the edge caused local flow separation and an intermittent recirculating vortex. This would produce a low pressure area similar to the one found by Li but whether this mechanism could be modelled by Li is unclear.

The experiments described in this chapter were designed to add to the current sparse knowledge of forest edge flows and attempt to explain general trends in the formation of canopy gusts.

5.2 Experimental Overview

The three model forests were exposed to onset winds with z_0 = 0.05 m (as described in the forest edge simulation outlined in Section 3.2). This is representative of open farmland with a few sparsely placed hedges. As with the mid-forest study, streamwise and vertical velocity components were measured with the Dantec LDA with 120 s observation times. The positions of measurement points are presented in Figure 5.2. The horizontal and vertical spacing between traverses were chosen to be more frequent closer to the edge, where rapid changes in velocity were expected.

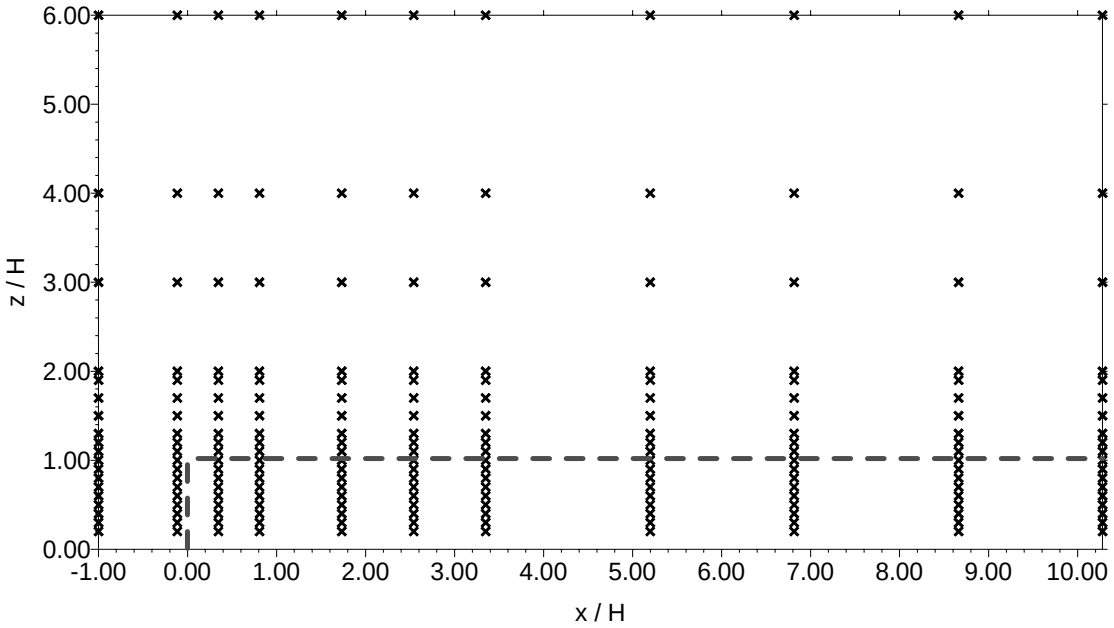

Figure 5.2 Positions of measurement in forest edge simulation.

5.3 Uniform Forest Velocity Statistics

Results in the following section are presented as ratios of velocity / U_{ref} (or $\overline{u'w'}$ / U_{ref}^2). Dimensions are in the form x/H and z/H where H is the height of the uniform forest (200 mm).

Contour plots of results for the uniform forest are shown in Figures 5.3-5.8. The white dotted lines indicate the edge of the forest. The contours are created using Surfer 32 software, which uses triangular linear interpolation between measurement points. A 1/10 vertical to horizontal anisotropy weighting was applied to account for the large mean horizontal spacing between points.

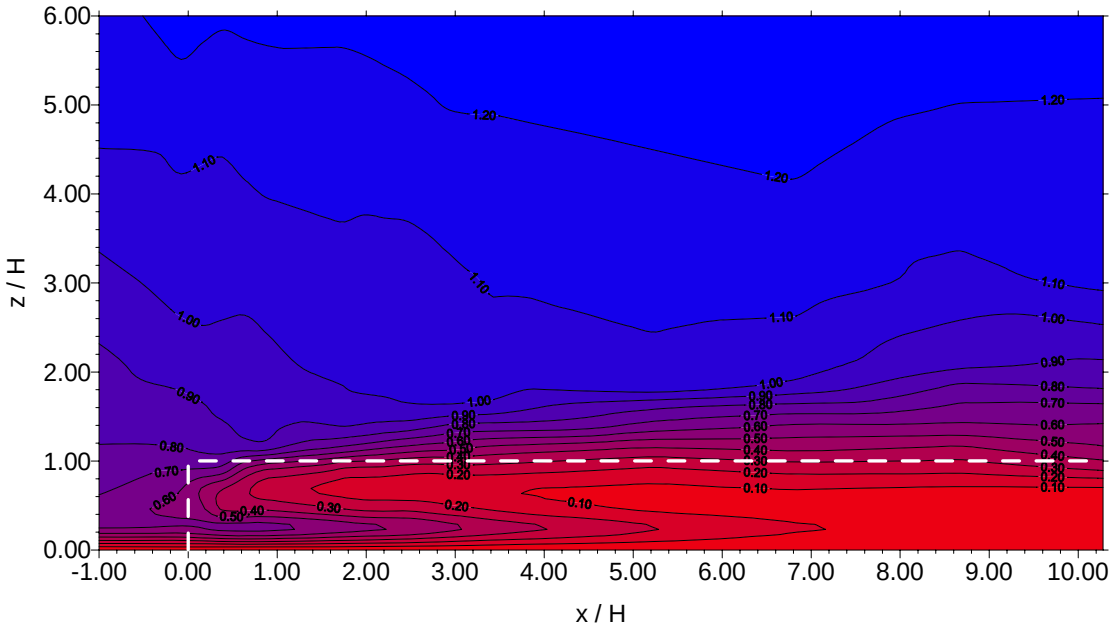

Figure 5.3 U / U_{ref} in and over uniform forest.

The mean streamwise velocities are represented in Figure 5.3. Considerable speed up over the leading edge is observed, as reported by numerous authors. The close spacing of contours across the top of the forest represents the inflexion region. The increase in depth of this region is quite evident further back into the forest. The streamwise velocities decrease

rapidly in the main branch region. Below this, in the less sheltered trunk region, the velocity decreases at a slower rate.

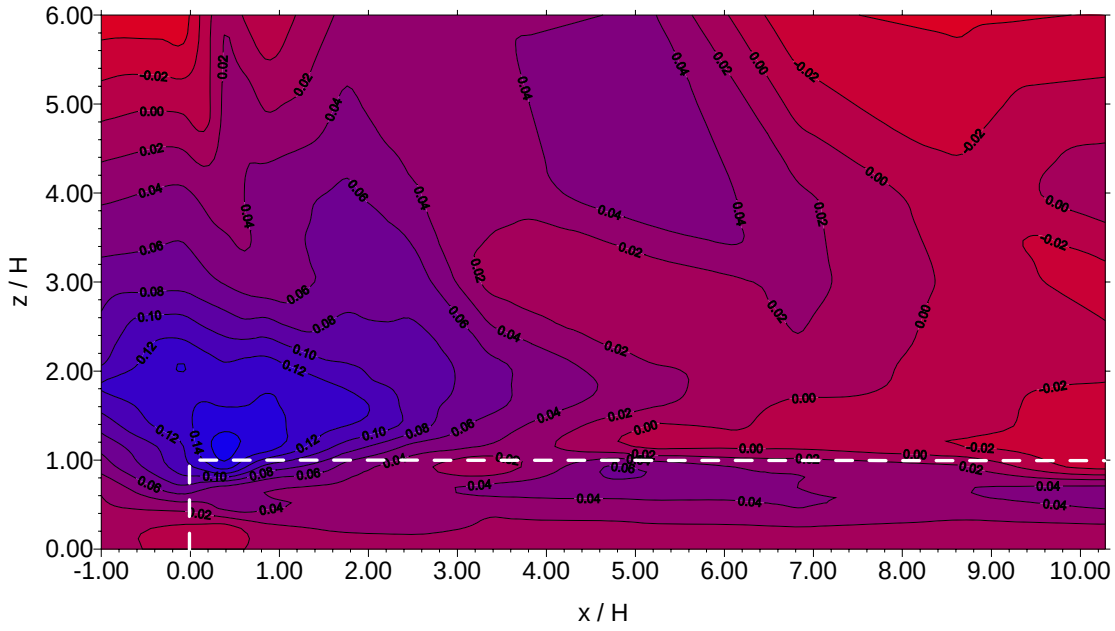

Figure 5.4 W / U_{ref} in and over uniform forest.

Figure 5.4 shows the mean vertical velocities and is dominated by the large increase in vertical velocity at the leading of the forest. This is simply where the flow is diverted by the forest obstruction. The combined vector components are represented in the mean velocity vector plot in Figure 5.5. Smoke visualisation did not confirm Raupach *et al.*'s (1987) observation of intermittent recirculation.

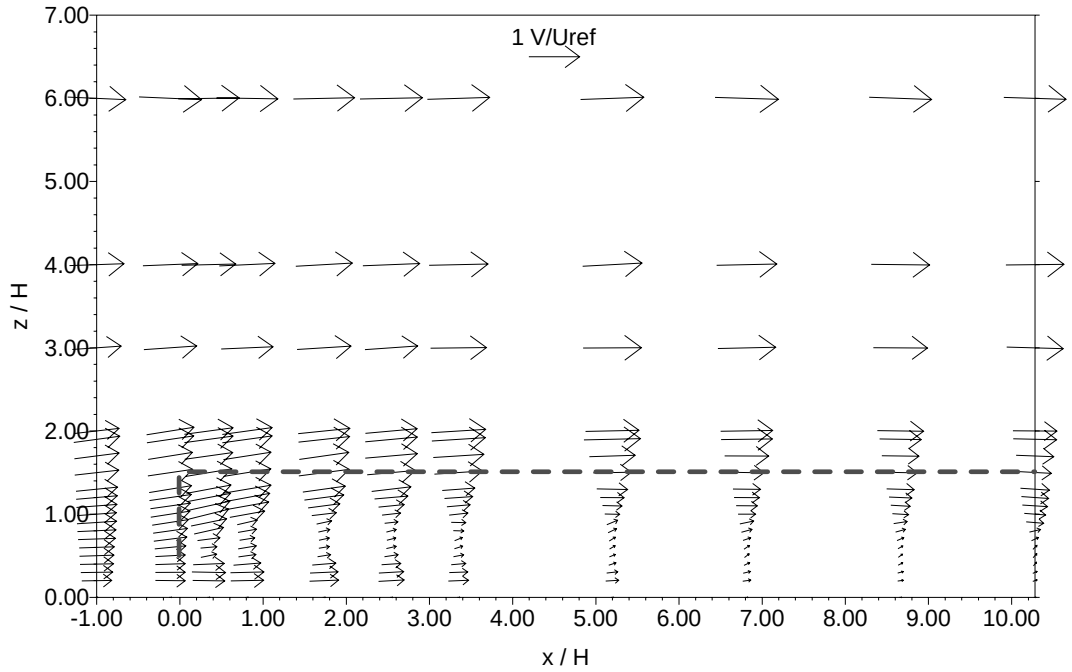

Figure 5.5 Mean velocity vectors in and over uniform forest.

The results become more interesting when studying the standard deviation and Reynolds stress plots. Figure 5.6 shows σ_u / U_{ref} and there are several points to note. First, above the forest there is a definite increase of σ_u / U_{ref} from background turbulence. This region starts almost at the leading edge and grows in the vertical direction and increases in value further downstream. σ_u / U_{ref} at the edge of the forest is *ca*. 0.16 and increases to *ca*. 0.22 at the opposite edge. Secondly, below the forest canopy the background rms values are significantly reduced. Lastly, the lowest value of σ_u / U_{ref} (*ca*. 0.06) is recorded in a concentrated region about 1-4.5*H* from the leading edge, at the height of the branches.

The vertical fluctuations represented by the ratio σ_w / U_{ref} are presented in Figure 5.7. Immediately it is observed that the vertical fluctuations do not start to increase until much further back into the canopy (*ca*. 3*H*). However, in the region associated with the small streamwise fluctuations, there is a corresponding region of small vertical fluctuations.

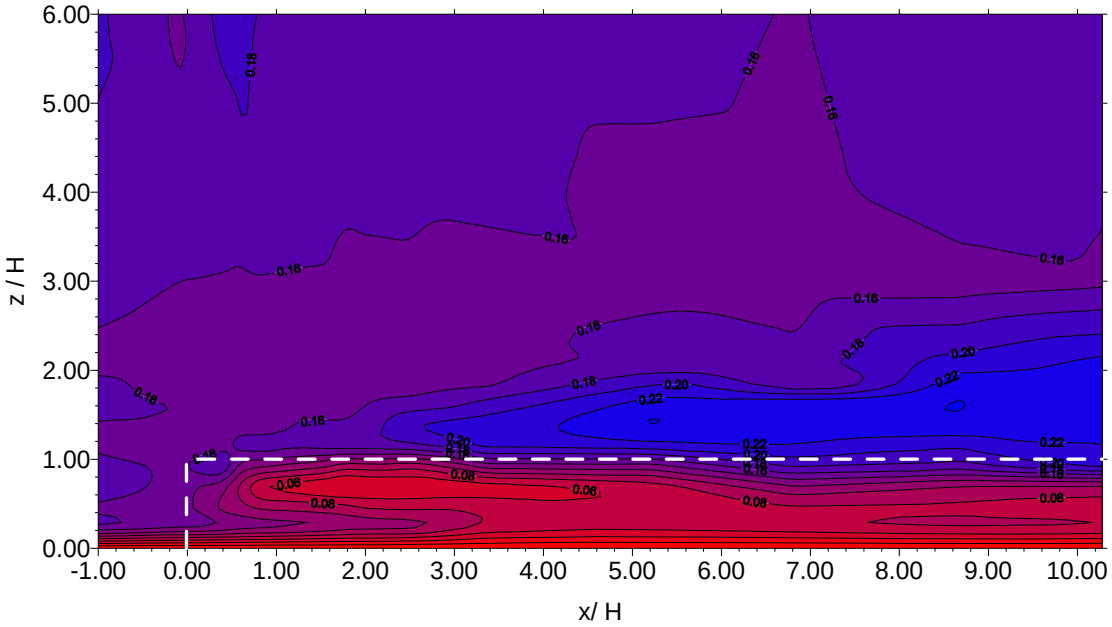

Figure 5.6 σ_u / U_{ref} in and over uniform forest.

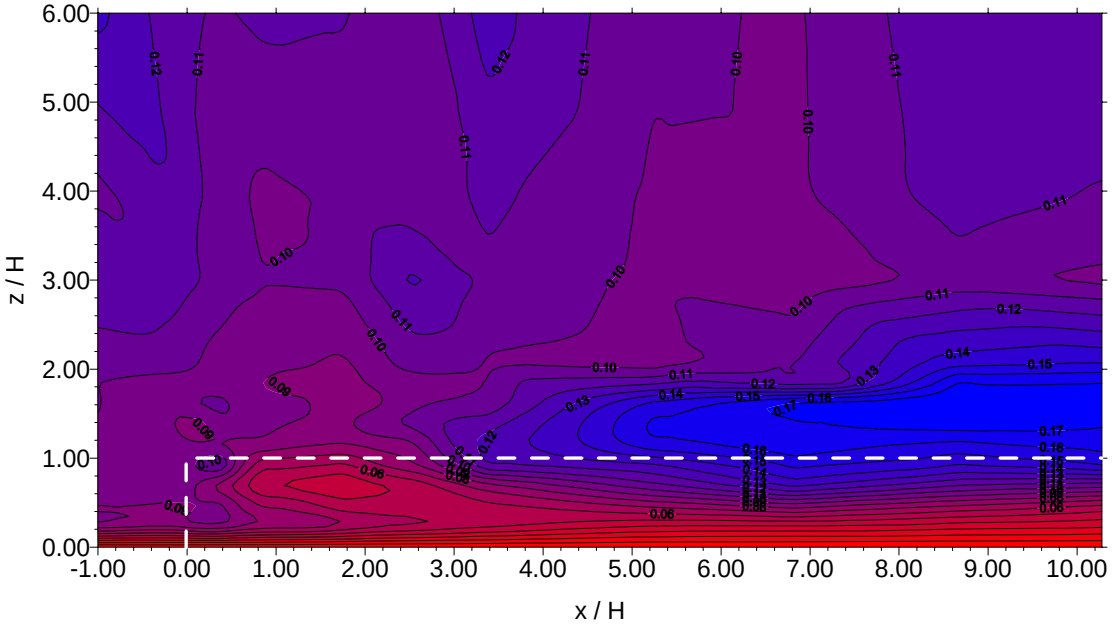

Figure 5.7 σ_w / U_{ref} in and over uniform forest.

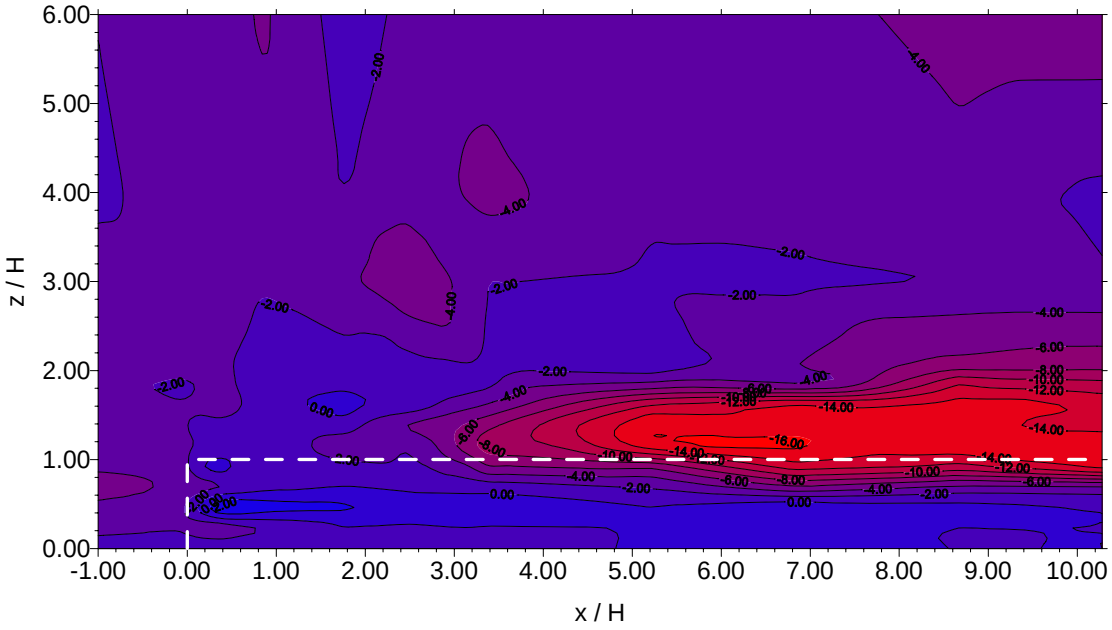

Figure 5.8 $\overline{u'w'} / U_{ref}^2$ **(x 10** $^{-3}$**)** ***in and over uniform forest.***

The absence of large vertical fluctuations for a distance after the leading edge would suggest an absence of large canopy gusts up to this point. This is probably best supported by the values of $\overline{u'w'} / U_{ref}^2$ shown in Figure 5.8. The Reynolds stresses do not start to increase until 3*H*, where the vertical fluctuations also increase. The increase is dramatic and would suggest a distance after which the flow becomes unstable and gusts start occurring. Values of $\overline{u'w'} / U_{ref}^2$ in this region approach those of mid-forest and thus it is not unreasonable to assume that Honami-type gusts exist in this region. The depth of the shear at the end of the forest is also similar to that in the mid-forest simulation, see Figure 5.9.

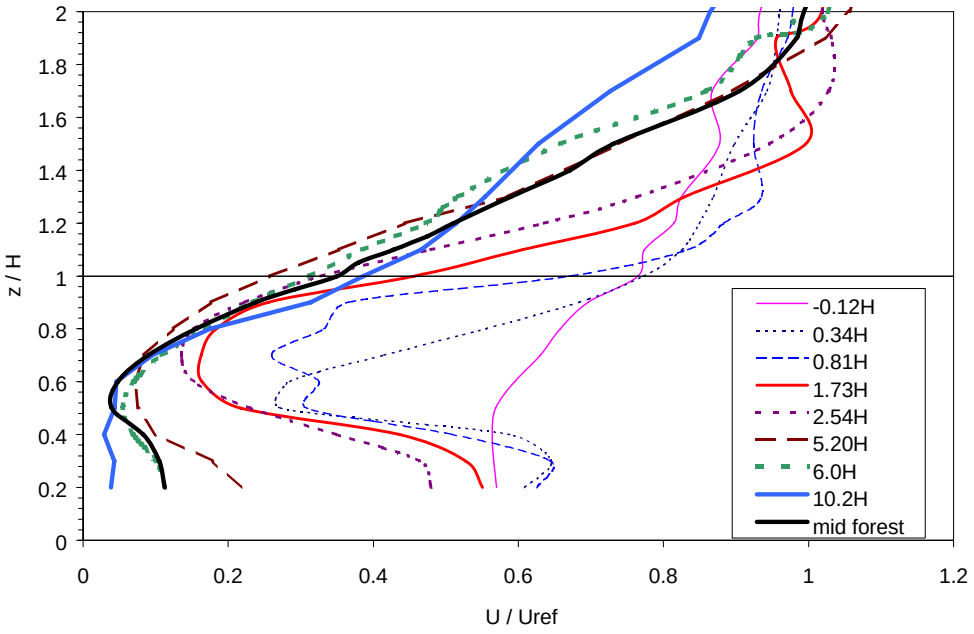

Figure 5.9 Profiles of mean streamwise velocity near the front of the uniform canopy. Distances in key are from leading edge.

Thus the key points from these profiles are:

- An apparent dramatic increase in $\overline{u'w'} / U_{ref}^2$ away from the immediate forest edge.
- This rise is in accordance with increases in vertical fluctuations but not with horizontal fluctuations, which increase at the leading edge.
- There is a region of small turbulent fluctuations just after the leading edge and in the main canopy branch region.

5.4 Frequency Analysis of Uniform Forest Data

Frequency analysis was carried out on the LDA velocity data, in a similar manner to that described in Section 4.4, to investigate evolution of structures in the flow over the forest edge.

5.4.1 Vertical Velocity Gust Spectra

The contour plots of σ_w / U_{ref} in Figure 5.7 reveal that large vertical fluctuations arise within the forest, approximately 3*H* in from the forest edge. Spectral analyses show that in this region vertical velocity fluctuations are dominated by structures in the 5-7 Hz frequency band, similar to those in Figure 4.14, and are shown in Figure 5.10. These have already been shown to be related to the coherent canopy gusts and the movement of the trees. Downstream of this position the gust peaks rise in strength.

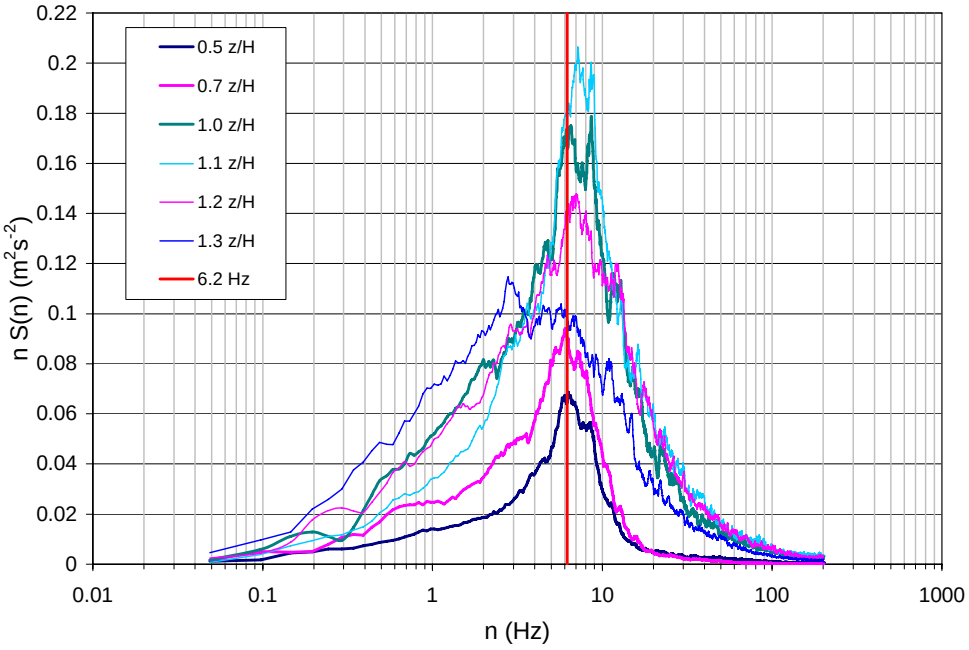

Figure 5.10 W velocity gust spectra at x/H = 3.3.

The origin of these gusts appears to be in the region of slow, lightly fluctuating air around 1.7*H* from the edge. Gust spectra of vertical fluctuations at *x*/*H*=1.7, *z*/*H*=0.6-0.9 are shown in Figure 5.11 as well as the sway frequency of the uniform forest. Upstream of this position there are no obvious 5-7 Hz peaks in the vertical gust spectra. To help visualise this, Figure 5.12 is a detail of the edge and vectors in Figure 5.5. Superimposed dots marks the presence of these 5-7 Hz spectral peaks with the diameter of the dot being proportional to the height of the spectral peak. It shows that the gusts originate in the slow moving region and move

upward in the direction with the mean wind vectors. The largest gusts are downstream and further up in the shear region.

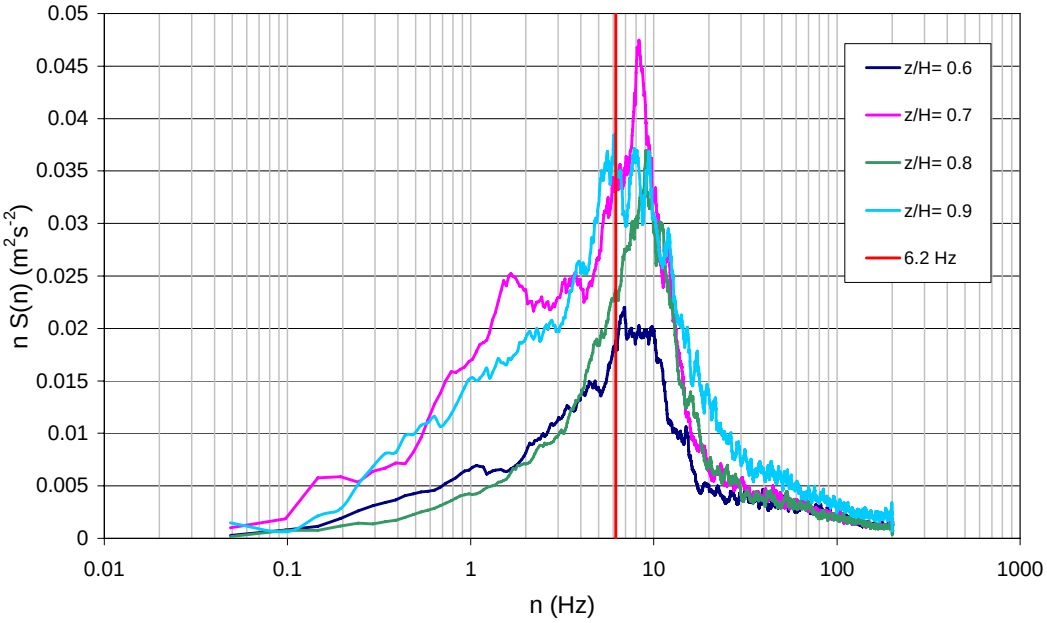

Figure 5.11 W velocity gust spectra at x/H= 1.7.

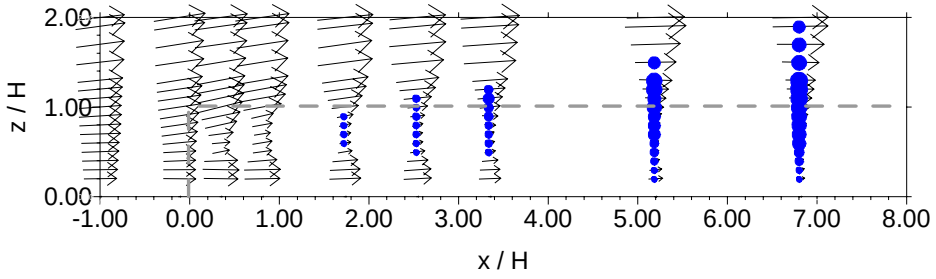

Figure 5.12 Diagram of the general trend of gust generation at the forest edge. Superimposed dots mark the presence of 5-7 Hz spectral peaks, the diameter of the dot being proportional to the height of the spectral peak.

5.4.2 Streamwise Velocity Gust Spectra

Figure 5.6 reveals that the streamwise turbulence is increased at the leading edge and over the top of the forest, rather than a distance downstream as with the vertical turbulence. Plotting the gust spectra across the top of the forest at inflexion height (z/H=1.1) generates the plot in Figure 5.13. The spectral peak appears to be around 1-2 Hz up to a downstream distance of x/H = 1.7. After this distance the peak tends to increase to 2-3 Hz. Further downstream at x/H = 5.2 the streamwise spectrum becomes more energetic and is similar to the spectrum of the mid-forest simulation, see Figure 4.9.

When compared with the vertical velocity spectra it is difficult to pick out the clear existence of canopy gusts in the streamwise velocity spectra. At x/H =1.7 the vertical velocity spectra shows signs of coherent gusts emerging, but this is not evident in the streamwise velocity at the same position, see Figure 5.14. Also interesting to note in Figure 5.14 is the extreme difference in spectral energy between z/H= 0.8 and z/H= 0.9. This seems to reflect the fact that the streamwise turbulence, σ_u, increases from the leading edge of the forest but does not penetrate further than just below the canopy height.

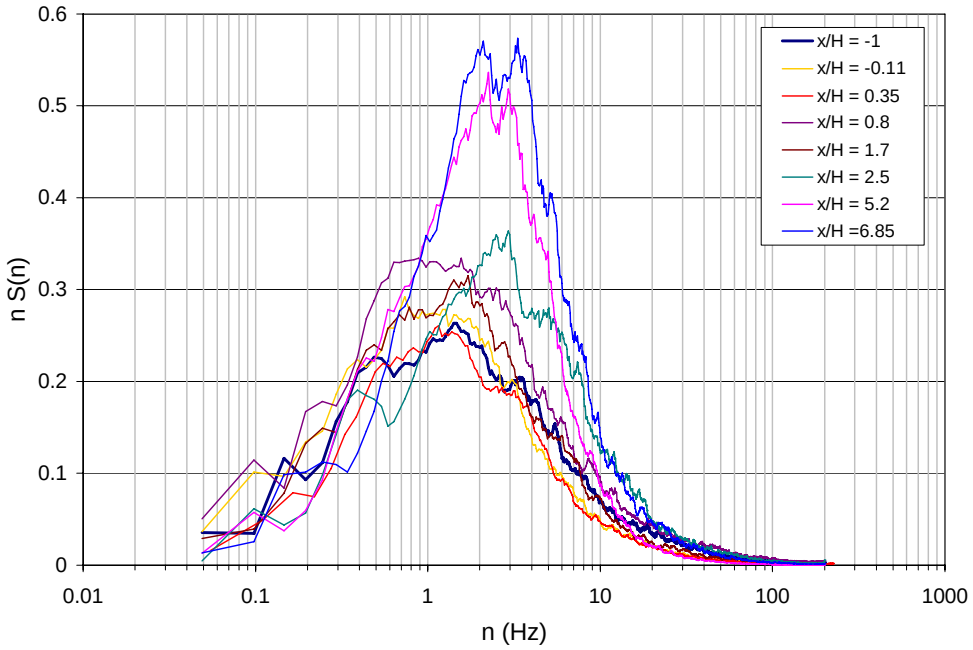

Figure 5.13 Streamwise gust spectra at z/H= 1.1 showing the transition to canopy flow regime over x.

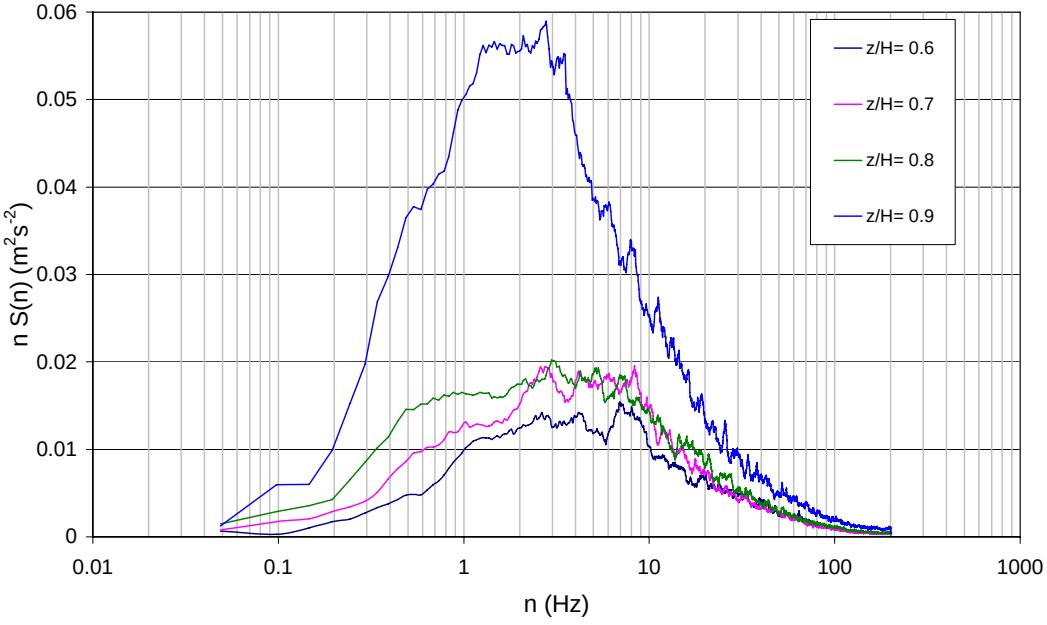

Figure 5.14 Example of streamwise gust spectra at x/H= 1.7. Unlike the vertical gust spectra at these positions it is difficult to identify canopy gusts.

5.5 A Mechanism for the Generation of Gusts

The evidence presented so far in this chapter clearly indicates that there is a transition region between the continuation of oncoming turbulence structures and the onset of canopy shear driven turbulence structures. From Chapter 4, the conditions for production of Honami-type canopy gusts are shear instability in the mean velocity profile and mechanical vibration input from swaying trees. The previous section showed that vertical fluctuations at tree frequency are present at 1.7*H*, in the branch region, but are not large in comparison with the rest of the flow. As these fluctuations are carried upward by the mean flow they enter the large shear region and it is at approximately 3*H* that large gusts occur.

Taking account of all these observations, we are now in a position to propose a mechanism hypothesis to explain the formation of forest canopy gusts. The hypothesis begins with the realisation that the movement of trees upstream of approximately 1.7*H* is very important in gust generation. This movement has to be caused by the oncoming turbulence. In other words, the energy of the oncoming turbulence is transmitted into mechanical sway of these edge trees. The sway energy is then transmitted into the shear layer as initial gust vibration energy. It can therefore be postulated that if the energy of the oncoming turbulence is reduced, then the growth of canopy gusts may also be reduced.

To test this hypothesis an experiment was carried out to compare the change in $\overline{u'w'} / U_{ref}^2$ across the top of the uniform forest (z=1.1H) in high, medium and low turbulent conditions. The mid-forest and forest edge simulations were used to create the first two conditions. The low turbulence simulation was simply created by removing all turbulence generating devices in the wind tunnel. This allowed a boundary layer to grow naturally along the length of the tunnel floor (referred to herein as the ‘natural boundary layer’). Figure 5.15 shows gust

frequency spectra (in $nS(n)$ form at z/H=1) obtained with the LDA, and similarly Figure 5.16 shows the velocity and turbulence intensity profiles, obtained from hot-wire measurements. Figure 5.17 presents the result of these different simulations with the change in $\overline{u'w'} / U_{ref}^2$ across the length of the forest at z/H= 1.1.

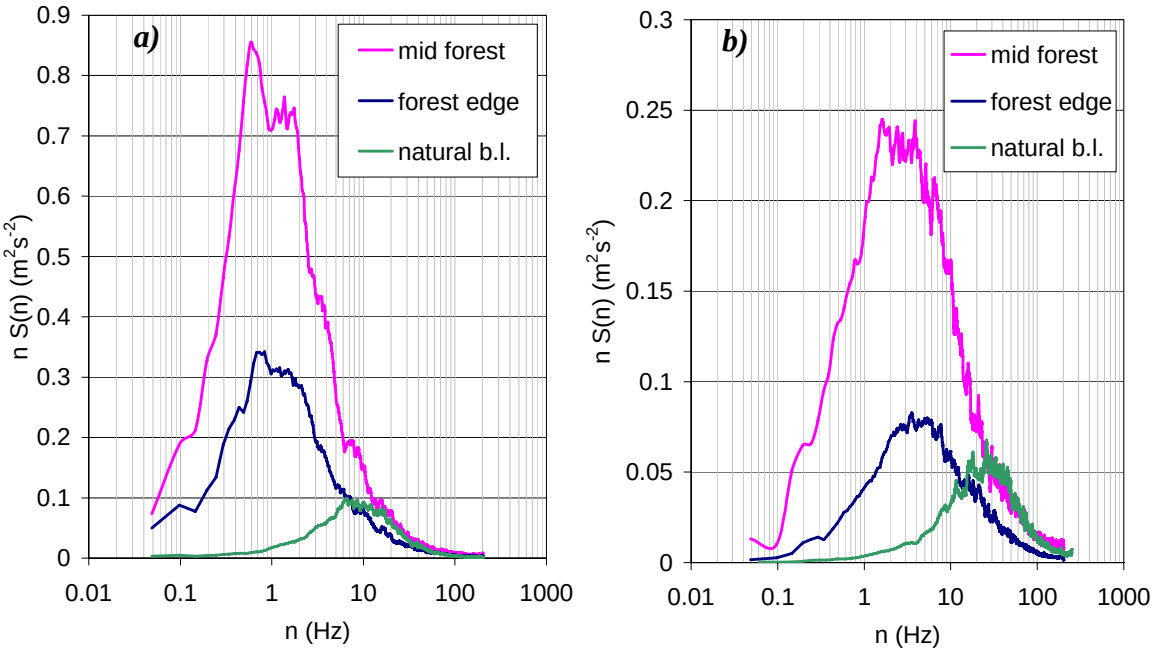

Figure 5.15 Comparisons of gust frequency spectra a) u spectra b) w spectra.

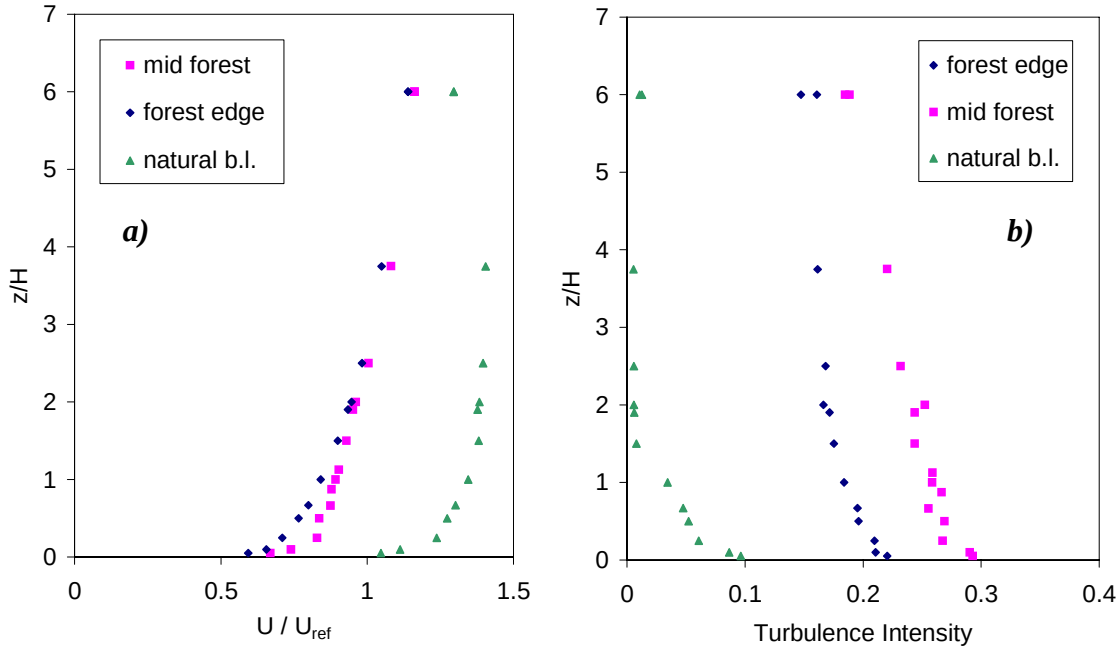

Figure 5.16 a) U velocity b) Turbulence Intensity (σ/ U).

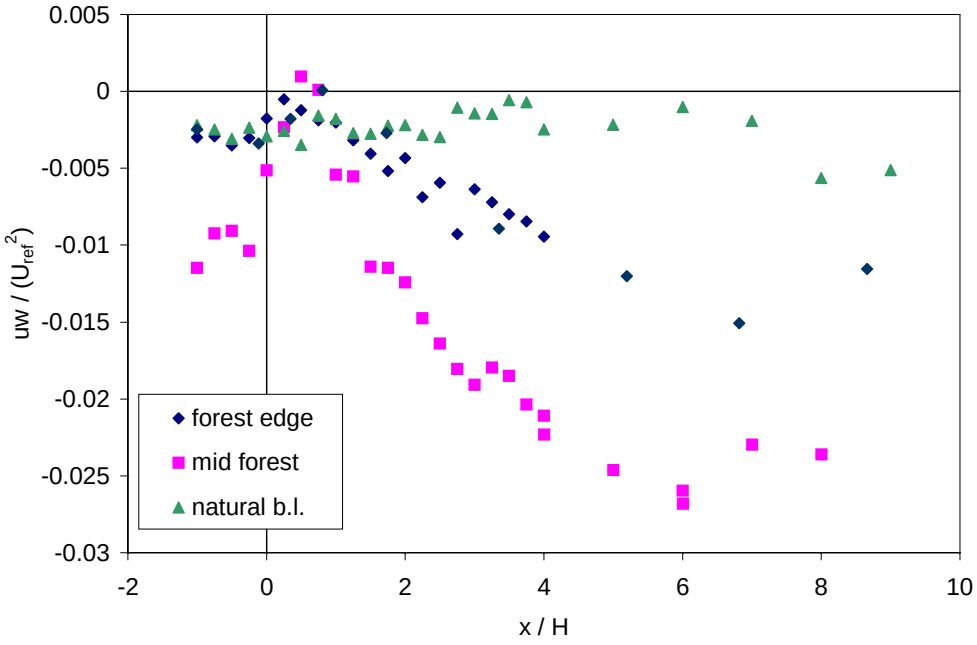

Figure 5.17 Comparisons of $\overline{u'w'}$ / U_{ref} at z=1.1H across uniform forest. x/H=6 is the centre of the forest model.

As can be seen in Figure 5.17, the effect of oncoming turbulence is impressive. The value of shear stress for the forest edge simulation is almost half that of the mid-forest, whilst the natural boundary layer exhibits very little shear stress at all.

The results must be interpreted with caution, as there is one problem associated with an experiment of this kind. It is impossible to change the turbulence intensity profile of the flow without changing the velocity profile. Thus, although the turbulence may be increased, the magnitude of shear may also be altered. However, inspection of Figure 5.9 shows that the scale of shear in the mid-forest is not dissimilar to that of forest edge simulation at the same measurement position (x=6H). Thus we may conclude that it is the magnitude of the oncoming turbulent fluctuations rather than the difference in shear that is the major cause of the difference of $\overline{u'w'} / U_{ref}^2$.

Gardiner and Stacey (1996) did not consider swaying edge trees when designing edge treatments to reduce forces in forests, yet they still arrived at a reasonable solution. They streamlined the forest edge by tapering it with smaller trees, thus preventing any sudden changed in flow. However, careful examination of their experiments, reveal that the streamlines direct the more energetic turbulence, *i.e.* at tree height, over the forest. This means less energetic turbulence, *i.e.* from a lower height, penetrates the edge trees, and in turn induces less sway.

The results in Figure 5.17 also shed new light on the use of the mid-forest simulation for future experiments. Figure 5.17 shows that the gradient of $\overline{u'w'} / U_{ref}^2$ in the mid-forest simulation adjusts quickly and ‘flattens out’ towards the centre, which is an encouraging result. However, the hypothesis proposed suggests that the mid-forest model is, in a sense, a forest edge model ‘in disguise’. The physical edge of the model causes the dominant mechanism to be the turbulence-controlled sway of edge trees, associated energy absorption

and re-injection of energy at tree frequency. What effect a far longer forest model would have on the peak of $\overline{u'w'} / U_{ref}^2$ is not clear.

5.6 Irregular Forests

With a mechanism hypothesis for the generation of gusts in a uniform forest, the next section looks at how results from the edges of irregular forests provide evidence in support of this theory.

In Figure 5.18 contour plots of $\overline{u'w'} / U_{ref}^2$ for the three types of forest are presented. The height parameter, *H*, is still defined as the uniform height of 200 mm for ease of comparison. White dotted lines, represent the extreme edges of the forest.

Considering Figure 5.18, there are differences in the rate of increase of $\overline{u'w'} / U_{ref}^2$ between the forests, represented by the frequency of the contours. As previously mentioned in Section 4.3, the uniform forest was the roughest surface because it had the greatest density of drag elements per unit height. The random forest was the least rough. It was therefore expected that the uniform forest would show the greatest rate of increase of $\overline{u'w'} / U_{ref}^2$ downstream from the edge. Figure 5.18 shows that the uniform and group selection forests have very similar rate of increase of $\overline{u'w'} / U_{ref}^2$, but the random forest has a definite delay in the increase of $\overline{u'w'} / U_{ref}^2$.

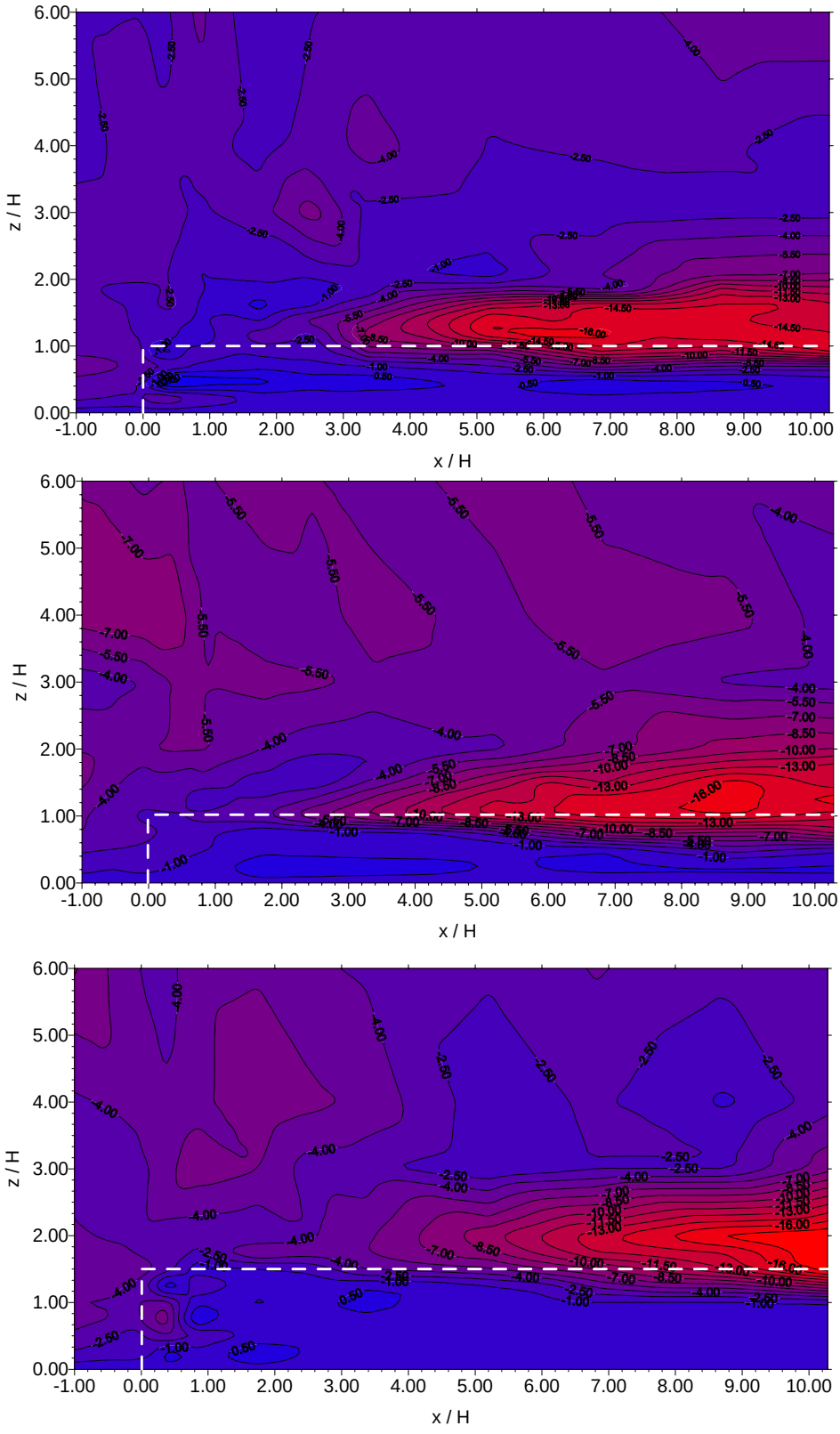

Figure 5.18 a) uniform b) group selection and c) random forests $\overline{u'w'} / U_{ref}^2$ ***(x10^{-3}).***

All three forests exhibit the largest values of $\overline{u'w'} / U_{ref}^2$ at the position just penetrating the top of the forest (as was shown in the mid-forest results). This suggests that the smaller trees in the random and group selection forests are not exposed to damaging canopy gusts. Bending moment results in Chapter 6 support this idea.

The region of small vertical fluctuations near the edge of the uniform forest is also present in these other two forests, although in the random forest this is less well defined, see Figures 5.19 and 5.20. In the last section, the generation of coherent canopy gusts was found to be initially perturbed in this region, where the branches input sway energy. What is of interest to the study of irregular height forests is whether a mix of tree frequencies will actually inhibit the growth of frequency-triggered shear layer instabilities. In the group selection forest any input from the sway of the 100 mm trees (12.4 Hz sway frequency) is not clear. Figure 5.21 shows that at x/H= 1.7 there is a slight peak at z/H=0.2 in this frequency band, but it is not significant. Downstream, at x/H= 5.2, the 5.2 Hz sway frequency of the 200 mm tree tends to dominate, as shown in Figure 5.22.

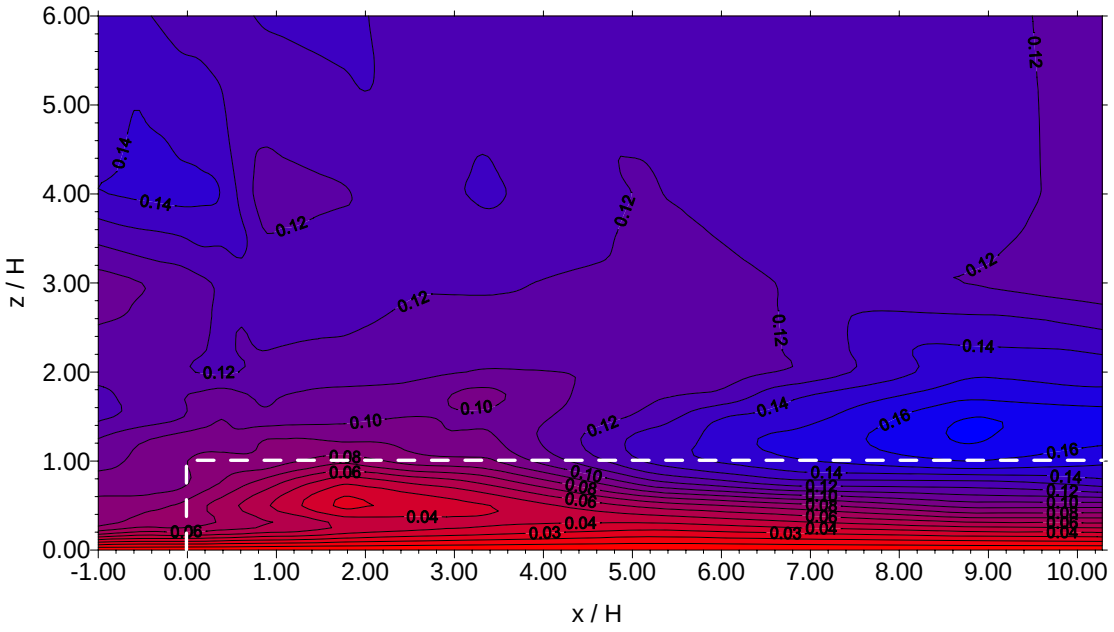

Figure 5.19 σ_w / U_{ref} for group selection forest.

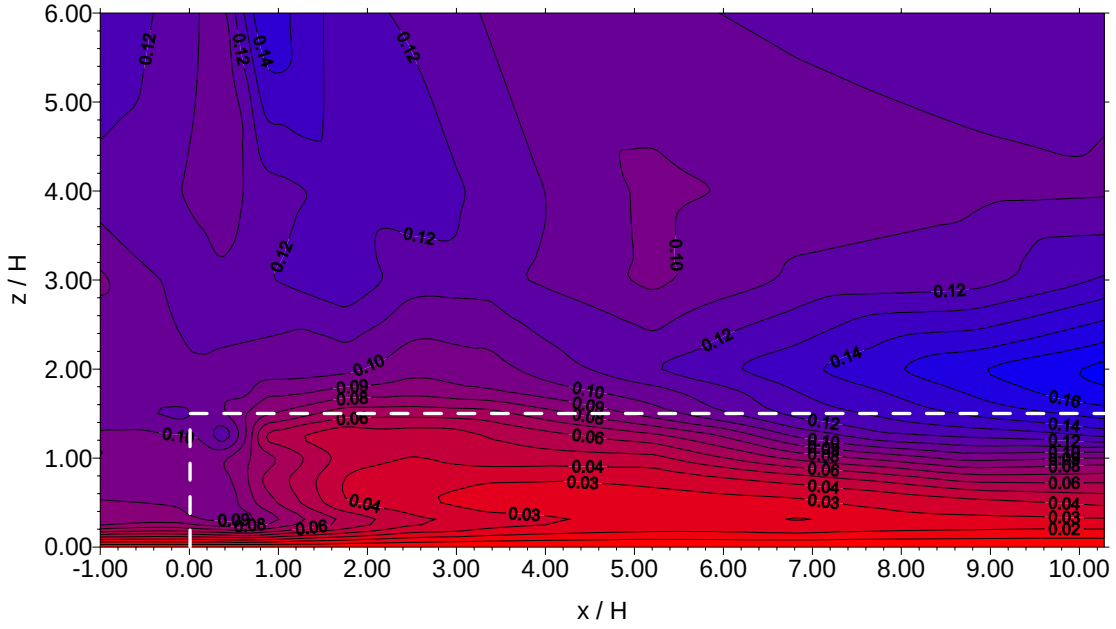

Figure 5.20 σ_w/ U_{ref} for random forest.

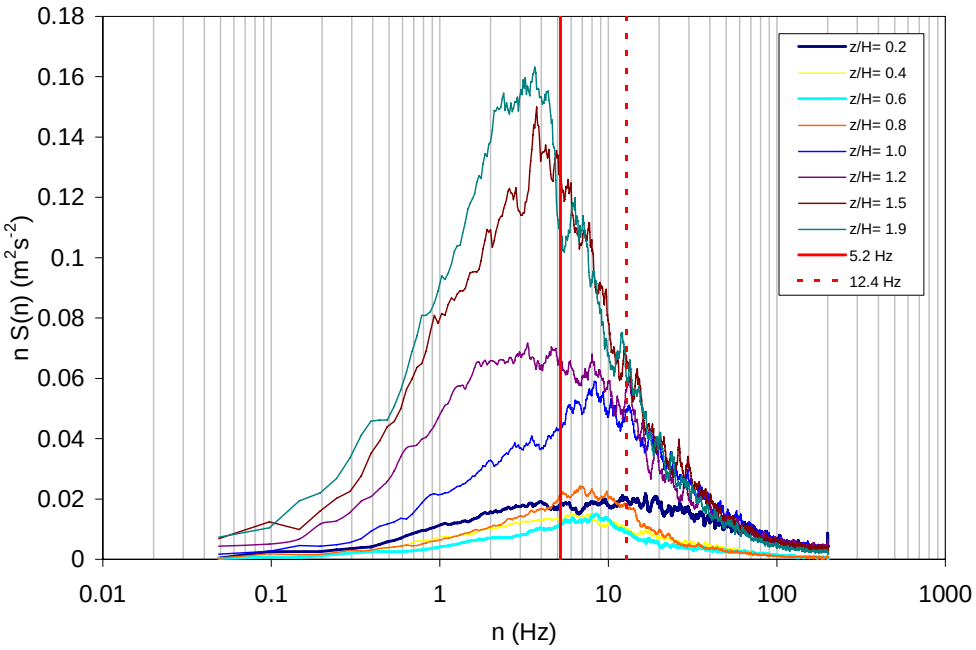

Figure 5.21 W spectra at x/H= 1.7 in the group selection forest.

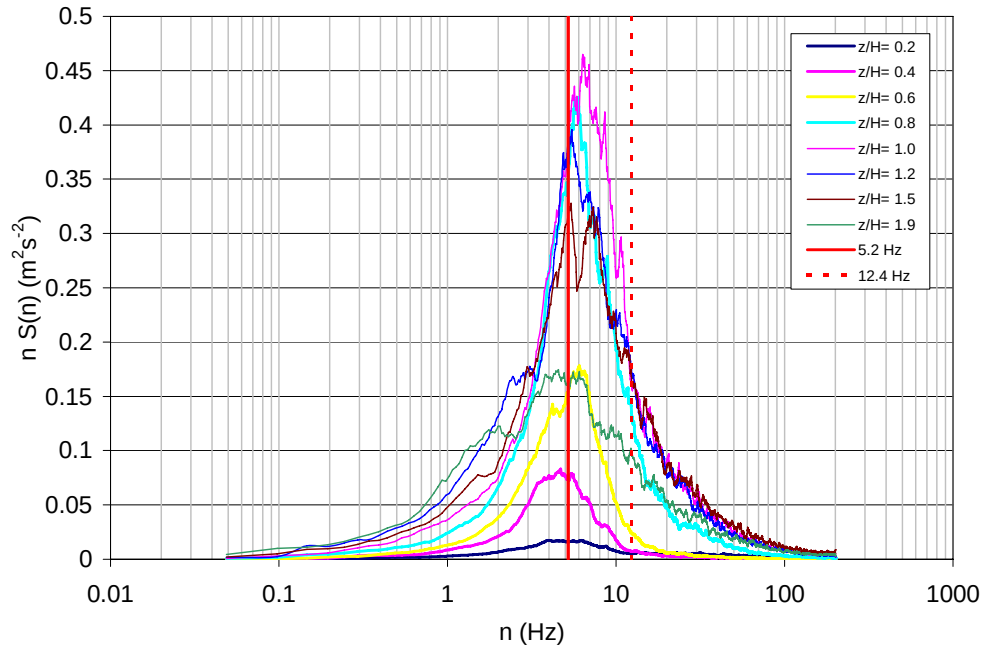

Figure 5.22 W spectra at x/H= 5.2 in the group selection forest.

In the random forest the region of slow fluctuations is less well defined. At x=2.54H, it is not clear that there any dominant tree sway frequencies in the w spectra, as shown in Figure 5.23. However, Figure 5.24 beautifully illustrates the fact that further downstream, at x=5.2H, the 4.8 Hz sway frequency has totally dominated the flow. Thus, once again, the trees in the higher part of the forest appear to have had the largest influence in the creation of canopy gusts.

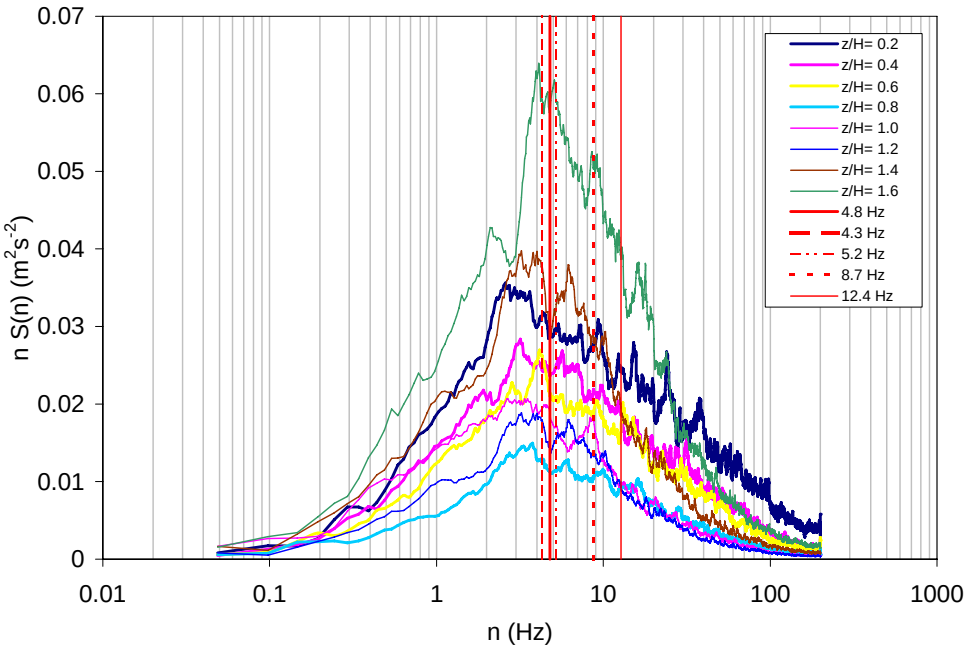

Figure 5.23 W spectra at x/H= 2.54 in random forest. Red lines denote sway frequencies of the different trees.

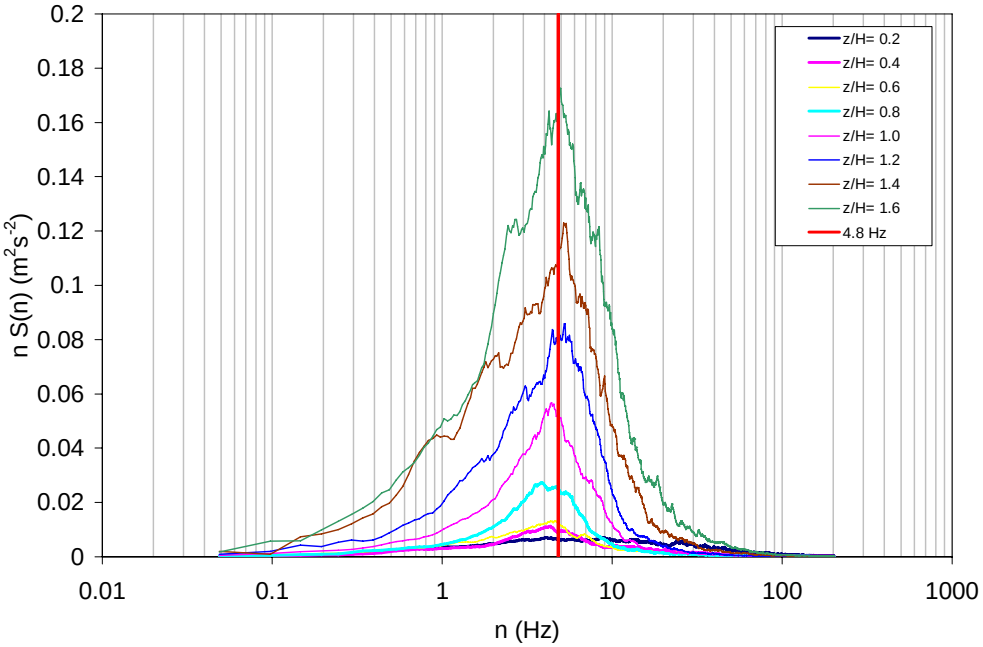

Figure 5.24 W gust spectra for random forest at x/H= 5.2.

5.7 Horizontal Scaling Parameters

The previous section showed that contour plots of the results from all three forests contain very similar trends and patterns. In Chapter 4, the shear length scale, L_s, was demonstrated as a successful scale in the vertical direction, and it would be desirable to scale the horizontal distance in a similar fashion. This would enable the rate of generation of gusts, as well as the position of sudden transition, to be determined when designing a forest environment. However, the data available in this study is insufficient to investigate thoroughly any possible scaling parameters. In this chapter it has also been introduced that the rate of increase of $\overline{u'w'}$ is sensitive to the initial flow conditions and physical characteristics of the trees. These are different in each of the three forest layouts and a more controlled study is needed. Section 8.1 gives suggestions for further investigation into this topic.

5.8 Conclusions

This chapter has provided evidence for the existence of a gust generation mechanism. The following summarises the evidence:

- The flow appears to be slowed and diverted at the front on the forest. Where the flow does penetrate the forest, turbulent energy is reduced.
- Studies of vertical velocity spectra show a tree sway frequency peak emerging in this low σ_w area and increasing in energy further downstream in the shear layer.
- There is a corresponding rise in the Reynolds stress downstream of this area.
- Experiments using different upstream turbulence levels show significant differences in the rise of Reynolds stress.
- The larger trees in the forests appear to be the stimulus for the canopy gust frequency. Downstream, the large turbulent motions do not affect the smallest trees.

The trees at the forest edge appear to be blown by the oncoming turbulence, making them sway. However, a little further downstream of the edge, the sheltering effect of the trees reduces the level of turbulent energy by absorbing and re-emitting it at tree sway frequency. As the shear layer develops within the forest, the likelihood of instability is increased. The tree sway provides a forcing frequency to initiate roll up of the shear layer, giving rise to the creation of a canopy gust.

The significance of such a mechanism on a naturally growing forest is clear. If the trees at the forest edge can be either sheltered from the upstream turbulence, or grown at a different sway frequency, the onset of the generation of gusts can be delayed. Whether gusts would grow to significant levels along a long enough fetch is not clear from the present studies. In recognition of the work of nature, trees at the edge of forests do tend to be far stronger than

trees downstream of the edge. They are stiffer and therefore have a higher sway frequency. This is generally thought to be due to the trees growing to adapt to the stronger wind forces experience at the edge. However, a secondary desirable effect of this may be to create a different gust frequency downstream (possibly an explanation of why Gardiner's (1995) tree sway frequency measurements are not at the same frequency as the velocity fluctuations).

This mechanism is still a hypothesis at this stage, requiring more rigorous experimentation (some experiments are suggested in Chapter 8), but will hopefully provide a stimulus for far more detailed study on the importance of a forest edge.

Chapter 6: Tree Forces

6.1 Introduction

Chapters 4 and 5 described an investigation of flows that occur in wind tunnel forest models. This has led to a well-supported hypothesis concerning the mechanism whereby coherent canopy gusts are formed. Considered in this chapter are the bending moments experienced by individual trees and the relative benefits of growing forests of irregular height rather than uniform height.

The way in which bending moments are related to velocity fluctuations is covered in detail in Chapter 7.

6.2 Experimental and Data Analysis Overview

Experiments were carried out in the mid-forest and edge flow simulations. Overturning bending moments on individual sample trees were measured using the miniature two-component balance detailed in Section 3.6.

Failure due to overturning is obviously represented by the largest values of bending moments rather than mean values. A way of statistically accounting for these maximum values is by the method of extreme value analysis, EVA. EVA is commonly used in wind engineering and briefly described below.

6.2.1 Extreme Value Analysis

The probability distributions of any continuous time-variable $x(t)$ (*e.g.* wind speed) may be discussed most easily if discrete values taken at regular intervals are considered. The parent probability function, calculated using all samples from a sufficiently long observation, is then $F(r)$ which defines the probability that any value r will be exceeded by the next sample.

For the present purpose however, it is useful to define the probability $P(r,1)$ that the value r will NOT be exceeded by a single future sample of x:

$$P(r,1) = 1 - F(r) \qquad [6.1]$$

Extreme value analysis starts from a consideration of the probability that a chosen value r will not be exceeded not by a single sample but by an arbitrary number n of independent samples of x from the same parent distribution. This is the product of all the single sample probabilities and is given by:

$$P(r,n) = \{P(r,1)\}^n \qquad [6.2]$$

If the parent function $P(r,1)$ is of exponential form and if n is large, it has been shown (Fisher and Tippet 1928) that the extreme value probability function $P(r,n)$ approximates to a Fisher-Tippett Type 1 function. Figure 6.1 illustrates the relationship between $P(r,1)$ and $P(r,n)$.

The Fisher-Tippet Type 1 distribution is given by:

$$P(r,n) = \exp(-\exp(-Y(r,n))) \qquad [6.3]$$

where Y is the *reduced probability* such that:

$$Y(r,n) = \alpha_x (r - u(x)) \qquad [6.4]$$

The advantage of this representation is that the reduced probability $Y(r,n)$ is a linear function of the value r, and is defined by the intercept $u(x)$ which is also the mode, or most probable

value corresponding to the steepest slope of $P(r,n)$. The slope is α_x and $1 / \alpha_x$ is called the dispersion.

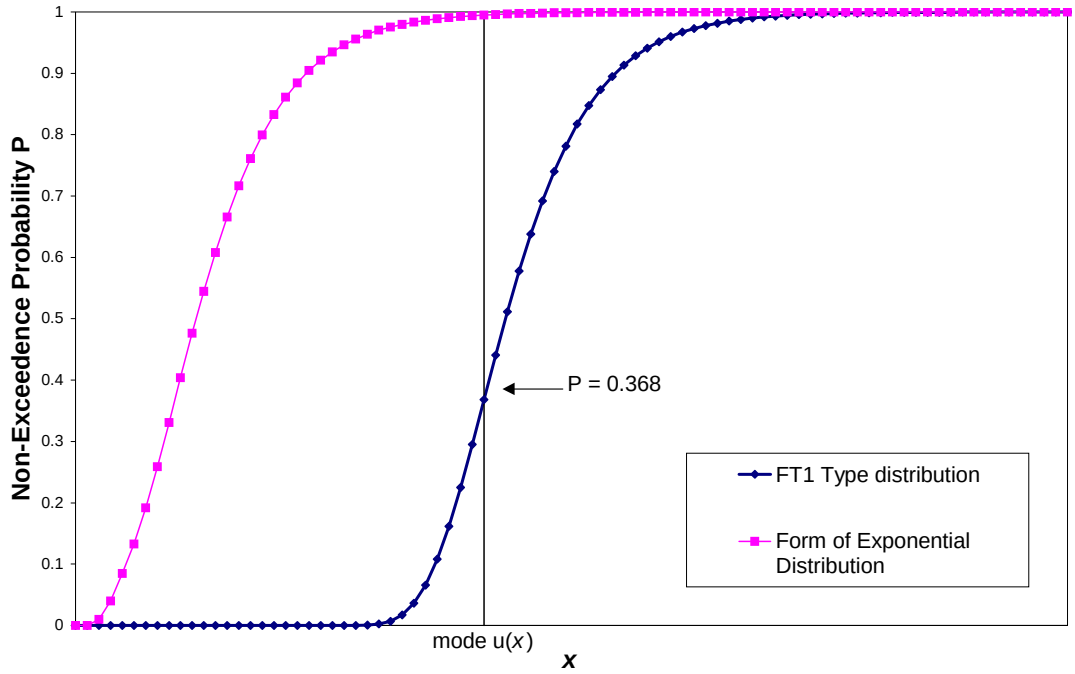

Figure 6.1 Exponential parent probability distribution and resulting Fisher-Tippet Type 1 distribution.

If the reduced probability is plotted against x, a near straight line results (Figure 6.2), the linearity of which improves as n increases. From this plot the values of mode and dispersion can be determined from the horizontal axis intercept and the inverse slope of the straight line.

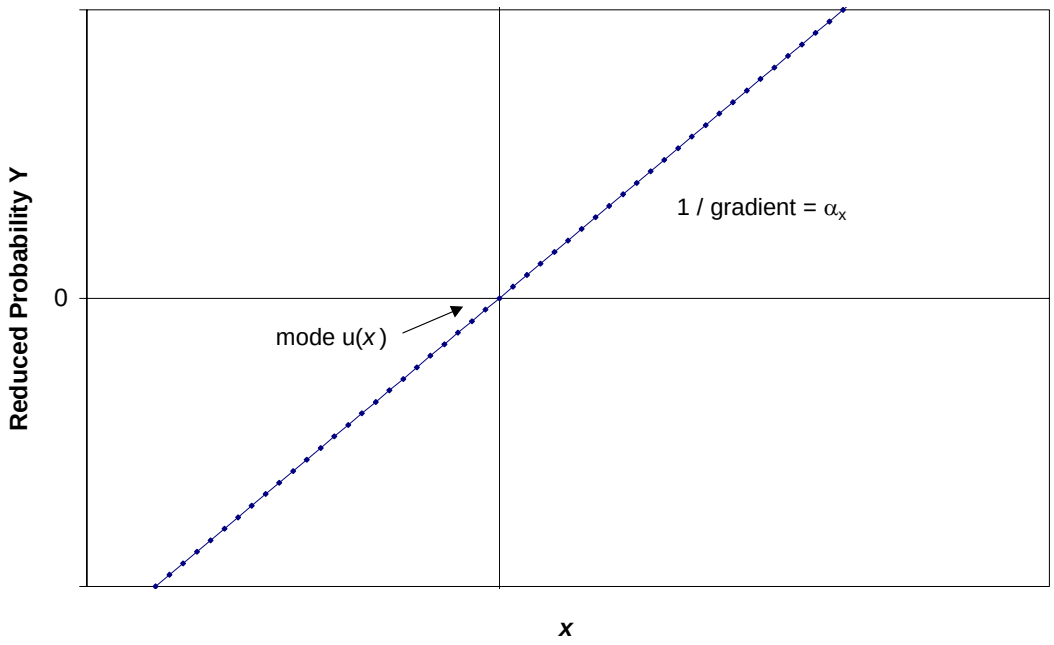

Figure 6.2 Reduced probability plotted against variable x.

Gumbel (1958) suggested the following method of estimating $1/\alpha_x$ and $u(x)$ directly from extreme values, as opposed to using the parent distribution.

1) Samples are ranked in descending order from 1 to n, *i.e.* the largest is ranked number 1, and the smallest number, n.
2) The non-exceedance probability of the vth largest sample is $P(x_v) = 1 - v/(n+1)$.
3) The probabilities, $P(x_v)$, are transformed into the reduced variate, Y.
4) The reduced variates, Y, are plotted against the corresponding values of x_v.
5) This plot is linear as long as the samples meet the requirements of a FT1 distribution. A line of best fit is drawn through the data points.
6) From this line $u(x)$ and α_x can be determined.

From Figure 6.1, the mode value has a probability estimate of 0.368 of non-exceedance. Therefore the maximum value from the next independent trial will have a 0.368 probability of not exceeding that mode value.

The number of independent trials, or observation periods, increases the accuracy of the mode estimate. Mayne and Cook (1980) found that the use of extremes extracted from 16 independent trials gave an efficiency of 98%. This number is a minimum and is used in the present analysis.

6.2.2 Application of EVA to Bending Moments

In this study the 16 independent trials each had an observation period of 40 s (equivalent to 10 minutes full scale). The instantaneous value of bending moment (unfiltered) was recorded at 5 ms intervals throughout the observation period, but at the end, only the largest value was retained. The sampling rate and observation period were chosen to match those of Stacey *et al.* (1994), because later in this chapter experimental results are compared with his.

In this report, only mode values are quoted. These represent values of bending moment with probability of 0.632 of exceedance (0.368 of non-exceedance) in any future observation period of 40s (10 minutes full scale).

6.2.3 Comparing Tree Bending Moments

Stacey *et al.* (1994) expressed bending moments in terms of a bending moment coefficient, Q_m:

$$Q_m = Q / (1/2\ \rho\ U_{ref}^2\ H^3) \qquad [6.5]$$

where Q is the measured base bending moment, ρ the density of air and U_{ref} the mean reference velocity. The problem with using this coefficient for trees other than the 200 mm tree is that they do not have the same drag or amplitude properties, and thus the coefficient is not inter-comparable. Instead all values in this study are presented as a ratio of bending

moment coefficient Q_m (with H always 200 mm) divided by the bending moment coefficient Q_r of the 200 mm tree in a 6 ms^{-1} uniform flow. The value of Q_r is 0.014302.

A method was also needed to predict what the expected bending moment would be on one type of tree when given the value of bending moment for another type of tree under the same conditions in a forest. For instance if the bending moment of a 200 mm tree in the group selection forest was found then what would be the expected bending moment on a 100 mm tree? If the expected value was greater than the measured value then it was possible to say that the 100 mm tree was sheltered in that forest configuration. To address this problem the uniform-flow bending moment on each tree was expressed as a ratio of the bending moment of the 200 mm tree under the same flow conditions. The relative bending moment ratio, RBMR, for all the trees is shown in Table 6.1. This table is simplistic, in that it does not take into account dynamic effects. Nevertheless it still gives an estimate of how bending moments vary between the five tree sizes.

Tree Size (mm)	Tree Bending Moment / 200 mm Tree bending moment ratio (RBMR)
100	0.339
150	0.577
200	1.000
250	1.932
300	2.413

Table 6.1 Comparison of model tree bending moments in uniform flow.

An important point to note is that tree failure will be caused by a resultant bending moment rather than a single arbitrary component (*e.g.* about an axis normal to the flow). Therefore, the extreme bending moment values presented in this study are resultants. Mean bending

moments are about an axis normal to the flow only, because there is no mean transverse velocity. Estimates of the cross-stream contribution to the extreme bending moments range from 6% at most, with a mean of 2% (example taken from the range of values along the uniform forest edge).

As described in Section 3.6 the bending moment balance was calibrated by replacing the test tree with a stiff arm and adding known loads. Care was taken during the experiments to stop clashing with surrounding trees.

6.3 Mid-Forest Bending Moments

Bending moments were first measured on trees in the centre of the model forest, in the mid-forest flow.

6.3.1 Uniform Forest

Concern was expressed in Section 5.8 that the viability of the mid-forest simulation was in doubt because of the finite size of the model forest. To investigate this possibility, Figure 6.3 shows the bending moments of a test tree at, and on either side of, the centre of the model forest (where $x/H = 0$). It can be seen that there was little variation of bending moment in the immediate vicinity, suggesting a peak in bending moments had been reached. Figure 6.3 also shows the difference between mean and mode. The difference is considerable with a mode to mean ratio (MMR, also known as gust factor for velocity measurements) of 11. The average bending moment ratio at the mid-forest position was 0.048 for the mean and 0.56 for the mode.

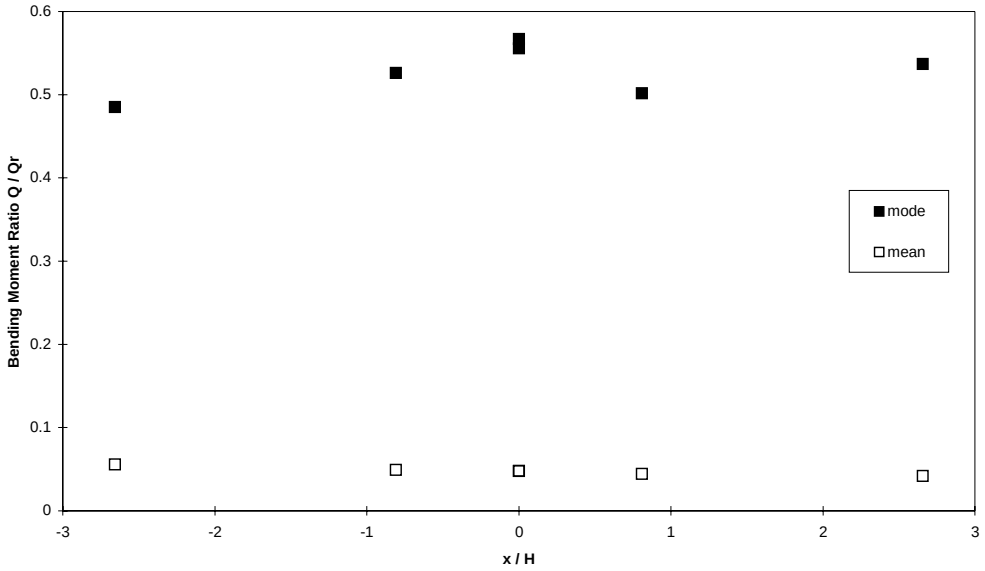

Figure 6.3 Variation of uniform forest bending moments in mid-forest simulation. Centre of forest at x/H =0.

6.3.2 Group Selection Forest

Recall, the group selection forest was a 50/50 mix of alternate 100 mm and 200 mm trees. Bending moments were measured on both types of tree and are presented in Figure 6.4. If the 100 mm trees were to be removed carefully this plantation would be the same as the 50% thinned forest investigated by Stacey *et al.* (1994). Therefore bending moments from the thinned forest are shown alongside the group selection bending moments.

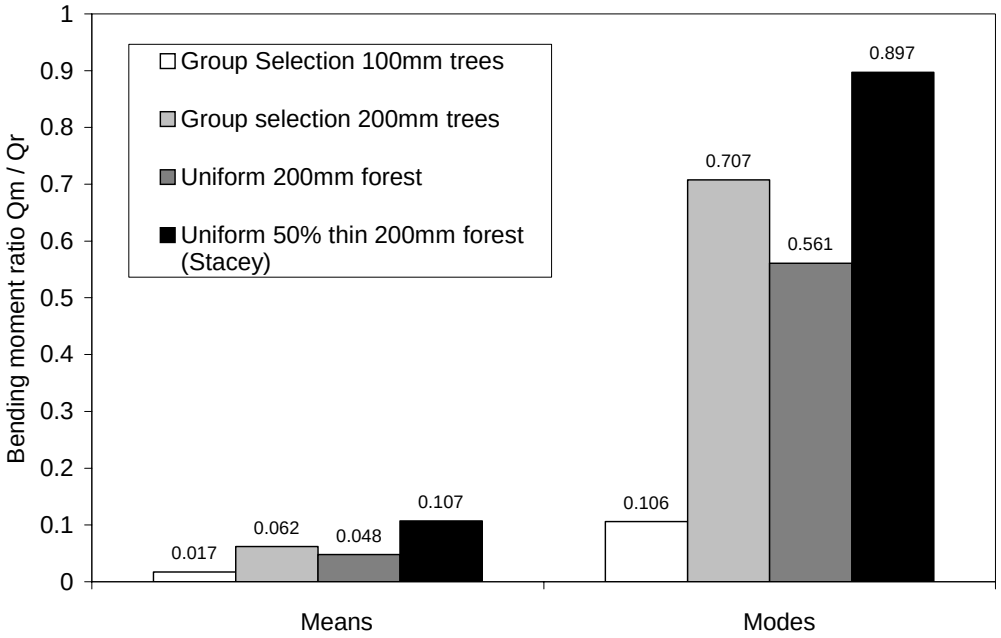

Figure 6.4 Mid-forest base bending moments for group selection forest.

The first point to notice in Figure 6.4 is that in the group selection forest the 200 mm tree experiences higher mean and extreme bending moments than the same tree in the uniform forest. This is most probably due to the decreased shelter at the top of the canopy in the group selection forest. Secondly, the bending moment is still lower than that experienced in the 50% thinned forest. Therefore the small trees do protect the larger trees. Finally, using the RBMR relationship (see Table 6.1) to calculate the expected bending moment on the 100 mm tree from the bending moments of the 200 mm tree, it was found the 100 mm tree experiences half the equivalent bending moment mode (see Table 6.2). The mean is approximately the same as expected.

	200 mm tree Q_m/Q_r in group selection	**Estimated value of Q_m/Q_r for 100 mm tree**	**Actual Value of Q_m/Q_r for100 mm tree**
Mean	0.062	0.021	0.017
Mode	0.707	0.239	0.106

Table 6.2 Estimated values of Q_m/Q_r for the 100 mm tree.

The reduction in mode might be anticipated since, as was shown in Section 4.3, the most turbulent areas of the velocity profiles did not occur in the region of the 100 mm trees.

Bending moment results from the group selection forest would therefore suggest that this type of plantation is a reasonable proposition for foresters. The tallest trees may not be as sheltered as they may be in a dense forest, but the addition of the smaller trees does provide some protection. The smallest trees are also well protected by the larger trees.

6.3.3 Random forest

Mid-forest bending moments for the random forest are shown in Figure 6.5. The large overturning bending moments of the 300 mm tree in the random forest reflects the large moment arm, coupled with the exposure experienced at the top of the forest canopy. The 200 mm tree is sheltered quite dramatically in this situation when compared with the uniform 200 mm forest.

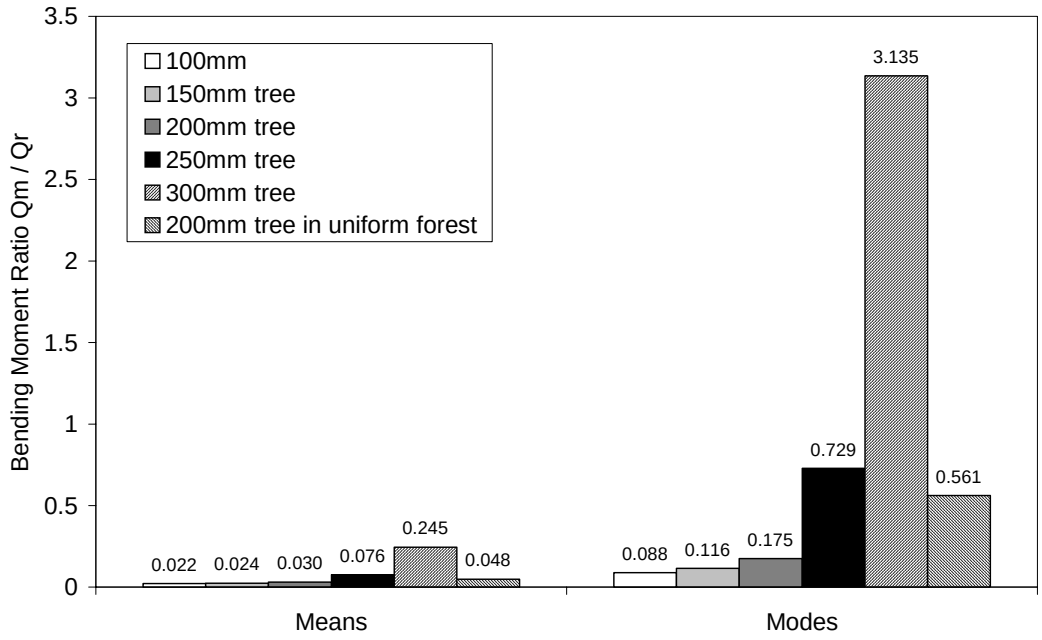

Figure 6.5 Mid-forest base overturning moments of trees in the random forest pattern compared with the 200 mm tree in the uniform forest pattern.

Shelter is again quantified by multiplying the measured 200 mm tree bending moment by the RBMR factor in Table 6.1. The results are presented in Table 6.3 and the most notable figure is the 300 mm / 200 mm mode ratio. This value is approximately 7.5 times larger than the estimated value, suggesting that extreme gusts are hitting the 300 mm tree but not penetrating far enough into the forest to hit the 200 mm tree. To a lesser extent the 250 mm tree also shows signs of being sheltered.

Tree	**Mean Q_m / Q_r**	**Mode Q_m / Q_r**
200 mm	0.030	0.175
Experimental 100 mm Estimated 100 mm	0.022 0.010	0.088 0.059
Experimental 150 mm Estimated 150 mm	0.024 0.017	0.116 0.101
Experimental 250 mm Estimated 250 mm	0.076 0.058	0.729 0.338
Experimental 300 mm Estimated 300 mm	0.245 0.072	3.135 0.422

Table 6.3 Estimated bending moment ratios for random forest.

In practical terms, the random forest would be little help to foresters. The 300 mm tree experiences tremendously large bending moments and its extra size would bring down even more trees if it overturned!

6.3.4 Mode to Mean Ratio (MMR)

A useful presentation of data is the mode to mean ratio. Foresters believe that trees are damaged by extreme winds but adapt in response to the mean climate (Gardiner *et al.* 1997). Table 6.4 shows that for all trees, except the 300 mm tree, the ratio is lower than that for the uniform 200 mm tree. This gives extra credence to the use of the group selection forest, and a further reason not to use the random forest.

	Model Tree Height (mm)	**Mode / Mean Bending Moment Ratio**
Random Forest	100	4.11
	150	4.90
	200	5.79
	250	9.62
	300	12.79
Group Selection Forest	100	6.14
	200	11.48
Uniform Forest	200	11.70

Table 6.4 Mode to mean bending moment ratios for all forests.

Further inspection of Table 6.4 reveals all the data fall into two distinct groups. The first group is the tallest trees in the plantations, which give an approximate ratio of 12. The second group, the smaller trees in the plantations, have an approximate ratio of 5. All these results support the evidence that canopy gusts only penetrate the upper section of forests (see Section 4.3). For comparison with real trees, Gardiner *et al.* (1997) obtained a MMR of 11.5 for a spacing / height ratio of 0.14 over a uniform forest. It is obviously difficult to determine

the spacing / height ratio of some of the wind tunnel model patterns but the uniform 200 mm forest gave a ratio of 0.12.

6.4 Forest Edge Bending Moments

In addition to measurements at the model centre in the mid-forest wind simulation, bending moment measurements were also carried out along the length of each of the forests in the forest edge wind simulation.

6.4.1 Uniform Forest

The forest edge bending moment ratios for the uniform forest are presented in Figure 6.6.

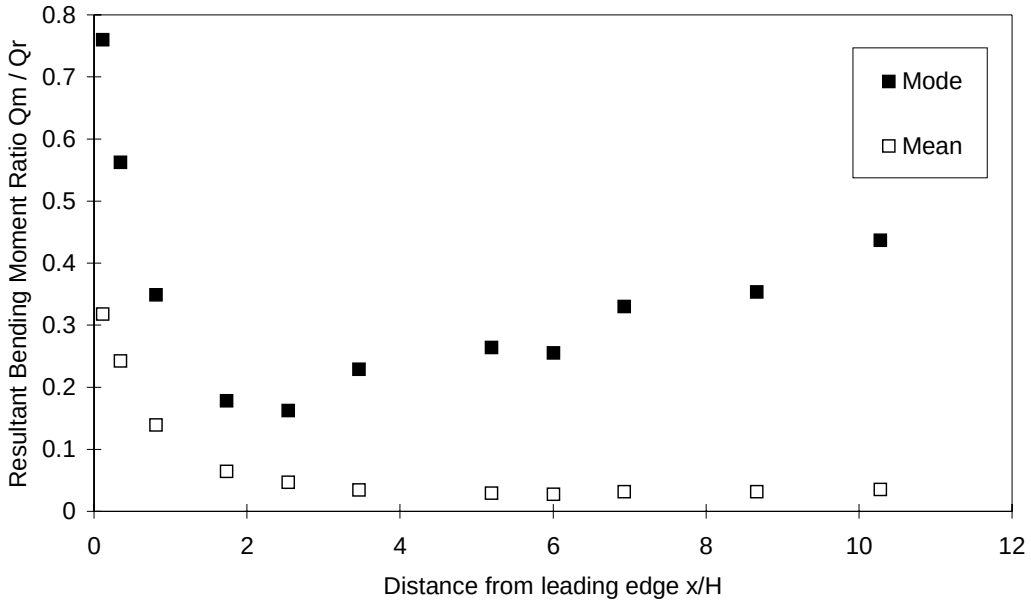

Figure 6.6 Bending moments downstream of leading edge in uniform forest.

Not surprisingly, Figure 6.6 shows similar trends to the variation of wind velocity near the forest edge (see Figures 5.3-5.8). First there is a decrease in the bending moment as the drag of the trees slows down the mean wind. Then the mode increases once past a minimum point, which is about 2-3 *H* downstream of the edge. Interestingly the mean does not appear to increase, if at all, at the same rate as the mode.

6.4.2 Group Selection Forest

Results from the group selection tests presented in Figure 6.7 show that for the 200 mm tree, when compared with the same tree in the uniform forest, the mode bending moment increases by 49% on average. Mean bending moments only increase by an average 30%. Shelter for the 200 mm trees has decreased because of the lower density of high trees. As might be expected, the 100 mm trees are well sheltered at all locations.

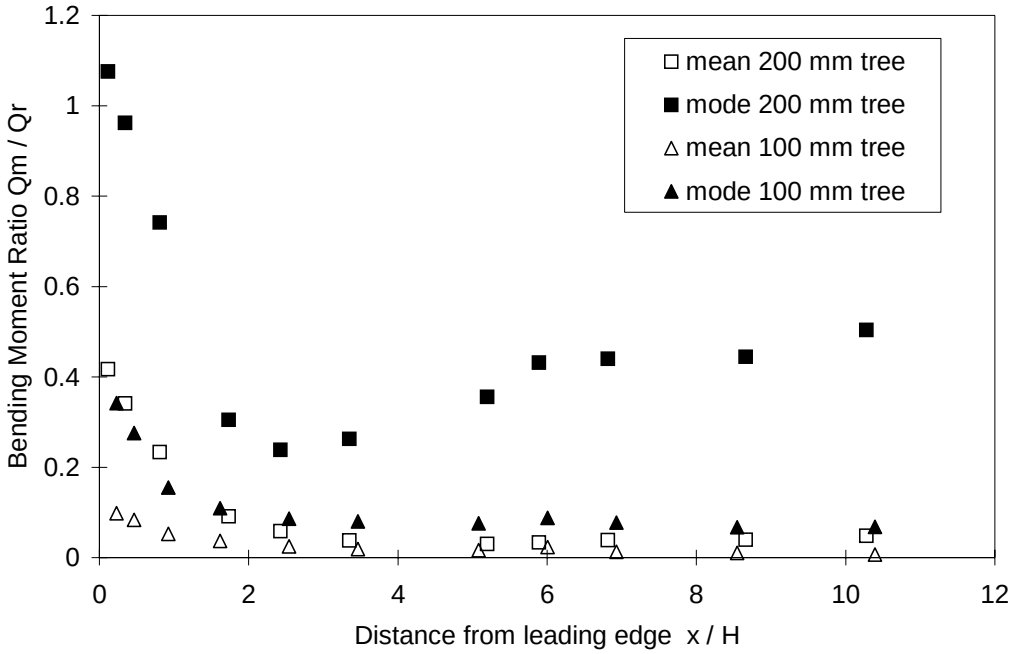

Figure 6.7 Bending moment ratios downstream of forest edge for group selection forest.

6.4.3 Random Forest

Mean bending moments for the random forest are presented in Figure 6.8 whilst modes are presented in Figure 6.9. Like the group selection forest, the random forest trees also demonstrate the presence of a minimum in the extreme bending moment. Similarly, only the top 300 mm trees, and to a lesser extent the 250 mm trees, are significantly affected by the canopy gusts. As stated earlier, this would not enhance the prospects of growing large trees, since not only are they subjected to the largest gusts, but also have the largest bending moment arm.

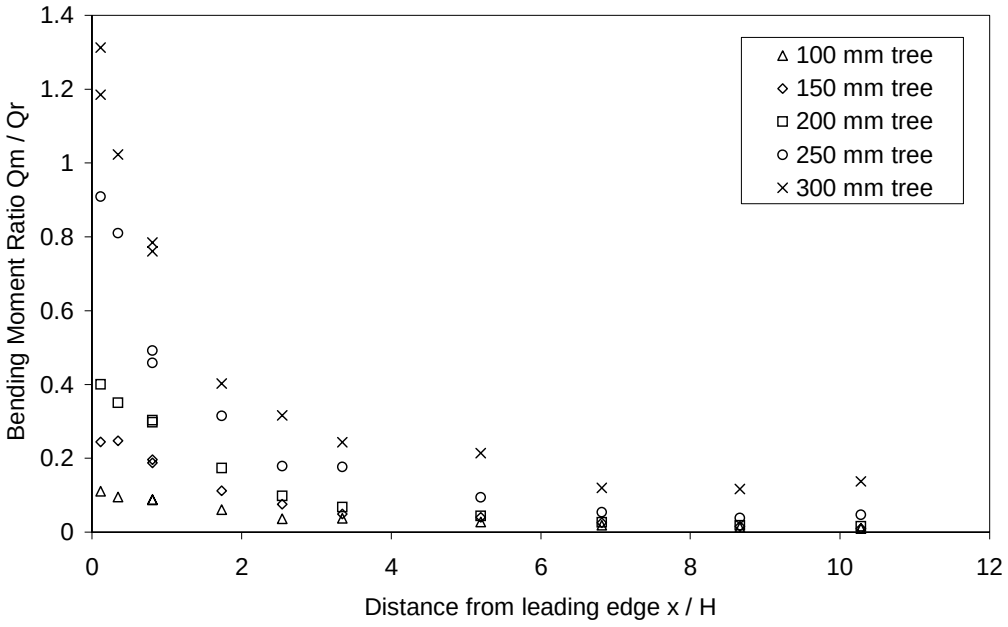

Figure 6.8 Resultant bending moment ratio means for the random forest.

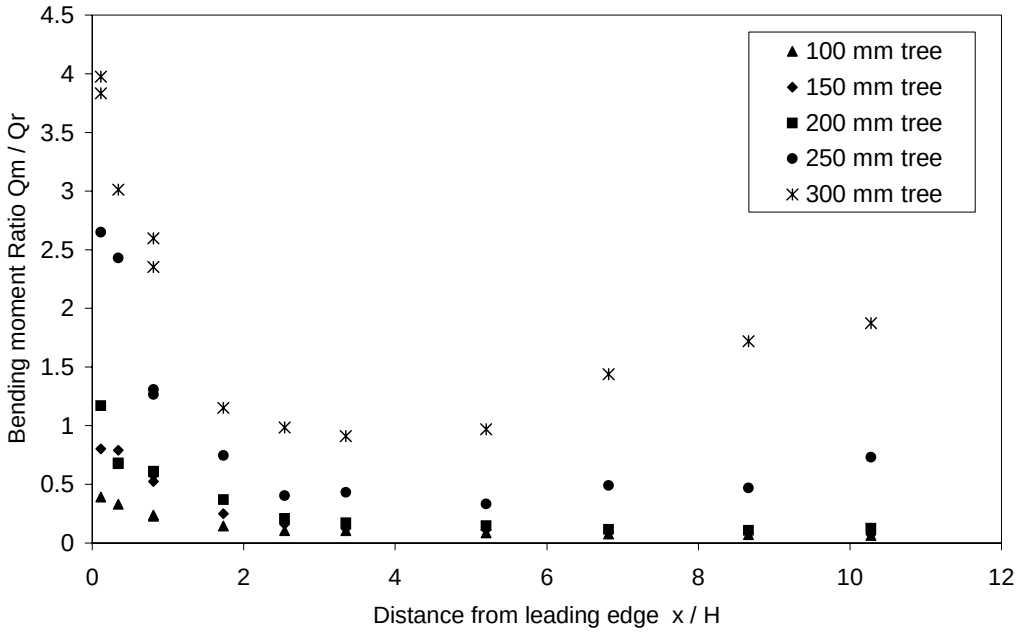

Figure 6.9 Resultant bending moment ratio modes downstream of random forest edge.

6.4.4 Mode to Mean Ratios for Forest Edges

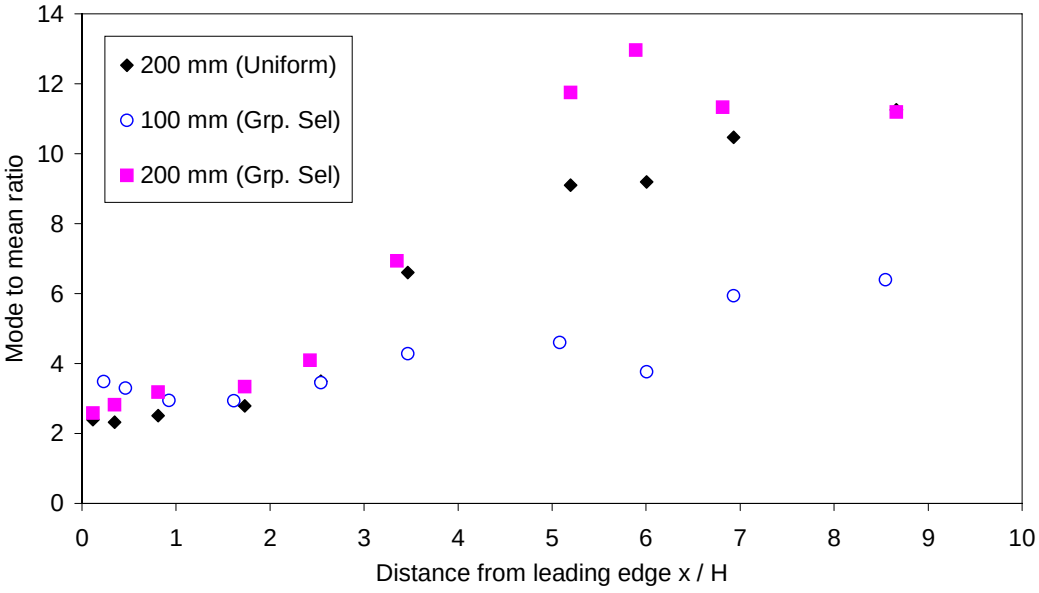

Figure 6.10 Mode to mean bending moment ratio for the uniform and group selection forest.

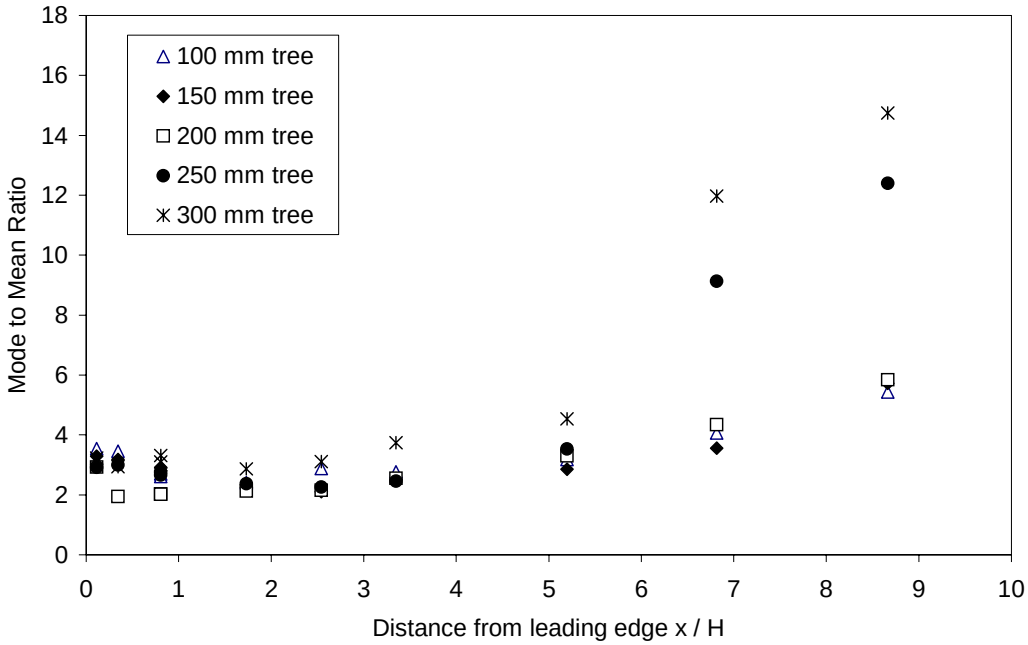

Figure 6.11 Mode to mean bending moments for the random forest.

Interestingly, Figures 6.10 and 6.11 both show that the oncoming turbulence causes a MMR of around 2-3 at the forest edge. However, when the canopy gust regime develops, the upper trees are subjected to far higher gusts than the trees lower down. This is in agreement with the mid-forest results. If trees do grow in response to mean wind, then the low MMR ratio near the front of the forest would also increase the chances of survival of the edge trees compared with the trees further downstream.

6.5 Failure Criteria

The only data available for the failure of the individual trees was breakage failure of the stem, obtained from the Forestry Commission. Table 6.5 shows the maximum bending moment ratios Q_m/Q_r required to break each tree stem and a summary of the bending moment ratios experienced in the mid-forest simulation.

	Maximum Bending Moment Ratio	Wind Tunnel Bending Moment Ratio
200 mm tree Uniform Forest	0.622	0.561
100 mm tree G.S. Forest	0.232	0.106
200 mm tree G.S. Forest	1.105	0.707
100 mm tree Random Forest	0.232	0.088
150 mm tree Random Forest	0.491	0.116
200 mm tree Random Forest	1.105	0.175
250 mm tree Random Forest	1.538	0.729
300 mm tree Random Forest	3.580	3.135

Table 6.5 Maximum stem breakage moments against mode bending moments experienced in the wind tunnel. All bending moments are in terms of ratio Q_m / Q_r.

Table 6.5 shows that all trees are within their failure limits. However, it should be borne in mind that overturning moments are usually significantly less in practice, depending upon soil strength and root depth *etc*..

6.6 Conclusions

This chapter can be regarded as having two distinct conclusions drawn from the experiments:

- The first is the conclusion drawn from the bending moment measurements, that the group selection forest appears to be a theoretically viable proposition for future forest plantations. The presence of smaller trees in the forest does offer some protection to the larger trees, when compared to 50% thinned forest. Foresters have been reluctant to use a group selection type plantation because they believed that gusts would more easily penetrate the exposed canopy top and damage the weaker, small trees. In fact, the smaller trees are more sheltered than would be expected. Unfortunately, the practicalities of managing such a forest design are far more complicated. One of the reasons group selection is being considered is that after felling it does not leave a large area of

devastated land. However, extracting single trees, without damaging surrounding trees, is very expensive, and there are also many other practicalities beyond the scope of this discussion.

- The second significant conclusion to be made from the bending moment data is that patterns observed in mode to mean bending moments support the hypothesis that canopy gusts are created downstream of the edge of a forest. The MMR appears to fall into two distinct categories far downstream of a forest edge, with ratio values of approximately 12 for the tallest trees, and 6 for the smallest trees. This also supports the idea that canopy gusts do not penetrate low down into a forest and are confined to the shear layer, as would be expected with a mixing layer. Another point of interest is that trees near the edge experience a low mode to mean ratio, but a high absolute mean bending moment. This may increase their strength and chances of survival in high winds.

Chapter 7: Conditional Sampling of Canopy Gusts Using Wavelet Analysis

7.1 Introduction

The discrete nature of gust movement through a forest means that traditional statistical aerodynamic admittance methods cannot be used to quantify wind forces on trees. Baker (1995) suggested a step-input wind loading, combined with extreme value theory, to determine overturning moments of trees. The natural frequency and gust loading times were seen to be the most sensitive and significant parameters in this model. Marshall *et al*. (1998) demonstrated that a wave shape input may be a more appropriate model and also stressed the importance of the input wavelength with respect to tree resonance. Taking the theory one step further, this chapter aims to investigate the structure, frequency of occurrence, and strengths of the gusts in the wind tunnel and how they can then be used to determine overturning moments.

To carry out this study a method must be employed to extract the structure of canopy gusts from the wind tunnel data. What is needed is a 'snapshot' of the flow field, from which the strength and structure of the coherent gusts can be extracted. There are direct ways of doing this (for example Particle Image Velocimetry - PIV) but these require equipment which was not available. The technique described here was developed to produce a *pseudo snapshot* of the flow field built up from separate LDA point measurements. This fell into the category of *condition sampling* because, using the LDA one point at a time, it was necessary to select measurements that coincide with a defined *event*. This type of method was possible only if such events were repeated consistently.

This chapter describes a conditional sampling method using *wavelet analysis*. The flow over the uniform forest is investigated, with relationships derived between peak gusts and peak bending moments (note since only the 200 mm trees are used, all bending moment results are expressed as bending moment coefficients). The method also allows a pseudo snapshot of a gust to be produced and its structure investigated.

7.2 Conditional Sampling Methods

Conditional sampling relies upon the assumption that coherent flow *events* produce distinctive and reccurring patterns in a control data series. Thus when the time series meets certain criteria, or *condition*, that part of the time series is associated with a particular flow structure event. For instance, a gust causes a particular shape in the velocity time series, V_c, as shown in Figure 7.1. If another velocity, V_1, is sampled simultaneously with the control velocity, that part of the V_1 time series is associated with the flow event and the data is *conditional data* dependent upon V_c. If V_c position is kept stationary then V_1 can be moved to a new position after the end of each observation period.

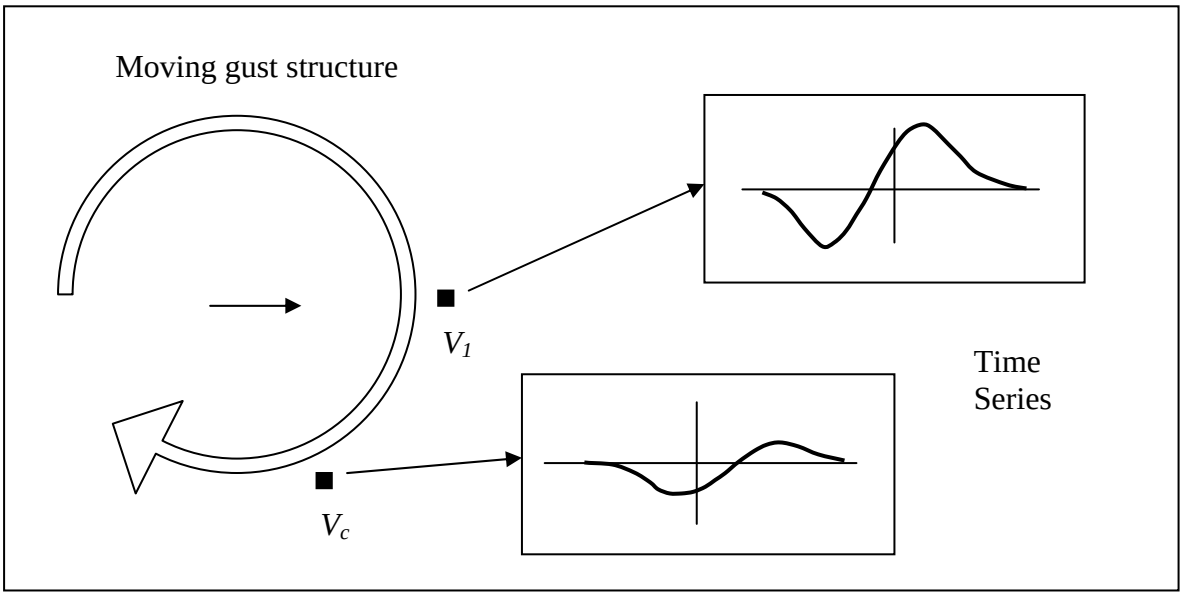

Figure 7.1 Two simultaneous measurements in a flow field. V_c is the control velocity (e.g. vertical in this case), V_1 the moveable measurement.

In this study the control measurement was the total pressure, P_T, measured, at inflexion height, with a pressure sensor. The LDA was the moveable instrument so a velocity field could be built up from a collection of measurements each coinciding with a pressure event. The next stage was to decide on what condition was used to recognise an event. Marwood 1996 used the occurrence of low pressure on the roof of a building to indicate the presence of a vortex structure above it. Using just the pressure magnitude was possible because the vortex was relatively stationary. A gust moving through a forest is harder to identify. Not only does the gust move, but the flow is very turbulent, so the time series is noisy and the gust itself is very difficult to identify. Therefore more sophisticated methods of recognition have been used. Gardiner (1994) applied the instantaneous $\overline{u'w'}$ time series, the VITA (Variable-Interval Time Average, devised by Blackwelder and Kaplan 1976) method. The VITA involves thresholding the standard deviation of the signal in a arbitrary time window. Alternatively several authors (Collineau and Brunet 1993b, Gao and Li 1993 and Qui *et al*. 1995) have used the relatively new technique of *wavelet* analysis to detect ramp patterns in forest temperature time series. This type of analysis is far more flexible and comprehensive than the VITA method. It was chosen for this study and is explained in the following sections.

7.3 Wavelets: A Word of Warning

The novelty and wide generality of the wavelet discipline means that there are many varied approaches to its use. Consequently, much that is written is quite irrelevant to the present problem. Furthermore, discussion of the technique is often shrouded in mathematical complexity and there is little clear guidance in practical explanation and application. To focus on the present discussion, it is pointed out at this stage that the wavelet analysis used here is the one dimensional Continuous Wavelet Transform (CWT) method which is related to the

time-frequency analysis of time series. This type of transform is described in full mathematical detail by Chui (1992) and successfully used on applications ranging from gear failure detection (McFadden and Zheng 1993) to wall flow structures (Kaspersen 1996).

7.4 Introduction to Wavelets

A wavelet is an artificially created curve which is taken to represent a short, single feature in the time variation of a variable. The wavelet function has a *scale* or *dilation factor*, *a*, that compresses or stretches the function. Figure 7.2 and Equation 7.1 show the wavelet used in this analysis. It is a first derivative of a gaussian (FDG) function and thus termed in this thesis as the FDG wavelet:

$$\psi(t) = \frac{-t}{a} \exp \frac{-(t/a)^2}{2} \qquad [7.1]$$

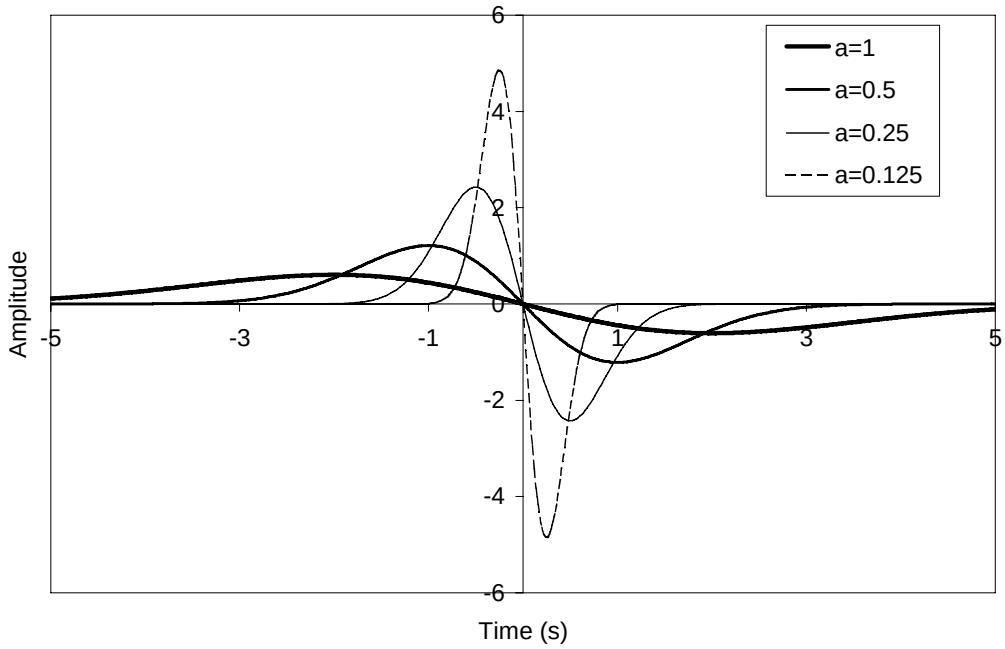

Figure 7.2 FDG wavelet showing the compression abilities of the changing scale parameter a (1/a height scaling parameter, see below).

Briefly, a wavelet also has a *translation factor*, *b*, that allows the wavelet to move along a time signal. The wavelet is then integrated with a time signal to form *wavelet coefficients*. This is called the *wavelet transform*. In the simplest sense, when the wavelet is moved across a signal, the highest wavelet coefficient will occur when the signal matches a shape similar to that of the wavelet. By changing the dilation factor the shape that it matches can be identified. This makes the wavelet ideal for turbulence work since it can identify coherent signals from an apparently random signal. Figure 7.3 shows the FDG wavelet translating across a sinusoidal signal (top plot) with a sinusoidal hump in the centre of it. Whilst the wavelet is small (second plot down) the small scale fluctuations are permitted through the wavelet transform process to give the corresponding wavelet coefficients (third plot down). However, a large wavelet will pick out the large scale hump as shown in the last two plots.

Different wavelet shapes are used to pick out different signals. The situation does become more complex because some wavelets are also good at picking out rapid changes in signal and frequency analysis.

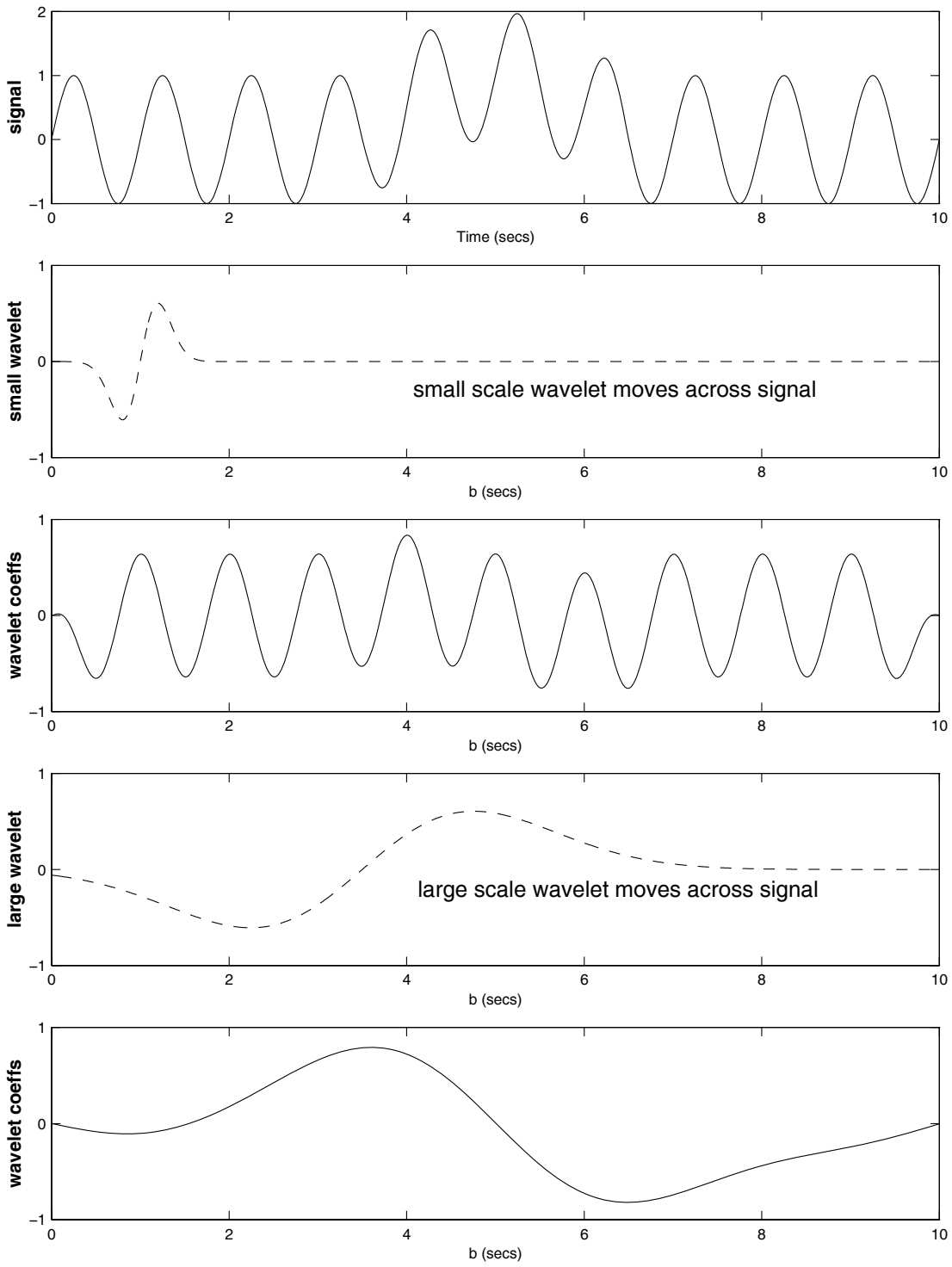

Figure 7.3 Basic operation of wavelet transform.

7.5 Wavelet Transform Definition

A wavelet, ψ, must have finite energy (integral of $\psi(t)^2$), be non-zero in a localised time window, but have a zero mean. This is called the admissibility condition where:

$$\int_{-\infty}^{\infty} \psi(t)\, dt = 0 \qquad [7.2]$$

The scale and position of a wavelet is achieved by *dilating* and *translating* the basic wavelet, ψ, to create a wavelet family:

$$\psi^{a,b} = \frac{1}{\sqrt{a}}\, \psi\left(\frac{t - b}{a}\right) \qquad [7.3]$$

The parameters *a* and *b* control the dilation and translation respectively. The dilation of the wavelet stretches or compresses the wavelet, so that at high frequencies it is narrower and at low frequencies it is wider. The translation parameter moves the wavelet over the signal. The **standard** continuous wavelet transform (CWT) is defined as:

$$W(a,b) = \frac{1}{\sqrt{a}} \int_{-\infty}^{\infty} h(t)\, \psi^{*}\left(\frac{t-b}{a}\right) dt \qquad [7.4]$$

The resulting *W(a,b)* are called the wavelet coefficients. *h*(*t*) is the signal to be analysed and * denotes complex conjugate. The $a^{-1/2}$ factor before the integral is arbitrary. This term is often used because it conserves the energy of the wavelet signal (ψ^2) , but has a tendency to attenuate the amplitudes of the transformed signal at high scale values. However, for this study the factor a^{-1} is used instead of $a^{-1/2}$. This allows the relative amplitudes of events in the original signal to be compared. This is because *a* is proportional to the variance σ^2 of the wavelet and so the wavelet transform coefficient can be seen as a type of correlation coefficient, but with the variance of only one signal used instead of the standard deviations of two. Thus, amplitudes of the remaining signal can be quantified. For a FDG wavelet the

coefficient $W(a,b)$ of analysis with a similar sized and dilated FDG wavelet is 0.886. Therefore if $W(a,b)$ is divided by 0.886 it causes the coefficient to be unity when the match is perfect. Of course, because of the simplicity of the wavelet integral this is not always necessarily true, but is a useful guide. Where $W(a,b)$ is divided by 0.886 in the following work it is denoted by $W'(a,b)$.

7.6 Scale-Frequency Relationship

The wavelet transform can be re-written in terms of the Fourier Transform (FT). From Fourier theory, the scaling and translation of a function can be represented by magnitude and frequency scaling of a, and a phase shift proportional to b. The similarity of the CWT to a convolution integral means that in frequency space the signal is multiplied by the wavelet function:

$$W(a,b) = \int_{-\infty}^{\infty} H(\omega).\Psi^{*}(a\omega)e^{ib\omega}\,d\omega \qquad [7.5]$$

The consequence of this property is that the wavelet acts as a band pass filter on the input signal. The FT of the particular wavelet functions becomes important at this point since the better functions will be well localised in frequency space. The FDG wavelet has the advantage that its FT is well localised (see Figure 7.4), whereas a discontinuous function such as a step wave function (HAAR wavelet) has side lobes which 'smear' the frequency information.

Note the form of Equation 7.5 permits the Fourier transform of *h(t)* to be calculated only once and is multiplied by the changing transform of $\Psi(a\omega)$. This therefore eliminates the need for laborious convolution integrals and can be calculated quickly with Fast Fourier Transforms. Ideally the input signal *h(t)* should be periodic due to the use of FFT. The lack of a periodic

signal, and the translating nature of the wavelet, causes edge effects. These are taken into account in the analysis by having a longer than necessary sample time and neglecting the first and last few seconds of transform.

Looking again at Equation 7.5 reveals that the frequency centre of the band pass filter is at 1/*a*. Frequency is therefore inversely proportional to *a* and a *scale frequency Fa* can be used for an arbitrary frequency indication. At a=1 the frequency peak f_p of the FDG is 0.159 Hz, ω_p =1 rad s^{-1} and thus the general relationship is:

$$f_p = Fa / 2\pi \qquad [7.6]$$

Figure 7.4 shows the frequency range used in the present set of experiments according to the frequency scale, *Fa*. Note the largest scale allowed is 50, which permits the whole response curve to be fitted into the Nyquist frequency limit (25 Hz for this experiment).

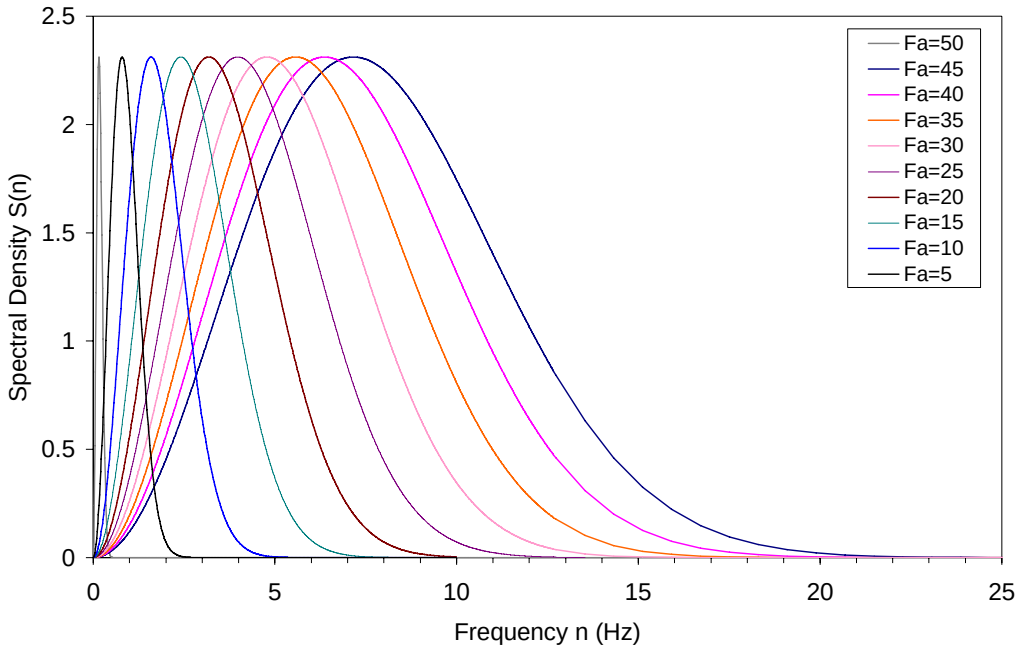

Figure 7.4 Fourier transform of the FDG wavelet.

The wavelet coefficients, $W(a,b)$, are sometimes displayed in the form of a time-frequency map (Figure 7.5). The transform reveals where the oscillations occur, not only *in time* but also in *frequency space*. The shape of the FDG means that when the centre of the function is

aligned with the zero crossing of the sinusoidal wave there is a high coefficient. Note that even though the sinusoidal waves have different widths, the magnitudes of the coefficient peaks are the same. Figure 7.5 shows the outcome of a CWT on two superimposed sinusoidal signals, of frequency 2 Hz and 6 Hz (comparable to frequencies expected in the model uniform forest flow). The 6 Hz wave is continuous but the 2 Hz wave occurs ten times, at positions interspersed throughout a ten second period (note only a five second section is shown). The time-frequency map is useful for a qualitative view of the frequency components of the signal. As can be seen in the plot, the 2 Hz signals appear as red areas near the bottom of the map. The wide frequency bandwidth at high frequencies gives rise to the 6 Hz components stretching across the upper part of the map (as with many presentations of frequency variables these can be shown with a log scale).

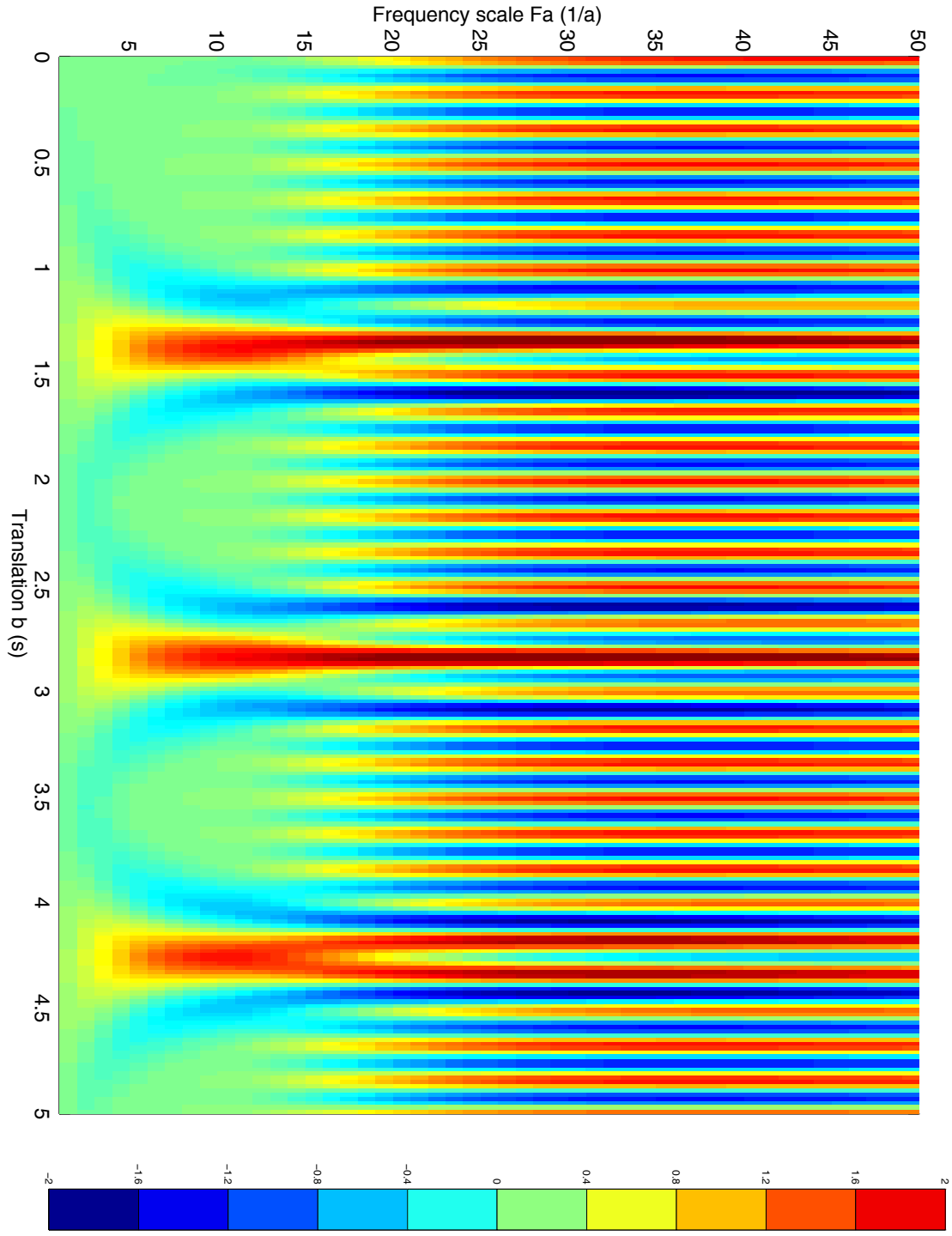

Figure 7.5 CWT of an artificial signal consisting of a continuous 6 Hz sinusoid and three superimposed single oscillation 2 Hz waves (Real part of transform shown).

Using the relationship $f = Fa / 2\pi$, the cross sectional plot at the 2 Hz scale can be generated, see Figure 7.6.

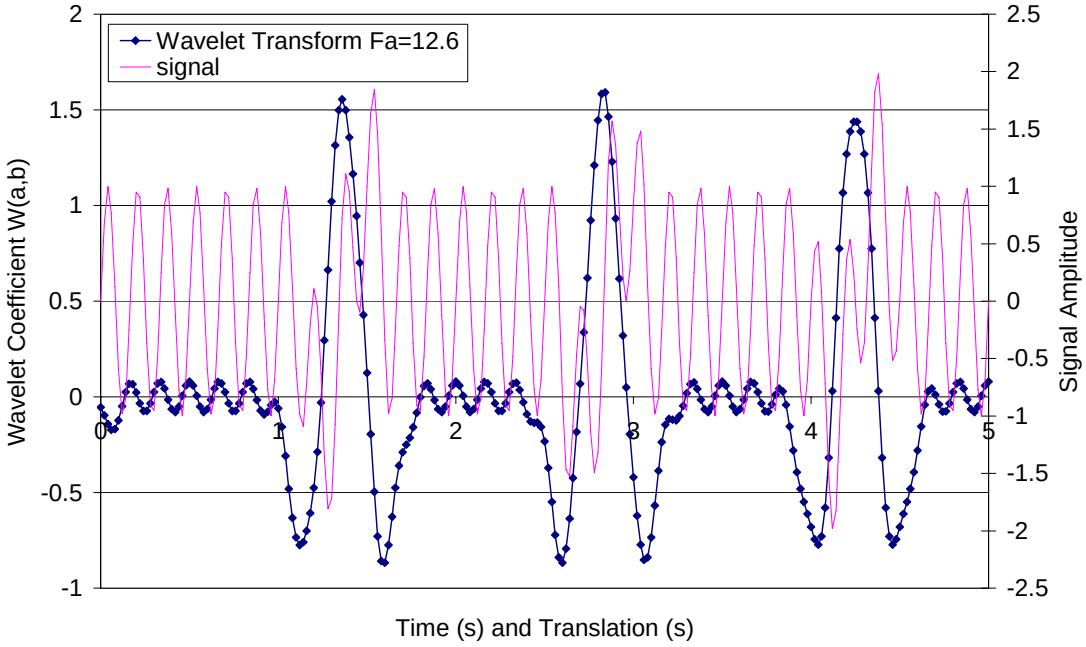

Figure 7.6 Plot of W(a,b) where Fa = 12.6.

It can be seen at this scale that the high frequency components are attenuated to small coefficients. Matches of the wavelet shape with the 2 Hz signal are clearly shown with large coefficient peaks at the time of best match. A histogram of the positive wavelet peaks (termed *PWP*, or *PWP'* if divided by 0.886) of this coefficient series gives a clear distinction between the two types of signal present, see Figure 7.7. Thus it is necessary to apply a threshold *TH* to the coefficients to de-noise the transform. If $TH = 1$, in this case there are 10 remaining coefficient peaks which correspond to the 2 Hz signal. The positions of these peaks can then be used to reconstruct the original signal (Figure 7.8). The degree of noise of the reconstructed signal is dependent upon the number of isolated signals, and the random positioning of the high frequency signal superimposed on top.

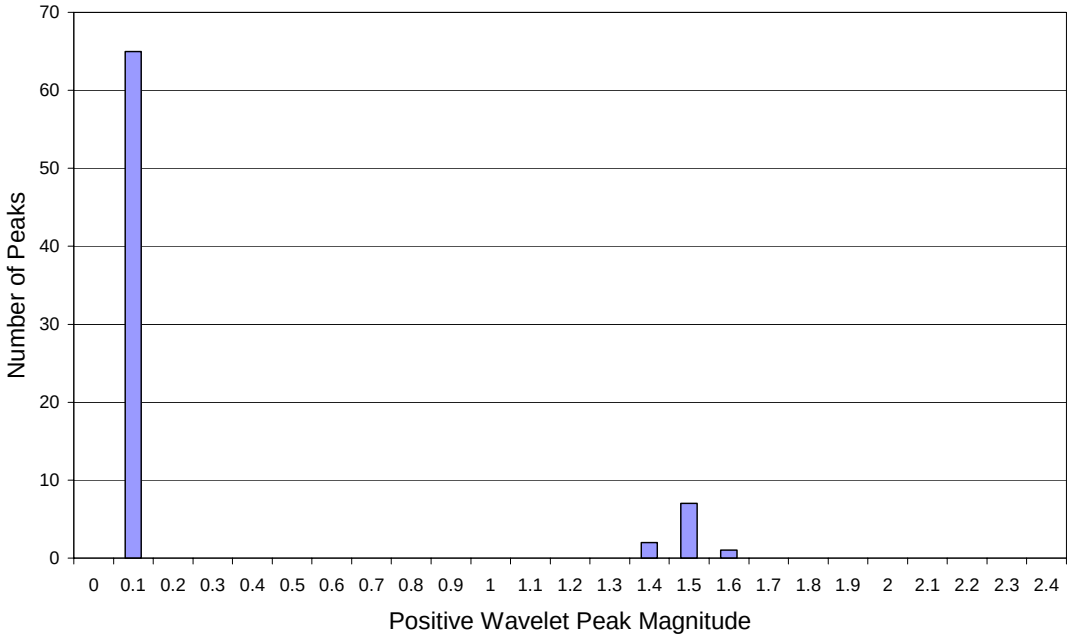

Figure 7.7 Histogram of Positive Wavelet Peaks (PWP) for Fa = 12.6.

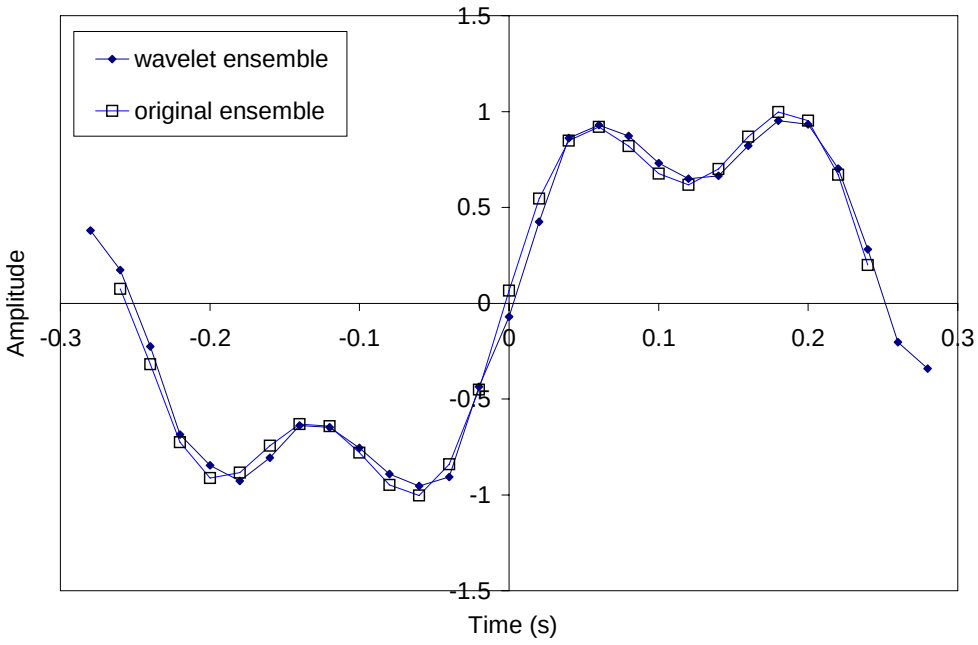

Figure 7.8 Reconstructed ensemble signal Fa =12.6 , TH = 1.

The same process can be applied to the 6 Hz signal (*Fa* = 37.7). In this case, 60 peaks in the wavelet time series are recovered as expected. The *WP* histogram and reconstructed ensemble signal are given in Figures 7.9 and 7.10 respectively. Note, the low frequency component

does not cause the same low *PWP* noise problem as illustrated in Figure 7.7 but is manifested as a larger spread of the *PWP* coefficients. The effect other signals have is to cause the distribution of *PWP* to become less well defined. If a 20% 'random noise' (turbulence levels that might be expected in the forest) is added to the original signal in Figure 7.5, the *PWP* histogram for *Fa*=37.7 (Figure 7.11) becomes more spread out although the number of positive matches remains the same.

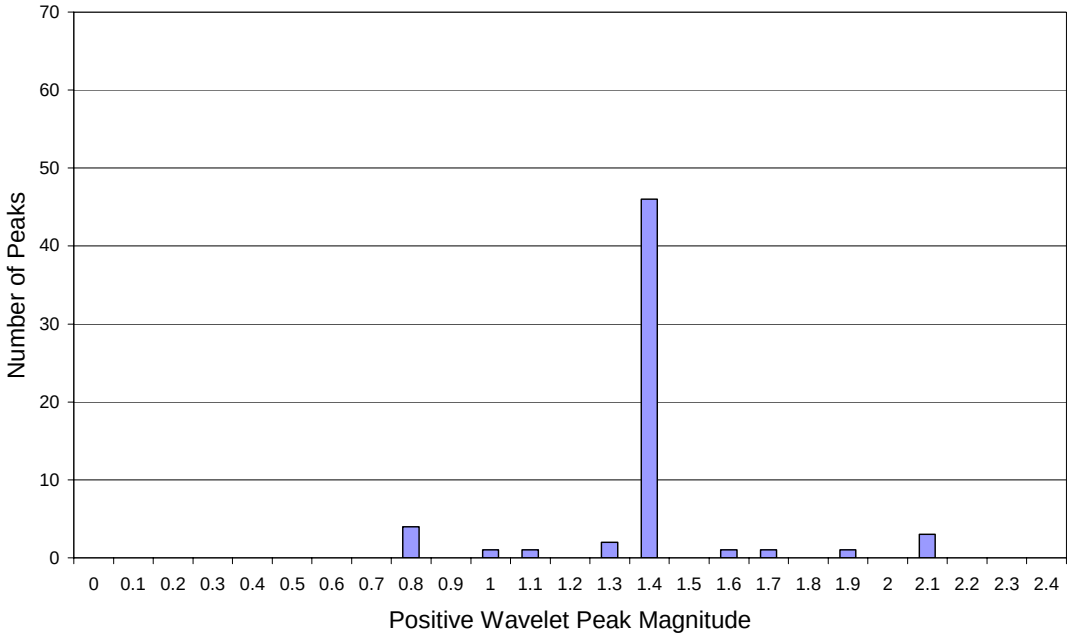

Figure 7.9 Histogram of PWP for Fa = 37.7.

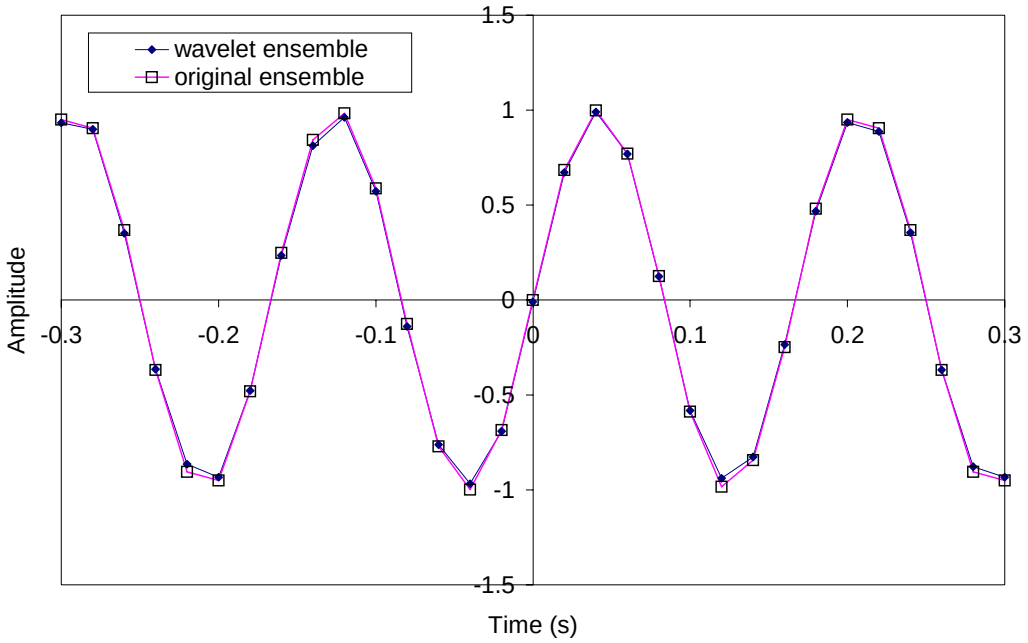

Figure 7.10 Reconstructed ensemble signal for Fa= 37.7.

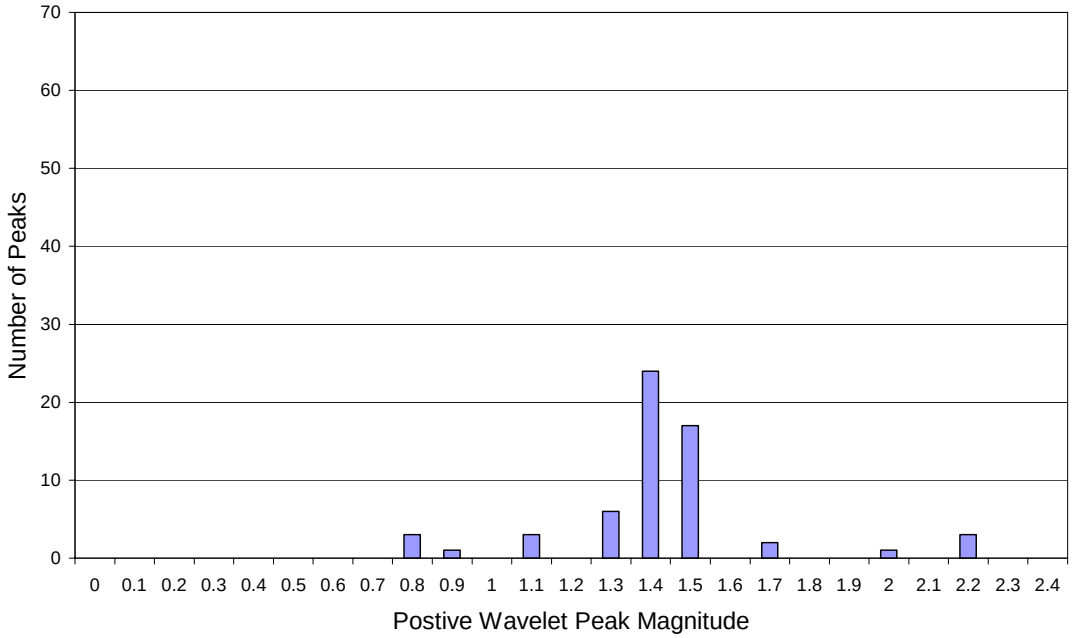

Figure 7.11 Histogram of PWP for Fa = 37.7 (original signal + 20% noise).

7.7 Application to Conditional Sampling Routine

The apparent benefits of wavelets are that they can be used to analyse the whole time series for patterns similar to the wavelet but also at different frequency scales. The better the pattern match then the higher the coefficient. Instead of using just pure magnitudes as a conditional trigger (*e.g.* Marwood 1996) there is a mechanism to look for shapes in the time series, making the conditional sampling more reliable.

7.8 Apparatus and Experimental Description

It would be useful to identify the processes and equipment used in the final experiments. There were several practical conditions that had to be met.

- Identification of trigger signal and instrument
- Use of LDA as a roving point measurement
- Simultaneous sampling of the bending moment to ascertain gust / tree bending moment relationship
- Simultaneous sampling of standard tunnel U_{ref} measurements

The identification of the trigger signal became a very important issue. Initially the streamwise bending moment was the obvious choice because then the largest bending moments could be related to the relevant gust structures. However, it became apparent that the dynamic behaviour of the tree did not allow a reliable trigger condition to be achieved. In essence the previous movements had such a large effect on the tree bending moment, that the maximum bending moment may not occur at exactly the same time when a gust passes by. Alternative use of hot-wires as a control instrument was dismissed because of the damaging interference caused by the LDA airborne seed. Eventually, a signal of total pressure measured above the

forest was found to be adequate. This was chosen mainly so that a simple total-pressure pitot tube could be used, which gave an acceptable control signal. It was placed above the forest at inflexion height, h_i, so that there would be no interference to the tree movement, and its position would allow the analysis of the low and high frequency events over the forest that were revealed in Figure 4.9.

The experimental set up is shown in Figure 7.12. The pitot tube support was designed so that the tube could be positioned at h_i, vertically above the test tree whose bending moment is measured.

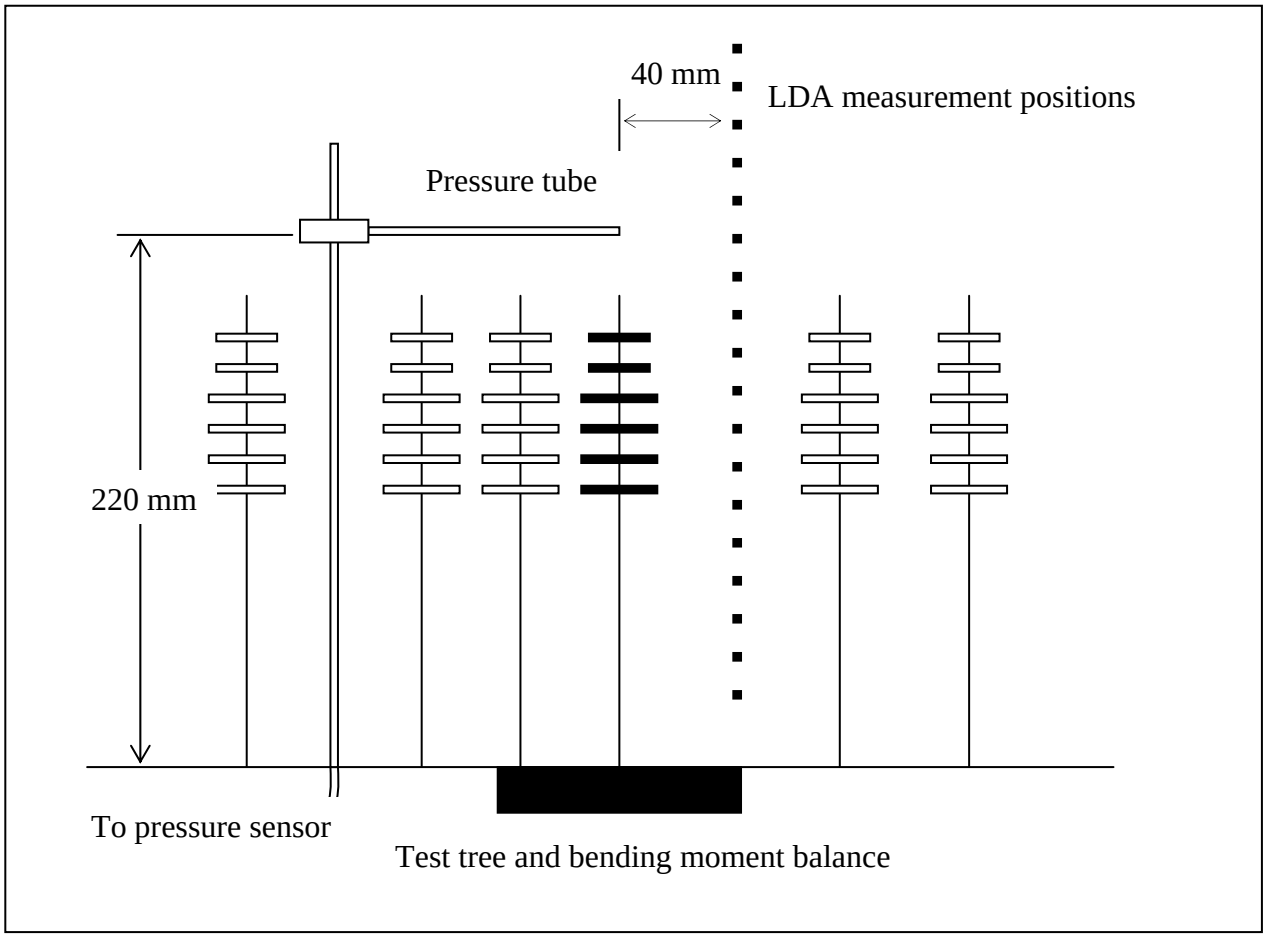

Figure 7.12 Experimental set up of conditional sampling apparatus. Tree in centre of forest in mid-forest simulation.

The tree in front of the test tree had to be moved to avoid obstructing the LDA laser beams. The LDA traverse positions ranged from z = 40 to z = 400 mm in 20 mm increments. Only a vertical traverse of measurements was taken, because the Taylor's Hypothesis of frozen turbulence was used to transform the time series into horizontal lengths.

7.8.1 Pressure Tube Design

When measuring fluctuating pressures with a remote sensor, it is essential to avoid amplitude and phase distortion caused by acoustic resonance in the connecting tube. Work originally carried out by Irwin *et al.* (1979) and Surry and Stathopoulos (1977) showed that restricting the flow area at points along the tube could alleviate the problem. They showed with good design a tube can achieve a unity frequency response and a linear phase lag over a desirable range. Gumley (1982) devised an analytical approach to this problem that was then enhanced by the computer programs of Letchford (1987). These computer programs were used to design the current tubing system.

A linear relationship of phase lag, θ, against frequency causes a uniform time lag between actual and measured signals. This occurs since phase lag θ equals a constant k multiplied by frequency n. Therefore:

$$\text{Time lag} = \frac{\theta}{n} = \frac{kn}{n} = k \qquad [7.7]$$

The tube specifications and frequency response are shown in Appendix B. The time lag = 0.0173 s. This is effectively just less than the sampling interval of the experiment (0.02 s) and thus any delay could be seen to be one point apart.

7.8.2 Practical Details of Simultaneous Sampling

The pitot tube is attached to a scanivalve and Sentra pressure sensor with sensitivity approximately 273 Pa V^{-1}. The signal from the pressure sensor is then sampled by a CED analogue to digital converter and sent to 286 PC computer. The two bending moment components are acquired, as described in Chapter 3, and also sampled by the CED A/D along with tunnel reference dynamic pressure and temperature. The number of channels available limited the sampling frequency to 50 Hz. Using the CED built in digital filter, the signal was then low pass filtered to 25 Hz. The use of the LDA caused two significant problems in setting up simultaneous sampling. First it is an independent system and cannot be sampled with the other data channels. Secondly, it requires post-processing and interpolation between seeding sample points to fit the correct sampling rate. It was important during the experiments to obtain a high seeding rate to ensure reliable post-processing interpolation. The sampling problem was overcome as follows. The LDA sampling program was initiated. The CED sampling program was started and simultaneously sent an ‘on’ signal impulse to the LDA Burst Analyser. This ‘on’ impulse was recorded in the LDA time series with an identifier code. A post-processing program then took both sets of data and interpolated and grafted the LDA data onto the CED data at the correct starting time.

7.9 Wavelet Programs

The compiled data from the canopy gust experiments were analysed with wavelet analysis programs written in Matlab. The main program operations were as follows:

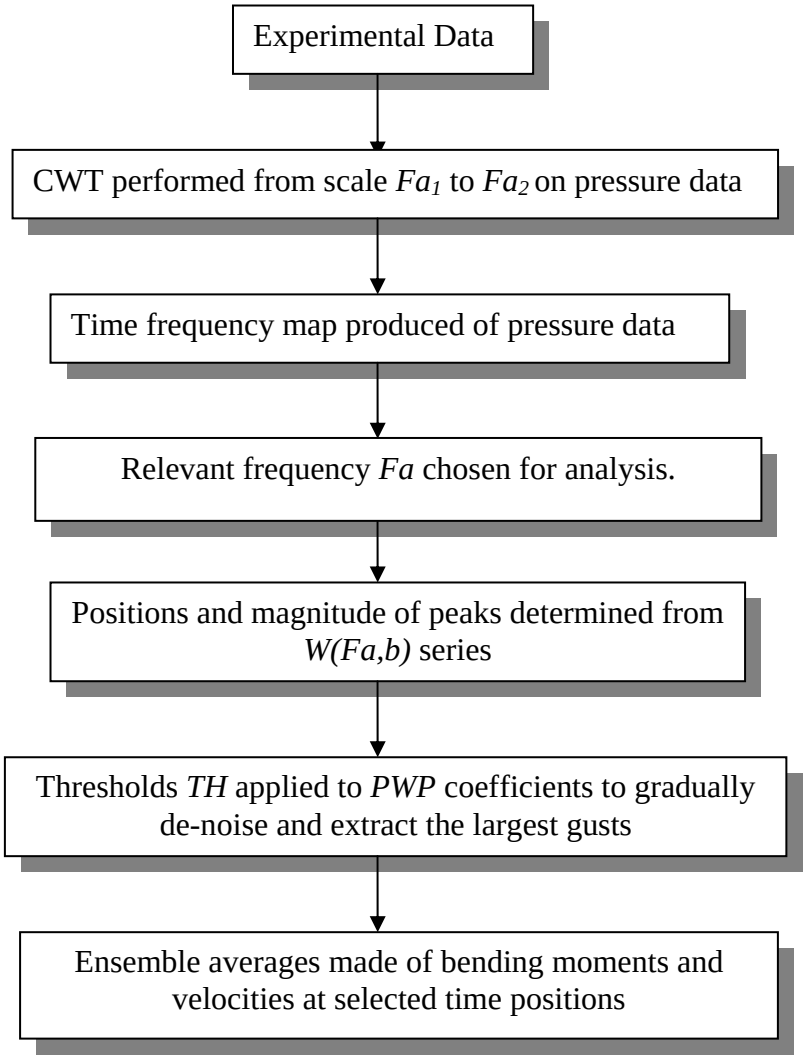

Figure 7.13 An overview of the main tasks addressed in the wavelet conditional sampling program.

7.10 Suitability of FDG Wavelet Applied to Pressure Data

As mentioned earlier the wavelet chosen for the analysis was the FDG wavelet. It was chosen because of the similarities with patterns observed in the total pressure time series, P_T, that occur at a time close to large bending moment excursions. Examples in Figures 7.14 and 7.15 show high and low frequency pressure event ensembles. These ensembles were made up of 30 arbitrarily picked extreme bending moments, 10 each from 3 independent samples. The ensembles were aligned at the zero crossing point. Both plots showed a characteristic small drop in pressure followed by a large peak and decayed via a shallow curve. This pattern could be explained by the small burst / large sweep characteristics of canopy gusts, and was therefore a suitable control signal. Also shown on the plots of Figure 7.14 and 7.15 are examples of FDG detected conditional pressure fluctuations from 16 independent samples. The thresholds refer to the largest 50% and 25% of events (see next section). The two figures show encouragingly similar patterns.

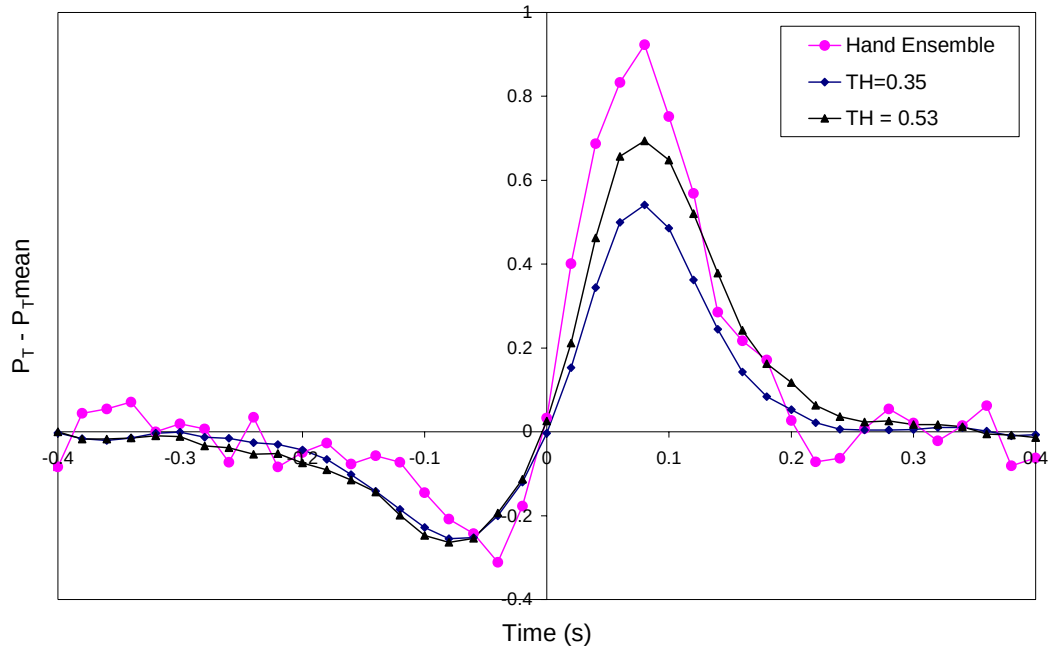

Figure 7.14 Hand ensemble of P_T patterns compared to wavelet obtained patterns for low frequency patterns (Fa=12.6).

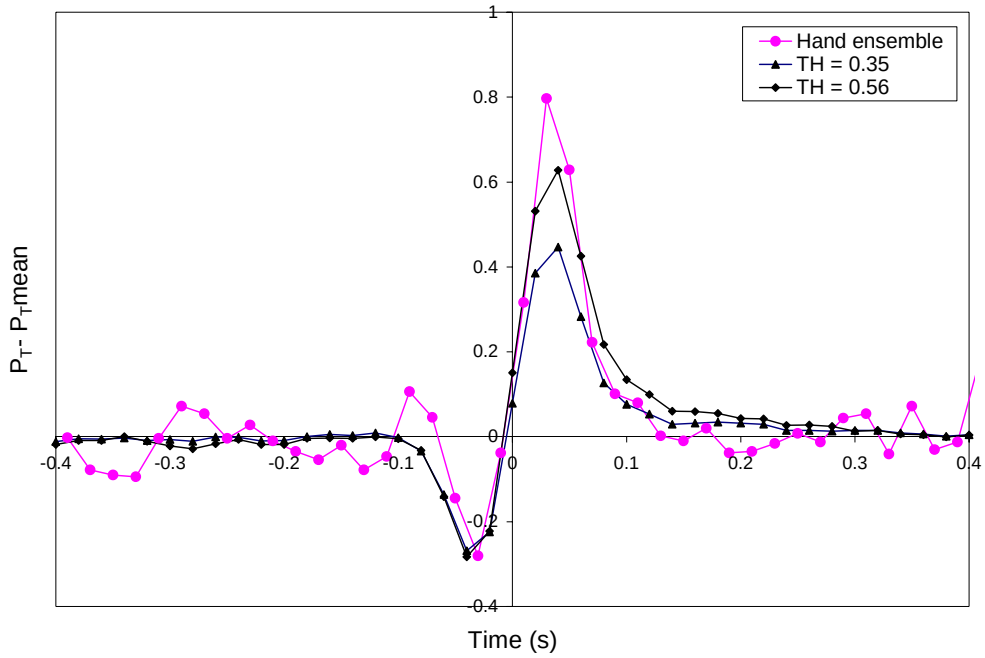

Figure 7.15 Hand ensemble of P_T patterns compared to wavelet obtained patterns for high frequency patterns.

An example of the time-frequency map of the total pressure time series is shown in Figure 7.16. The long, red streaks represent the high frequency events, whilst the larger red areas near the bottom of the graph represents the low frequency. The original total pressure signal is shown in Figure 7.17.

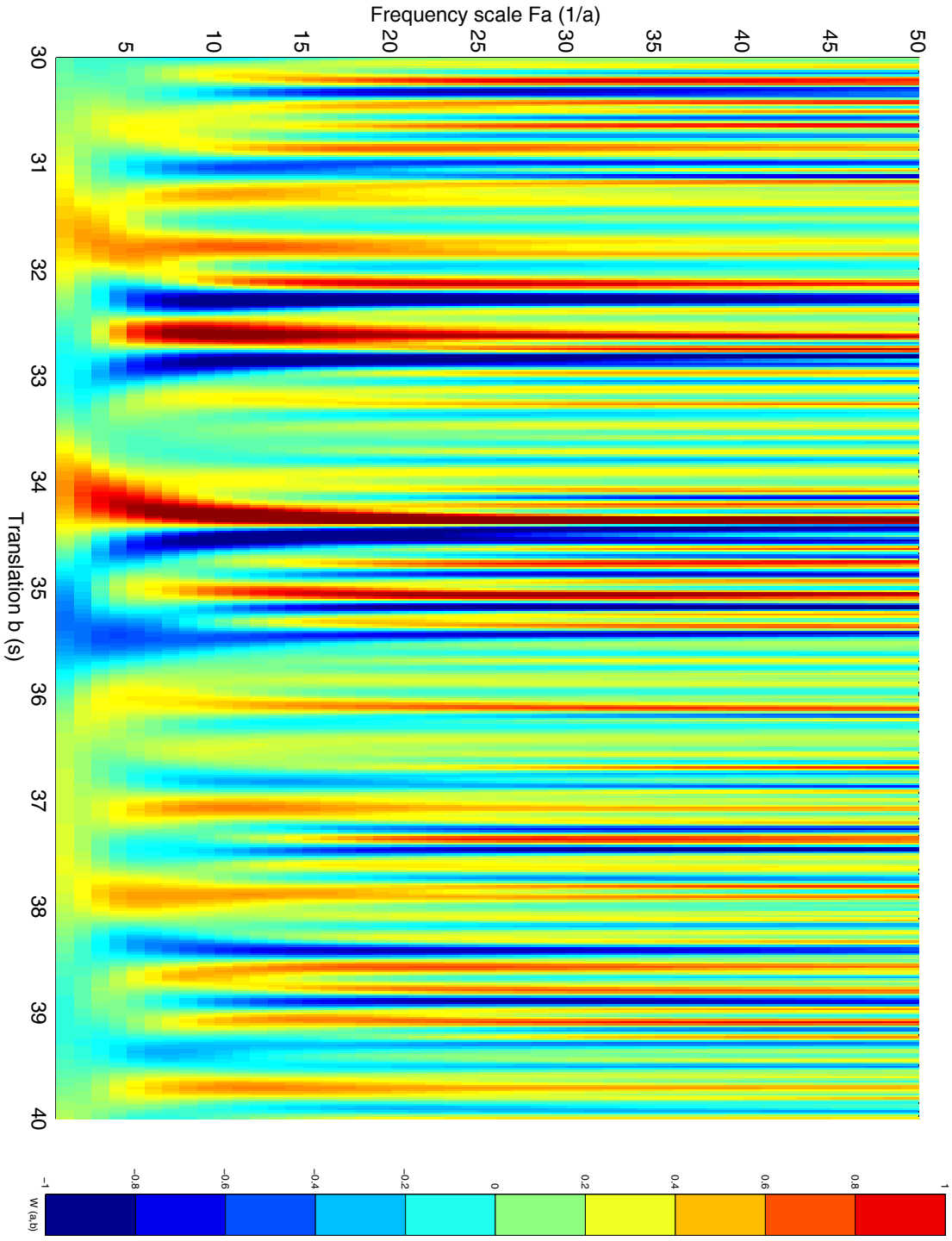

Figure 7.16 Time-Frequency map of total pressure signal above uniform forest. Real part of transform shown.

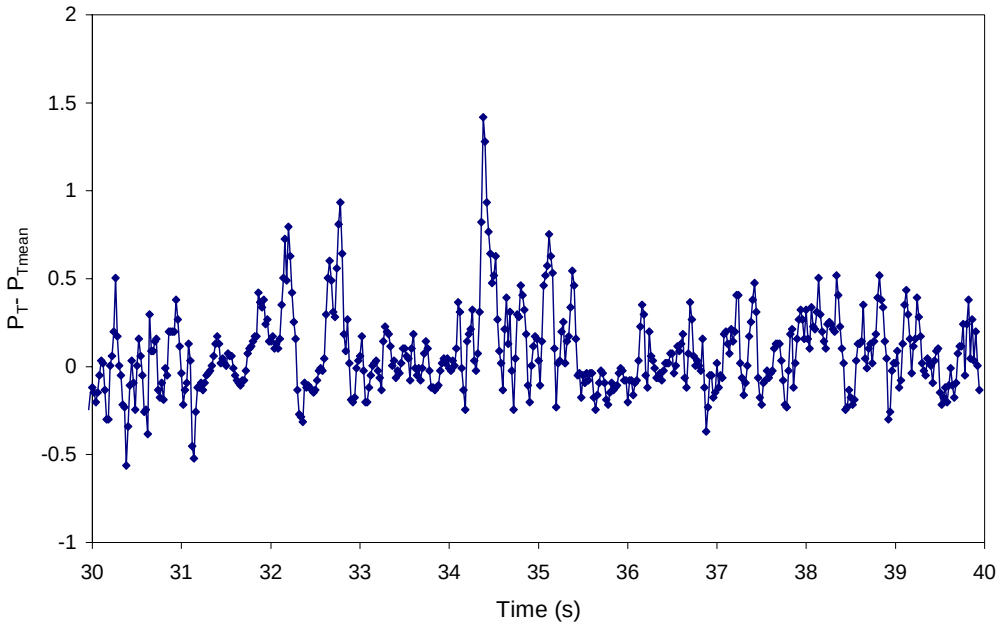

Figure 7.17 Total pressure signal analysed in Figure 7.16.

To demonstrate further that the total pressure signal is a reasonable trigger signal for velocity events, Figure 7.18 shows the frequency spectra for P_T and U. As might be expected the similarity between it and the U velocity spectra at that height is reasonable. Especially evident is the peak at approximately 6 Hz in both signals.

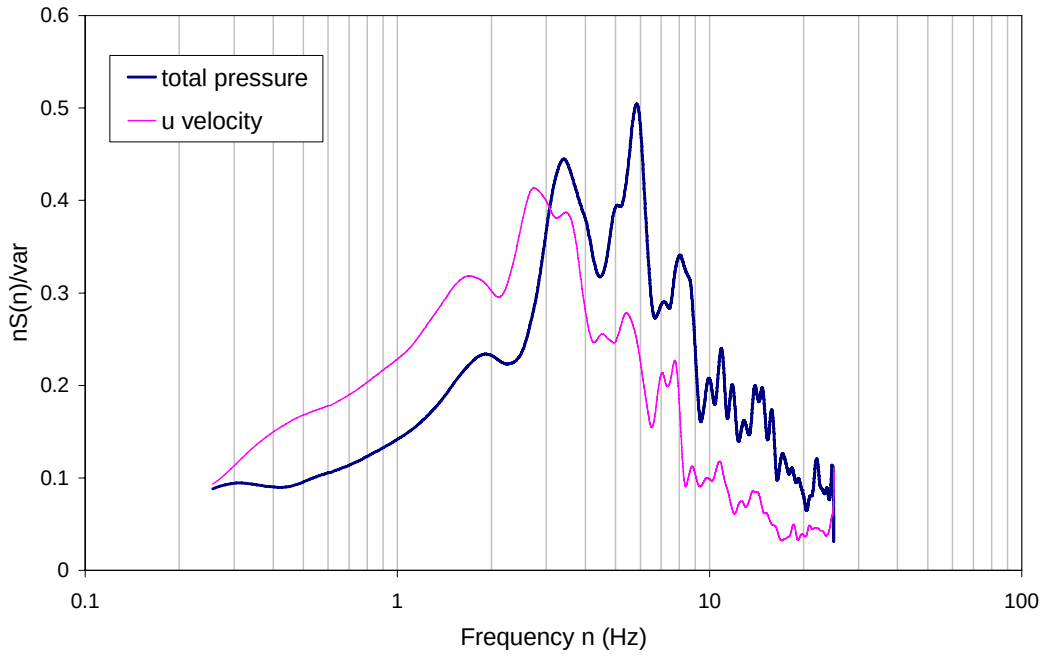

Figure 7.18 Power spectra of P_T and U.

7.10.1 Structures of Interest

From Chapters 4 and 5, frequency spectra evidence suggested the structures of interest in the uniform forest are high frequency gusts at approximately 5-7 Hz. Also of interest are the low frequency peaks in the U spectra at approximately 2 Hz and how these larger scale fluctuations are related to the generation of the higher frequency 6 Hz structures. They are believed to increase the shear in velocity profile so as to encourage gust generation (Raupach *et al*. 1996). By inspection, the simultaneous time series show some of the more extreme bending moments are also caused by fluctuations of this scale. Therefore the wavelet analysis was carried at a frequency of 6.2 Hz (at the peak bending moment frequency, see Chapter 3), thus Fa = 38.9, and also at 2 Hz where Fa =12.6.

7.10.2 Magnitude of Events

The wavelet detection program was run on sixteen independent 120 second samples of P_T, at the above frequency scales, to determine the number of events per 0.05 PWP' threshold bin. The number of events detected in each bin are presented in Figure 7.19, and Figure 7.20 shows the percentage of conditional events remaining after thresholding.

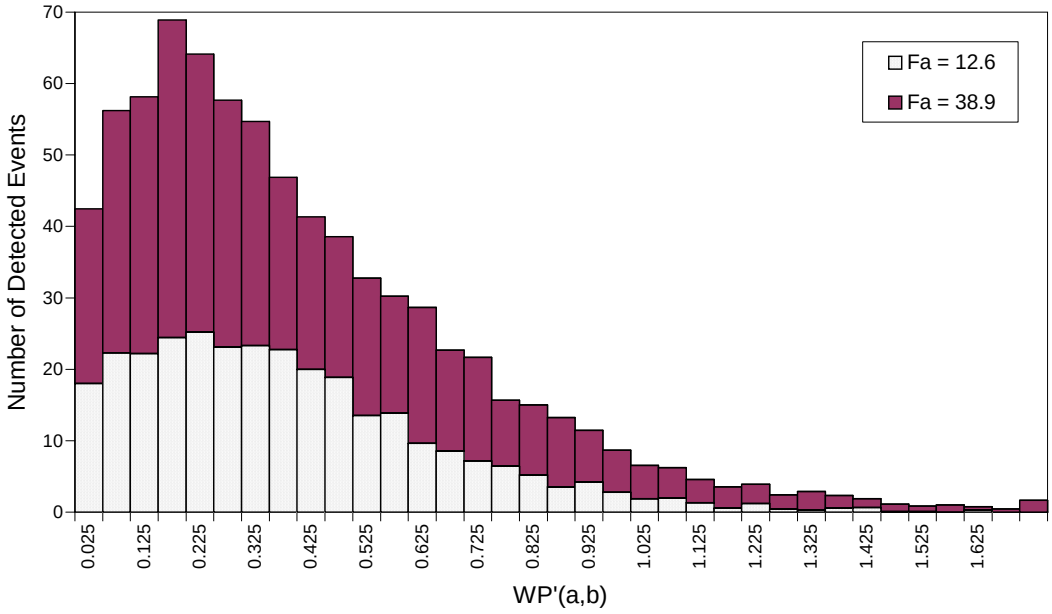

Figure 7.19 Number of events detected after undergoing thresholding TH of PWP'.

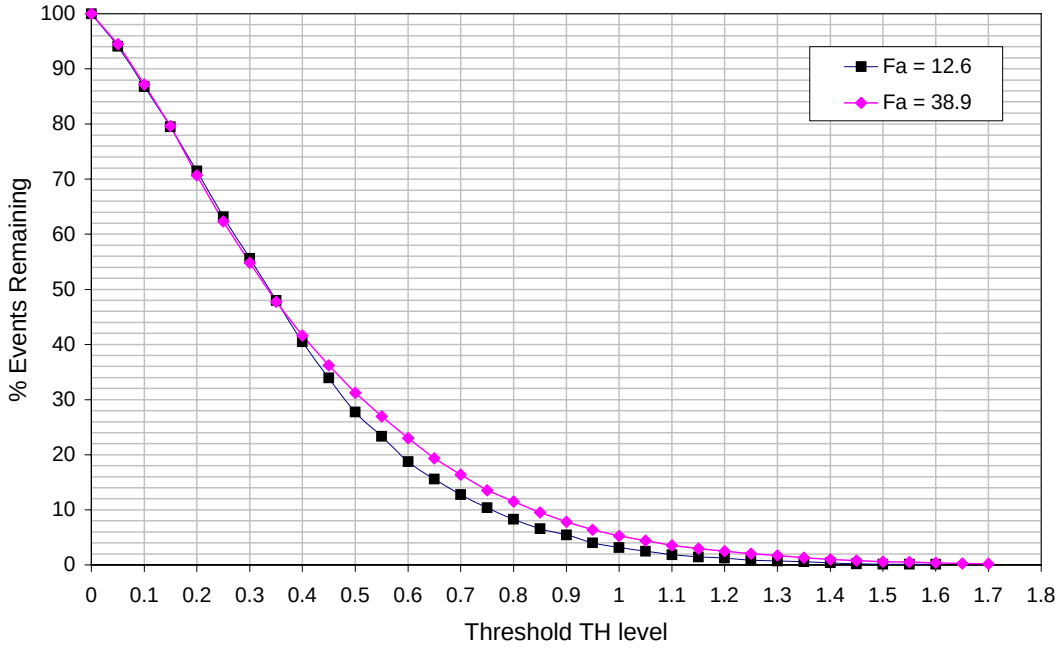

Figure 7.20 Percentage of events remaining after thresholding TH of PWP'.

Although the number of events detected is almost three times the value for Fa = 38.9 compared to Fa = 12.6 (as might be expected with 6.2 Hz / 2 Hz in terms of time), Figure 7.20 shows two very similar curves. This figure allows threshold values to be allocated a

certain percentage of events. In the following analysis it was found that the lower 50% of events were associated with noise and so the threshold level concentrates on the upper 50% (where, of course, we are interested in the highest gusts). Table 7.1 presents the positive wavelet peak (*PWP'*) magnitudes associated with the percentage of events.

	PWP' limits (Fa = 12.6)	***PWP' limits (Fa =38.9)***
Below 50%	0.337	0.334
50% - 60%	0.337 – 0.404	0.334 – 0.414
60% - 70%	0.404 – 0.481	0.414 – 0.514
70% - 80%	0.481 – 0.586	0.514 – 0.642
80% - 90%	0.586 – 0.76	0.642 – 0.840
90% - 100%	0.76 -	0.840 -

Table 7.1 The PWP' magnitudes associated with the percentage of events for both frequencies of interest.

7.11 High Frequency Results

Using the *Fa* = 38.9 FDG wavelet on the above *PWP'* bands allowed ensemble averages to be calculated around the located trigger points. Figure 7.21 shows the normalised total pressure P_T (by reference pitot dynamic pressure) patterns found by the wavelet detection.

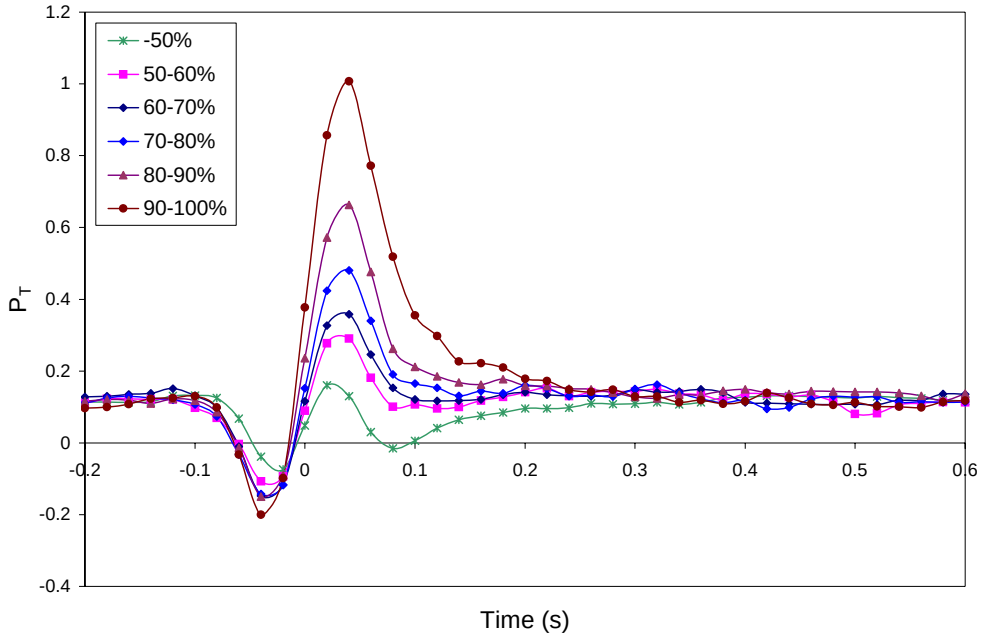

Figure 7.21 Ensemble average of normalised total pressure.

As expected, the lowest *PWP'* band has the smallest pressure fluctuation and is made up mostly of noise. Note how the initial lower dip changes very little compared to the positive peak. The associated streamwise bending moment response is shown in Figure 7.22. The largest bending moments correspond to the largest pressure fluctuations. The clarity of the response is particularly encouraging, especially the in-phase motions after the main peak. What is noticeable however, is that the peak moments are under half those expected from extreme value analysis (0.008). Examination of the individual peaks in the top 10% of *PWP'* coefficients however show that this value is reached and surpassed. Concordant with the pressure patterns in Figure 7.21, the larger peaks tend to be slightly longer in time as well as magnitude. The effect that the width of the forcing signal has on the peak bending moment is investigated later in this chapter.

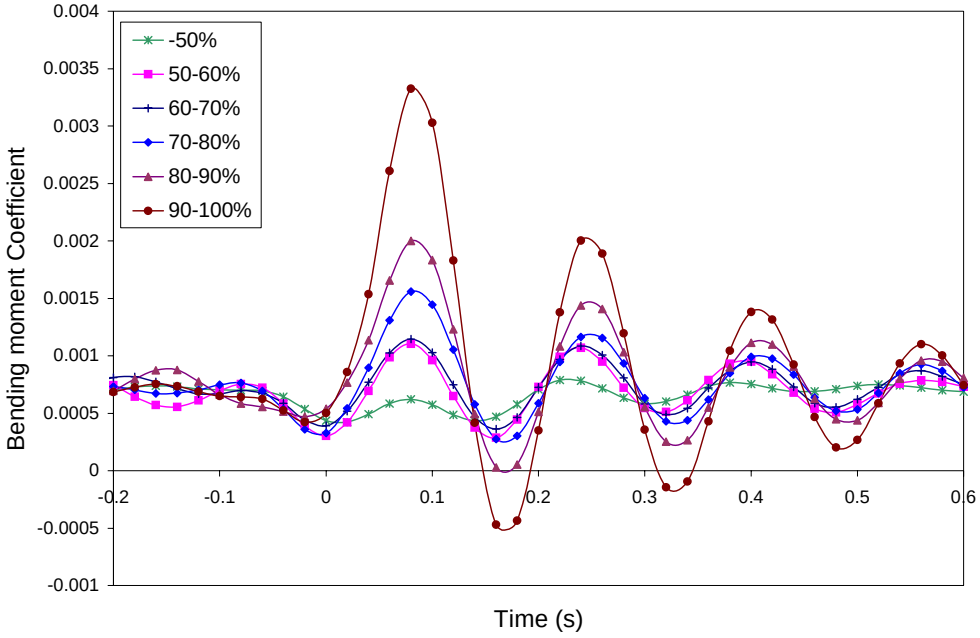

Figure 7.22 Wavelet derived total pressure conditional bending moment ensemble.

There is a linear relationship between the peak in P_T and the peak in the streamwise bending moment. Figure 7.23 shows this relationship. However, since total pressure is rarely measured it is far more useful to compare with velocity. The ensemble streamwise velocity fluctuations at tree top height (z/H = 1.0) are presented in Figure 7.24. The drag coefficient defines that drag is proportional to the velocity squared so it might be expected that any relationship between bending moment and velocity would be similar. Indeed a linear relationship between the peak in U^2 and peak bending moment is achieved, and is shown in Figure 7.25. The figure shows that the forest top velocity is a feasible measurement for use by foresters, who may want to estimate peak bending moments from velocity measurements only. The height of the centre of pressure (where the sum of all forces that act on a tree can theoretically act) would be a more appropriate position for measurement, but practically it is difficult for foresters to measure there due to limited space and interference. It was also found that the U velocity has no significant difference in correlation than the resultant velocity.

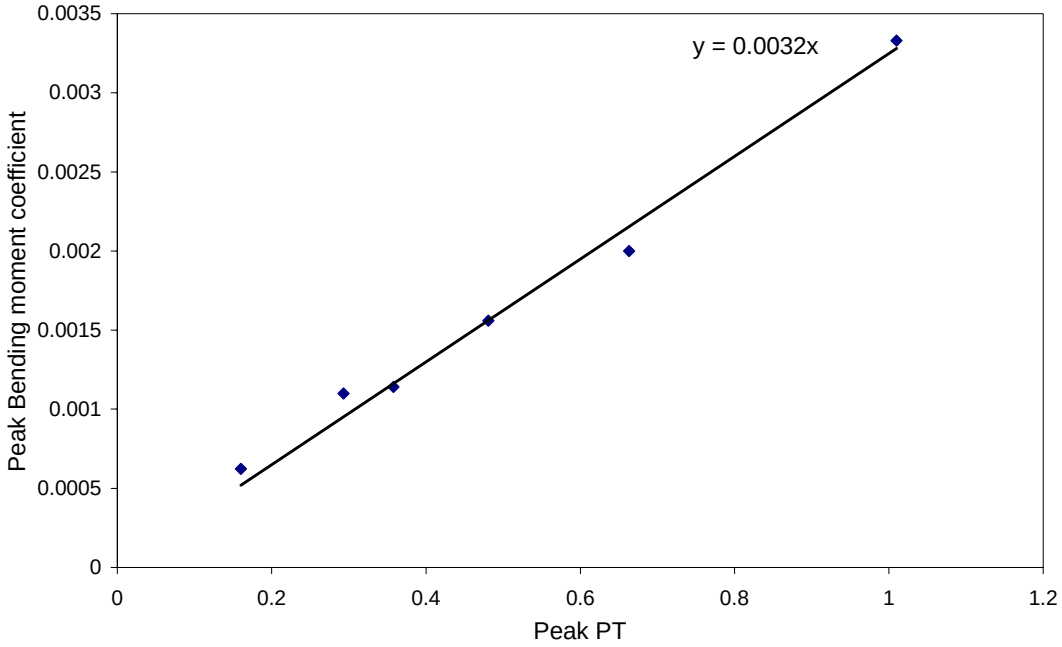

Figure 7.23 Normalised total pressure peak to bending moment coefficient peak relationship.

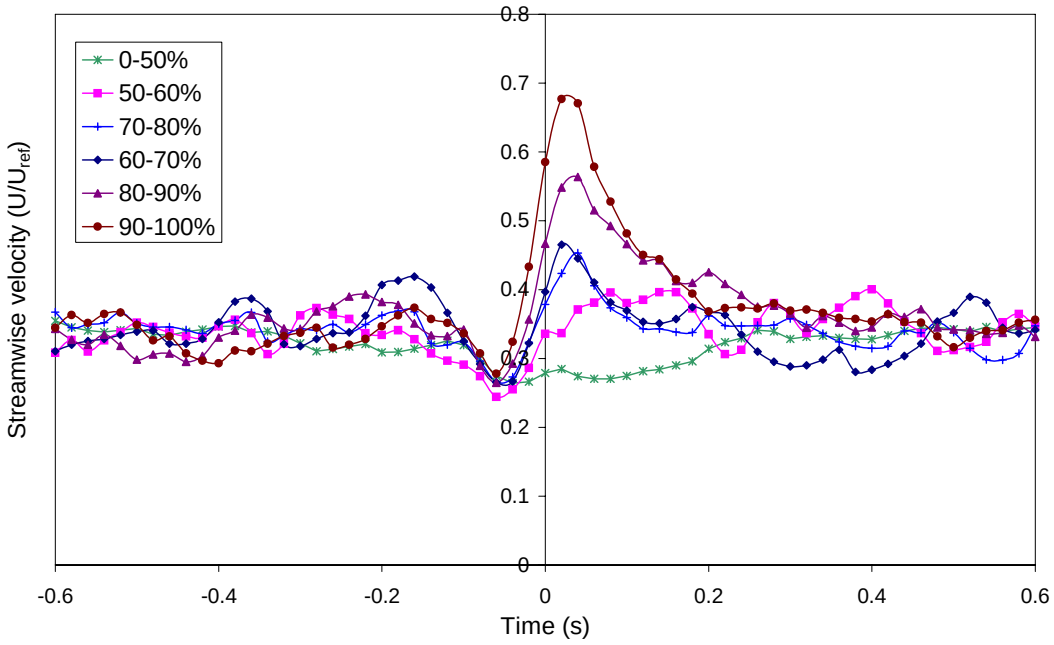

Figure 7.24 U velocity at z / H= 1.0.

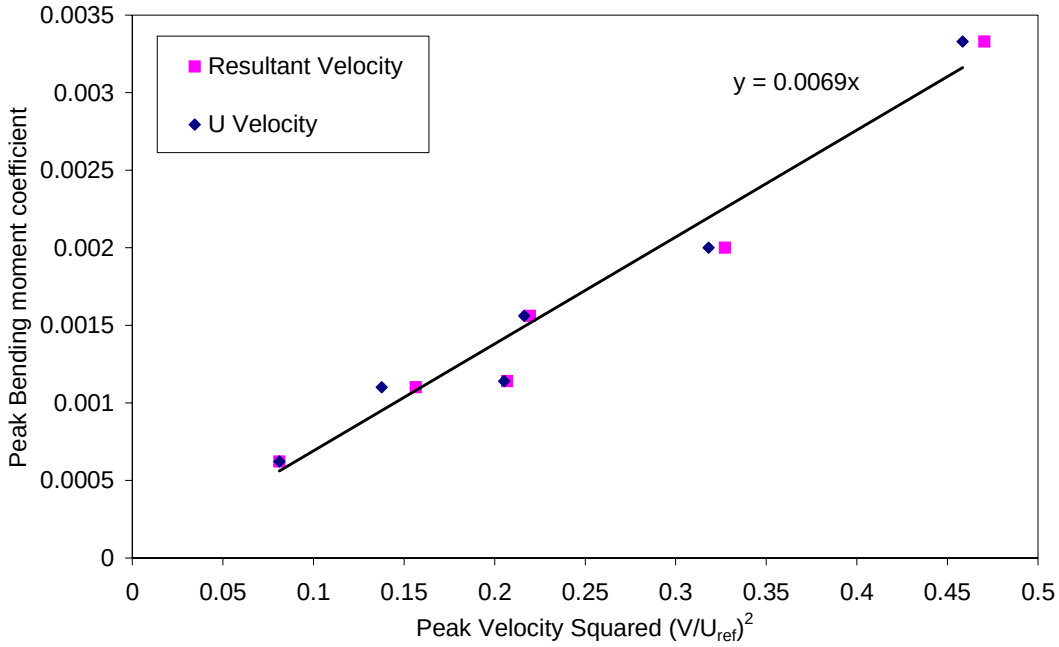

Figure 7.25 Peak velocity squared and peak bending moment relationship.

7.12 Gust Structure

To enable the visualisation of the canopy gusts into a physical dimension, rather than time, it is necessary to transform the time series using Taylor's Hypothesis of frozen turbulence. As the name suggests, this hypothesis assumes that a turbulent eddy is 'frozen' in the mean velocity field and therefore can be extracted using a simple $\Delta T.U$ relationship. However, as reported by Shaw *et al.* (1995) and Irvine (1994), the convection velocity for a forest canopy is faster than the mean velocity at the inflexion point, which usually renders the use of Taylor's Hypothesis invalid. However, in this case the convection velocity was obtained so that the transform could be used. To obtain an estimate of gust convection velocity a two point correlation was carried out between the streamwise bending moments of two spatially separated test trees. The trees were separated at varying downstream distances and the correlation lag observed. From these results a velocity ratio, U_c/U_{ref}, of 0.71245 was obtained,

where U_c is the mean convection velocity. The ratio, U_c to the inflexion height mean velocity was found to be 1.45.

Using Taylor's Hypothesis we can obtain pseudo snapshots of the flow, as presented in Figures 7.26 a, b, c, d, e, and f. To represent distance, the time is reflected about 0 seconds, so that the events at $-t$ are on the right hand side of the flow and have passed through the trigger point. Starting with the upper 10 % of events, it can be seen how the air is ejected from the forest, ahead of a large downsweep of air following behind. This action is widely reported in all canopy flows and the snapshot is very similar to other studies to capture the gust structure (Gardiner 1994, Gao and Li 1993, Zhuang and Amiro 1994).

a

Figure 7.26a) A pseudo snapshot of the strongest 10% gusts over the uniform forest.

Figure 7.26b) A pseudo snapshot of the 80-90% strength gusts over the uniform forest.

Figure 7.26c) A pseudo snapshot of the 70-80% strength gusts over the uniform forest.

Figure 7.26d) A pseudo snapshot of the 60-70% strength gusts over the uniform forest.

Figure 7.26e) A pseudo snapshot of the 50-60% strength gusts over the uniform forest.

Figure 7.26f) A pseudo snapshot of the lowest 50% strength gusts over the uniform forest.

Figure 7.26g) Structure of strongest 10% gusts obtained by subtracting mean convection velocity from pseudo snapshot vectors.

The downsweep appears to stretch from approximately –2 *H* to 0 *H*. It penetrates down to approximately 0.5 *H*, as expected from the mean velocity statistics in Chapter 4. The high velocity also appears to drive a weak recirculating bubble, below the forest canopy centred at *–H*.

With percentage magnitudes from 100%-50 %, it is clear from Figures 7.26a, b, c, d, e, and f, that the gust downburst reduces in magnitude with decreasing wavelet coefficient, thus adding further evidence for the validity to the wavelet method. With the lower 50 % of events, the velocity profile is almost constant and there is no downsweep into the forest.

Figures 7.26a, b, c, d, e, and f present the instantaneous flow field picture but because the gust is moving over a mean flow it is difficult to determine the stationary eddy structure. A large but not improbable assumption has to be made, that if the 'camera' is moving at the same mean velocity as the eddy, an instantaneous snapshot of the structure is obtainable. Figure 7.26g portrays this by subtracting the mean convection velocity from the streamwise velocity component. Encouragingly, it reveals a large negatively inclined eddy to the left of the trigger position. Also it is centred near the inflexion height. To the right of the trigger position, and slightly higher the main eddy, there appears to be a weaker eddy. Unfortunately, further away from the trigger point, some definition is lost because of increasing random averaging, and so the exact closure of the eddies is not clearly visible. This structure is very similar to the mixing layer, including the expected stagnation point between the eddies, see Figure 4.26. A diagrammatic view of the general canopy flow characteristics is shown in Figure 7.27.

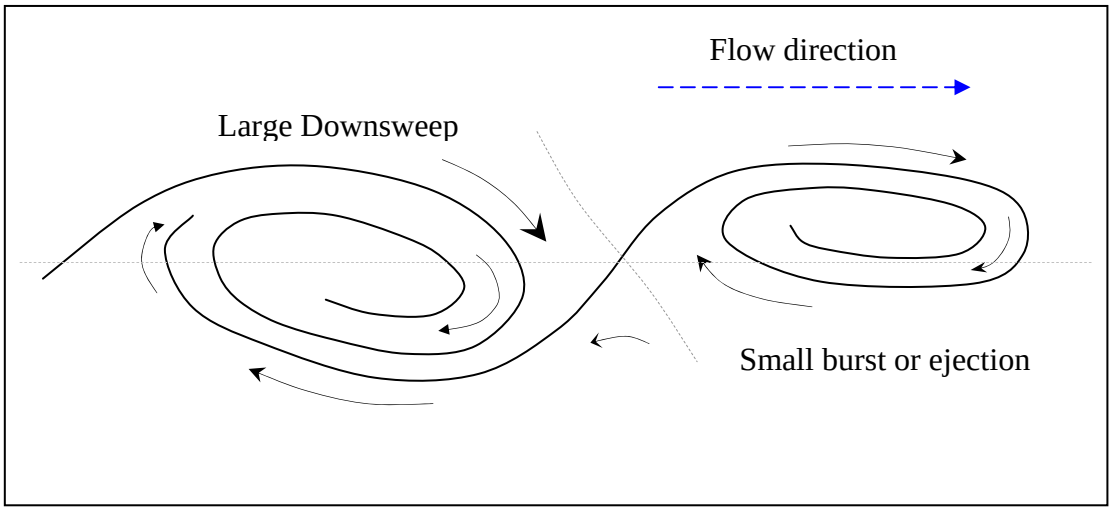

Figure 7.27 Explanation of forest wind movements in terms of eddy positions.

Section 7.14 addresses the issue of the number of eddies generated at any one time, and shows that the second eddy is not simply a result of ensemble averaging adjacent gusts.

7.13 Low Frequency Structures

Raupach *et al*. (1996) suggested that the low frequency band (1-3 Hz) of the streamwise spectra is responsible for modulating the size of shear at the inflexion point, and hence enhancing conditions for gust generation. It is believed the oncoming turbulent wind carries these lower frequency eddies across the forest, but recalling forest edge effects in Chapter 5, it is also possible that they are generated locally in the internal boundary layer. Wavelet analysis, carried out in a similar manner as the last section, was inconclusive but did reveal that that 2 Hz gust structures do exist in the canopy. The characteristic total pressure pattern for 2 Hz is shown in Figure 7.28 and the corresponding bending moment response in Figure 7.29.

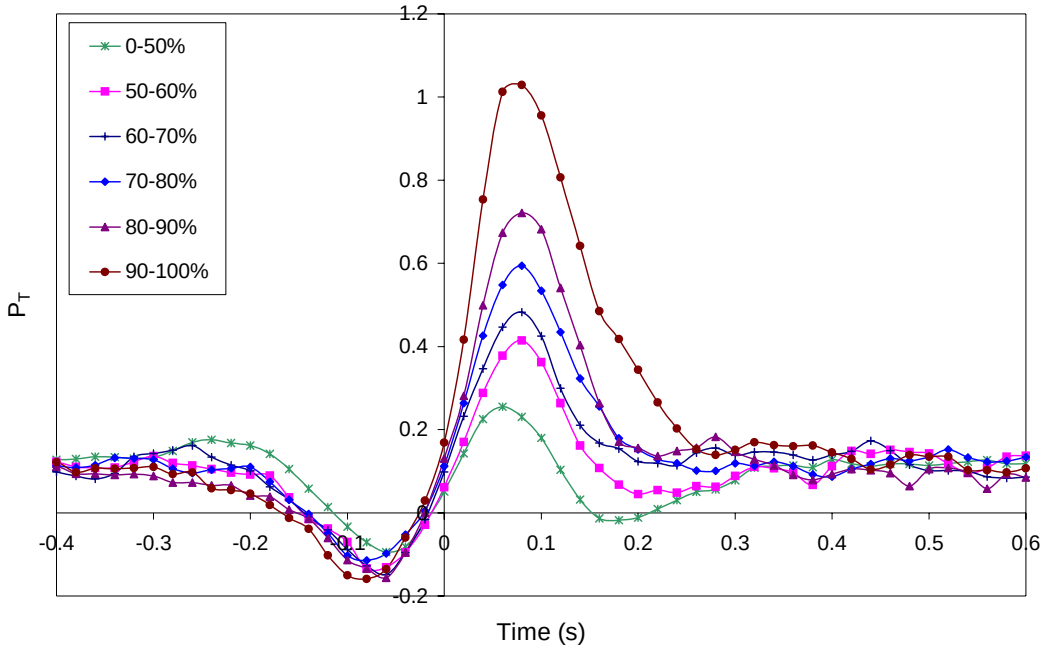

Figure 7.28 Total pressure time pattern for Fa=12.6.

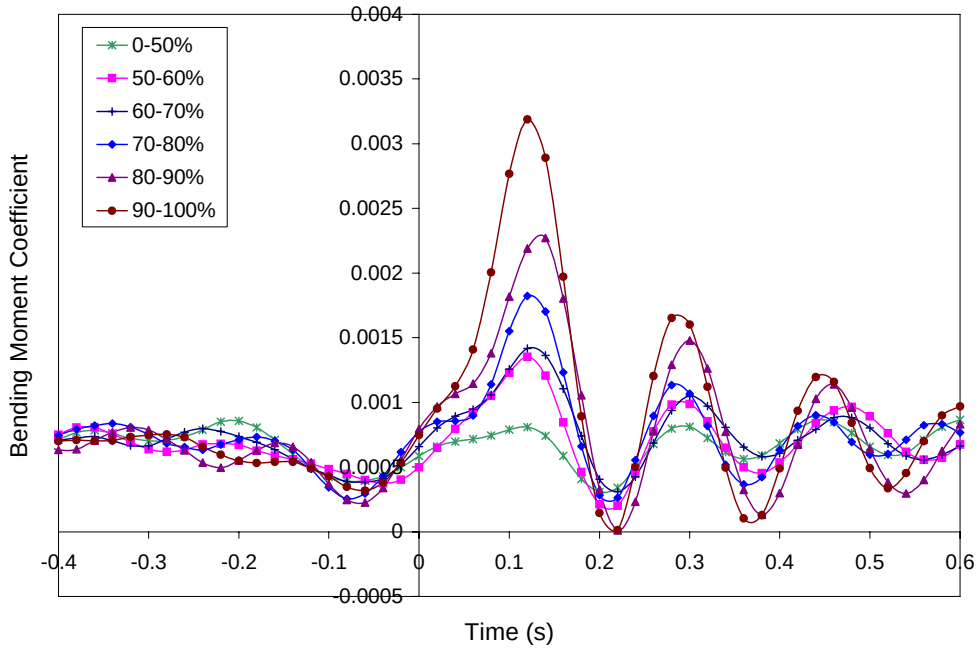

Figure 7.29 Pressure conditional bending moment response.

The peak bending moments are just slightly less than the 6.2 Hz frequency. Note that after a slow build up, the response is very similar to that of the high frequency gusts. There is also a similar linear relationship between the peak bending moment coefficient and peak total pressure coefficient of $B_{peak} = 0.0031\ P_{Tpeak}$. The pseudo snapshot of the flow field is shown

in Figure 7.30 for the top 10% of events only. The plot appears to be very similar to the 6.2 Hz snapshot. On closer inspection it reveals that the downsweep is not as strong, but the length of time it penetrates the forest is longer.

Figure 7.31 shows the gust velocity comparison at tree top height $z/H = 1$ and also at $z/H = 2$, near the top of the shear region. This plot allows us to study the relationship between the change in shear and the presence of the low frequency structures. As can be seen there is an overshoot of the mean, and hence and an increase in shear, but the 6.2 Hz structure also shows this. This could be for two reasons, the first being that the 2 Hz structure is similar to the higher frequency structures. Another is that the 2 Hz structure is related to the generation of gusts and the higher frequency structures 'piggy-back' onto its presence. Indeed, careful examination of the trigger event times show that 40% of the lower frequency events occur in the same region as the high frequency events (for the top 10% of events at both frequencies). Further examination of streamwise time series show a frequently occurring structure, where a sharp drop is followed by a large increase with several high frequency gusts. This is investigated in the next section, and a typical time series is given in Figure 7.32.

Figure 7.30 Pseudo-snapshot for the strongest 10% gusts over the uniform forest, for low frequency structure (2 Hz).

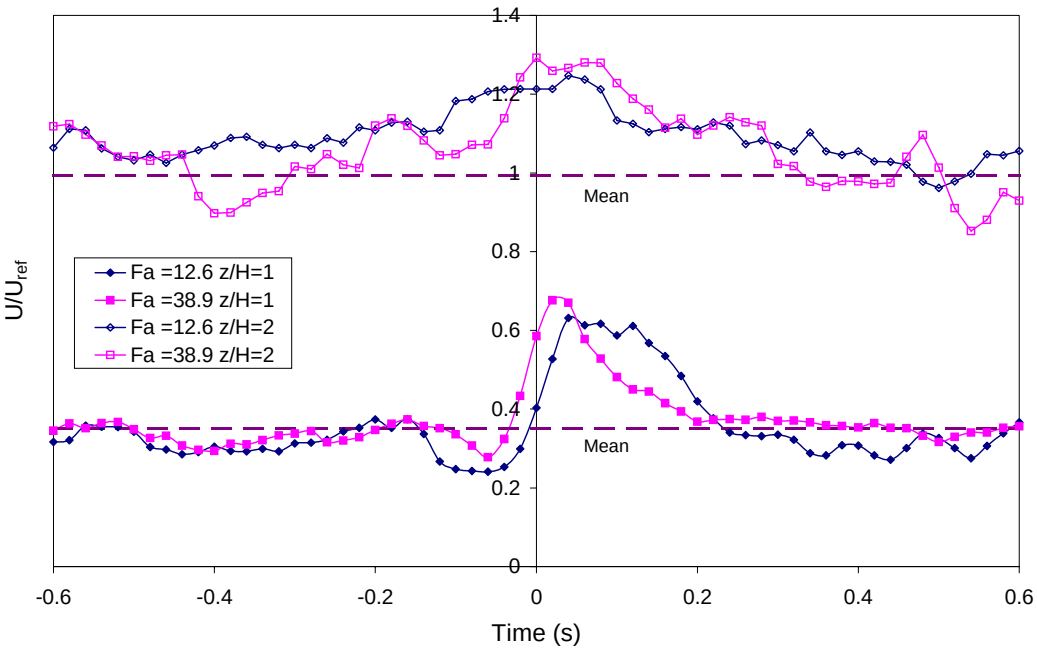

Figure 7.31 Comparison of pressure conditional streamwise velocities. For 90-100% PWP' magnitudes.

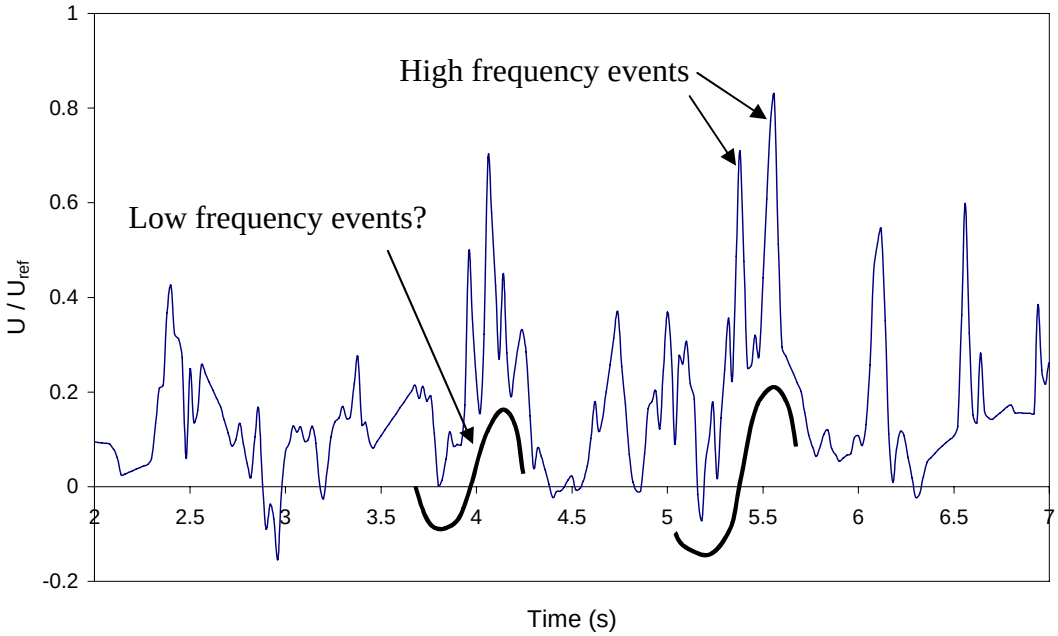

Figure 7.32 U velocity time series showing possible complex structure.

Evidence presented here for these types of structures is not conclusive. Speculation of their origins include the pairing process of smaller eddies (Ho and Huang 1982), an interaction between the oncoming flow and the internal boundary layer, or possibly from the influence of the instability wavelength of the flow (see Section 4.5).

7.14 Time Interval Between Gust Arrivals

As mentioned in the last section there is some evidence that canopy gusts occur in groups or *packets*. Finnigan (1979b) observed that gusts tend to arrive in packets of three or four. Most studies of the arrival of gusts have concentrated on the mean time between events (Qui *et al.* 1995, Collineau and Brunet 1993) and not on the patterns of arrival. The conditional wavelet analysis allows us to study the patterns in which the gusts arrive. The following analysis does not explore every perturbation and combination of gust arrivals, but supports the idea that repetitive gust loading can greatly affect the peak bending moments on trees. However, it is made clear that all the evidence in the presented study point to the fact that the largest bending moments appear to be caused by large isolated gusts.

Using a time separation limit, the number of consecutive events can be quantified. Assuming that any events under 50% of *PWP'* are due to noise, the top 50% of events are only considered (using 6.2 Hz wavelet analysis). The bar chart in Figure 7.33 has a mean separation between events of 0.16 s (6.25 Hz) and shows that more than half the events are in packets, or groups, rather than occurring individually. The mean wavelet coefficient peak, ***PWP',*** for the first four groups are presented in Table 7.2.

Number of events in group	1	2	3	4
Mean PWP’	0.638	0.616 0.660	0.623 0.649 0.691	0.633 0.674 0.649 0.683

Table 7.2 Mean PWP’ values for groups.

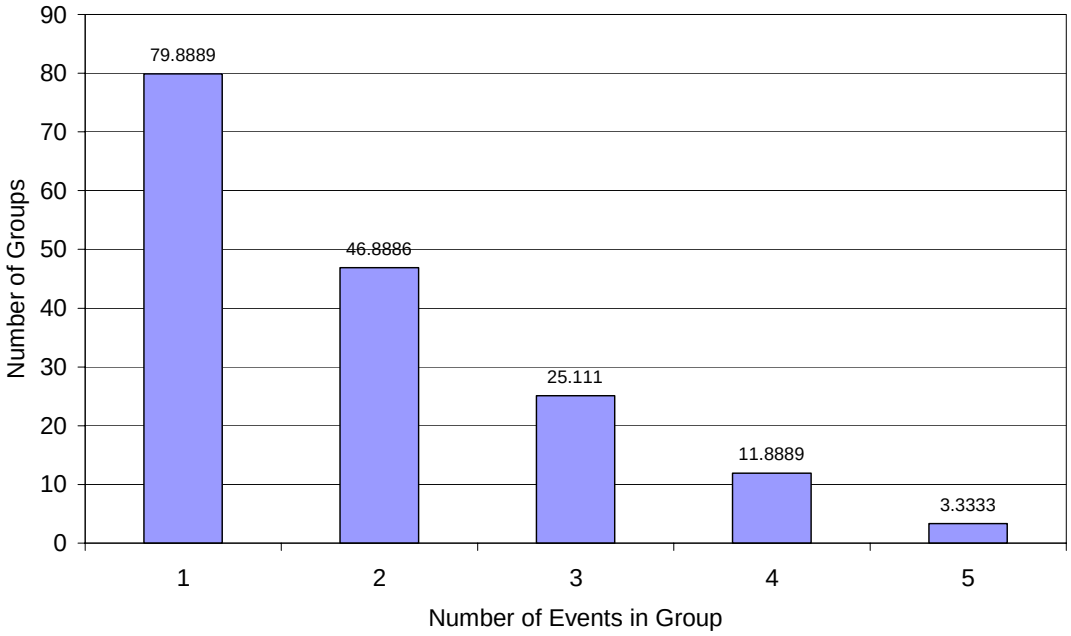

Figure 7.33 Mean number of events in groups of mean separation time of 0.16 s in total 120 s period.

The mean *PWP’* values tend to lie within the 80-90% range of events, but this may be an effect of simple averaging. It shows that the strongest gust appears last in the packet. Of most interest are the packets of strongest gusts, in the 90-100% *PWP’* category. In Figure 7.34 are the number of 90-100% gusts per packet for changing mean time separation.

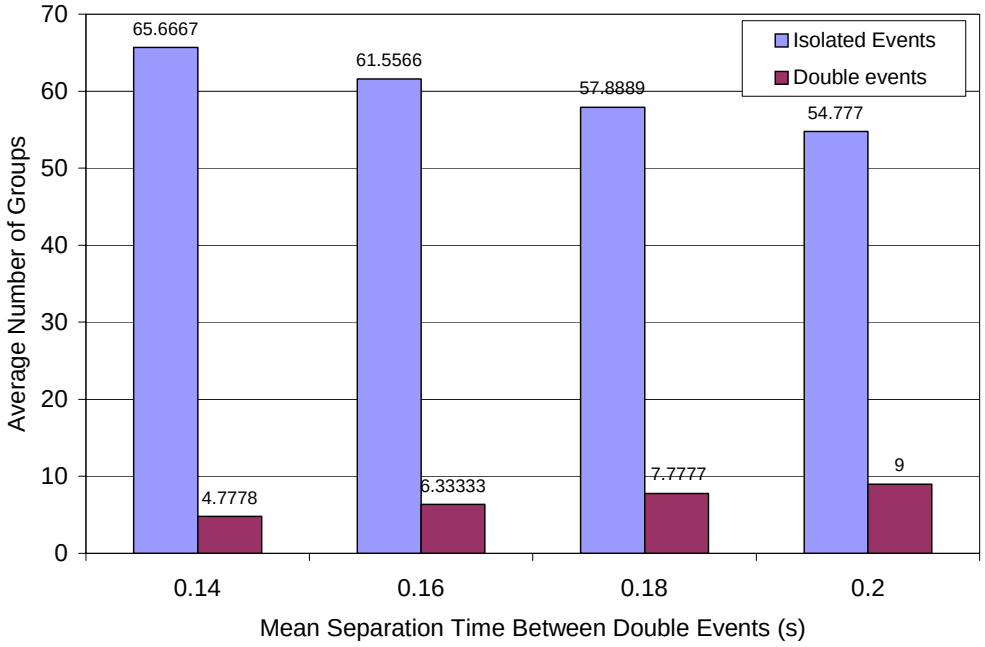

Figure 7.34 Gusts per packet with varying mean time separation using 90-100% WP' at 6.2 Hz.

The first thing to note is that there are no packets of three or above at this magnitude. The number of double groups is very small which supports the representation of an isolated gust in Figure 7.26a. Therefore, a so-called 'isolated' gust, may actually be an eddy pair. As would be expected, in Figure 7.34 the number of double gusts increase with the mean separation limit.

7.15 Transient Response of Tree Bending Moment

The wavelet analysis suggests further areas of research into the area of gust response. First, what is an ideal time length for a large strength gust, and what is the effect of packets of gusts hitting a trees? A simple model has been derived to demonstrate some of these effects. First, a tree can be considered to be a simple lumped mass on the end of a light flexible cantilever (see Figure 7.35).

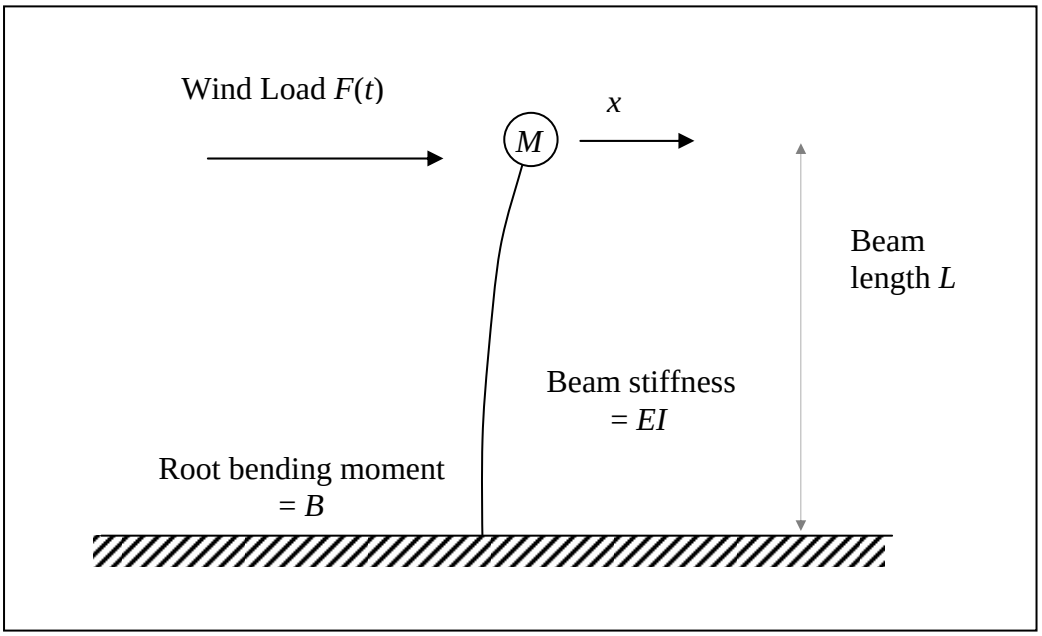

Figure 7.35 Tree simplified as a lumped-mass light-uniform cantilever model.

For no rotation, the equation of motion in the x direction can be approximated to:

$$M\frac{d^2x}{dt^2} + \frac{3EI}{L^3}x = F(t) \qquad [7.8]$$

Dividing through by M, and adding a damping term, gives the familiar expression:

$$\frac{d^2x}{dt^2} + 2\zeta\omega_n\frac{dx}{dt} + \omega_n{}^2x = \frac{F(t)}{M} \qquad [7.9]$$

If small angles are considered, the effect of gravity is to reduce the sway frequency of the tree such that:

$$\omega_n{}^2 = \frac{3EI}{ML^3} - \frac{g}{L} \qquad [7.10]$$

The theoretical and measured values of $\omega_n{}^2$ are shown in Table 7.3 for the tree upright, on its side, and upside down. Considering the simplicity of the model, and the assumption that EI is constant (taken as an average 5.425×10^{-4} N m^2) the comparison is good.

Natural Sway Frequency (Hz)	Upright	On side	Upside down
Calculated	5.6	5.7	5.9
Measured	5.48	5.85	6.05

Table 7.3 Effect of gravity on natural frequency.

For a general forcing function, $F(t)$, any solution of the equation has to be solved using the well established Convolution Integral Method (*e.g.* Steidel 1989). The method simplifies each forcing sample, $F(t)$, to an impulse from which the response of the system can be easily solved. The impulse response from each time sample, τ, before the time, t, is then integrated to solve the equation of motion for that time. Thus:

$$x(t) = \int_0^t F(\tau)\, g(t - \tau)\, d\tau \qquad [7.11]$$

where:

$$g(t-\tau) = \frac{1}{M\omega} \exp\{-\zeta\omega_n (t - \tau)\} \sin\{\omega (t - \tau)\} \qquad [7.12]$$

When considering the forcing function, $F(t)$, some major assumptions have to be made. First, the force is derived from the drag coefficient $F(t) = C_D\, 0.5\rho U^2$ and the velocity is taken as that at the centre of pressure (160 mm for a 200 mm tree). The velocity is taken as the streamwise velocity rather than resultant and the actual relative velocity is $(U-u_t)$ where u_t is the swaying velocity of tree. The largest assumption is that the centre of pressure is at the same height as the centre of mass. The centre of mass is at 0.105 mm from the ground, and the centre of pressure is at 0.160 mm. Comparison of terms show that the wind forcing term is larger than the mass acceleration term by a factor of 1000, thus justifying the use of the centre-of-pressure moment arm. Finally, the desirable end result variable is the bending moment for which the relation between the displacement and equivalent force, F', of a light cantilever is used as given in Equation 7.13.

$$x = \frac{F'L^3}{3EI} \qquad [7.13]$$

and so the bending moment is:

$$B = F'L = \frac{3EI}{L^2}x \qquad [7.14]$$

The parameters of the test tree were the natural sway frequency (corrected for damping) of 5.48 Hz and damping ratio in a mean wind speed of 0.081 (as given in Section 3.4.2).

7.15.1 Numerical Considerations

A problem occurs generating the solution due to the calculation of relative drag velocity. The tree sway velocity is calculated from a discrete derivation of position and therefore to calculate the next relative velocity value at the next position is actually needed. To reduce the effect of this problem the tree sway velocity is predicted using a first order Taylor series prediction. Acceleration is calculated using the first three position points, and the velocity predicted from that.

7.15.2 Investigation of Gust Length

The advantage of using the wavelet method to detect canopy gusts is that a characteristic velocity pattern has been established for a gust, and any further analysis can use this as a starting point. Using the top 10% of positive wavelet peaks from the high frequency analyses the tree response can be tested, as shown in Figure 7.36.

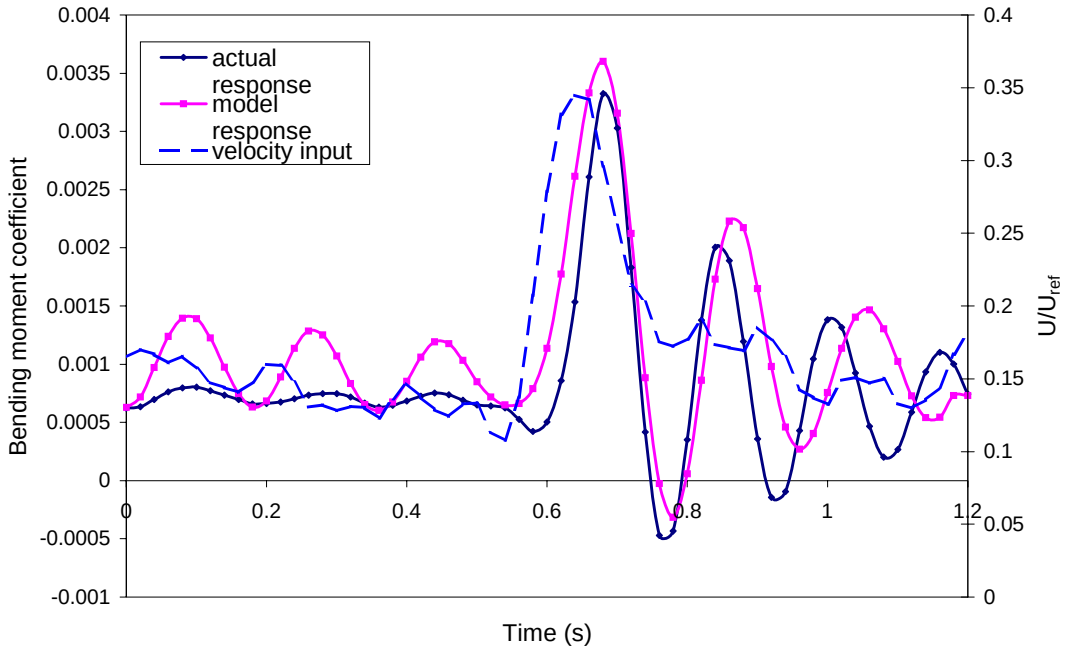

Figure 7.36 Actual response and model response of streamwise velocity wind loading.

The match, especially for the large gust, is reasonable, but after the gust there appears to be a difference in phase and frequency. It is possible that the conditional data, at a frequency of approximately 6 Hz, could be affected by the ensemble averaging process. Nevertheless, the peak moments are a good match for a simple model. The velocity signal can now be simplified, making it easier to manipulate (see Figure 7.37). Figure 7.31 shows that main difference between velocity signals of high and low frequency events, is the change in width of the main velocity peak. Although the lower dip also changes width, Figure 7.36 shows its contribution to the response of the tree is minimal. Therefore in a simplified study of lower frequency events, only the width of the main gust is adjusted, as presented in Figure 7.37.

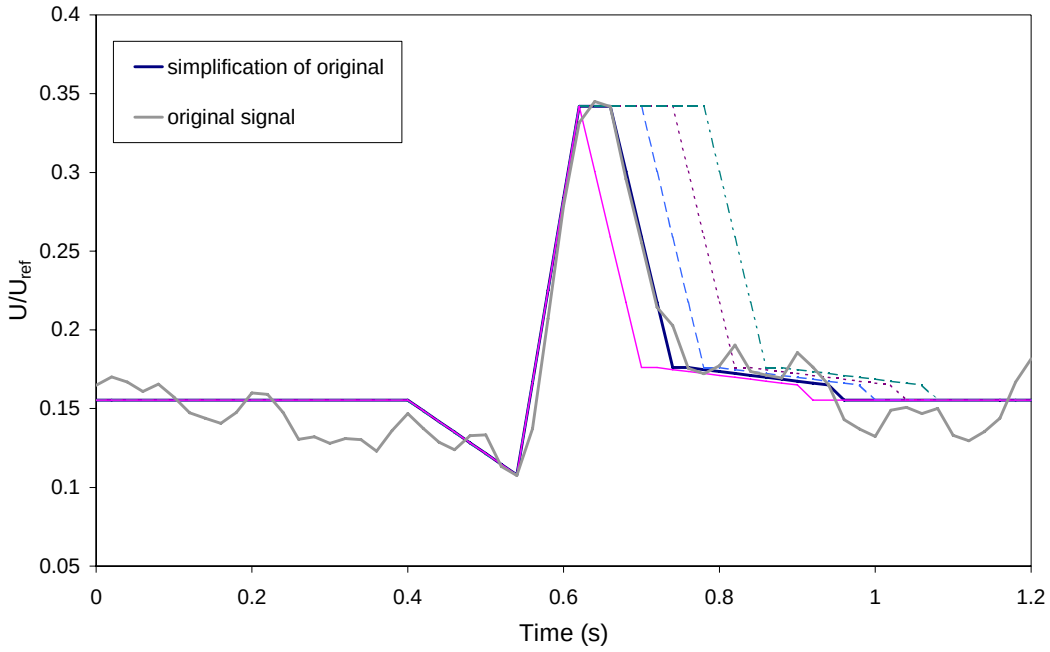

Figure 7.37 Simplification of original U signal. The dashed colour lines indicate an increase in width of main gust.

The response of these input waves are shown in Figure 7.38 which reveals that the velocity-wave obtained from the wavelet analysis produces the largest response from the test tree, and also the minimum overshoot. As the signal becomes wider the response approaches a step type, with oscillations about a new mean.

The tree model also allows analysis of multiple gusts. Once again, using the simplified *U* signal, some synthetic forcing functions can be produced, as demonstrated in Figure 7.39.

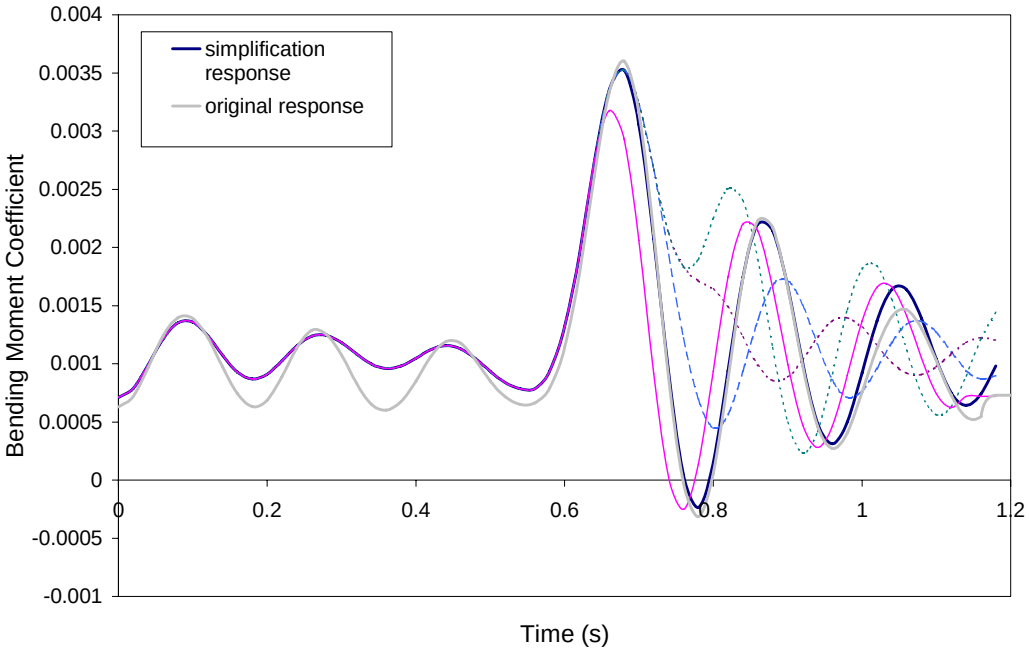

Figure 7.38 Response of velocity inputs of Figure 7.37.

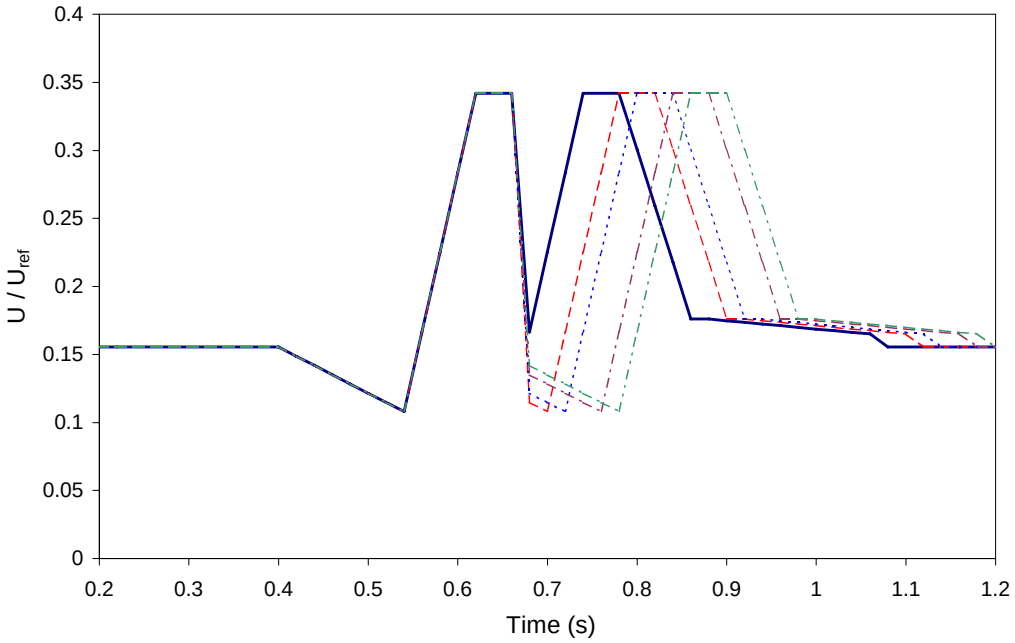

Figure 7.39 Synthetic multiple gust signals.

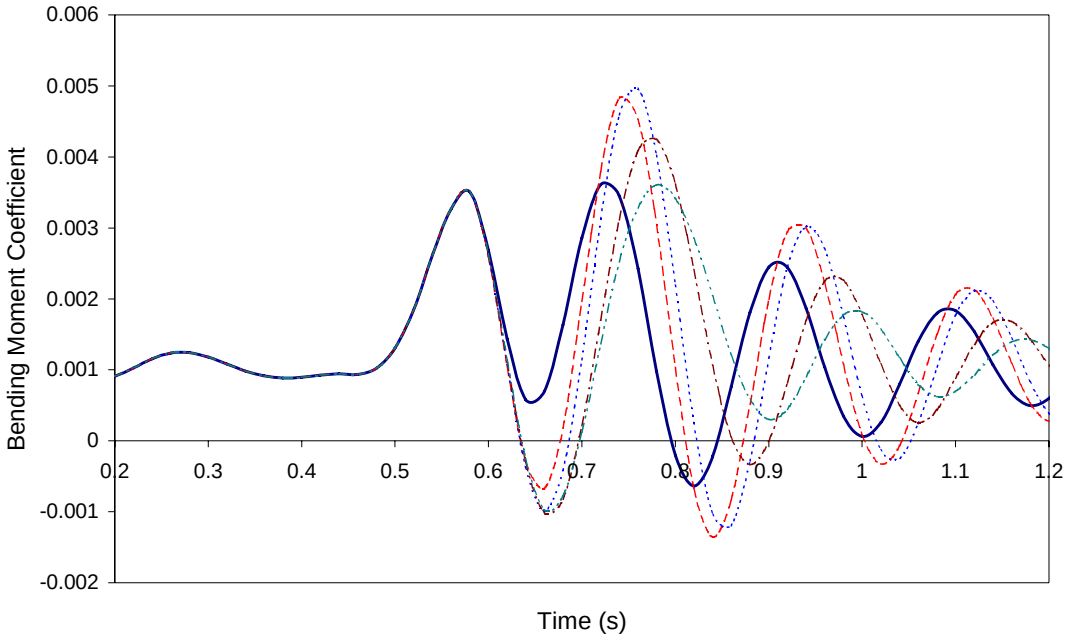

Figure 7.40 Response from multiple gust signals.

The response of the multiple signals in Figure 7.40 shows that the maximum bending moment is increased by approximately 1.66 times when the time between the gusts is 0.18 s. This is equivalent to 5.55 Hz whilst the tree frequency is 5.47 Hz, hence there is resonant effect occurring. If another gust is added to the line, then the maximum peak will increase further still. From Figure 7.34, there are approximately 8 packets of two gusts, every 120 s, of this mean separation and thus there is a high possibility of this type of mechanism occurring in the flow.

7.16 Conclusions

This chapter has shed light on the structure of canopy gusts by the use of conditional sampling methods on the flow over the uniform forest.

- The main structure of a gust appears to be an eddy-pair. The leading eddy is smaller and higher up, whilst the trailing eddy is larger and inclined towards the ground. This formation causes the characteristic small ejection, large downsweep of air widely reported

in canopy flows. This formation is also very similar to mixing layer flows, and thus provides more evidence for the mixing layer hypothesis.

- The largest bending moments are as expected, associated with the large downsweeps of air.
- Eddy-pairs appear to occur in packets, possibly caused by the modulation of the shear by lower frequency structures.
- A simple dynamic model of a tree revealed that the most damaging gusts are of the same frequency as the tree frequency. Any decrease in frequency approximates to a step input response. The model also showed that it is possible to increase the bending moment peak by pulsing gusts at the resonant frequency of the tree.

Chapter 8: Conclusions

In contrast to many field studies, and the few wind tunnel studies to date, the present work has benefited from the ability to provide detailed velocity and bending moment measurements at many locations throughout a forest model. The stability benefits on individual trees have been studied for forests of mixed ages, and this has also permitted an investigation of shear driven turbulence structures in the canopy.

8.1 Universal Flow Structures and a Gust Generation Mechanism

Evidence supports the theory that canopy flow coherent structures are related to a plane mixing layer type flow. The method suggested by Raupach *et al*. 1996 of using the shear length, L_s, to scale velocity profiles in the shear region has been shown to work well on the three different types of forests.

A mixing layer assumption was strongly supported by conditional analysis of the flow over the uniform forest. The eddy-pair structure found in many of the stronger canopy gusts is typical of a mixing layer flow. The leading eddy causes a weak, upward ejection of air out of the canopy, as reported by many observers. A large, downward inclined, eddy then produces the expected strong downsweep of air that ensues. The present experiment has confirmed that these strong downsweeps are responsible for the largest bending moments on individual trees. The peak bending moment was created by a canopy gust of equal period to the tree sway period. It was also shown that if gusts are generated one after another, at intervals of one tree-sway period, the maximum bending moment can be increased each time another gust passes.

Frequency analysis of the canopy flows have shown that the main fluctuating structures coincide with the sway frequency of the tallest trees, and it is hypothesised that these frequencies drive the shear layer instability roll up. In addition, detailed studied of the flow at the forest edge show these fluctuations originate from swaying of the edge trees.

To explain all these points a mechanism has been suggested for the generation of gusts in forests with a upstream edge. The mechanism depends upon the turbulence of the upstream flow to induce the swaying of the upwind edge group of trees. The swaying motion of these trees then perturbs the air further downstream, at tree sway frequency. Also immediately downstream of the edge, the shear layer begins to form near the top of the canopy. The fluctuating air causes a perturbation frequency to initiate the instability roll up of the shear layer. Canopy gusts are then formed from this roll up.

The current set of experiments has provided many pieces of evidence that has led to the current thinking outlined above. It is hoped that dedicated experiments will be carried out to prove such claims.

8.2 Implications for Forests of Irregular Height

Extreme bending moment measurements revealed that the group selection forest (a 50/50 mix of 200 mm and 100 mm trees) was worthy of further study. Velocity measurements confirmed that canopy gusts do not sufficiently penetrate the forest to disrupt the small trees. Bending moments also showed that the tallest trees in the forest sheltered the smaller trees very successfully, whilst the small trees limited the exposure of the tallest trees. The loads on the taller trees were lower in the group selection forest than in a thinned forest (in the absence of the smaller trees).

The mode to mean bending moment ratio for all three forest arrangements revealed a consistently low value at the upstream forest edge of approximately 2-4. Downstream the values fall into two groups, with a ratio of approximately 12 for the highest trees, and a ratio of approximately 6 for the protected, smaller trees in a forest. If current theories are correct, and tree growth adaptation is dependent upon mean, rather than extreme wind loading, this parameter may be vitally important in modelling and predicting future forest growth and risk to wind damage.

8.3 Suggestions for Further Work

It has become evident through the course of this work, that entwined within one another, are two very complex issues in their own right. These are, the fluid dynamics of porous, compliant, surfaces and the tree growth response to winds. Below are some suggestions for future experimentation and investigation.

8.3.1 Fluid Dynamic Investigations – Some Simple Experiments

The current project has led to a hypothesis that canopy gusts are generated by an upstream turbulence/ tree sway / shear layer instability mechanism. The limitations, and unnecessary complexity, of the forest model do not make it easy to study this mechanism. A future experiment would possibly involve the construction of a simplified ‘tree’ as shown in Figure 8.1. This model would have a well-defined centre of mass, centre of pressure and sway frequency, properties that lend easily to mathematical modelling. Practically, arrays of these models would be spaced so there is no clashing of elements. A longer fetch of model would be highly desirable. The edge gust generation mechanism could be investigated in several ways, for instance:

- Replacing edge trees with very stiff trees.

- Streamlining the edge.
- Forcing the edge trees mechanically to measure sway energy transferred into air movement.

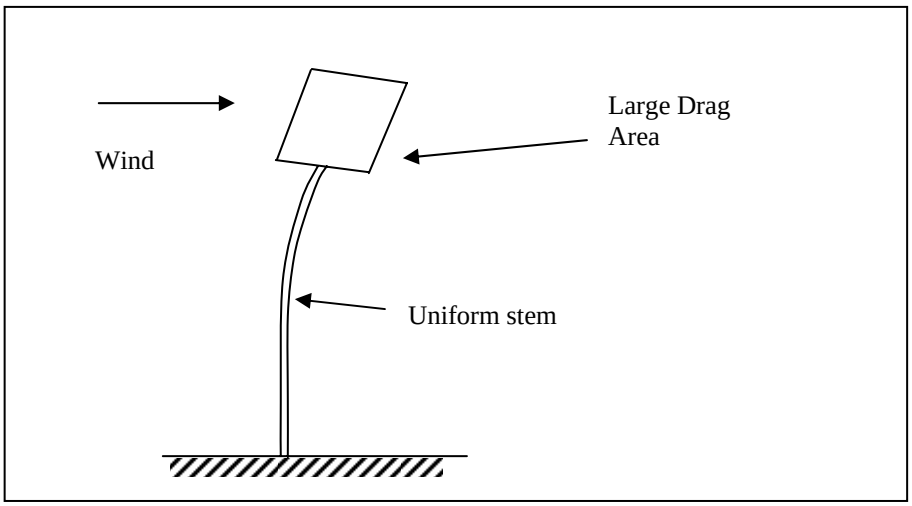

Figure 8.1 Possible 'simplified' tree with well-defined centre of pressure and centre of mass.

In addition, the present study has neglected the three-dimensionality of canopy gusts. Experimentation with a plane of laser light shone across the top of the forest allowed the movements of trees tops to be clearly observed. Such an experiment, used in conjunction with digital imaging, would allow the paths of flow structures to be tracked. An additional bonus, if the tree models are of sufficiently simple design, would be that simultaneous bending moments of *every* tree in the forest could be calculated from the movements of the tree tops only.

8.3.2 Forestry and Tree Investigations

One of the biggest limitations of wind tunnel testing of forests is that although the tests may produce useful results in terms of wind forces in existing forest plantations, it is not possible to predict how new plantations will grow and adapt to a changing wind environment. More detailed and accessible models of growth, and subsequent changes in physical parameters, are

required if results obtained from wind tunnel testing are to be truly representative of field measurements.

References

Acton E. 1976, ‘The modelling of large eddies in a two-dimensional shear layer’, Journal of Fluid Mechanics, 76, pp561-92.

Adrian R.J. 1986, ‘Multi-point optical measurements of simultaneous vectors in unsteady flow – a review’, International Journal of Heat and Fluid Flow, 7, pp127-145.

Baldocchi D.D., and Meyers T.P. 1988a. ‘Turbulence structure in deciduous forests’, Boundary Layer Meteorology, 43, pp345-364.

Baldocchi D.D., and Meyers T.P. 1988b. ‘A spectral and lag correlation analysis of turbulence in a deciduous forest’, Boundary Layer Meteorology, 45, pp31-58.

Baker C.J. 1995, ‘The development of a theoretical model for the windthrow of plants’, Journal of Theoretical Biology, 175, No. 3, pp355-372.

Baker C.J. 1996, ‘Measurements of the natural frequencies of trees’, University of Nottingham Report Number:FR96008.

Baines G.B.K. 1972, ‘Turbulence in a wheat crop’, Agricultural Meteorology, 10, pp93-105.

Blackwelder R.F. and Kaplan R.E. 1976, ‘On the wall structure of the turbulent boundary layer’, Journal of Fluid Mechanics, 76, pp89-112.

Bradley E.F. 1968, ‘A micrometeorological study of velocity profiles and surface drag in the region modified by a change in surface roughness’, Quarterly Journal of the Royal Meteorological Society, 116, pp361-379.

Brown G.L. and Roshko, A. 1974, ‘On density effects and large structures in turbulent mixing layers’, Journal of Fluid Mechanics, 64, pp775-816.

Cantwell B.J. 1981, ‘Organised motion in turbulent flow’, Annual Review of Fluid Mechanics, 13, pp457-515.

Chandrsuda C., Mehta R.D., Weir A.D. and Bradshaw P. 1978, ‘Effect of free-stream turbulence on large structures in turbulent mixing layers’, Journal of Fluid Mechanics, 85, pp693-702.

Chui C.K. 1992, ‘An Introduction to Wavelets’, Academic Press, London.

Collineau S., Brunet Y. 1993 ‘Detection of turbulent coherent motions in a forest canopy. Part II: Time-scales and conditional averages’, Boundary Layer Meteorology, 66, pp49-73.

Coutts M.P. and Grace J. 1995, ‘Wind and Trees’, Cambridge University Press, UK.

Den Hartog J.P. 1956, ‘Mechanical Vibrations’, Fourth Edition, McGraw-Hill, New York

Dimotakis P.E. and Brown G.L. 1976, ‘The mixing layer at high Reynolds number: large structure dynamics and entrainment’, Journal of Fluid Mechanics, 78, pp535-560.

Durst F., Melling A., and Whitelaw J.H. 1976, ‘Principles and practice of laser Doppler Anemometry’, Academic Press, London.

Edwards R.V. and Jensen A.S. 1983, ‘Particle sampling statistics in laser anemometers’, Journal of Fluid Mechanics, 133, pp397-412.

ESDU International Ltd., ‘Strong winds in the atmospheric boundary layer’, Wind Engineering Series, Data Items 82026, 83045, 84011, 85020.

ESDU International Ltd., ‘Characteristics of atmospheric turbulence near the ground’, Wind Engineering Series, Data Items 74030, 85020.

Finnigan J.J. 1979a, ‘Turbulence in waving wheat I’, Boundary Layer Meteorology, 16, pp181-211.

Finnigan J.J. 1979b, ‘Turbulence in waving wheat II’, Boundary Layer Meteorology, 16, pp213-236.

Finnigan J.J. and Brunet Y. 1995, ‘Turbulent airflow in forests on flat and hilly terrain’, In Wind and Trees. Eds. M.Coutts and J.Grace, Cambridge University Press, UK.

Fisher R.A. and Tippett L.H.C. 1928, ‘Limiting forms of the frequency distribution of the largest or smallest member of a sample’, Proceedings of the Cambridge Philosophical Society, 28, pp180-190.

Fraser A.I. 1962, ‘The soil and roots as factors in tree stability’, Forestry, 23, pp117-127.

Gao W. and Li B.L. 1993, ‘Wavelet analysis of coherent structures at the atmospheric-forest interface’, Journal of Applied Meteorology, 32, pp1717-1725.

Gardiner B.A. 1989, ‘Mechanical characteristics of Sitka Spruce’, Forestry Commission Occasional Paper 24.

Gardiner B.A. 1992, ‘Mathematical modelling of the static and dynamic characteristics of plantation trees’, In Mathematical Modelling of Forest Ecosystems, Eds. Franke J. and Roeder A., Sauerlanders Verlag, Frankfurt am Main, pp40-61.

Gardiner B.A. 1994, ‘Wind and wind related forces in a plantation Spruce Forest’, Boundary Layer Meteorology, 67, pp161-186.

Gardiner B.A. 1995, ‘The Interactions of wind and tree movement in forest canopies’, In Wind and Trees, Eds M.Coutts and J.Grace, Cambridge University Press, UK, pp41-59.

Gardiner B.A. and Stacey G.R. 1996, ‘Designing forest edges to improve wind stability’, UK Forestry Commission Technical Paper 16.

Gardiner B.A., Stacey G.R., Belcher R.E., Wood C.J. 1997, 'Field and wind tunnel assessment of the implications of respacing and thinning on tree stability', Forestry, 70, pp233-252.

Garrat J.R. 1992, 'The Atmospheric Boundary Layer', Cambridge University Press, UK, pp316.

Gash J.H.C. 1986, 'Observations of the turbulence downwind of a forest-heath interface', Boundary Layer Meteorology, 36, pp227-237.

Gumbel E.J. 1958, 'Statistics of Extremes', Columbia University Press, New York.

Gumley S.J. 1982, 'A detailed design method for pneumatic tubing systems', OUEL Report 1407/1982.

Head M.R. and Bandyopadhyay P.R. 1981, 'New aspects of turbulent boundary layer structure', Journal of Fluid Mechanics, 107, pp297-338.

Ho C. and Huang P. 1982, 'Subharmonics and vortex merging in mixing layers', Journal of Fluid Mechanics, 119, pp443-473.

Inoue E. 1955a, 'Studies of phenomena of waving plants ('Honami') caused by wind. I. Mechanism and characteristics of waving plant phenomena' (in Japanese), Journal of Agricultural Meteorology (Tokyo), 11, pp18-22.

Inoue E. 1955b, 'Studies of phenomena of waving plants ('Honami') caused by wind. II. Spectra of waving plants and plants 'vibration' (in Japanese), Journal of Agricultural Meteorology (Tokyo), 11, pp97-109.

Irvine M.R. 1994 'Turbulence and turbulent transport above and within coniferous forests', Ph.D. Thesis, University of Liverpool, UK.

Irwin H.P.A., Cooper K.R. and Girard R. 1979, 'Correction of distortion effects caused by tubing systems in measurements of fluctuating pressures', Journal of Wind Engineering and Industrial Aerodynamics, 5, pp1775-1786.

Kaimal, J.C. and Finnigan J.J., 1994, 'Atmospheric Boundary Layer Flows', Oxford University Press.

Kaspersen J.H. 1996, 'A study of coherent structures using wavelet analysis', Ph.D. Thesis, Norwegian University of Science and Technology, Trondheim, Norway.

Kruijt B., Klassen W., Hutjes R.W.A. 1995, 'Edge Effects on diffusivity in the roughness layer over a forest', In Wind and Trees, Eds. M.Coutts and J.Grace, Cambridge University Press, Cambridge UK.

Lee X., Shaw R.H and Black T.A. 1994, 'Modelling the effect of mean pressure gradient on the mean flow within forest', Agricultural and Forest Meteorology, 68, pp201-212.

Lesieur M. 1997, ‘Turbulence in Fluids’, Second Edition, Kluwer Academic Publishers, The Netherlands.

Letchford C.W. 1987, ‘Pneumatic averaging and its application in wind engineering’, D.Phil. Thesis, University of Oxford, UK.

Li Z.J, Miller D.R., and Lin J.D. 1985, ‘A first-order closure scheme to describe counter gradient momentum transport in plant canopies’, Boundary Layer Meteorology, 33, pp77-83.

Li Z.J., and Lin J.D. 1990, ‘Air flow over and through a forest edge: a steady state numerical simulation’, Boundary Layer Meteorology, 51, pp179-197.

Marshall B.J., Marwood R., Belcher R.E. and Wood C.J. 1998, ‘Laser Doppler Anemometry and Conditional Sampling’, Journal of Wind Engineering and Industrial Aerodynamics, In Press.

Marwood R. 1996, ‘An investigation of conical roof edge vortices’, D.Phil. Thesis, University of Oxford, UK.

Mattheck C. 1991, ‘Trees – the Mechanical Design’, Springer Verlag, Berlin.

Mayhead G.J., Gardiner J.B.H., and Durrant D.W. 1975, ‘Physical properties of conifers in relation to plantation stability’, Unpublished Report, Forestry Commission, Edinburgh.

Mayne J.R. and Cook N.J. 1980, ‘Acquisition, analysis and application of wind loading data’, Wind Engineering: Proceedings of the 5th International Conference (1979), Eds. Cermak J.E., Pergamon Press, Oxford, pp1339-1355.

McFadden P.D. and Zheng G.T. 1993, ‘Application of the wavelet transform to the early detection of gear failure by vibration analysis’, OUEL report 1999/93, Oxford University.

Meyer H. 1987, ‘Wind induced tree sways’, Trees, 1, pp195-206.

Michalke A. 1964, ‘On the inviscid instability of the hyperbolic-tangent velocity profile’, Journal of Fluid Mechanics, 19, pp543-556.

Michalke A. 1965, ‘On spatially growing disturbances in and inviscid shear layer’, Journal of Fluid Mechanics, 23, pp521-544.

Minson A.J. 1993, ‘Use of laser Doppler anemometer measurements near model buildings to determine wind loading on building attachments’, D.Phil. Thesis, University of Oxford, UK.

Mumford J.C. 1982, ‘The structure of the large eddies in fully developed turbulent shear flows. Part 1. The plane jet’, Journal of Fluid Mechanics, 118, pp241-268.

Mumford J.C. 1983, ‘The structure of the large eddies in fully developed turbulent shear flows. Part 1. The plane wake’, Journal of Fluid Mechanics, 137, pp447-456.

Perry A.E., Henbest S., and Chong M.S. 1986, ‘A Theoretical and Experimental Study of Wall Turbulence’, Journal of Fluid Mechanics, 165, pp163-199.

Qui J., Paw U.K.T., and Shaw R.H. 1995, 'Pseudo-wavelet analysis of turbulence patterns in three vegetation layers', Boundary Layer Meteorology, 72, pp177-204.

Quine C.P. 1995, 'Assessing the risk of wind damage to forests: practice and pitfalls', In Wind and Trees, Eds. M.Coutts and J.Grace, Cambridge University Press, Cambridge UK.

Raupach M.R., Bradley E.F, and Ghadiri H. 1987, 'A wind tunnel investigation into the aerodynamic effect of forest clearings on the nesting of Abbot's Booby on Christmas Island', Progress report on a study commissioned by the Australian National Parks and Wildlife Service.

Raupach M.R., Finnigan J.J., Brunet Y. 1996, 'Coherent eddies and turbulence in vegetation canopies: The mixing-layer analogy', Boundary Layer Meteorology, 78, pp351-382.

Rogers M.M. and Moser R.D. 1992, 'The three dimensional evolution of a plane mixing layer: the Kelvin-Helmholtz rollup', Journal of Fluid Mechanics, 243, pp183-226

Schlichting H. 1979, 'Boundary Layer Theory', Seventh Edition, McGraw-Hill, New York.

Seigner I., Mulhearn P.J., Bradley E.F. and Finnigan J.J. 1976, 'Turbulent flow in a model plant canopy', Boundary Layer Meteorology, 10, pp423-453.

Somerville A. 1980, 'Wind stability: forest layout and silviculture', New Zealand Journal of Forestry Science, 10, No.3, pp476-501.

Shaw R.H., Brunet Y., Finnigan J.J. and Raupach M.R. 1995, 'A wind tunnel study of air flow in waving wheat: two point velocity statistics', Boundary Layer Meteorology, 76, pp349-376.

Simpson R.L. 1991, 'The structure of the near-wall region of two-dimensional turbulent separated flow', Philosophical Transactions of the Royal Society of London A, 336, pp5-17.

Stacey G.R., Belcher R.E., Wood C.J. and Gardiner B.A. 1994, 'Wind and wind forces in a model Spruce Forest', Boundary Layer Meteorology, 69, pp311-334.

Steidel R.F. 1989, 'An Introduction to Mechanical Vibrations', Third Edition, John Wiley and Sons, New York.

Surry D. and Stathopoulos T. 1977, 'An experimental approach to the economical measurement of spatially averaged wind loads', Journal of Wind Engineering and Industrial Aerodynamics, 2, pp385-397.

Townsend A.A. 1976, 'The Structure of Turbulent Shear Flow', Cambridge University Press, Cambridge UK, pp429.

Williamson C.H.K. 1996, 'Vortex dynamics in the cylinder wake', Annual Review of Fluid Mechanics, 28, pp477-539.

Wood C.J. 1977, ‘The Oxford University 4m x 2m Industrial Aerodynamics Wind Tunnel’, Oxford University Experimental Laboratory Report 1188/77.

Wood C.J. 1995, ‘Understanding wind forces on trees’, In Wind and Trees, Eds. M.Coutts and J.Grace, Cambridge University Press, Cambridge, UK.

Wood C.J. and Neild S.A. 1998, ‘Estimating stem and root –anchorage flexibility in trees’, submitted to Tree Physiology.

Wood D.H. and Bradshaw P. 1982, ‘A turbulent mixing layer constrained by a solid surface. Part 1. Measurements before reaching the surface’, Journal of Fluid Mechanics, 122, pp57-89.

Wood D.H. and Bradshaw P. 1984,‘A turbulent mixing layer constrained by a solid surface. Part 2. Measurements in the wall-bounded flow’, Journal of Fluid Mechanics, 139, pp347-361.

Wygnaski I., Oster D., Fiedler H.E., and Dziomba B. 1979, ‘On the perseverance of a quasi-two-dimensional eddy-structure in a turbulent mixing layer’, Journal of Fluid Mechanics, 93, pp325-335.

Zhuang Y. and Amiro B.D., 1994, ‘Pressure fluctuations during coherent motions and their effects on the budgets of turbulent kinetic energy and momentum flux within a forest’, Journal of Applied Meteorology, 33, pp704-711.

Appendix A: Stodola Method for Vibration Solutions of a Tapered Beam with Multiple Point Loads

The model trees needed for the irregular forest study were developed using the Stodola method for obtaining mode shapes and vibration frequencies. The method was originally developed between 1905 and 1920 and is explained in detail in Den Hartog (1956). Although originally developed as an iterative graphic solution it is readily implemented on a spreadsheet. In this case the design was carried out on a core Excel spreadsheet program written by C.J. Wood with the facility for multiple loads added by the author.

Stodola Method

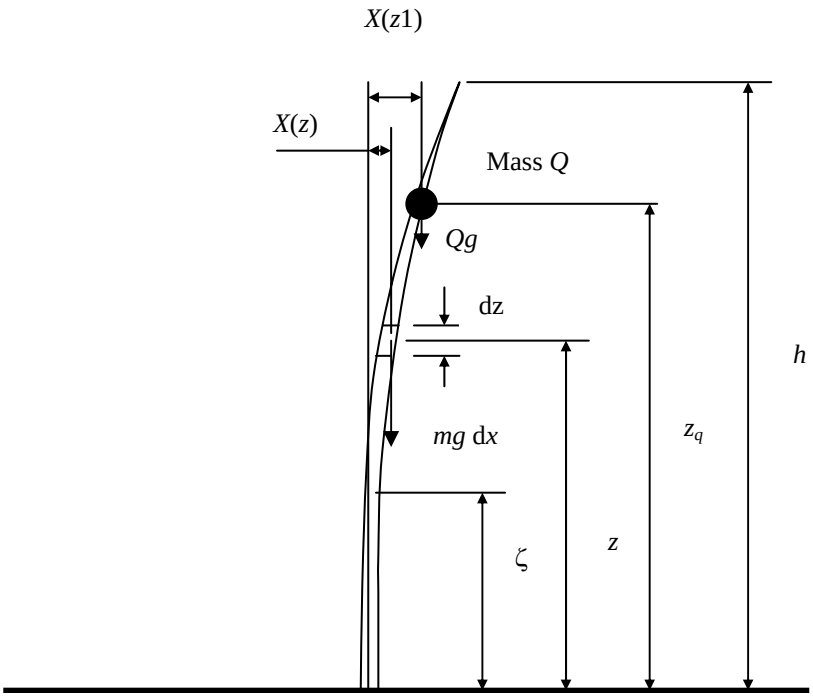

Figure A.1 Diagram for bending notation.

The deflection $x(z,t)$ at any height z is assumed to be sinusoidal with amplitude $a(z)$ and angular frequency ω. The spatial distribution of sway amplitude $a(z)$ (i,e, the mode shape), is unknown.

$$x(z,t) = a(z) \sin(\omega t) \qquad [a1]$$

The lateral acceleration of the tree at height z is then found by differentiating the displacement twice with respect to time t.

$$\ddot{x}(z,t) = - a(z) \ \omega^2 \sin(\omega t) \qquad [a2]$$

To cause this acceleration, a force $w(z,t)$ dz must be exerted on each height-element dz of the tree. This can only arise as the difference between horizontal shear forces exerted on the element by the adjoining parts of the tree stem above and below. If the tree has mass distribution $m(z)$ per unit length, then shear force $w(z,t)$:

$$w(z,t) = m(z) \ a(z) \ \omega^2 \sin(\omega t) \qquad [a3]$$

The bending moment at any height ζ arises primarily from the distributed inertia loading $w(z,t)$ at all heights above ζ. However, this moment is increased by the weight $m(z)\ g$ dz of the tree elements at all heights above ζ and $Q\ g$ of the point mass. The former overhangs at any instant by a horizontal distance $x(z,t) - x(\zeta,t)$ and the latter by $x(z_q,t) - x(\zeta,t)$ (***[ ]*** in Equation a4 represents the Macaulay indicator). Including these contributions, the bending moment is given by

$$M(\zeta,t) = \int_z^h w(z,t) \, (z - \zeta) \, dz \ + \ \int_z^h m(z) \, g \, \{ x(z,t) - x(\zeta,t) \} \, dz$$

$$+ \ Q \, \ddot{x}(z_q,t) \, [z_q - \zeta] \ + \ Q \, g \, \{x(z_q,t) - x(\zeta,t)\} \, [z_q - \zeta]^{\,0} \qquad [a4]$$

For the special case when ζ = 0, the ground-level bending moment is given by

$$M(0,t) = \int_0^h w(z,t)\, z\, dz \;+\; \int_0^h m(z)\, g\, x(z,t)\, dz + Q\,\{\, \ddot{x}(z_q,t)\, z_q + g\, x(z_q,t)\,\} \qquad [a5]$$

By virtue of the assumed single frequency vibration associated with each mode shape, it is also reasonable to expect that the bending moment $M(\zeta,t)$ will also be sinusoidal and in phase with the sway deflection

$$M(\zeta,t) = M(\zeta)\sin(\omega t) \qquad [a6]$$

Thus, when Equations a1, a2, a3, a5 & a6 are substituted in Equations a4 and a5, the periodic terms vanish, to leave an equation for the moment amplitude $M(\zeta)$ in terms of the displacement amplitudes $a(z)$.

$$M(\zeta) = \int_z^h m(z)\, a(z)\, w^2(z-\zeta)\, dz \;+\; \int_z^h m(z)\, g\{a(z) - a(\zeta)\}dz \;+\; Q\, a(z_q)\, \omega^2\, [z_q - \zeta]$$

$$+\; Q\, g\, \{a(z_q) - a(\zeta)\}[z_q - \zeta]^0 \qquad [a7]$$

$$M(0) = \int_0^h m(z)\, a(z)\, w^2 z\, dz \;+\; \int_0^h m(z)\, g\, a(z)\, dz + Q\, a(z_q)\,\{\omega^2 z_q + g\} \qquad [a8]$$

Definition of Stiffness

For small deflections, the curvature is related to the distribution of bending moment M(ζ) by the Euler-Bernoulli theory of bending

$$M(\zeta) = EI(\zeta)\frac{d^2a}{d\zeta^2} \qquad [a9]$$

where E is a nominal value of Young's Modulus, and $I(\zeta)$ is a nominal second moment of area of the tree cross section. For homogeneous circular stem cross-sections at all heights, the second moment of area would be defined in terms of the tapering diameter $D(\zeta)$ by

$$I(\zeta) = \frac{\pi \ D(\zeta)^4}{64} \qquad [a10]$$

Moment-Area Theorem for Displacement Distribution

Given that the stem has a distribution of curvature and an additional inclination at ground level, the second moment area theorem gives the deflection distribution $a(z)$ as follows

$$a(z) = \int_0^z \{ z - \zeta \} \frac{d^2a}{d\zeta^2} \, d\zeta \qquad [a11]$$

Substituting Equations a8 and a9 to introduce the bending moments in place of the curvature and inclination terms, the Moment-Area theorem may be written:

$$a(z) = \int_0^z \{ z - \zeta \} \frac{M(\zeta)}{EI(\zeta)} \, d\zeta \qquad [a12]$$

Equation a7 gives the bending moment distribution $M(\zeta)$ in terms of the displacement distribution $a(z)$, while Equation a12 gives the deflection distribution $a(z)$ in terms of bending moment distribution $M(\zeta)$. These two equations must be solved simultaneously to find the mode shape $a(z)$ and thus the angular frequency ω.

The Stodola spreadsheet program iteratively calculates these parameters until convergence criteria level is met. Extra points are easily added in Equation a7. The method was tested using known results for uniform cantilevers, and also for an existing 200 mm model tree. The maximum error for the tree calculation was 3.3%.

Model Tree Parameters

The design parameters for the new set of model trees are listed below.

LW = Large Whorl Drag Element, SW = Small Whorl Drag Element

	100 mm tree	**150 mm tree**	**250 mm tree**	**300 mm tree**	**Original 200 mm**
Branch Heights (mm)	LW – 46 LW – 62 LW – 78 SW - 94	LW – 74 LW – 90 LW – 100 LW –122 SW - 138	LW – 144 LW – 160 LW – 176 LW – 192 LW - 208 LW – 224 SW - 240	LW – 178 LW – 194 LW – 210 LW – 226 LW – 242 LW – 258 LW – 274 SW – 290	LW – 92 LW – 107 LW – 124 LW - 141 SW – 156 SW – 171

Table A.1 Positioning of drag elements on model trees.

LW mass = 0.1305 g, SW mass = 0.059 g.

Stem density ≈ 1.11 g cm^{-3}. Tree stem made from Nylon 66, Modulus of Elasticity used in calculations = 6.25 N mm^{-2}. Taper ratios for trees given in Table 3.3.

Appendix B: Pitot Tube Design

Section 7.8 details the use of a pitot tube for measuring total pressure over the canopy top. Shown below is the tube design specifications and graphs of phase response and amplitude ratio response are shown in Figures B.1 and B.2.

Part of Tube	Length (mm)	Diameter (mm)
Steel tube to air	39	1.02
Polythene tube	310	1.3
Restrictor	6	0.305
Polythene tube to scanivalve	200	1.3

Table B.1 Pitot tube design specifications.

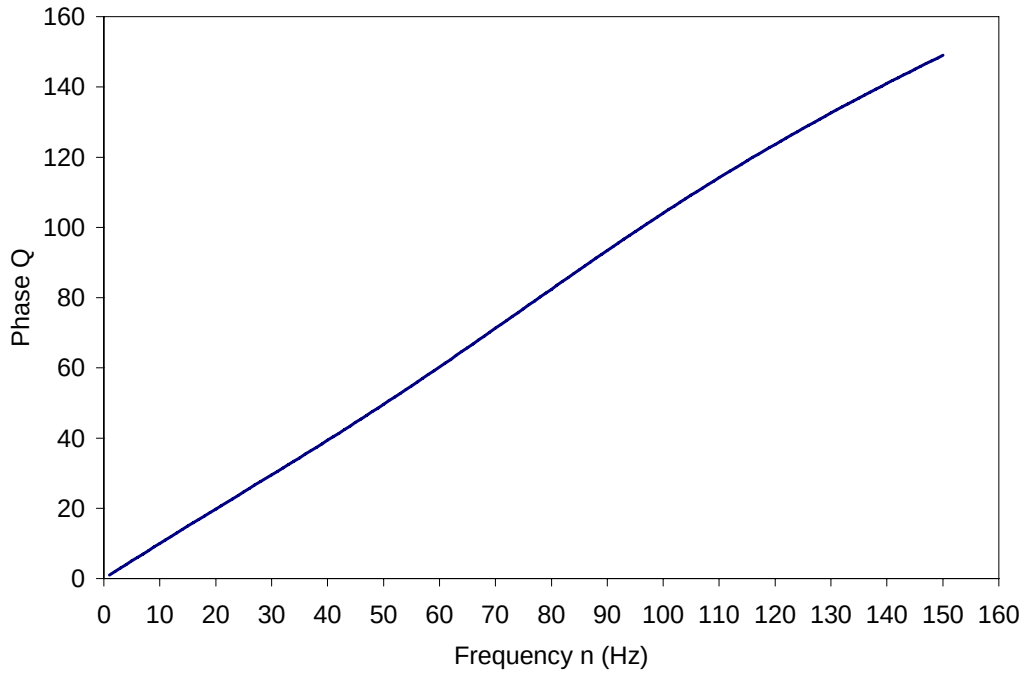

Figure B.1 Phase response of pitot tube.

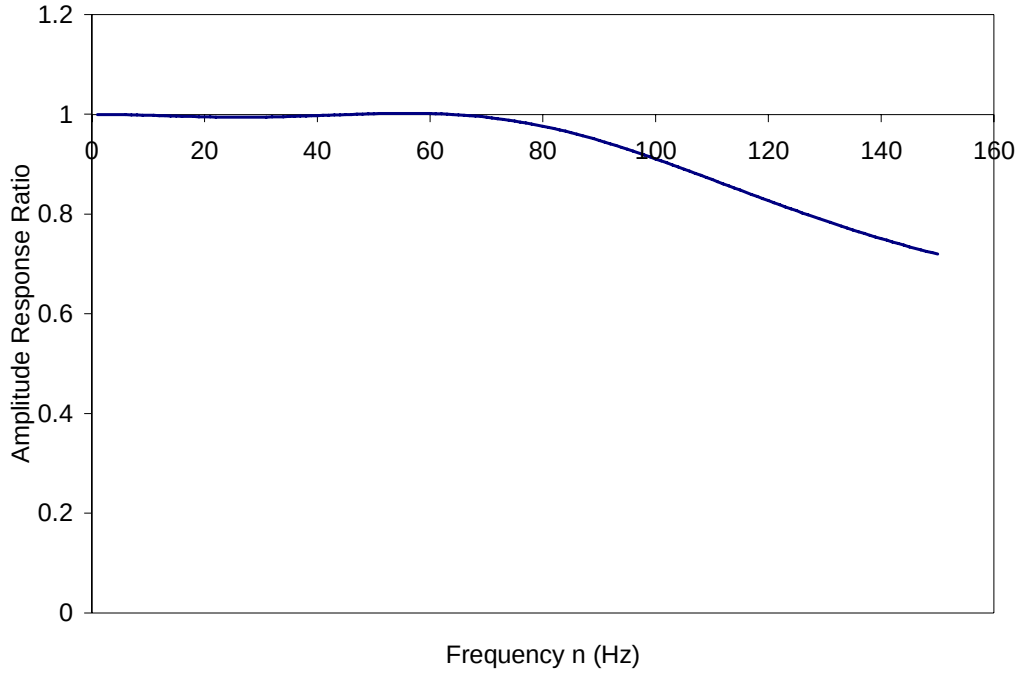

Figure B.2 Amplitude response of pitot tube.